



**Multiscale modelling of intracranial aneurysm
evolution: A novel Patient-specific
Fluid-Solid-Growth (p-FSG) framework
incorporating endothelial mechanobiology**

Yuqian Mei
Supervisor: Paul N.Watton

A thesis submitted for the degree of PhD
Department of Computer Science

Jan 2019

A thesis submitted for the degree of PhD.

**Multiscale modelling of intracranial aneurysm evolution:
A novel Patient-specific Fluid-Solid-Growth (p-FSG)
framework incorporating endothelial mechanobiology**

By Yuqian Mei, Department of Computer Science

Abstract

IAs (intracranial aneurysms) affect 2-5% of the adult population with a high fatality rate upon rupture. However, the rupture rate is around 0.1%-1% per year which indicates most aneurysms are stable. This leads to a strong demand for clinicians to have a better understanding of the aneurysm stability for treatment planning. Aneurysm stability is thought to be linked to its mechanical environment from both the blood flow and the pulsatile pressure giving the mechanistic signals to vascular cells. A cascade of subsequently biological reactions through the routine of cellular mechanotransduction within the aneurysm tissue determine the development of aneurysms. It is envisaged that mechanistic modelling of biological processes that govern aneurysm growth may help to distinguish between vulnerable and stable aneurysms.

We developed an integrated Patient-specific Fluid-Solid-Growth (p-FSG) framework for simulating the growth of existing intracranial aneurysms. An aneurysm and connected arteries are modelled as fibre-reinforced nonlinear elastic soft-tissue in the commercial software ANSYS. Computational Fluid Dynamics (CFD) simulation quantifies haemodynamic stimuli that act on endothelial cells. Here, we link the morphology of the cells (spindle, hexagonal) to a novel flow metric (Anisotropic Ratio, AR) that characterizes the oscillatory nature of the flow pattern. We then proposed a hypothesis that the endothelial permeability could be regarded as a function of the morphology of endothelial cells which is associated to the growth and remodelling of the aneurysmal tissue. Mass density of elastin and collagen decreases in the region of high endothelial permeability via the inflammatory pathway. Collagen growth (mass changes) is driven by stretch based stimuli of fibroblast cells. Collagen remodelling

employs a stress-mediated method that restores the Cauchy stress on collagen fibres to homeostatic levels in the course of the aneurysm enlargement. Principal destructive and self-protective activities during the aneurysm evolution involving elastin, collagen fibres, endothelial cells and fibroblasts are mathematically represented by our p-FSG framework. Our research suggests that the collagen growth function is a vital mechanism for the stability of aneurysms.

This is the first framework models the aneurysm evolution on the basis of the patient-specific aneurysm geometry. Also, we incorporated the functionality of endothelial cells quantified by a novel flow metric to the aneurysm growth and remodelling (G&R) model. This automatic p-FSG framework fully integrated into ANSYS engineering software provides a foundational platform for modelling the aneurysm growth and might become a practical tool in the estimation of aneurysm stability.

Statement of Originality

I hereby declare that this submission is my own work and to the best of my knowledge it contains no materials previously published or written by another person, or substantial proportions of material which have been accepted for the award of any other degree or diploma at the University of Sheffield or any other educational institution, except where due acknowledgement is made in the thesis.

Any contribution made to the research by others, with whom I have worked at the University of Sheffield or elsewhere, is explicitly acknowledged in the thesis.

I also declare that the intellectual content of this thesis is the product of my own work, except to the extent that assistance from others in the project design and conception or in style, presentation and linguistic expression is acknowledged.

YUQIAN MEI

July 5, 2019

Acknowledgement

I would like to express my sincerely gratitude to my supervisor Dr. Paul Watton, for his unwavering guidance and support throughout my doctoral study in the University of Sheffield. And he also gave me fascinating opportunities for attending the national and international academic conferences which allows me to present my research and receive priceless feedbacks. I would like to thank Dr. Xishan Li and Dr Maria-Cruz Villa-Uriol who also gave me lots of professional ideas in improving my research throughout my doctoral study. I also would like to thank Dr Kewei Li, who works at University of Graz, who continuously encourages me and spares no effort to help me on my structural model. We also have a big warm research family supporting each other as a strong group and all my colleagues, Catherine, I-Tung, Katia, Raj, Hamna, Shakti, and Giulia help me a lot during my study, both in the academic research and my daily life. Specially, I would like to thank I-Tung, Hamna, Junmin Xiao, Pinxi Liu and Li Zhang who accompany me during the period in Sheffield like family members and we share lots of memorable moments here. Finally, I have to thank my family for supporting me to study abroad and promote myself. I could not make this far without your unconditional love and continuous support.

A very special gratitude I would like to give to the Chinese Scholarship Council and University of Sheffield for helping and providing funding for my doctoral study.

Dissemination

Conference Proceedings and Presentations

Watton, P., Mandalzi, A., Wong, W., **Mei, Y.**, Robertson, A., & Gundiah, N. (2016). *Modelling the mechanobiological evolution of intracranial aneurysms: an integrative in vivo, in vitro and in silico approach*. In Proceedings of the 7th European Congress on Computational Methods in Applied Sciences and Engineering. Crete Island, Greece, June 5-10.

Chan I., Watton P. N. and **Mei, Y.**. *A novel Fluid-Solid-Growth-Transport framework for arterial growth and remodelling*, Summer School on Biomechanics of Soft Tissues, Graz University of Technology, Austria, July 4th-8th, 2016.

Mei, Y., Chan, I., Chen, D., & Watton, P. (2017). *A Novel Fluid-Solid-Growth Transport (FSGT) Framework For Modelling the Evolution of Intracranial Aneurysm Disease*. In Proceedings of the 5th International Conference on Computational & Mathematical Biomedical Engineering (pp.1271-1272). Pittsburgh, USA, April 10-12.

Mei, Y., Evans, P., Gundiah, N., Robertson, A., Watton, P. (2018). *Intracranial Aneurysm: Mechanistic Modelling of Aneurysm Stability*. International Neurovascular Exploratory Workshop - iNEW'2018. Zurich, Switzerland, Feb. 07-09.

Mei, Y., Evans, P., Gundiah, N., Robertson, A., Watton, P. (2018). *Modelling the Evolution of Patient-Specific Intracranial Aneurysm*. UK Conference On Multiscale Biology, University Of Nottingham, Nottingham, UK. Apr. 16-18.

Mei, Y., Evans, P., Gundiah, N., Watton, P. (2018). *Intracranial Aneurysms: A Patient-Specific Fluid-Solid-Growth (FSG) Framework with Modelling of Endothelial Response*. Insigneo Showcase, Sheffield, UK, May-03.

Mei, Y., Evans, P., Gundiah, N., Robertson, A., Watton, P. (2018). *A Patient-Specific Growth Model of Intracranial Aneurysm for Assessing Stability*. VPH-CaSE. University College London, London, UK, Jul. 19-20.

Mei, Y., Evans, P., Gundiah, N., Watton, P. (2018). *Intracranial Aneurysms: A Patient-Specific Fluid-Solid-Growth (FSG) Framework with Modelling of Endothelial Response*. Multi-scale

hard and soft tissue modelling workshop, The Edge, Endcliffe, Sheffield, UK. Jun. 18-20.

Mei, Y., Evans, P., Gundiah, N., Robertson, A., Watton, P. (2018). *Intracranial Aneurysm: A Patient-Specific Fluid-Solid-Growth (FSG) Framework with Modelling of Endothelial Response*. Abstract on Virtual Physiological Human - VPH for in silico Medicine. Zurich, Switzerland, Sep. 05-07.

Awards

First Presentation Prize (2017): Training day for PhD students and RAs, SoftMech, University of Glasgow, Glasgow, UK.

First Poster Prize (2018): Multi-scale hard and soft tissue modelling workshop, The Edge, Endcliffe, Sheffield, UK. Jun. 18-20.

ACRONYMS

AAAs	aortic abdominal aneurysms	IFs	intermediate filaments
AFI	Aneurysm Formation Indicator	MRI	magnetic resonance imaging
CFD	computational fluid dynamics	P-FSG	patient-specific fluid-solid-growth
CT	computed tomography	OSI	Oscillatory Sear Index
ECM	extracellular matrix	SMCs	smooth muscle cells
ECs	endothelial cells	SEF	strain energy function
EEL	external elastin lamina	TAWSS	Time-Averaged Wall Shear Stress
F-actin	actin filaments	WSS	wall shear stress
FSG	fluid-solid-growth	WSSAR	WSS anisotropic ratio
GON	Gradient Oscillatory Number	WSSG	Temporal and Spatial Wall Shear Stress Gradient
GR	growth and remodelling		
IAs	intracranial aneurysms		
IEL	internal elastin lamina		

Contents

1 Introduction: Intracranial Aneurysms	0
1.1 Intracranial Aneurysm Disease	0
1.1.1 Classification	1
1.1.2 Locations	2
1.1.3 Treatment Options	2
1.1.4 Motivation: Clinical Demands	4
1.2 Structure of Cerebral Arterial Wall	5
1.2.1 Type of Intracranial Arteries	5
1.2.2 Tunica Intima	7
1.2.3 Tunica Media	7
1.2.4 Tunica Adventitia	8
1.2.5 Key Vascular Components	9
1.3 Variations of Arterial Tissue over Aneurysm Evolution	14
1.4 Aneurysm Rupture Risk Estimation	16
1.4.1 Features of Ruptured and Unruptured Aneurysms	16
1.4.2 Challenges in Aneurysm Risk Assessment	19
1.5 Research Outline and Thesis Organization	19
2 Review of Fluid-Solid-Growth(FSG) Framework in the Modelling of Aneurysm Evolution	22
2.1 Constitutive Model of Healthy Artery	23
2.2 Review of the Modelling of Aneurysm Evolution	25

2.2.1	Solid-Growth Models	25
2.2.2	Fluid-Solid-Growth Models	26
2.2.3	Thin-walled to Thick-walled Models	27
2.3	Overview of the Developed Fluid-Solid-Growth(FSG) Model	29
2.3.1	Geometry Reconstruction	29
2.3.2	CFD Simulation and Structural Analysis	31
2.3.3	G&R: Elastin Degradation Function	32
2.3.4	G&R: Collagen Growth and Remodelling	34
2.4	Limitations of the State-of-the-art FSG framework	36
2.5	Novelties of the p-FSG Framework	37
3	Implementation of a Novel Hemodynamic Index for Representation of Endothelium Permeability	40
3.1	Computational Fluid Dynamics Simulation	41
3.1.1	CFD Theory	41
3.1.2	3D Patient-Specific Intracranial Aneurysm Geometries	42
3.1.3	Mesh Generation and Boundary Condition	46
3.1.4	Simulation Implementation	49
3.1.5	Spatial and Temporal Grid Independence Study	50
3.2	Hemodynamic Results	56
3.2.1	Haemodynamic indices for analysis	56
3.2.2	Results and Discussion: Representative Hemodynamic Distributions	61
3.3	Correlation Analysis between Hemodynamics and Aneurysm Growth	71
3.3.1	Review: Hemodynamics and Aneurysm Growth	71
3.3.2	Correlation Analysis	73
3.4	A Novel G&R Hypothesis: WSSAR-Endothelium Permeability-G&R function	76
3.4.1	Morphology of Endothelial Cells in Aneurysm	76
3.4.2	Endothelial Cells Morphology Characterized by Flow Pattern	77
3.4.3	Hypothesis: Endothelium Permeability to Aneurysm Growth	80
3.5	Conclusion	81
4	Structural modelling of Patient-Specific IA Models	84
4.1	Generation of the Thick-walled Aneurysm Model	85
4.2	Meshing and Boundary Conditions	87

4.2.1	Meshing Methodology	87
4.2.2	Imposition of Boundary Conditions	88
4.2.3	Grid Independence Study in Structural Modelling	89
4.3	Mechanical Parameters Study of Elastineous Constituents and Collagen Fibres	90
4.3.1	Constitutive Models	93
4.3.2	Parametric Study of the Mechanical Properties for Elastin and Collagen Fibres	95
4.4	Collagen Fibres Alignment Distribution	102
4.4.1	Methodology of Principal Curvature Acquisition on Irregular Geometries	103
4.4.2	Collagen Fibres Distribution on Patient-Specific IA Models	105
4.5	Model Implementation with ANSYS	106
4.5.1	Partition of the Structural Model	106
4.5.2	Transformation of Global Coordinate System	107
4.5.3	ANSYS Implementation	109
4.6	Results and Discussion	110
4.6.1	Displacement Distribution	110
4.6.2	Distribution of Equivalent Strain	112
4.6.3	Distribution of Equivalent Stress	113
4.6.4	Conclusion	114
5	Aneurysm Evolution Modelling using the p-FSG Framework	116
5.1	Development of the Patient-Specific FSG (p-FSG) framework	117
5.1.1	Improvements in contrast to FSG framework	118
5.1.2	Workflow of the p-FSG framework	119
5.2	Key Hypotheses in Aneurysm Growth and Remodelling	122
5.2.1	Elastin Degradation	122
5.2.2	Collagen Remodelling	123
5.3	Illustrative Model: p-FSG linking with steady flow - low WSS	126
5.3.1	Contribution of low WSS to Aneurysm Growth	126
5.3.2	Results and Discussion	128
5.4	Renovated p-FSG with A Pulsatile Flow Metric - WSSAR	133
5.4.1	Motivation: Key Pathological Contributions to Aneurysm Continuous Growth and Rupture	133
5.4.2	Hypothesis of Aneurysm Growth with Respect to WSSAR	135

5.4.3	Results	138
5.4.4	Discussion and Conclusion	143
6	An integrated P-FSG Framework Incorporating Collagen Growth Function	146
6.1	Collagen Growth Function Represented by Fibroblasts	147
6.1.1	Mechanisms Between Fibroblasts and Collagenous Constituents	148
6.1.2	Remodelling the Recruitment Configuration of Fibroblasts	149
6.1.3	Growth/Atrophy of the Collagen Fabric	150
6.1.4	Implementation with ANSYS	151
6.2	Summary: An integrated P-FSG framework	152
6.3	Two Comparative Cases with Collagen Growth Function Turning on/off	154
6.3.1	Models Setting Up	155
6.3.2	Results of Two comparative Cases	157
6.3.3	Collagen Remodelling	161
6.3.4	Adaption of Collagen Mass	163
6.3.5	Collective Variation from Collagen Degradation and Adaption	165
6.4	Illustrative Results Link with Flow Metric with An Updated Prismatic Mesh	167
6.4.1	Prismatic Mesh Generation	167
6.4.2	p-FSG link with WSSAR	168
6.4.3	p-FSG link with OSI	170
6.5	Discussion	172
6.6	Concluding Remarks	174
7	Conclusion: Summaries and Considerations for Future Development	176
7.1	Summaries and Contributions	177
7.1.1	Brief Summaries for Preceding Chapters	177
7.1.2	Main Contributions	178
7.2	Limitations	180
7.3	Potential Improving Points in Future Work	181
7.3.1	Sophistication of the Structural Model	181
7.3.2	Modelling Endothelium Permeability Mechanobiologically	182
7.3.3	Transport Model with Thrombosis	183
7.3.4	Model Validation by Clinical Follow-up Data	184
7.4	Concluding Remarks	184
A	Procedures of Getting Principal Directions of Flow	210
B	Representative Validation Models of Principle Curvature Distribution	214

C Endothelial Cells Alignment under Combined WSS and Cyclic Stretch	218
D Matlab Script of G&R Function in the P-FSG Framework	230

List of Figures

1.1	Illustrative morphological representation of healthy artery and different aneurysm types	1
1.2	The most frequent locations for aneurysm formation in intracranial vasculature	3
1.3	Major treatment options of intracranial aneurysms	4
1.4	Schematic diagram of vascular structure of elastic artery, muscular artery and arteriole	6
1.5	General arterial wall structure of detailed fibre alignment and specific schematic structure of intracranial arterial wall	8
1.6	Diagram of endothelial cell structure and the cell-cell junction	10
1.7	Three types of matrix contacts distinguished from fibroblasts on the two-dimensional substrates	12
1.8	Schematic diagram of elastic fibre	13
1.9	Pathological mechanism of cerebral aneurysm formation and rupture	15
2.1	The pressure-diameter distension of an artery showing the nonlinear behaviour especially at higher pressures; Tension-radius relationship tested on treated and untreated external iliac artery where the treated artery contains only elastin or collagen fibres respectively	23
2.2	Fluid-Solid-Growth computational framework	30
2.3	Reconstructed model with the aneurysm part substituted by a cylinder membrane	31

2.4 A circular patch in the center of the unfolded cylinder is defined for the elastic constituents degradation	33
3.1 Schematic of the original physiological aneurysm geometries in phase I and II and corresponding aligned geometries	43
3.2 Schematic of the original physiological aneurysm geometry with anatomical structure names and corresponding optimized geometry for modelling	44
3.3 Subdivision of the vascular domain and quantitative terms for the morphology analysis of the aneurysm geometry	45
3.4 Translucent upstream and downstream parent vessels on the sides of aneurysm connect to the inserted aneurysm part to fulfil the mesh generation. The updated aneurysm replaces the original geometry constituting an integrated geometry.	47
3.5 Pulsatile boundary conditions obtained through @neufuse in a full cardiac cycle	49
3.6 Distribution diagrams of statistics of element quality for case 1 and case 4	51
3.7 Grid independence study using the ICA-2 model: WSS magnitudes distribution on the same extracted profile from point A to point B on the aneurysm region of case 1-4.	53
3.8 Grid independence independence study using the ICA-2 model: WSS distributions on the aneurysm geometry of case 1-4 are plotted and the specific locations with significant difference are marked by rectangles.	54
3.9 Unstructured tetrahedron mesh along with 4-layer prisms of ICA-1 and ICA-2 model	54
3.10 Time-step independence study: WSSAR distributions on the aneurysm geometry of five scenarios	55
3.11 Representative shear rosettes show the WSS variation during one cardiac cycle including the accelerating phase and decelerating phase	60
3.12 Primary haemodynamic results of steady flow condition	62
3.13 Counter plot of TAWSS distribution over one cardiac cycle with follow-up configuration	63
3.14 Counter plot of TAWSS distribution over one cardiac cycle with follow-up configuration of ICA-1 model(translucent). The color map is limited to 0-2.5 Pa.	63
3.15 Counter plot of OSI distribution on the patient-specific geometries of ICA-1 and ICA-2 cases	65
3.16 AFI contour plot at midsystolic deceleration (MSD) mapped on the patient-specific geometries of ICA-1 and ICA-2 cases	66

3.17 Counter plot of spatial WSSG distribution on the patient-specific geometries of ICA-1 and ICA-2 cases	68
3.18 GON distribution mapped on the patient-specific geometries of ICA-1 and ICA-2 cases over the cardiac cycle	69
3.19 WSSAR distribution mapped on the patient-specific geometries of ICA-1 and ICA-2 cases over the cardiac cycle	71
3.20 The DI index distribution plotted as a surface map of the G_1 geometry for the ICA-1 case	74
3.21 The ASR index distribution plotted as a surface map of the G_1 geometry for the ICA-1 case	75
3.22 Microscopy images of endothelial cells morphology and alignment on the parent artery and aneurysm apex with different haemodynamic conditions	76
3.23 TAWSS distribution plotted on ICA-2 model and shear rosettes of 3 points with similar TAWSS magnitude	78
3.24 WSSAR distribution in the bifurcation region and the downstream sections with the colour map limited to 0.5 to 1	79
3.25 WSSAR distribution on the ICA-2 model and corresponding endothelial cells morphology distribution over one cardiac cycle	80
4.1 Extraction of the aneurysm segment and the generation of the thickness on the aneurysm model	86
4.2 Illustrative model of solid mesh with hyperelastic property	87
4.3 Boundaries condition applied on the thick-wall aneurysm model consisting of pressure on the inner surface and fixed constraints on the connection surfaces	88
4.4 Displacement distributions on aneurysm after the structural modelling of Scenario 1 and Scenario 4	90
4.5 Collagen fibers configuration in the adventitia of the carotid artery at different pressures	91
4.6 Constituents difference between cerebral arterial wall and aneurysm wall	92
4.7 Unloaded and loaded configurations of the analytical model of a cylinder	96
4.8 Collagen fiber architecture in the media and the adventitia layer of arterial wall	97
4.9 Mechanical behaviours of elastin, collagen and the total arterial wall in the healthy artery; Load bearing ratio of elastin and collagen under various pressures for healthy artery	99
4.10 Unloaded and loaded configurations of the analytical model of sphere	100

4.11 Mechanical behaviours of elastin, collagen and the total arterial wall in the healthy artery; Load bearing ratio of elastin and collagen under various pressures for aneurysm	102
4.12 Schematic diagram of the definition of principal curvatures and the calculation procedures	103
4.13 Schematic diagram of the first and second principal curvatures and principal directions represented by unit vectors	104
4.14 Distribution of first principal curvature direction on aneurysm surface	106
4.15 Segments of the structural model: aneurysm, parent vessel, transitional region	107
4.16 Coordinate system transformation for entire geometry	108
4.17 TB table which defines the input format for anisotropic hyperelasticity model.	110
4.18 Initial distributions of mass density of elastineous constituents, k_1 and k_2 distributions on the aneurysm model	110
4.19 Color coded imaging of aneurismal wall displacement at peak systole	111
4.20 Distribution of the von-Mises elastic strain on the aneurysm model	112
4.21 Distribution of the von-Mises stress on the aneurysm model	114
5.1 Schematic diagram of the p-FSG framework	120
5.2 Illustrative workflow of the p-FSG framework	121
5.3 Illustration of the influence of k_2 magnitude on pressure-stretch relationship on aneurysm model	124
5.4 Elastin degradation function $\mathcal{F}_D(\tau)$ utilising WSS threshold values	127
5.5 Initial distributions of material parameters of the structural model	128
5.6 Displacement distribution through the thickness of aneurysm model and the corresponding inner surfaces of the growing aneurysms	129
5.7 WSS spatial distribution on the inner surface of aneurysm model at $t=0$ and $t=18$	130
5.8 Spatial evolution of normalised mass density of elastin in the aneurysm model at $t = 0, 9, 18$	131
5.9 Elastin degradation proportion distributes on aneurysm model at $t=9$ and $t=18$	132
5.10 Spatial evolution of collagen parameter k_2 in the aneurysm geometry at $t = 0, 9, 18$	132
5.11 Elastineous constituents degradation function $\mathcal{F}_{D(WSSAR)}^E$ varies with WSSAR ($WSSAR_{crit} = 0.5$ and $WSSAR_{max} = 0.75$).	136
5.12 Comparison of elastineous constituents degradation function $\mathcal{F}_{D(WSSAR)}^E$ and $\mathcal{F}_{D(WSSAR)}^C$ varies with WSSAR	138

5.13 Total displacement distributions on the aneurysm model and the corresponding enlarged inner surface showed with translucent contour at t=0 and t=46 respectively	139
5.14 WSSAR distribution on aneurysm models at t=0 and t=46 with rectangular boxes where shows relatively recognizable variation	140
5.15 The $\mathcal{F}_{D(WSSAR)}^E$ distribution dependent on the WSSAR calculated from the fluid simulation and the subsequent m^E evolution	142
5.16 The $\mathcal{F}_{D(WSSAR)}^C$ distribution dependent on the WSSAR calculated from the fluid simulation and the subsequent m^E evolution	142
5.17 Spatial distribution of k_2 at t=0, 23, 46 indicates mechanical behaviour changing of collagen fibres as the aneurysm evolution	143
6.1 Detailed design of the whole P-FSG framework shows the key hypotheses and the workflow from the medical images to achieve the stability of the aneurysm model	153
6.2 A sphere model is located at the larger bulb of the aneurysm model, which restricts the degradation region for elastin and collagen fibres	155
6.3 Comparison of deformations from the original state of aneurysm between Case 1 and Case 2	158
6.4 Mass density evolution of elastin in the aneurysm model	159
6.5 Mass density evolution of collagen in the aneurysm model	160
6.6 Cauchy stress distribution at homeostasis, the stress deviation from the homeostatic level and the corresponding k_1 remodelling results of first collagen family	161
6.7 Cauchy stress distribution at homeostasis, the stress deviation from the homeostatic level and the corresponding k_1 remodelling results of second collagen family	163
6.8 Fibroblasts stretch in the direction of collagen families and consequent mass density variation of collagen fibres	164
6.9 Collective mass density of two families of collagen fibres from the destructive degradation and growth function in case 1.	165
6.10 Effective stiffness distribution of two families of collagen fibres for case 1 and case 2	166
6.11 Prismatic mesh on the aneurysm model	168
6.12 Spatial distribution of WSSAR at initial state and normalised mass density of collagen fibres as aneurysm evolves with degradation linked to WSSAR from left to right at t=3 and t=6.	169

6.13 Left (A-B) and right (C-D) lateral views of pressurized aneurysm and the final state of the aneurysm growth.	169
6.14 Left (A-B) and right (C-D) lateral views of pressurized aneurysm and the final state of the aneurysm growth.	170
6.15 Spatial distribution of OSI at initial state and normalised mass density of collagen fibres as aneurysm evolves with degradation linked to WSSAR from left to right at t=4 and t=7.	171
6.16 Left (A-B) and right (C-D) lateral views of pressurized aneurysm (t=0) and the final state (t=7) of the aneurysm growth mediated by OSI.	172
7.1 A conceptual model of aneurysm with a thrombus layer embedded	183
A.1 Schematic diagram of the three manipulation angles in the calculation of the principal directions	211
B.1 Schematic diagram of the first and second principal curvatures on a cylinder surface and an artificial cylinder model	215
B.2 Distributions of principal curvature direction on an ellipsoidal model	216
B.3 Mesh of the artificially cylindrical and ellipsoidal model	217
C.1 Summary of the signal transduction pathway involved in human cerebral microvascular endothelial cells activated by physiological and pathological stretch tension	220
C.2 Schematic diagram of different χ^{BSI} ranges and the responses of endothelial cells to the cyclic stretches in every scenario	224
C.3 Schematic diagram of the influence weight of WSS and CS to ECs orientation varied with different WSS magnitude range	224
C.4 Schematic diagram of the final orientation of endothelial cells influenced by WSS and cyclic stretch in a 2D space	225
C.5 Schematic diagram of the final orientation of endothelial cells influenced by WSS and cyclic stretch in a 3D space	227
C.6 Schematic diagram of the final orientation of endothelial cells influenced by WSS and cyclic stretch in a cylindrical model. (red arrow: WSS; blue arrow: cyclic stretch; white arrow: endothelial cells orientation)	227

List of Tables

1.1	Constituents in intima, media and adventitia layers of elastic artery, muscular artery and arterioles.	6
3.1	General clinical information of the patient	44
3.2	Statistics of the morphology information of the aneurysm	46
3.3	General mesh information of different study cases	50
4.1	Mesh statistic information and key results of four study scenarios	89
4.2	Summary of geometrical parameters and mechanical parameters of elastin and collagen constituents for arterial wall and aneurysmal wall	107
5.1	Summery of WSSAR in different levels at t=0 and t=46	141
6.1	Summary of geometric information of aneurysms models at different stages	157
C.1	Key parameters information of representative endothelial cells in Fig C.4	226



Introduction: Intracranial Aneurysms

1.1 Intracranial Aneurysm Disease	0
1.2 Structure of Cerebral Arterial Wall	5
1.3 Variations of Arterial Tissue over Aneurysm Evolution	14
1.4 Aneurysm Rupture Risk Estimation	16
1.5 Research Outline and Thesis Organization	19

1.1 Intracranial Aneurysm Disease

Aneurysm is an abnormal dilation happened to vascular system and it can present at any blood vessel. Due to the low blood pressure in venous system, normally the word 'aneurysm' means the arterial aneurysm. When the diameter of the bulge out region is 1.5 folds larger than the diameter of its connected arteries, we call a aneurysm is formed. The most common aneurysms are abdominal aneurysms and intracranial aneurysms while this research focuses on intracranial aneurysms.

Intracranial aneurysm (IAs), also named as cerebral aneurysm, is a life-threatening vascular disease due to the weakening of blood vessel wall happened in the brain vasculature and leads to a high mortality and disability rate. Saccular intracranial aneurysms are discovered in a small population group (<5%), usually in elderly population and more prevalent in females reportedly (Sekhar, Heros, 1981; Mettinger, 1982). Toshio Nakagawa found the incidence of asymptomatic and unruptured intracranial aneurysms was 6.5% in a dataset of 400 volunteer (Nakagawa, Hashi, 1994). Even though the rupture rate is relatively low about 0.1%-1% per year (Wiebers et al., 2003; Thompson et al., 2015) but it could lead to severe consequence, like perpetual brain damage or death (Juvela et al., 2008; Weir, 2002). It is reported that approximately 25% of cerebrovascular deaths are induced by ruptured aneurysms (Fogelholm et al., 1993) and 5 to 15% of stroke cases are related to ruptured IAs (Bederson et al., 2000). It's difficult to estimate the exact number of people who are affected by cerebral aneurysms because they are usually asymptomatic and remain undetected.

1.1.1 Classification

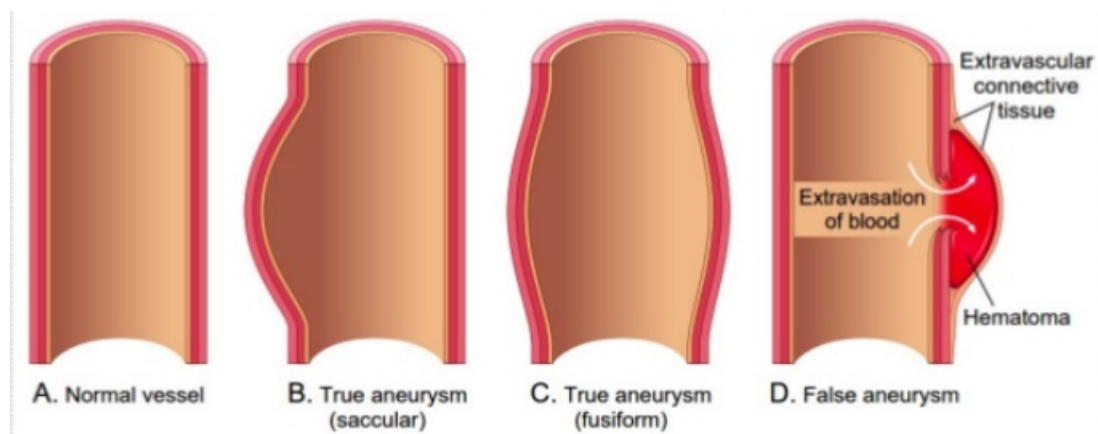


Figure 1.1: Illustrative morphological representation of healthy artery and different aneurysm types.

(<https://www.slideshare.net/csbrprasad/cvs-aneurysmsampdissectioncsbrp>)

Morphologically, the distinction between healthy arteries and aneurysms is the abnormal dilation. According to the dilation form, aneurysms are normally divided into saccular aneurysms and fusiform aneurysms (Figure 1.1 B,C) which are one-side dilation and two-side symmetric dilation respectively. Another distinction criterion is the formation reason: true aneurysm is owing to the weakening of arterial wall and eventually the aneurysm is surrounded by the real wall tissue; false aneurysm (pseudoaneurysm) is starting from a small leak

hole on the wall and which forms an extravascular hematoma without a real wall surrounded by. Intracranial aneurysms usually belongs to the saccular type while most of abdominal aneurysms are fusiform aneurysms. These two types of aneurysms are often studied separately on the ground that the pathogenesis, symptoms and treatments vary significantly between them (Lasheras, 2007).

1.1.2 Locations

Theoretically, aneurysm can occurs at any site in our vascular system. In venous system, it is less common to see aneurysms because of the low blood pressure. In terms of vascular artery, aneurysms are often located on the aorta artery, femoral artery, iliac artery, popliteal artery and cerebral artery. In a general way, aneurysm easily occurs at bifurcations, origins of branching and zones with sharp curvature (Krings et al., 2011).

Figure 1.2 highlights the most prevalent sites of intracranial aneurysm formation in the Circle of Willis. Anterior communicating artery has the highest incidence rate around 30% while the posterior inferior cerebral artery has the lowest probability which is 3% (Brisman et al., 2006).

1.1.3 Treatment Options

Aneurysm disease is often asymptomatic resulting in that most of aneurysms are diagnosed incidentally. Clinically, the identification and diagnosis of an intracranial aneurysm is dependent on the computed tomography (CT), magnetic resonance imaging (MRI) or intracranial angiography (Forsting, Wanke, 2009). The treatment of aneurysms should consider the size, state of aneurysms as well as the patient condition (Brisman et al., 2006). There mainly are five options for the treatment protocol for IAs: observation, clipping, the utilization of detachable coils (coiling), stent-assisted coiling and blood flow diverters (Figure 1.3) and the later three options aim at stopping the blood supply to the aneurysm region with the assistance of thrombus formation.

Observation requires patients to take periodic follow-up images with physician visiting to review the development of aneurysms. Clipping is an effective and developed surgical treatment for brain aneurysms which has achieved excellent results but it has a major limitation from patient physical conditions, such as patients who already have severe brain injury are not suitable. Coil embolization has been reported that it produces significantly fewer complications than surgical clipping (Claiborne Johnston et al., 2000). Studies have indicated that the morbidity rate for surgical clipping and coiling range from 4.0–10.9% and 3.7–5.3%,

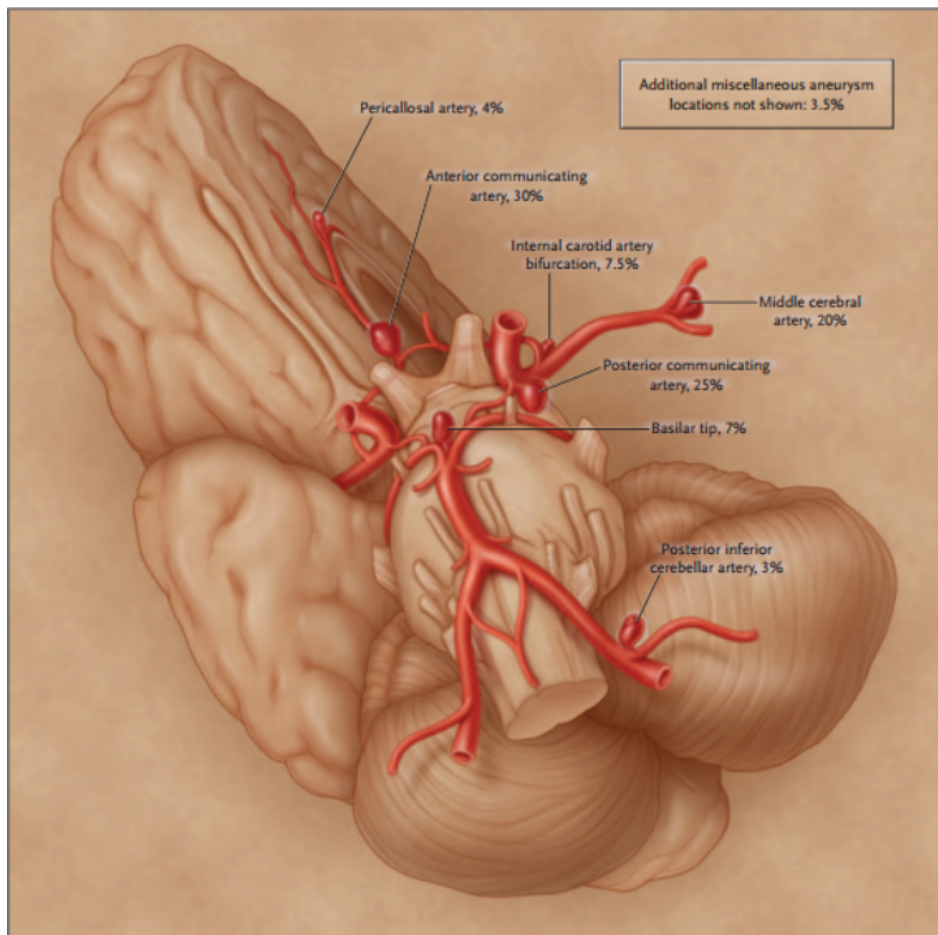


Figure 1.2: The most frequent locations for aneurysm formation in intracranial vasculature (adapted from (Brisman et al., 2006))

whereas mortality rates for that two are 1–3% and 1.1–1.5% respectively (Brisman et al., 2006). Moreover, stent-assisted coiling can achieve a significantly higher progressive thrombosis rate and lower recurrence rate than the coiling independently although the initial occlusion rate is relatively lower (Hong et al., 2014). The flow-diverter devices have emerged as a new generation of intraluminal implants that are designed as a treatment protocol for aneurysm through reconstructing the diseased parent artery (Nelson et al., 2011). It was reported by a Meta-analysis that the early and late mortality are 2.8% and 1.3% respectively and also current clinical employment of flow diverter was not supported by high quality evidence which needs further investigation (Arrese et al., 2013).

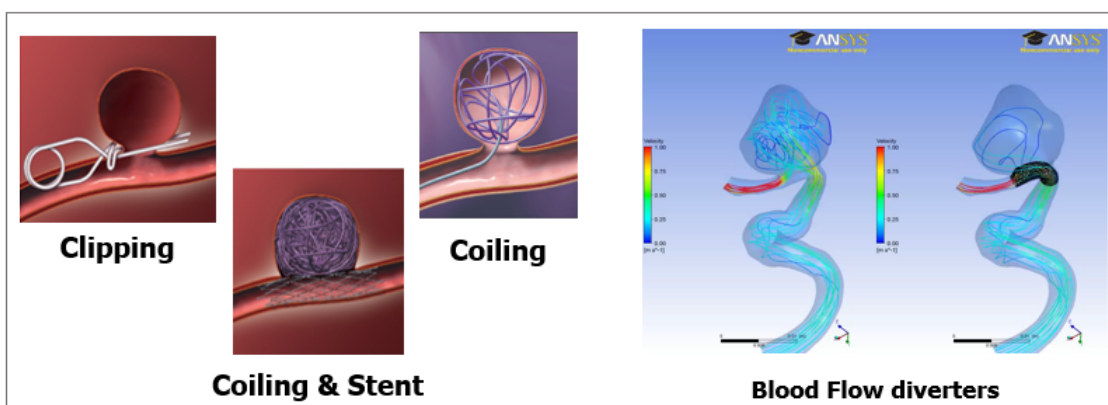


Figure 1.3: Major treatment options of intracranial aneurysms

1.1.4 Motivation: Clinical Demands

The rupture of intracranial aneurysms often cause devastating subarachnoid hemorrhage and death. According to statistics from NHS (National Health Service) in the UK, it could be as high as 1 in 20 people are affected by brain aneurysms. Most aneurysms are stable aneurysms which can remain in the body safely and only need the periodically observation by medical images clinically. Therefore, it is important to differentiate the stable aneurysm and vulnerable aneurysms, which can avoid the unnecessary of treatment.

There is so far no specific treatment to prevent IA growth or rupture. When clinicians estimate a high risk of rupture mostly based on the morphological characteristics, surgical clipping or endovascular coiling remain the preferable options. However, these treatment methods are accompanied with risks during the implementation of procedures in the surgery themselves, and also carry risks of complications in a long-term consideration. Therefore, identification of unruptured aneurysms is significant to reduce surgical risks and relief commercial burdens for patients. However, an accurate assessment of the risk of rupture remains challenging and most likely leads to an overtreatment of IAs (Diagbouga et al., 2018). This leads to an urgent demand in the estimation of the stability of aneurysms, i.e. predicting the growth of aneurysms. A meta analysis found that a higher rupture rate was associated with growing aneurysms which was 3.1% per year compared with 0.1% per year for non-growing aneurysms (Brinjikji et al., 2016). However, it is extremely hard to differentiate the stable aneurysms and vulnerable aneurysms depending on images. Hence, the evaluation of the rupture risk is an important issue to investigate. In terms of the rupture risk for unruptured intracranial aneurysms, there is a heated debate and the criteria for the quantification of rupture varied from different aspects. The most common way to give a coarse estimation is

depending on the aneurysm size and position.

As the increasing of the detection rate of unruptured intracranial aneurysms, the determination of treatment is also exposed to various difficulties due to the lack of diagnostic criteria. This criteria include the assessment of the rupture risk and the risks brought by the surgical intervention per se. Therefore, it is hugely significant and urgent to build applicable criteria for planning therapeutic protocols which is able to provide accurate prediction of aneurysm growth and rupture. Mathematical models with capability of predicting the tissue adaption in aneurysm have attracted considerable interests in scientific field, also contribute to oodles of practical applications. A large number of studies has investigated the aneurysm stability through morphological analysis, computational fluid dynamics and structural modelling, aiming to understand the difference of mechanobiological features between ruptured and unruptured aneurysms. But there is still no reliable functional index can be applied to serve the clinical preoperative planning.

For the sake of making it applicable in predicting rupture risk of existing aneurysms, it is essential to model the structural variations over the aneurysm development under the mechanical stimuli from blood flow with the consideration of its pulsatility. In this research, we build up a patient-specific Fluid-Solid-Growth (p-FSG) framework which is able to simulate the structural and mechanical behaviour variation within the aneurysm wall. It includes the computational fluid dynamics and structural modelling, as well as the growth and remodelling function in the course of aneurysm evolution, which can capture the mechanobiological features more comprehensively and simulate the tissue variation in aneurysms. The clinical state of aneurysms can get enlarged as the tissue growth and remodelling which provides the possibility to assess the stability of aneurysms.

1.2 Structure of Cerebral Arterial Wall

Heart is the engine of our human body, pumping blood flow to all arteries around the body with oxygen and nutritions. Healthy artery wall is comprised of three concentric layers: tunica intima, tunica media and tunica adventitia, from lumen side moving outward. And microstructure of arteries varies with different positions in the artery tree, the age as well as the pathological state of the artery itself.

1.2.1 Type of Intracranial Arteries

There are three main types of arteries, elastic artery, muscular artery and arterioles. Fig 1.4 shows schematic sketch of the structure of three artery types and the constituents in different

layers of these arteries are listed in Table 1.1 below.

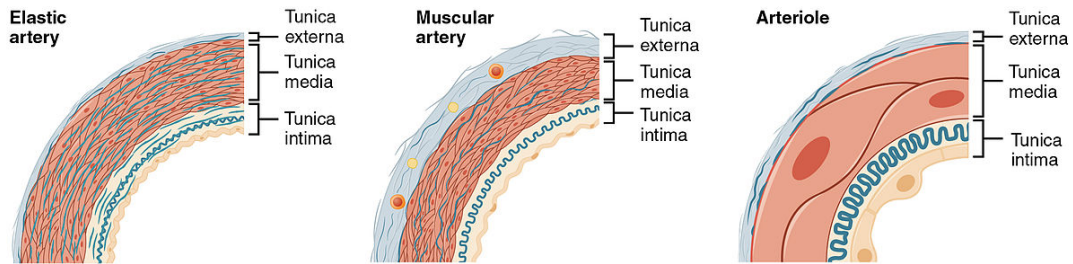


Figure 1.4: Schematic diagram of vascular structure of elastic artery, muscular artery and arteriole

(https://commons.wikimedia.org/wiki/User:CFCF/gallery/Archive_1)

Table 1.1: Constituents in intima, media and adventitia layers of elastic artery, muscular artery and arterioles.

	Elastic artery	Muscular artery	Arterioles
Intima	single layer of epithelial cells fibroblasts myointimal cells	endothelial cells	squamous epithelium
Media	concentric fenestrated sheets of elastin and collagen few smooth muscle fibres	a layer of smooth muscle elastin collagen	1-2 layers of smooth muscle
Adventitia	vasa vasorum	collagen and elastin	collagen bundles nerve endings some fibroblasts

Elastic arteries mainly consist of aorta artery and pulmonary artery which are the pipelines connecting with left ventricle and right ventricle, respectively. These arteries have abundant elastin in the wall for providing enough stretch ability to receive the ejected blood from heart contraction. These arteries recoil in the period of the heart relaxing gradually to maintain enough pressure gradient driving continuously transportation of the blood flow through the arterial system. While the diameters of arterioles are in the micron order of magnitude which are the smallest arterial channels. Those arterioles deliver the blood to capillaries where the highest drop occurs in the velocity of blood and blood pressure. It also requires the capability of contraction or dilation of arterial wall in regulating the blood flow which is carried out by the concentric annulus of smooth muscle.

As to muscular arteries (distributing arteries), the feature of this type of arteries is lots of smooth muscle cells (SMCs) are embedded in the wall. They are responsible for distributing

blood to separated parts of body which also have the contraction ability to dilate the vessel. The most broad part in the vascular structure is tunica adventitia. The diameter of this kind of artery ranges from 0.1 to 10 mm in size. In most arteries, the media layer is separated by internal elastin lamina (IEL) and external elastin lamina (EEL) which are two concentric elastin sheets.

Obviously, the intracranial artery belongs to the muscular artery which satisfies the general structural characteristics of this type of artery(1.5 (A)). However, specially, nearly all the elastin is confined in the IEL with the absence of the EEL (1.5 (B)). Following sections will introduce the constitutes and structure of tunica intima, tunica media and tunica adventitia respectively with more detail.

1.2.2 Tunica Intima

The tunica intima layer is the innermost layer which directly contacts with the blood flow going through the blood lumen. It consists of a mono-layer of endothelial cells basically showed in Figure 1.5. This layer of cells are connected with the media layer by the subendothelial connective tissue and supported by the internal elastic lamina. In straight sections of blood vessels, endothelial cells align and elongate towards the blood flow direction with the torpedo shape. They respond to the haemodynamic stimuli to mediate the permeability of the arterial wall as an effective barrier, but this layer has little contribution on the mechanical load bearing. Endothelial cells with normal function can maintain vascular homeostasis such as the balance between vasodilator and vasoconstrictors, and perform protective reactions to inflammaton, angiogenesis in wound healing (Eroschenko, Di Fiore, 2013).

1.2.3 Tunica Media

Tunica media sits in the middle of arterial wall separated by the internal elastin lamina and it contains the most abundant constituents: closely packed layers of smooth muscle cells (SMCs), various types of collagen, elastic connective tissue and proteoglycans where the later three comprise the extra-cellular matrix (ECM). As showed in Figure 1.5(A), the collagen fibres align helically along with the long axis of arteries (Holzapfel et al., 2000). Normally, the elasticity represented by arterial wall is managed by SMCs and bundles of elastin fibres rather than collagen fibres with crimple shape in the unloaded condition. SMCs responding to the blood pressure could be active or passive via vasoconstriction and vasodilation leading to the diameter changing (Wang, Thampatty, 2006) while the response of elastin and collagen fibres is totally passive.

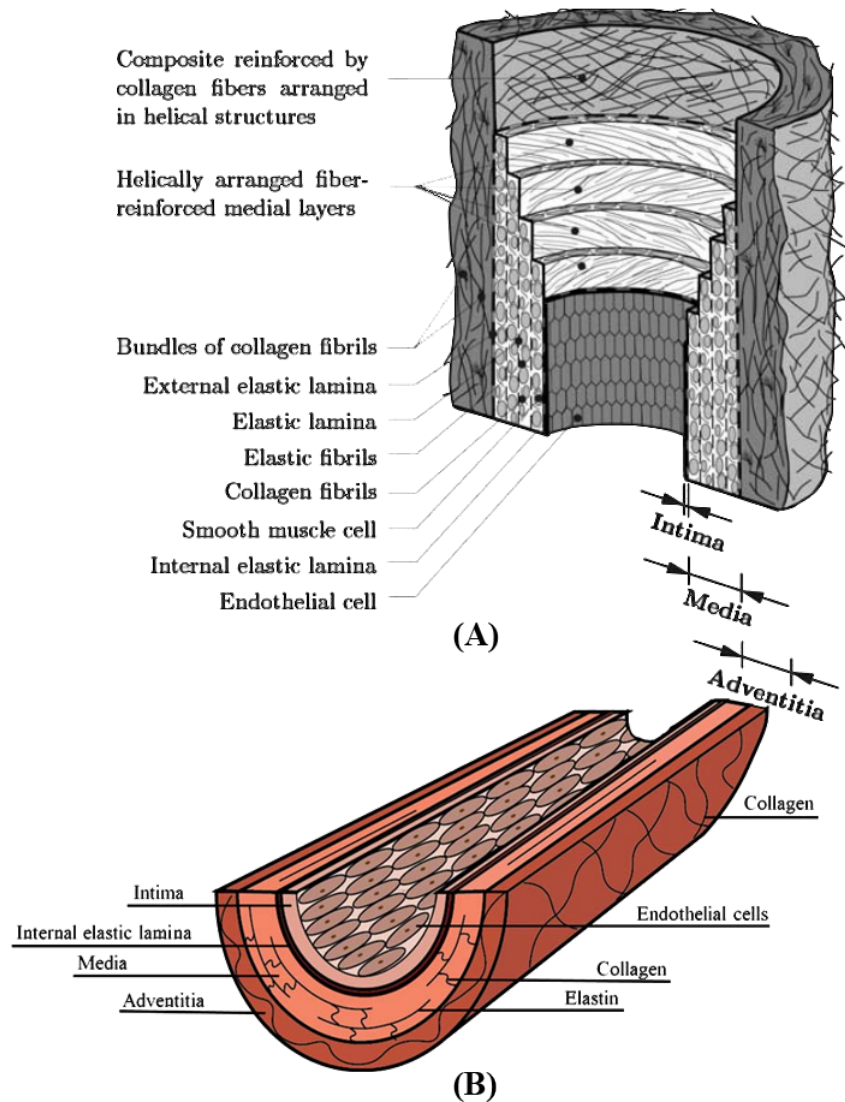


Figure 1.5: General arterial wall structure of detailed fibre alignment (A) and specific schematic structure of intracranial arterial wall (B). (adapted from (Holzapfel et al., 2000) and (Kohn et al., 2015))

1.2.4 Tunica Adventitia

There is no external elastin lamina in intracranial arteries to separate the tunica adventitia from the media layer (Lee, 1995). Tunica adventitia is a protective layer to prevent the overdistension of the artery and it is mainly composed of crimped collagen fibres and fibroblasts. Two families of collagen fibres both helically align with the azimuthal axis in the media

and adventitia layer, but more close to circumferential direction in the media and span more widely in adventitia layer (Holzapfel et al., 2000; Gasser et al., 2005). Fibroblasts are not only responsible for the collagen (Type I and III) and ECM synthesis, also in charge of the assemblies and arrangement of mature collagen fibres. Moreover, the ECM maintenance is also dependent on fibroblasts which can produce various growth factors and matrix metalloproteinases (MMPs) that play a pivotal role in the aneurysm inception and evolution.

1.2.5 Key Vascular Components

This section will introduce the structure of vascular wall in a different way focusing on each key component which is closely related to the aneurysm inception and development. Two important vascular cells are endothelial cells and fibroblasts in this research and two types of fibres for bearing the passive load: elastin and collagen fibres.

1.2.5.1 Vascular Cells - Endothelial Cells

The monolayer of endothelial cells (ECs), possessing the torpedo shape, resides in the most inner layer of the vascular wall in the healthy physical condition. It composes a permeability barrier and delivers biomechanical and chemical signals between the blood conflux and the vessel wall. The apical surface of ECs next to the blood flow has the highest vertex propping up by the nucleus. While the basal surface is implanted with integrins family (heterodimeric α/β chains) attaching to the ECM. Determining the morphology and deformation of the plasma membrane is mainly attributed to the cytoskeleton which composes of three primary categories, actin filaments (F-actin), intermediate filaments (IFs) and microtubes. F-actin is most abundant in quantitative terms and locates in the nearest area to the cell membrane (Osborn et al., 2006). The talin and filamin connect the F-actin to β -integrin tails directly and the bridges of F-actin and cadherin are vinculin and catenins (Stossel et al., 2001; Wheelock, Johnson, 2003). In terms of IFs, they are rather deformable proteins that can be stretched several times longer than their initial length (Herrmann et al., 2007). The F-actin has the properties of viscoelastic gel due to the organization of these cross-linking proteins. At the same time, these proteins are the interconnections between transmembrane proteins and signaling complexes which are situated at adhesion sites.

The cell-cell junction of endothelial cells contains the major adhesive protein VE-cadherin which is a particular composition for endothelial cells. Another composition, the platelet endothelial cell adhesion molecule-1 (PECAM-1) composes a significant proportion of endothelium intercellular junctions, which is also known as cluster of differentiation 31 (CD31). VE-cadherin has the capability of transferring information intracellularly by interacting with

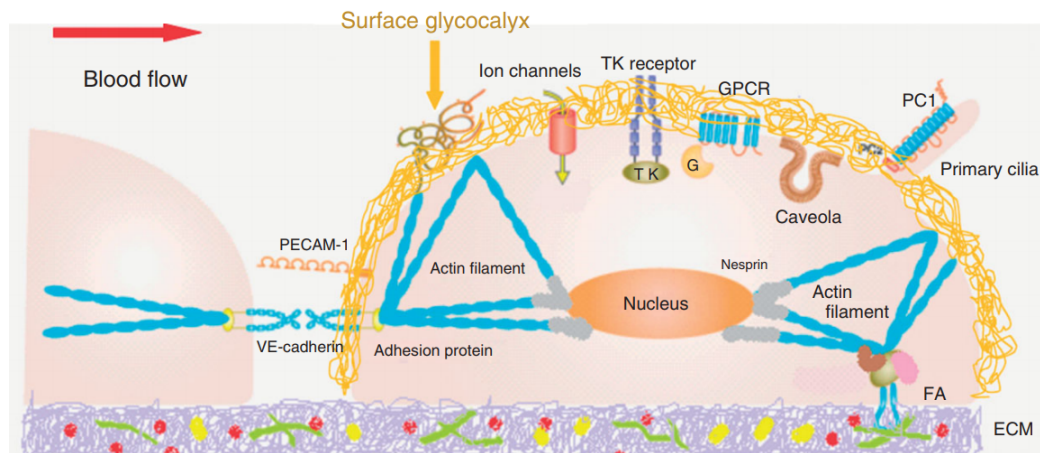


Figure 1.6: Diagram of endothelial cell structure and the cell-cell junction.
(Adapted from (Fu, Tarbell, 2013))

the cytoskeleton via several anchoring molecules. β -integrin molecules are recruited to bind onto intracellular regions of the cadherin. Meanwhile, α -catenin plays as the bridge to associate β -catenin and actin filaments, a crucial protein directly binding to the actin fibers. The connection between this complex, including E-cadherin, α -catenin and β -catenin, and the actin filaments is relatively weak (Nelson, 2008). In the condition that epithelial sheet is complete, β -catenin probably also has the function of transferring the contact inhibition signal to cells to stop cells dividing. Therefore, the link between adherent junctions and the actin cytoskeleton is dynamic, rather than stable (Brembeck et al., 2006). It is suggested that PECAM-1 may responds flow with a quick variation which proves PECAM-1 probably serves as a mechanoreceptor or sensor (Fujiwara et al., 2001).

Three groups of potential shear stress sensors have been proposed over the past two decades (Figure 1.6): 1) cell membrane-associated molecules such as glycoalyx, ion channels, adhesion molecules (integrin) and receptors; 2) specific membrane microdomains, like primary cilia and caveolae; 3) general support structure in cells such as the cytoskeleton and the lipid bilayer membrane itself. These mechanoreceptors receive the haemodynamic stimuli from the blood flow and transfer the producing mechanical signals to chemo-biological signals which further impact on the morphology and function of endothelial cells.

The ECs layer performs significant functions in the aspects of cell behaviors (deformation, apoptosis, remodeling, migration, proliferation), biological responses and further involves in the vascular tone regulation (the balance between vasodiators and vasoconstrictors), prevents the platelet aggregation and eliminates the influence of anticoagulant effects.

1.2.5.2 Vascular Cells - Fibroblasts

Fibroblasts produce tropocollagen and ground substance, which are the precursor of collagen and an amorphous gel-like matrix that fills the spaces between cells and fibres in connective tissue.

When the fibroblasts are cultured in two-dimensional substrates, fibroblasts are large, flat cells with the spindle shape. Their nucleus are also flat with the oval shape. Meanwhile, under this condition, three different types of matrix contacts can be distinguished which are focal complexes, focal adhesions and fibrillar adhesions (Chiquet et al., 2009). Fibroblasts firstly interact with ECM by its focal complexes showed in Fig 1.7 A. This type of contacts are small and dynamic, the primary integrin of which is $\alpha v \beta 3$ allowing focal complexes to recognise different ECM proteins. After the activation of integrins and the establishment of a mechanically stable contact, focal complexes mature into larger focal adhesions (Fig 1.7 B). The mechanical stress is a vital factor for the maturation and maintenance of focal adhesions. The final stage is the fibrillar adhesions (Fig 1.7 C) which are abundant with fibronectin receptor $\alpha 5 \beta 1$ and the adaptor protein tensin. Fibroblasts use fibrillar adhesions for assembling secreted fibronectin monomers into matrix fibrils (Zamir et al., 2000). These matrix contacts act as a force conveyor which transmit forces from the ECM substrate to the inside of fibroblasts, involving the elasticity information of the ECM substrate. In turn, they also transfer the force generated from cytoskeleton to the exterior, i.e. ECM substrate.

Instead of two-dimensional culture environment, fibroblasts present varies shape from stellate to bipolar which are mediated by the arrangement and the orientation of collagen matrices in the culture medium (Weiss, 1959). This is a manifestation of the feedback regulation, the force from the ECM transfers to cytoskeleton resulting in the interior arrangement changing and the further macroscopical morphology variation. On the other hand, the force exerted from fibroblasts enables cells to remodel the extracellular component of the matrix. During fibroblast–collagen matrix remodeling, the mechanisms used by fibroblasts to remodel the matrix are dependent on the level of mechanical tension within the collagen matrix (Grinnell, 2003). With respect to the vascular wall, collagen fibrils in the adventitia are principally produced by fibroblasts. In the course of aneurysm development, fibroblasts act a pivotal character during the collagen growth and remodelling which is the key constituent variation within the tissue.

1.2.5.3 Elastin

The elastic material is almost compacted in the internal elastin lamina with fenestrae in contrast to the muscular arteries in other positions. Elastic fibres are generated by fibroblasts

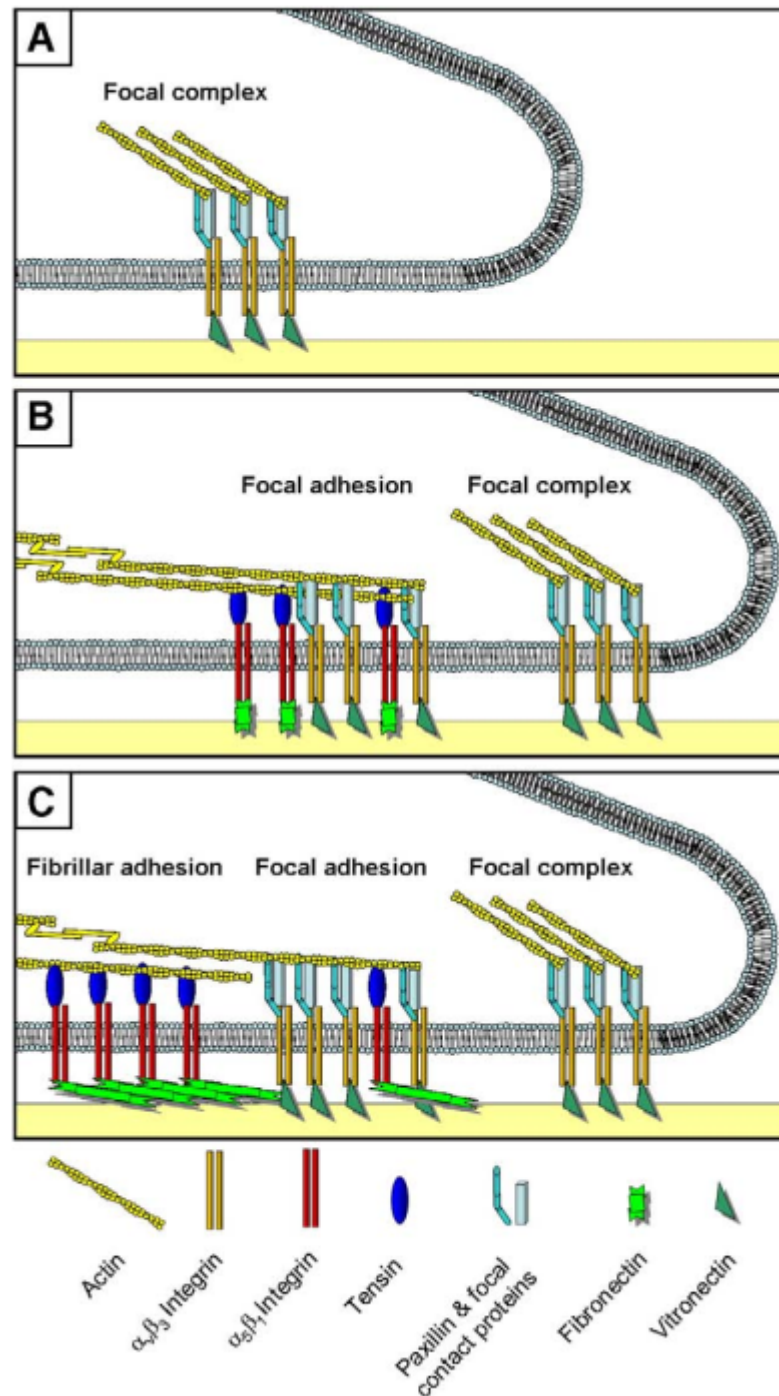


Figure 1.7: Three types of matrix contacts distinguished from fibroblasts on the two-dimensional substrates. (adapted from (Chiquet et al., 2009))

which exist in the media layer of arterial wall and SMCs. The micro-structure of elastic fibres is shown in Fig 1.8, an elastin core surrounded by a sheath of microfibrils.

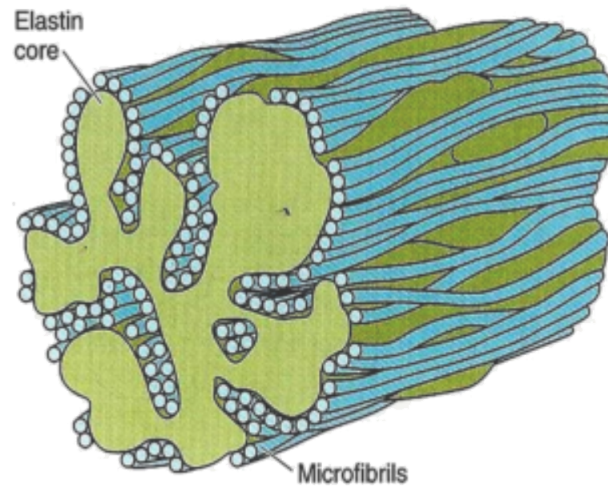


Figure 1.8: Schematic diagram of elastic fibre
[\(https://www.memorangapp.com/flashcards/49294/Connective+Tissue/\)](https://www.memorangapp.com/flashcards/49294/Connective+Tissue/)

Elastin fibres are highly elastic resulting in large stretch in response to wall tension and the half-life of which is about 180 days (Darnell et al., 1990). The elasticity of arterial wall is mainly dependent on the concentric elastic sheet in the media layer under lower pressure which needs the help from collagen fibres when pressure goes higher.

1.2.5.4 Collagen Fibres

Fibril-forming collagens are assembled by tropocollagen molecules which consist of three α -polypeptide chains with a triple right-hand helix configuration. Those fibrils in the arterial wall are closely packed to form collagen fibres, playing the most significant role in bearing the load from high blood pressure.

The morphology of collagen fibres perform a crimped and wavy feature in unloaded arteries. Two families of collagen fibres are arranged helically in both media and adventitia layers with different angles. The diameter of collagen fibrils in the adventitia layer is about 50-100nm (Finlay et al., 1998; Merrilees et al., 1987).

Three prominent collagen types in arterial wall are collagen type I, III, and V and type I collagen is the most abundant type. Thick fibrils (75nm) with distinct variation in diameter assemble densely into bundles, i.e. collagen fibres with diameters about 2-10 μ m. Compare to type I, the fibrils in collagen type III are thinner and perform a looser package to form

reticular fibres. The diameter of individual collagen type III fibres was reported to be around 0.5 -1.5 μm with more uniform diameters of fibrils (45 nm) (Montes, 1996). Collagen type I and III are two key components in response to the passive mechanical resistance in both axial and circumferential directions. They account for approximately 60% and 30% of the total arterial collagen while collagen type V and other collagen types compose the remaining 10% (Borel, Bellon, 1985).

1.3 Variations of Arterial Tissue over Aneurysm Evolution

Looking into the biological difference between healthy and diseased arterial tissue assists us in understanding more about the disease etiology and enables us to find out the ways in which aneurysms might evolve and eventually rupture. Extremely limited clinical data is available used in the research of the aneurysm pathogenesis. But on the other side, the biological variation found by experimental studies provides more possibility to investigate the contributing factors in the course of aneurysm development. In this section, general constituents change of the arterial wall will be firstly outlined and subsequently the experimental evidence according to this biological variation will be summarised.

Healthy arteries are organised into 3 distinct layers while the wall of aneurysm turns to a mixed tissue merging into one complicated layer. Firstly, the intact internal elastin lamina is broken from the neck region showed by the black line in Figure 1.9 (Chalouhi et al., 2013) which is necessary to aneurysm formation (Schumacher, Allenberg, 2003). This pathological variation is owing to the dysfunction of endothelial cells and fibroblasts that involve the inflammatory activities. When the permeability barrier is unable maintain its normal function, that is to say that it paves the way for the macro cells to invade the media and adventitia layer and allows the SMCs to migrate into the intima layer producing myointimal hyperplasia (Kosierkiewicz et al., 1994; Amenta et al., 2015). Dysfunction of the endothelium and VSMCs promotes a chronic pathological inflammatory response that progressively weakens the vessel wall (Amenta et al., 2015).

It is of note that the media layer and the SMCs are almost replaced by collagen fibres after the development of an intracranial aneurysm. As the degeneration of elastin, the collagen fibres take the responsibility of bearing the load from the blood pressure. The collagen fibres appear mostly intact in the adventitia, but might be stretched (Stehbens, 1963). The degeneration of ECMs, primarily the collagen degradation, is driven by MMPs which leads to the eventual rupture of aneurysm, mainly the MMP-2 and MMP-9 (Bruno et al., 1998;

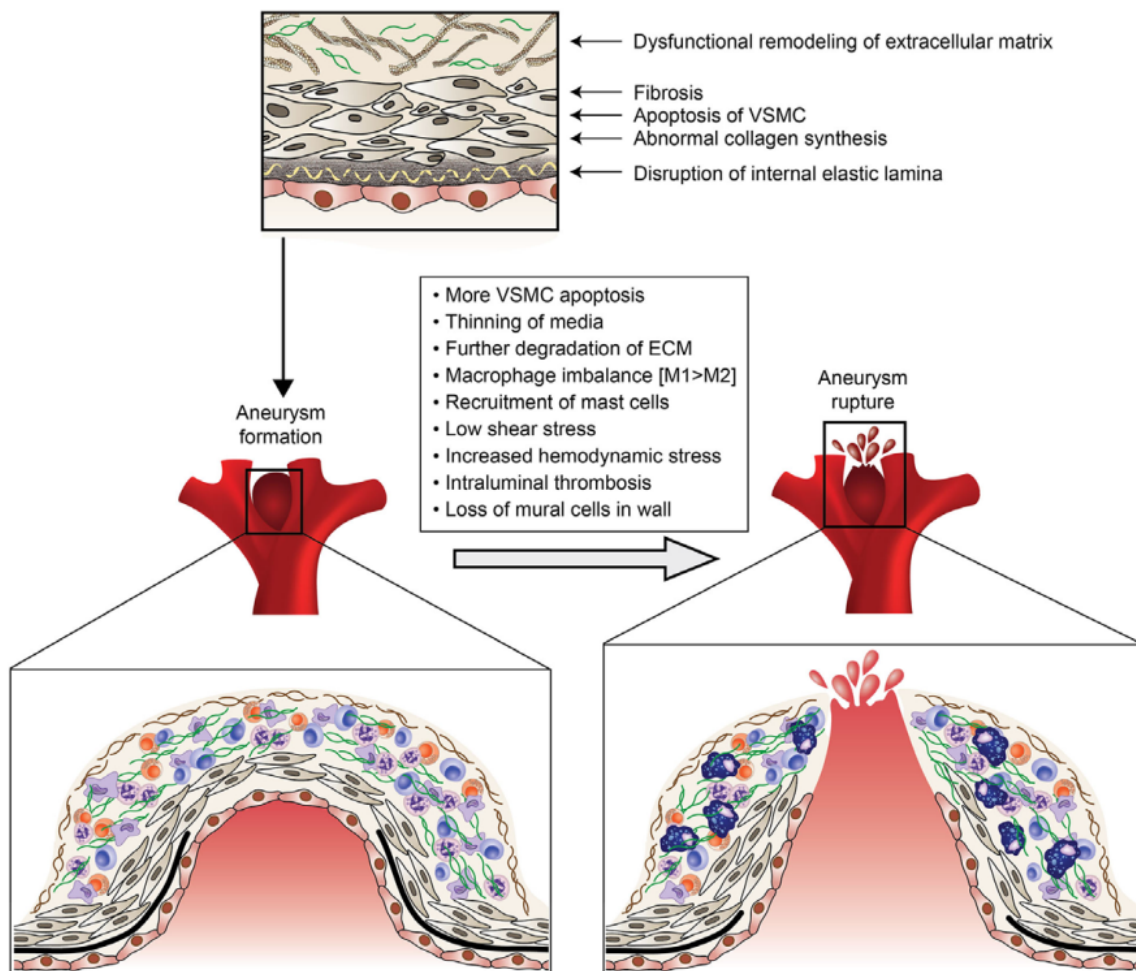


Figure 1.9: Pathological mechanism of cerebral aneurysm formation and rupture (adapted from (Chalouhi et al., 2013))

Kassam et al., 2004). And the collagen turn over is also an important factor in contributing to aneurysm enlargement and rupture (Langille, 1993). It was reported that newly formed aneurysms might be more likely to rupture, since the new collagen have not yet been attached to the ECM after the damage of old collagen fibres (Mitchell, Jakubowski, 2000). Constituents within aneurysm wall could vary largely in different ways with respect to different stages in the course of aneurysm evolution. More importantly, to differentiate stable aneurysms and vulnerable aneurysms, understanding of the features of ruptured aneurysm compared to unruptured aneurysms will provide more insights on the aneurysm stability assessment.

1.4 Aneurysm Rupture Risk Estimation

Rupture risk estimation of intracranial aneurysms is a major issue for surgeons in the decision making of treatments. Due to the high percentage of stable aneurysms compared to rupture-prone aneurysms, an applicable indicator for rupture risk is in urgent requirements for avoiding the manipulation risk from the surgery and corresponding complications, also with the economy-saving consideration. The following sections will first summarise the features of ruptured and un-ruptured aneurysms from different angles, i.e. the geometric analysis, histological experiment and in silico modelling. Secondly, different estimations ways of aneurysm rupture risk and the challenges of assessment will be discussed.

1.4.1 Features of Ruptured and Unruptured Aneurysms

1.4.1.1 Geometrical Features

It is an undoubtable fact that the assessment of aneurysm rupture is too complicate to achieve. At present, the most available surrogate used in clinical diagnosis is the size of an aneurysm (Raghavan et al., 2005). International Study of Unruptured Intracranial Aneurysms Investigators recruited 2621 patients and found the aneurysms with diameters larger than 10 mm have a higher risk of rupture (Investigators, others, 1998). Based on this, aneurysms of < 10 mm were reportedly related to growth rates of 2.9% per year, while aneurysms of > 10 mm exhibited higher growth rates of 9.7% per year (Brinjikji et al., 2016). Another extensively used index is aspect ratio: Hiroshi Ujiie reported that the higher aspect ratio (>1.6) of unruptured cerebral aneurysm should be paid more attention which is characterized with extremely low flow in the aneurysm dome (Ujiie et al., 1999, 2001). Bryce Weir collected a greater chorus of 774 aneurysms, which also suggested that high aspect ratio might be an useful index in the clinical decision independent of the maximum size of aneurysms (Weir et al., 2003). A research on a database of 20 patients also found that the ruptured aneurysms more likely had irregular shape and had greatly higher maximum height and aspect ratio (Zhang et al., 2014). Other geometric indices were also developed, like size ratio (Dhar et al., 2008; Kashiwazaki, Kuroda, 2013), bottleneck factor (Hoh et al., 2007), and undulation index (UI) (Ma et al., 2004; Raghavan et al., 2005).

In general, larger aneurysms are inclined to rupture with higher risks. However, there is still a relative large amount of small aneurysms, reportedly 13% to 75%, ruptured (Varble et al., 2018). Therefore, it seems impossible to define a size cutoff depending on the isolated morphology information. And with respect to the distinguishing line between large and small

aneurysms, there is still no consensus (Oka, Nakai, 1987). Researches have found that the appearances of large and small aneurysms normally have different specialties which could be used for differentiate the small and large aneurysms. The walls of smaller aneurysms are usually thin, translucent and hypocellular. While larger aneurysms are characterized by thick and irregular wall with inundation of inflammatory cells (Crompton, 1966).

1.4.1.2 Histological Features

Understanding of the difference between stable aneurysms and ruptured aneurysms can shed light on the pathological of aneurysm evolution and rupture, which may help to identify vulnerable aneurysms. A greater quantity of degenerated and apoptotic SMCs in the wall of ruptured aneurysms led to thin walls compared to those unruptured aneurysms which contained at least one layer of SMCs (Sakaki et al., 1997; Frosen et al., 2004). SMCs proliferate and migrate towards luminal side in response to the hemodynamic stress elevation in the arterial tissue (Okamoto et al., 2001). Juhana Frösen et al. investigated two groups of aneurysm, i.e. ruptured and unruptured, with the similar dimensions by immunostainings and it reveals the significance of intracranial aneurysm wall structure for its vulnerability to rupture (Frosen et al., 2004). They summarized four categories of aneurysms associated with rupture characteristics of the aneurysm wall: endothelialized wall with well aligned SMCs; thickened wall filled with disorderly SMCs; hypocellular wall with either myointimal hyperplasia or organizing luminal thrombosis; hypocellular wall with extremely thin thrombus-lined which has 100% rupture rate. Elevated collagenolytic and elastolytic activities were presented in ruptured aneurysms and the quantity of cross-link between collagen fibres was also lower (Gae-tani et al., 1998; Vanrossomme et al., 2015). Compared to normal arteries, both ruptured and unruptured aneurysms showed lower expression of collagen III and IV, but collagen III was even lower in ruptured aneurysms in contrast to unruptured aneurysms (Kilic et al., 2005).

The inflammation changes in aneurysm wall have become understood as an important phenomenon in the course of aneurysm development and rupture (Tulamo et al., 2010; Chalouhi et al., 2013; Hasan et al., 2011). The expression of mast cells remarkably upregulated in ruptured aneurysms (Hasan et al., 2012). Early ferumoxytol uptake revealed by the high-contrast MRI images had been investigated and showed that it was not only related to the inflammation but also indicative for the stability of aneurysm (Hasan, Hesitad, 2013). Aneurysm stability relies on a dynamic balance kept by the competition between aneurysm wall repair and destruction, i.e. eutrophic/dystrophic collagen turnover and regeneration/degradation of the extracellular matrix (Etminan, Rinkel, 2016). However, the exact mechanism of inflammatory molecules results in the eventual aneurysm rupture is still ambiguous. The way to likely define a prone-aneurysm from the histological assessment at current stage is based on

radiological examination where can represent the infiltration by T cells, polymorphonuclear neutrophils and mast cells (Etminan, Rinkel, 2016).

1.4.1.3 Features from in Silico Modelling

From aneurysm inception to eventual rupture, the biological variations showed by histological studies are mediated by the interplay between mechanical stimuli and cellular signal transduction. A large number of researchers has been focusing on the relationship between mechanical stimuli from both fluid and solid side and certain microscopic activities within arterial wall tissue, aiming to find any predictive and practical indicator for aneurysm growth/rupture which could be adopted in clinical treatment.

Biomechanically, when the wall tension exceeds the strength of the wall tissue will lead to the rupture of an aneurysm where the wall tension could be calculated by numerical simulation. Utilizing the wall tension to estimate the rupture risk was firstly applied to abdominal aortic aneurysm (Fillinger et al., 2003; Wolters et al., 2005). One research modelled the flexible wall of intracranial aneurysm and indicated that the high wall tension and displacement located at the position where aneurysms usually ruptured (Isaksen et al., 2008), but did not give a threshold value for the wall tension. By testing the mechanical behaviour of aneurysm wall, the stiffer wall presented a lower rupture risk in contrast to softer aneurysms (Costalat et al., 2011; Sanchez et al., 2013; Brunel et al., 2018). In addition, strain limitation has also been reported to be associated with the aneurysm rupture risk prediction from 20% - 38% (Cebal et al., 2015; Robertson et al., 2015; Valencia et al., 2015; Brunel et al., 2017, 2018). Reasons leading to this strain difference could be temperature, testing protocol and the preprocessing, i.g. freezing. No matter the wall tension or the wall strain, the challenge of the rupture prediction by structural modelling is the accuracy of the material properties assignment of aneurysm wall which impacts the mechanical distribution significantly.

The importance of individual hemodynamics analysis in the etiopathogenesis of intracranial aneurysms is widely accepted which has been also broadly employed in the research of aneurysm rupture assessment. Liang-Der Jou et al. collected 26 patients with aneurysms and compared the WSS at the end of diastole (Jou et al., 2008). Results showed that only the mean WSS rather than maximum WSS was associated to rupture. Low WSS and high OSI were associated by aneurysm rupture by analysing 38 ruptured and 81 unruptured aneurysms (Xiang et al., 2011). However, Cebal et al. reported that the aneurysm rupture was related to high max WSS through the investigation of 210 cross-sectional aneurysm images (Cebal et al., 2011). Another research revealed that lower min WSS in ruptured aneurysms is remarkably lower than that in unruptured aneurysms and this lower min WSS often showed on aneurysm dome (Zhang et al., 2014). A longitudinal research of one patient with multiple aneurysms

observed that aneurysm grew firstly in high WSS region then changed to low WSS level and finally rupture occurred (Wang et al., 2018). As to the exact definition of low or high WSS, it is extremely hard to provide a threshold value which could be suggested to the clinical application due to the great individual difference.

1.4.2 Challenges in Aneurysm Risk Assessment

As discussed in the last section, the aneurysm rupture estimation has been investigated widely from different perspectives. Morphology analysis is the most intuitive and handy way for surgeons to plan for aneurysm disease. Histological features is a useful tool to understand the etiopathogenesis of aneurysm evolution and rupture, but this only could be achieved after the treatment like clipping. Structural and haemodynamic studies has been made extensively and they were trying to develop a numerical indicator which is able to effectively predict the rupture risk of aneurysms. Even though a tremendous amount of research data has been published on the progression of aneurysm growth and rupture, varying levels of evidence that leads to a low availability of the rupture risk assessment and also the preventive treatment (Etminan, Rinkel, 2016). One reason from the clinical aspect, W. Brinjikji pointed out that many longitudinal observational researches are limited by the not long-enough follow-up to witness aneurysm rupture (Brinjikji et al., 2016). On the computational side, the structural modelling aiming at predicting the rupture risk via stress/strain distribution on aneurysms is still under developing because of the complex spatial distribution of constituents, i.e. heterogeneity, leading to the difficulty in material parameter assignment. Haemodynamic simulation is an accepted way in the research of cardiovascular disease, but due to the individual and locational difference, the meaningful WSS level is still controversial and uncertain associated to specific disease.

Reasons for aneurysm rupture has not been well understood but it is clear that aneurysm development and rupture is a mechanobiological process with respect to mechanical stimuli, biological reactions and the signal transduction between them. This implies the prediction of aneurysm rupture should consider multiple mechanisms using a multiscale model which needs further goal-oriented researches.

1.5 Research Outline and Thesis Organization

This thesis develops a patient-specific fluid-solid-growth (p-FSG) framework aiming to model the growth of aneurysms and analyse the stability of existing intracranial aneurysms. We start with a patient-specific intracranial aneurysm model, through the iterations of varying

material properties of aneurysm spatially to achieve the growth of the aneurysm. However, the material properties are associated to the mechanical stimuli from the blood flow and the stress within the wall over one cardiac cycle with the involvement of cellular response, i.e. endothelial cells and fibroblasts. In the end, our aneurysm model is able to enlarge and present spatial heterogeneity of constituents and mechanical behaviours. Followings will introduce the outline of each chapter showing a step by step process to achieve my research goal:

Chapter 2: This chapter mainly reviews the development of mathematical models of healthy artery and aneurysm evolution, especially the fluid-solid-growth (FSG) framework. The constitutive model of healthy artery wall is the basement for modelling aneurysm development which is the structural-based evolution. Essential ideas of our p-FSG framework are derived from (Wotton et al., 2004), hence there is a brief introduction of key hypotheses and methodology in that research to get an overall understanding of the pathological process in the course of aneurysm development. Moreover, the limitations of current aneurysm growth models are also analysed in the end to point out the further improvement directions in researches of aneurysm development modelling.

Chapter 3: Haemodynamic environment plays a pivotal role no matter in the inception or evolution stage of intracranial aneurysms. One intracranial aneurysm model with follow-up images is employed in this chapter to find out the potential haemodynamic characteristics linking with aneurysm growth. Importantly, a novel flow metric is associated with endothelial cells morphology, further a function of which represents the endothelium permeability. This can be implemented into an inflammatory pathway in triggering aneurysm pathological progress. This is the first study of aneurysm growth model with the representation of endothelial cells mechanobiological function.

Chapter 4: Structural modelling of a thick-wall aneurysm model with patient-specific geometry is implemented in this Chapter. Parameters of structural-mediated strain energy functions for elastin and collagen fibres are investigated and determined by the load bearing percentage in the aneurysm section and healthy artery section respectively. With the assignment of hyperelastic material properties and boundary condition restriction, the general mechanical information distribution is available for providing the mechanical stimuli information in further analysis, such as Cauchy stress, strain, displacement.

Chapter 5: After the fluid and solid modules, the growth function is introduced elaborately in this chapter. There are two applications in this chapter, one illustrative model links with low WSS and another improved p-FSG model with the cooperation of the novel flow metric. Key hypotheses of aneurysm growth include elastin degradation and collagen remodelling regulated by WSS and Cauchy stress on collagen fibres respectively showed by an illustrative model to show this framework is working. Significantly, the novel flow metric

(WSSAR) associated with endothelial permeability represents an inflammatory pathway, i.e. elastase and collagenase activities. The elastin and collagen degrades with a function of WSSAR and collagen remodelling is mediated by Cauchy stress on collagen fibres. Consequently, this clinical aneurysm model is able to model the heterogeneity of arterial adaptation during the aneurysm evolution.

Chapter 6: Another cellular mechanism, fibroblasts secreting and degrading collagen fibres, is implemented in the G&R function in this chapter. To explicitly test the collagen growth function, here we do prescribed degradation of elastin and collagen instead of linking with haemodynamic environment. Two illustrative models of localized degradation are modelled, one with the collagen growth function and the other one without. Results indicate that the collagen growth function could decrease the enlargement degree which is beneficial for the stability of aneurysms. Due to the limited enlargement of our aneurysm model, we further built a prismatic mesh on this aneurysm model and test the large deformation ability of this mesh. Two illustrative cases were presented and results showed that this prismatic mesh indeed can improve the deforming capacity.

Finally, **Chapter 7** revisits the key points and results of our multiscale growth model presented in this thesis, and also suggests the limitations of current framework that inform the directions and outlook for further refinement and application of this research.



Review of Fluid-Solid-Growth(FSG) Framework in the Modelling of Aneurysm Evolution

2.1	Constitutive Model of Healthy Artery	23
2.2	Review of the Modelling of Aneurysm Evolution	25
2.3	Overview of the Developed Fluid-Solid-Growth(FSG) Model	29
2.4	Limitations of the State-of-the-art FSG framework	36
2.5	Novelties of the p-FSG Framework	37

This chapter will first give a general overview in terms of the constitutive model of a healthy artery which is the basement for the modelling of aneurysm evolution. Development of aneurysm evolution modelling is summarised in the second section which contains a cascade of recent computational models of aneurysm growth. The key basement of

the modelling framework proposed in this research is a developed Fluid-Solid-Growth (FSG) framework which will be depicted in the third section to have a general understanding of the methodology of growth and remodelling (G&R) function. In the end, the limitations of this developed FSG framework were listed indicating the improving directions for further development and the novelties of this p-FSG framework.

2.1 Constitutive Model of Healthy Artery

Healthy arteries are able to dilate to a large extent showing a highly deformable structure. Experiments reveal that arteries perform nonlinear, anisotropic and viscoelastic characteristics. They present a nonlinear stress-strain mechanical behaviour with a typical stiffening effect at higher pressures. The primary constituents in healthy arteries for bearing the load passively from the blood pressure are elastin and collagen fibres and the stress-strain behaviour of elastin and collagen was firstly investigated by (Roach, Burton, 1957) using in vitro experiment. Figure 2.1 shows the nonlinear mechanical properties of artery within the physiologic range of 80-120 mm Hg (left curve).

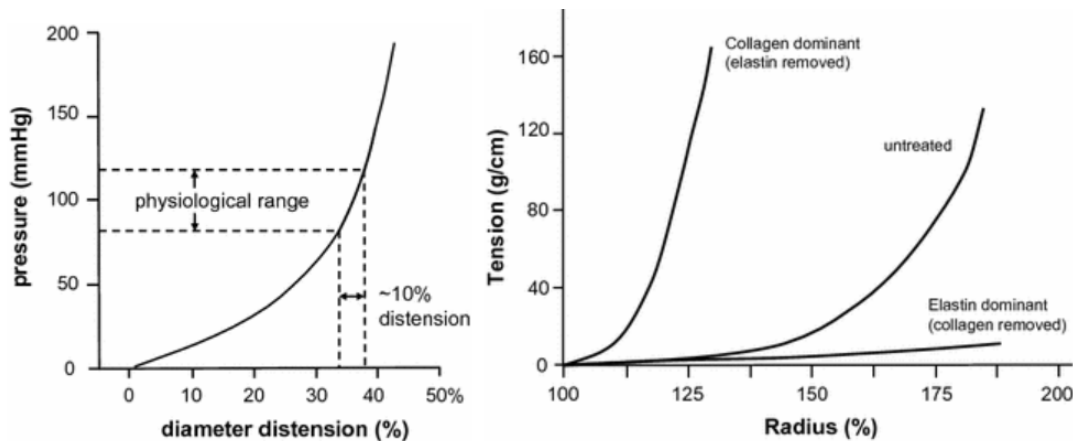


Figure 2.1: Left: The pressure-diameter distension of an artery showing the nonlinear behaviour especially at higher pressures. Right: Tension-radius relationship tested on treated and untreated external iliac artery where the treated artery contains only elastin or collagen fibres respectively.

(Adapted from (Roach, Burton, 1957))

(<https://thoracickey.com/the-arterial-system-i-pressure-flow-and-stiffness/>)

The right graph in Figure 2.1 also indicates the nonlinear mechanical behaviour of artery showed by the untreated curve. Moreover, it also figured out the different behaviours of

elastin and collagen respectively. As plotted in Figure 2.1 (right curve), the elastin mainly works under lower pressure with an approximately linear behaviour. As to collagen fibres, apparent nonlinear mechanical behaviour was presented. Note that for healthy artery under lower pressure, its mechanical behaviour is dominated by elastin constituents which is owing to the crimple structure of unloaded collagen fibres.

From the perspective of mathematical models, a distinct evolution of models can be found in literature. When the fluid exchange within the wall is not considered, the arteries could be regarded as incompressible. Constitutive models of arterial wall can only include a subset of its properties using some simplifications. A variety of studies treated the arterial wall as homogeneous constituents at every point in the model which considered the microscopic response of each point is assumed having a locally averaged properties (Malvern, 1969). With the clearer understanding of the micro-structure of arterial wall from the histological researches, the heterogeneous/structural models are developed including the representation of fibres and extracellular matrix. Parameters in this type of constitutive model have advantages on their physiological meanings which relates to the microstructure. Raymond P. Vito et al. summarized a series of constitutive models of blood vessel wall contained the researches from 1995 to 2002 (Vito, Dixon, 2003) which clarified the constitutive models to different types: pseudoelastic, randomly elastic, poroelastic, and viscoelastic. Fung et al. proposed a seven-parameter exponential strain energy density function for characterization of the pseudoelasticity for blood vessels (Chuong, Fung, 1983) based on experimental data of arterial wall under inflation and longitudinal stretch from (Fung et al., 1979). This constitutive model considered the artery wall as a homogeneous single layer constrained by the limited experimental studies on microstructure. Compared to three constitutive models in (Chuong, Fung, 1983; Maltzahn von et al., 1984; Takamizawa, Hayashi, 1987), Humphrey suggested an alternative form of strain energy density function for arteries to compensate the limitations of those models (Maltzahn von et al., 1984). Because the Fung model requires too many material parameters while von Maltzahn and Hayashi models does not includes the related anisotropic properties to adapt the equibiaxial stretch. Holzapfel et al. proposed a new constitutive framework, structurally-based model, for the mechanics of arterial wall embedded in the microstructure with different layers (Holzapfel et al., 2000). In his model, the healthy arterial wall is modelled as a non-linear hyperelastic two-layered cylindrical thick-walled tube. The passive mechanical response of media and adventitia layer was differentiated and the contributions of elastin and collagen fibres were separately characterised as linear/isotropic and non-linear/anisotropic materials. They proposed a new strain energy function (SEF) comprised of two parts with different proportions for media and adventitia layer: Neo-Hookean model to quantify

the linear behaviour of elastinous constituents; an exponential function to represent the high non-linear stress-strain behaviour of collagenous constituents. This nonlinear response of collagen fibres has been characterized by polynomial, logarithmic and exponential type and the exponential form was reported having a better fit for subjected arteries and more stable material parameters (Fung et al., 1979). And this type of SEF for arteries has been well implemented into ANSYS software, therefore, in this research, we employed this constitutive model for arteries and aneurysm both as the basement for structural modelling and the further aneurysm evolution model. The detailed description of the SEF in this constitutive model can be found in Chapter 4.

2.2 Review of the Modelling of Aneurysm Evolution

In mathematical models, the mechanical behaviour of arterial tissue should be preferentially considered to be modelled. The aneurysms are derived on the arterial basement, the structural modelling of healthy arterial wall is crucial to the development of aneurysm modelling which has been depicted in the last section. This section will focus on the review of the development of aneurysm growth models.

2.2.1 Solid-Growth Models

All aneurysm growth models are based on a common foundation, '*Remodelling of a collagenous tissue at fixed length*' published by Humphrey in 1999 (Humphrey, 1999). In this paper, the arterial constituents mixed by elastin, current-existing and newly-formed collagen fibres. The collagen fibres were assumed under a dynamic state of continuous turnover and the variation of mass fraction was assumed as a cell-mediated mechanism. The key idea is the tissue constituents which sustained increased or decreased mechanical stimuli were tending to restore the stress/strain to homeostatic level. This is a breakthrough from a conceptual approach shifted to a structurally-motivated model which links the microstructure to the mechanical behaviour of arterial tissue.

In 2004, Paul Watton et al. developed the first structurally-based growth model of aortic abdominal aneurysms (AAAs) (Watton et al., 2004). The aneurysm was grown from a cylindrical tube as arterial wall based on the constitutive model of (Holzapfel et al., 2000) with both the media and adventitia layers implemented. In this model, they conceived a key variable - *recruitment stretch* - which defined the tissue must be stretched to a certain level with reference to the undeformed configuration, when the collagen fibres started to bear load. Baek et al. seems the first person who firstly proposed a growth model of cerebral aneurysm (Baek

et al., 2005) and it was hypothesized that the enlargement of aneurysm was due to a stress-mediated regulation of collagen turnover. Their results showed that ellipsoidal aneurysms tended to form spherical shapes and they also suggested that the enlargement of the lesion region was determined by the competition between the radial expansion and wall locally thickening. In the next year, Baek and his colleagues developed a growth model for an axisymmetric fusiform cerebral aneurysm (Baek et al., 2006). The collagen production was mediated by fibroblasts and the number of fibroblasts was proportional to the volume change with the assumption (cell density/ unit volume is constant). Also, the proliferation of fibroblasts was stress-mediated activity which was dependent on the stress deviation to the homeostatic stress experienced by fibroblasts. The orientation of newly-formed collagen fibres was considered as a pivotal factor in G&R and they defined a unit vector for the preferred alignment for the deposition of newly-produced collagen fibres. In contrast to the stress-mediated G&R, Kroon and Holzapfel developed a membrane growth model of saccular aneurysm which both the collagen production by fibroblasts and the fibroblasts proliferation were assumed as a function of strain (Kroon, Holzapfel, 2007). The production rate of fibroblasts and the stretch sensed by fibroblasts were related to the reference configuration which was not necessarily a stress-free or unloaded configuration. In the following researches (Kroon, Holzapfel, 2008, 2009), they developed a realistic 3D setting for growth model of a human middle cerebral artery and also collagen production rate of the fibroblasts was newly assumed regulated by the cyclic deformation imposed on these cells over the cardiac cycle. Baek and his colleagues, Kroon and Holzapfel did not model the gradual degradation of elastin layer but a sudden degradation of this elastin layer, so the aneurysm growth was represented by adventitia only. Because the models were derived from cylindrical shape where the elastin contributes to the load-bearing function of the total artery, this ignorance of elastin contribution leads to a maximum stress at $t=0$ which is not reasonable. Furthermore, this over-estimated high stress resulted in the rapid failure of aneurysm wall enlargement which was limited between 1.2-3.6mm (Kroon, Holzapfel, 2008) compared to the failure cases ≥ 10 mm clinically reported. All above mentioned aneurysm growth models are structurally-based model without the consideration of haemodynamic influence to cells and the whole arterial tissue.

2.2.2 Fluid-Solid-Growth Models

It appears that the first aneurysm growth model involved the haemodynamic study was conducted by Feng et al. and the high WSS was assumed correlated with the wall degradation and aneurysm progression (Feng et al., 2004). In the structural part, their aneurysm wall was modelled as a single layer with an averaged mechanical behaviour and the haemodynamic

environment also did not targeted on individual arterial wall constituents. Hence, this kind of simplification limits the results interpretation from the view of pathological understanding. Humphrey firstly identified a new class of aneurysm growth model which combined the haemodynamics, mechanics and the internal variation of arterial tissue together to mimic the process of aneurysm evolution (named as *Fluid-Solid-Growth*, FSG) (Humphrey, 2008). His colleagues presented a patient-specific fluid-solid-interaction model of the entire circle of Willis and indicated the necessity of incorporating the information of mechanobiological responses by the cells to the computed hemodynamic loads to aneurysm growth (Di Achille, Humphrey, 2012). C. Alberto Figueroa et al. proposed a FSG framework which can apply to the modelling of cardiovascular models including vascular adaptations, disease progression, and clinical intervention, but not specific on aneurysm evolution (Figueroa et al., 2009). Based on the structural model (Watton et al., 2004), Paul Watton et al. extended that growth model to link G&R function with the response to local haemodynamic stimuli (Watton et al., 2009a; Watton, Hill, 2009; Watton et al., 2011) from the cellular level. In this series of G&R models, the arterial wall was modelled as structurally-motivated two-layered membrane wall with the combination of isotropic and anisotropic mechanical behaviour of vascular constituents. The aneurysm inception was triggered by the haemodynamic stimuli, i.e. low WSS, which led to the degradation of elastinous constituents in a prescribed region for aneurysm growth. This would elevate the local strain and the deformation of cyclic strain sensed by fibroblasts which govern the mass density variation of collagen fibres. Hence, the G&R algorithm here was strain-mediated which is coincide with (Kroon, Holzapfel, 2008, 2009). This FSG framework is the foundation of the research in this thesis, and the key idea will be elaborately introduced in the next section. Selimovic applied the same FSG framework to 4 patient-specific geometries and geometric comparison results of real aneurysms and modelled aneurysms suggested tentative support for the hypothesis that the low WSS contributes to the aneurysm evolution (Selimovic et al., 2014).

2.2.3 Thin-walled to Thick-walled Models

As illustrated in Section 2.2.1, constrained mixture models of growth and remodeling (G&R) has been developed with the implementation of cellular response. But most of these frameworks of aneurysm growth have been limited to simplified cases of membrane approximations (Valentin et al., 2013). First of all, the real arterial wall or aneurysmal wall has a multi-layered structure which requires a thick-walled model for the structural analysis. Secondly, the aneurysm rupture happens when intramural mechanical stress exceeds the local wall strength from a biomechanical standpoint. Hence, considerable interest has developed to in-

investigate the association between the evaluation of magnitude and distribution of wall stress and the rupture risk in the last few years (Gasser et al., 2010; Erhart et al., 2014; Pierce et al., 2015; Joldes et al., 2016). According to this, it is undoubted that the accurate simulation of wall stress is a determinate factor in assessing the rupture risk of aneurysms. When the vessel wall or aneurysmal wall is simulated as a membrane model, the membrane stress are average tension or compression stresses. Subjected to internal pressure, the simple membrane-stress concepts of aneurysmal wall which has complicated shape is not sufficient to give an adequate estimation of the true stress situation. The first reason is the membrane stresses are assumed to be uniform across the vessel wall in a tangential direction to its surface. But in thick-walled models, the radial stress cannot be ignored and formulas are also different from those membrane stresses. The other significant reason is thin-walled membrane elements have zero bending stiffness which will make difference to the mechanical behavior of arteries, e.g., the pressure-diameter curves. This is often regarded as a limitation of membrane models while the solid elements are typically utilized to represent 'bending-like' residual deformations (Liu et al., 2018). Additionally, aneurysm growth and remodelling are highly dependent on the distribution of stresses throughout the wall, which is not described by membrane stress (Karšaj et al., 2016). Therefore, the solid elements are superior to membrane models which is able to produce a more realistic stress distribution within the tissue.

There is a pressing need for a 3D finite element model capable of thick-walled, multi-layered arteries undergoing complex motions and subject to irregular boundary conditions proposed by J. D. Humphrey and G. A. Holzapfel (Valentin et al., 2013). They also suggested that the G&R framework need to be extended to satisfy this need. In 2015, Andrii Grytsan proposed the first thick-walled FSG framework for modeling the AAA evolution and found that the transmural distribution of elastin and collagen strains were heterogeneous which may contribute to the tortuosity of the aneurysm development (Grytsan et al., 2015). He pointed out that the thick-walled structure can provide a potential for transmurally nonuniform arterial G&R. The framework was further extended to a novel chemo-mechano-biological model where the collagen growth mediated by fibroblasts was implemented through a biochemical pathway (Aparício et al., 2016). Subsequently, the thick-wall models for (abdominal) aortic aneurysm were developed for a more explicit representation of the constituents growth within the tissue (Grytsan et al., 2017a; Lin et al., 2018, 2019).

However, even the patient-specific model has shown in literature for aneurysm growth, the initial state for all the aneurysm models were cylindrical membranes or thick-wall tubes as the growth platform. There is still no growth model based on the current patient-specific aneurysm morphology to further evolution simulation which is more practical in the prediction of aneurysm growth and eventual rupture. To overcome this limitation, we applied the

FSG framework proposed by Paul Watton to a patient-specific intracranial aneurysm in this research. The next section will give a brief introduction of the key ideas and hypotheses in the FSG framework which are the main basement for this study.

2.3 Overview of the Developed Fluid-Solid-Growth(FSG) Model

This section starts with introducing the work flow of the previously advanced FSG framework. Then the methodologies or hypotheses of each component in this FSG framework will be briefly depicted. It is worth to note that the setting up of certain parameters are specifically to better explain the methodology in the previous FSG framework, not related to this study itself.

The most recent FSG framework investigating of cerebral aneurysm evolution is depicted by Alisa Selimovic ([Selimovic et al., 2014](#)) which linked the low WSS to aneurysm growth mechanism on four clinical aneurysm models. The schematic of the FSG framework in that paper was adapted here to help understanding the work flow and the interactions among fluid, solid and growth (Fig.2.2).

As shown in Figure 2.2, the haemodynamic analysis, structural modelling and growth & remodelling are interacted with each other tightly. The CFD simulation and structural analysis could provide mechanical stimuli from the blood flow and the tissue wall to vascular cells; the growth & remodelling as the mainstay can receive the response from those cells and manipulates a cascade of variations of vascular responses leading to the aneurysm evolving.

This FSG framework was mainly operated by the academic programs package with the exception of CFD simulation which was operated in ANSYS CFX. In the geometry preprocessing stage, the clinical geometry was manipulated by cutting off the aneurysm part and replaced by a cylinder representing the healthy artery. This cylinder must be fit to the two boundaries of the parent vessel so that forms a spliced blood vessel without aneurysm. Then a simulated aneurysm will produce on the cylinder region via the growth and remodelling function. Here we just briefly introduce the significant procedures in each component amid the framework, more detailed information in this methodology can be found in ([Mandaltsi, 2016](#)).

2.3.1 Geometry Reconstruction

Firstly, the aneurysm 3D geometry was imported in @neuFuse, an integrated medical image-based computational hemodynamic simulation tool which is centered on intracranial aneurysms

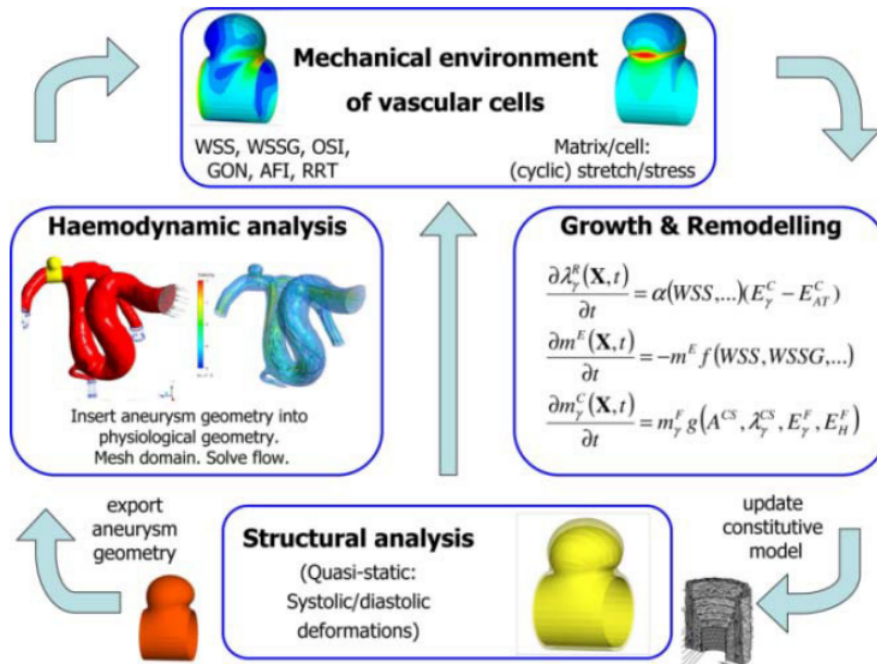


Figure 2.2: Fluid-Solid-Growth computational framework (adapted from (Selimovic et al., 2014))

and assessment of aneurysm rupture risk (<http://www.aneurist.org/>). The next step is producing a skeleton for the aneurysm geometry shown in Figure 2.3(b) and this skeleton will help to build the further segmentation of aneurysm part, connecting neck parts with parent vessels. The aneurysm was cut artificially and replaced by a cylinder which is the basement region for the aneurysm evolution (Fig. 2.3(a)).

In the wake of the cylinder inserted, the following problem was the unmatched boundaries of the cylinder and the remained geometry without the aneurysm, i.e. parent arteries. To solve this problem, the adjacent region were cut off with an appropriate length and the complementary sections were reproduced (Fig. 2.3(2-3)) to connect the aneurysm cylinder and parent vasculature (Fig. 2.3(4-5)) in the upstream and downstream respectively. In short, the method used in building the connection surface is using a cubic polynomial to produce a updated skeleton between the new boundaries of cylinder and up/downstream parent vessel. In the course of the above procedure, the adjacent parts (Fig. 2.3(2-3)) were maintained the same as the original geometry as much as possible to ensure the maximum facticity of the artificial segments. Based on the new skeleton showed by a red curve in Fig. 2.3(c), closed curves were created to construct a smooth transitional section and the corresponding surfaces were produced to fit between the cylinder and parent vasculatures.

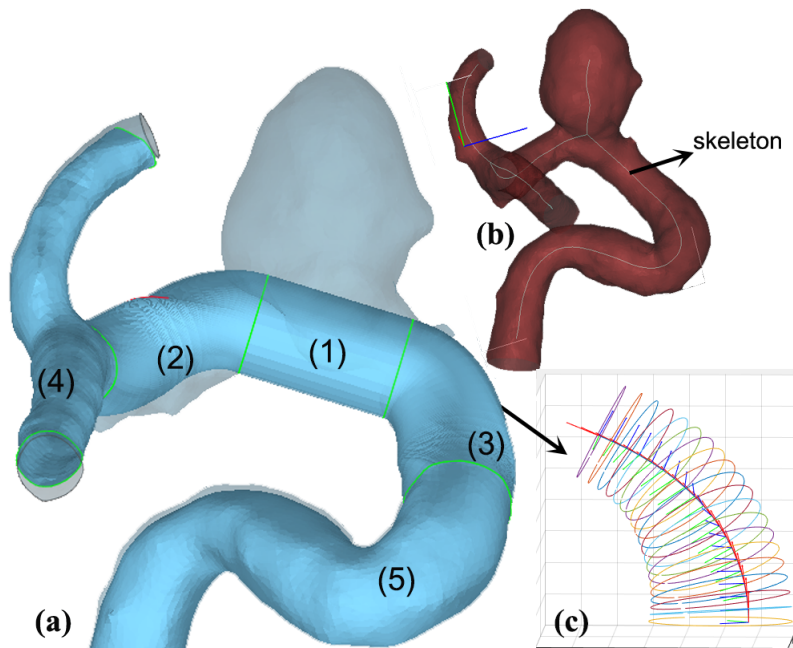


Figure 2.3: Reconstructed model with the aneurysm part substituted by a cylinder membrane which can be divided into 5 segments : (1) cylinder; (2) regenerated downstream connection; (3) regenerated upstream connection; (4) downstream parent vessel; (5) upstream parent vessel. (b) The skeleton of the original geometry produced in @neufuse; (c) the closed curves for the connecting upstream region used to produce surface

2.3.2 CFD Simulation and Structural Analysis

Since the reconstructed geometry was prepared regarded as the healthy arterial state before the inception of aneurysm, this new geometry was categorized to 2 parts, cylinder (A) and the remaining geometry (B). For the solid subsection in FSG framework, the cylinder geometry was employed only for the consideration of saving computational time and resource. Most importantly, this cylinder is essential in aneurysm evolution modelling which is the platform for elaborate operation and analysis. As to the remaining geometry B, it contributes to the CFD simulation which could provide the mechanical stimuli given by the blood flow to aneurysm pathological development.

The aforementioned two parts A and B were imported to ANSYS ICEM in order to generate the volume mesh for CFD simulation solver where the mesh was tetrahedron unstructured mesh combining with prism layers lining on the boundary. Boundary condition was derived from the @neuFuse which will be depicted in chapter [chapter 3](#) with detail. ANSYS

CFX served as the solving programme, the blood flow was modelled as a Newtonian fluid while the arterial wall was set to no slip, no flux boundary conditions. Steady or pulsatile flow analysis are both available for each FSG step. The part A is updated after each growth and remodelling cycle while the shape of part B is presumed unchanged during the whole FSG framework which merely used in CFD simulation part. The idea of this type of CFD simulation with combined geometries is also used in further researches.

Mathematical calculation of the structural analysis only performed on the cylindrical segment. The intima layer was omitted here due to its extremely thin structure and it has no contribution in bearing the load. Then this structural-based cylinder membrane model is composed of media and adventitia layers. The SEFs of elastinous constituents and collagen fibres are identical to those used in this thesis. In this membrane model, two families of helically arranged collagen fibres are presented in media and adventitia layer possessing different mechanical behaviours. It is because the initial setting of the model is the healthy artery model which has intact structures. For intracranial aneurysms, the media layer is degraded and then largely broken down which implies that the adventitia layer should be considered as the main structure in the aneurysm model. Next part will introduce the growth mechanisms of aneurysm in detail which consists of elastin degradation and collagen growth and remodelling, providing an understanding of pathological variation from a healthy artery to a dilated aneurysm.

2.3.3 G&R: Elastin Degradation Function

The 3D cylinder is considered as the major target providing the platform for aneurysm growth and remodelling. This method for simulating the mechanism of arterial wall growth and remodelling to aneurysm was firstly proposed by Paul Watton (Watton et al., 2004), a geometric nonlinear membrane model. Biological reactions in the pathological process mainly contain the elastin degradation and collagen growth and remodelling. It is helpful to mention that the word 'growth' demotes the mass density of arterial constituents have changed while the word 'remodelling' means only the structure of constituents changes rather than the mass.

Primitively, this unloaded cylinder could be described by these indices: radius R , length L_1 , thickness H , where $H = h_M + h_A$. The h_M and h_A represent the height of media and adventitia layer respectively. The elastin fibres of the media layer broken around the aneurysm neck has been shown in histological experiment data. To quantify this change, a mathematical function of elastin degradation was proposed. In the incipient stage of elastin degradation modelling, the degradation rate was prescribed through the entire aneurysm evolution (Watton, Ventikos, 2009; Watton et al., 2009b). As the understanding of haemodynamic analysis

and tissue biology develops deeper, the elastin degradation becomes reasonable to link with haemodynamic indices embracing more biological mechanisms. On account of the initial cylinder geometry, the WSS distribution is uniform which could not contribute to the elastin degradation function. Therefore, a prescribed degradation was given in the first step to form a small bulge on the cylinder surface which leads to the variation of the spatial WSS distribution. The inception of aneurysm is initiated by the prescribed elastin degradation in a local region. The prescribed region for elastinous constituent degradation pathological process during the aneurysm development is defined as follows:

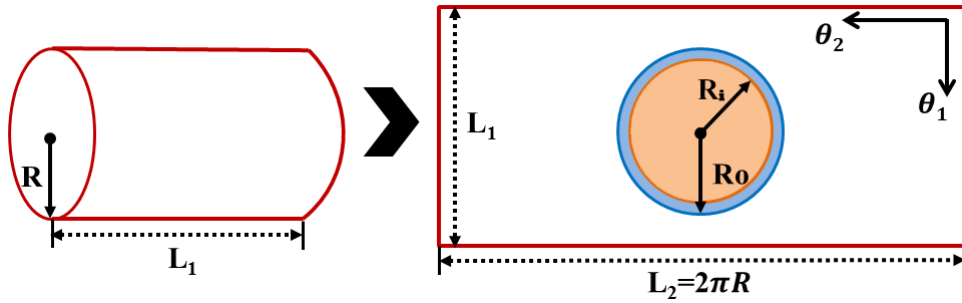


Figure 2.4: A circular patch in the center of the unfolded cylinder is defined for the elastinous constituents degradation. Elastin degradation function is prescribed in inner circular (orange) with the radius R_i and the exterior the outer circumference with the radius R_0 is defined as no degradation. In between (blue), the degradation adopts the radial splines method to realize linear interpolation.

This prescribed elastinous constituents degradation which could achieve an initial bulge on the surface of this cylinder. The m^E is the measuring parameter of the concentration (mass density) of elastin. The time-varying concentration of elastin is denoted as $m^E(\theta_1, \theta_2, t)$ and the initial concentration is defined as $m^E(\theta_1, \theta_2, t = 0) = 1$. In the inner patch with radius of R_i , the elastin degradation function is defined as

$$\begin{aligned}
 m^E(\theta_1, \theta_2, t) = & 1 - (1 - m_{min}^E(t)) \\
 & \times \left\{ \exp\left[-\omega_1 \left(\frac{\theta_1 - L_1/2}{L_1/2}\right)\right] \right. \\
 & \left. \times \exp\left[-\omega_2 \left(\frac{\theta_2 - L_2/2}{L_2/2}\right)\right] \right\}
 \end{aligned} \tag{2.3.1}$$

where $\theta_1 \in [0, L_1]$, $\theta_2 \in [0, L_2]$ shown in Fig 2.4 and the m_{min}^E represents the minimum elastin concentration (Watton et al., 2011). Parameters ω_1, ω_2 as the controlling factor which is responsible for the degree of localisation of the degradation function, here $\omega_1 = \omega_2 = 1$. The

lower limit of the concentration of elastin located at the point $(\theta_1 = L_1/2, \theta_2 = L_2/2)$ during the degradation should be specified which is the concentration at $t = T$, named as m_T^E . The way of the elastin decaying was assumed as an exponential form. The area out of the circular patch in Fig 2.4 has no degradation which means the concentration of elastin is constant there. Refer to the blue annulus, the concentration transformed linearly from the decaying concentration value on the edge of inner circle to the constant concentration area.

After the first prescribed degradation, the geometric variation could lead to the non-uniform spatial distribution of WSS. The in the following steps, the elastin degradation was linked with low WSS as a promotive factor and the degradation function linked to low WSS could be described as below(Watton et al., 2011):

$$m^E(\theta_1, \theta_2, t + \Delta t) = m^E(\theta_1, \theta_2, t)[1 - \mathcal{F}_D(\tau, |\nabla \tau|)D_{max}^{\Delta t}] \quad (2.3.2)$$

$D_{max}^{\Delta t}$ denotes the maximum degradation amount in each time increment Δt . And the WSS-related function \mathcal{F}_D as a weight factor is defined as:

$$\mathcal{F}_D(\tau(\theta_1, \theta_2, t)) = \begin{cases} 1, & \tau < \tau_X \\ \left(\frac{\tau_{Crit} - \tau}{\tau_{Crit} - \tau_X}\right)^2, & \tau_X \leq \tau \leq \tau_{Crit} \\ 0, & \tau > \tau_{Crit} \end{cases} \quad (2.3.3)$$

τ_{Crit} and τ_X represent two levels of WSS which aim to define different degradation rate of elastin. When WSS magnitude is larger than τ_{Crit} , the location has no elastin degradation. Whilst the maximum degradation occurs when WSS is less than τ_X . In between, the degradation function was assumed to be a quadratic form showed in the above equation.

2.3.4 G&R: Collagen Growth and Remodelling

As the elastinous constituents degrades, the collagen fibers start to compensate for bearing the load from blood pressure which is in charged by the lost elastinous constituents originally. To maintain the load bearing capacity of the aneurysmal wall, collagen grows and remodels responding to this repercussion. Owing to the specific wavy structure of collagen fibres in the non-load bearing state, several mechanical conceptions should introduce lucidly first. When the collagen fibres are tugged to straight shape, which indicates that they are recruited for bearing the load , the stretch at this state is dubbed as recruitment stretch (λ^R). The collagen stretch (λ^C) is equal to the tissue stretch (λ) dividing the recruitment stretch while

the equation is thus expressed as:

$$\lambda = \lambda^R \cdot \lambda^C \quad (2.3.4)$$

There is a prestretch, assumed on the depositing collagen, which is regarded as the homeostatic stretch responded by the system, called attachment stretch (λ^{AT}). Initially, the stretch of collagen fibre through the wall is taken as the attachment stretch according to the physiological axial stretch and circumferential stretch at systole. Once the configuration starts altering, the circumferential stretch increased thus the collagen stretch increased as well. The collagen need to remodel in the bulged geometry thereby restoring to an equilibrium level of strain E_{AT}^C .

In the remodelling scenario, the remodelling of collagen fibers in reference configuration leads to the deposition (turnover and attachment) of fibers in altered structure. In the process of restoring the Green-Lagrange strain, the recruitment stretches was remodelled:

$$\frac{d\lambda_{J_p}^R}{dt} = \alpha \frac{E_{J_p}^R - E_{AT}^C}{E_{AT}^C} \quad (2.3.5)$$

$$E_{AT}^C = \frac{1}{2}((\lambda_{AT}^C)^2 - 1) \quad (2.3.6)$$

where α is a remodelling parameter which corresponds to a prescribed half-life (months) of collagen fibers.

In another scenario which is the growth and atrophy of collagen fibers, the fiber concentration variation as a representation of the regulation of fibroblasts in the synthesis or atrophy of collagen fibres. The new collagen will deposit with the stretch deviation from the attachment stretch λ^{AT} and the collagen concentration is proportional to the concentration of fibroblasts. Meanwhile, the GL strain of collagen fibers and fibroblast are assumed to be identical ($E^F \equiv E^C$). On the grounds that the mass density of collagen is changing, the collagen fibres concentration $m_{J_p}^C$ is introduced here. The evolution equation for growth and atrophy of collagen fibres is defined as follows:

$$\frac{dm_{J_p}^C}{dt} = \beta m_{J_p}^C \frac{E_{J_p}^C - E_{AT}^C}{E_{AT}^C} \quad (2.3.7)$$

where β is a growth parameter which refers to the rate of change of collagenous constitutes mass responding to deviations of cyclic deformation from normotensive levels.

2.4 Limitations of the State-of-the-art FSG framework

- The FSG framework program integrates both academic program packages (Fortran, Perl, Matlab subroutines) and commercial software (ANSYS ICEM, CFX, Tecplot, etc) together in modelling the aneurysm evolution. The kernel solver of the structural modelling is assembled in an executive program, which is targeted to refresh the deformed aneurysm growing on the cylinder at each evolution step. To master this executive program and the possibility to make further improvements, it requires the fully understanding of the voluminous codes which is time-consuming and unwieldy.

- In consideration of the clinical application, this developed FSG framework designs a 3D cylinder to mimic the arterial wall in the healthy state. But clinically, most intracranial aneurysms are asymptomatic until the aneurysms have already been severe enough to threaten the normal life. In real cases, the majority of patients were confirmed with a definite diagnosis accidentally and seldom by related symptoms. No matter which is the case here, obvious aneurysms already exist in their brains which could be visualized by the medical imaging technology. Therefore, this healthy-to-pathological simulation is helpful in understanding the complex interactions during the aneurysm evolution, but inadequate to provide more practical application on the therapeutic schemes.

- The morphology of the full-grown aneurysms produced in current FSG simulation is relatively simple which performs generally close to part of a sphere. But the aneurysms often show variant geometric characteristics, such as tortuosity, elongation, secondary or multi-aneurysms. Hence, the developed aneurysms in this FSG framework are still unable to achieve high consistency with the real complex aneurysm modalities.

- Aneurysm model in FSG framework is a membrane model which integrates the thickness property in the form of parameter number. Allowing for the complex constituents variation and more elaborate reactions within the arterial wall which must entail the mechanical micro-environment changing, the membrane model is unable to satisfy the requirement of interior biological reactions explicitly. The real thickness incorporation of the aneurysm model will provide a high possibility in the representation of transmural responses like molecule transportation which has a wider application.

2.5 Novelties of the p-FSG Framework

To overcome the above limitations, we build up a patient-specific FSG (p-FSG) framework with the following novelties:

- **Aneurysm Growth Begins at Clinical Status**

Firstly, this p-FSG framework starts with a patient-specific geometry which has great complexity, leading to a big challenge in the following mesh deformation in the course of simulating the aneurysm evolution. Even though, the growth algorithm applied on anatomical aneurysms has a stronger potential to predict the rupture risk of existing aneurysms. There is still no mathematical models of aneurysm growth based on the clinical aneurysm directly.

- **G&R Methods (Paul Watton 2004) Fully implemented in Commercial Software using a Thick-walled Model**

This research generated a thick-walled aneurysm model from the clinical states using the commercial software ANSYS. In the previous framework, the structural modelling section was conducted by a programme package where the codes are hard to be adapted without a full understanding. Now we use ANSYS to generate mesh for the thick-walled model and solving the controlling functions. Because the p-FSG framework couples the fluid simulation and structural modelling together, one novelty is the transformation of fluid stimuli to the structural domain. The overlapped region between the structural domain and fluid domain is the inner surface of structural model and the surface of fluid model. The challenge is the information of haemodynamic stimuli transferring to the structural domain where the G&R occurs.

- **Representation of Endothelium by Implementing a Novel Flow Metric**

The previous FSG framework only considers the mechanical response of elastin and collagen fibres, which lacks an important component: endothelial cells layer. This layer is the directly receptor of fluid stimuli and its response can highly affect the following behaviour of elastin and collagen fibres in the media and adventitia layer. And in our p-FSG framework, we hypothesize a function between fluid stimuli and endothelial permeability, thus link to the G&R function through the inflammation pathway.

- **G&R function Linking with Pulsatile Flow**

As introduced in this chapter, the G&R function includes the elastin degradation, collagen growth and remodelling. Previously, the elastin degradation was linking to the flow metric calculated by the steady flow condition. Oscillatory flow characteristics can significantly

influence the mechanobiological response of cells , while the cell responses play critical roles in the G&R process. Hence, in this p-FSG framework, we started using the pulsatile flow as the hemodynamic stimuli to response of endothelial cells.



Implementation of a Novel Hemodynamic Index for Representation of Endothelium Permeability

3.1	Computational Fluid Dynamics Simulation	41
3.2	Hemodynamic Results	56
3.3	Correlation Analysis between Hemodynamics and Aneurysm Growth	71
3.4	A Novel <i>G&R</i> Hypothesis: WSSAR-Endothelium Permeability- <i>G&R</i> function	76
3.5	Conclusion	81

It is impractical to track the biological variation of the aneurysm wall tissue in the course of aneurysm evolution in vivo. The most common approach to investigate the pathological

alteration within the aneurysm tissue is to find the link between the haemodynamic environment and geometric features. The majority of academic researches in the literature pool are based on a similar methodology which is performing CFD simulations using the follow-up medical images of patients with aneurysms. Moreover, there are also parts of studies combine with the structural modelling of an aneurysm, which can provide the stress distribution within the tissue. The stress distribution as an analysis index could provide insight into the aneurysm rupture. In this research, we combined the fluid, solid and G&R to mimic the progress of aneurysm evolution, but this chapter we just focused on the hemodynamic analysis.

In this chapter, we employed two intracranial aneurysms named ICA-1 and ICA-2, and the later is further used to develop the p-FSG framework. With the implementation of boundary conditions, ANSYS CFX as the solver generates the haemodynamic solutions for the models. Endothelial cells firstly receive the mechanical stimuli from the blood flow and their function plays a crucial role in the pathological development of an aneurysm. This chapter aims to link an effective haemodynamic index to aneurysm G&R function through the representation of endothelial mechanobiology/permeability, which can imply the pathological growth of an aneurysm.

3.1 Computational Fluid Dynamics Simulation

3.1.1 CFD Theory

The methods underlying CFD are by now well-established, and are concerned with the numerical solution of the governing equations of fluid flow, i.e. the Naviér Stokes Equations. The solution of incompressible Naviér Stokes equations provides the predictive distribution of velocity, pressure, wall shear stress and other indices for the given geometries.

Naviér Stokes equations are used to describe the motion of viscous fluid substances including three key terms in below equation which are inertial force (1), pressure force (2), and viscous force (3) applied to the fluid. These equations depict how the velocity, pressure, and mass density of a progressing fluid are related.

$$\overbrace{\rho \left(\frac{\partial \mathbf{u}}{\partial t} + \mathbf{u} \cdot \nabla \mathbf{u} \right)}^1 = \overbrace{-\nabla p}^2 + \overbrace{\nabla \cdot (\mu (\nabla \mathbf{u} + (\nabla \mathbf{u})^T)) - \frac{2}{3} \mu (\nabla \cdot \mathbf{u}) \mathbf{I}}^3 \quad (3.1.1)$$

The above equation describes the momentum conversation which needs to be solved with the continuity equation for solving the mass conservation:

$$\frac{\partial \mathbf{u}}{\partial t} + \nabla \cdot (\rho \mathbf{u}) = 0 \quad (3.1.2)$$

The above two equations can achieve the approximate solution of velocity and pressure distribution for a specific geometry with rational simplification. The method to get the solution in complex geometry is discretization which divided the geometry into numerous elements by meshing. Then the fluid-flow equations that satisfy the conservation of mass and energy are then solved for each control volume.

To solve the mass and energy conservation equations, it is also necessary to provide boundary conditions for the given model which are normally pulsatile velocity and pressure curves in one cardiac cycle. With the boundary conditions given at the inlets and outlets, the solution for each element could be solved that satisfy the mass and energy conservation rule. In the end, the spatial and temporal distribution of haemodynamic indices could be represented all over the geometry, both magnitude and direction. The next section will introduce the two recruited models for CFD simulation and follows with the description of these two important components in the CFD simulation.

3.1.2 3D Patient-Specific Intracranial Aneurysm Geometries

3.1.2.1 Data Acquisition

This research recruited two clinical cases of intracranial aneurysms, both in the internal carotid artery (ICA) just before the branch of the anterior cerebral artery (ACA) and middle cerebral artery (MCA), from the group lead by Christian Doenitz ([Doenitz et al., 2010](#)) and research group of Anne Roberson. Here to simplify the appellations of these two models, they were denominated as ICA-1 and ICA-2 respectively. The 3D reconstructed geometries of the clinical cerebral aneurysms were obtained in vivo from 3D rotational angiography (3DRA) data with the technology of digital subtraction angiograms prior to clinical intervention. The intracranial aneurysm geometries employed in this study are both side-wall saccular IAs.

In the case of ICA-1, the patient underwent two screenings and the aneurysm geometries were reconstructed. Unfortunately, the clinical information of this ICA-1 case was not obtainable except the geometries at present. On the positive hand, the second follow-up geometry is able to provide effective validation for our growth and remodelling hypothesis. The screening in Phase I was scanned in 2008 and the follow-up one (Phase II) was conducted in 2010 respectively.

Initial locations of the two reconstructed aneurysm geometries were not in line with each other, leading to a puzzle of contrasting the aneurysm enlargement and variation in morphol-

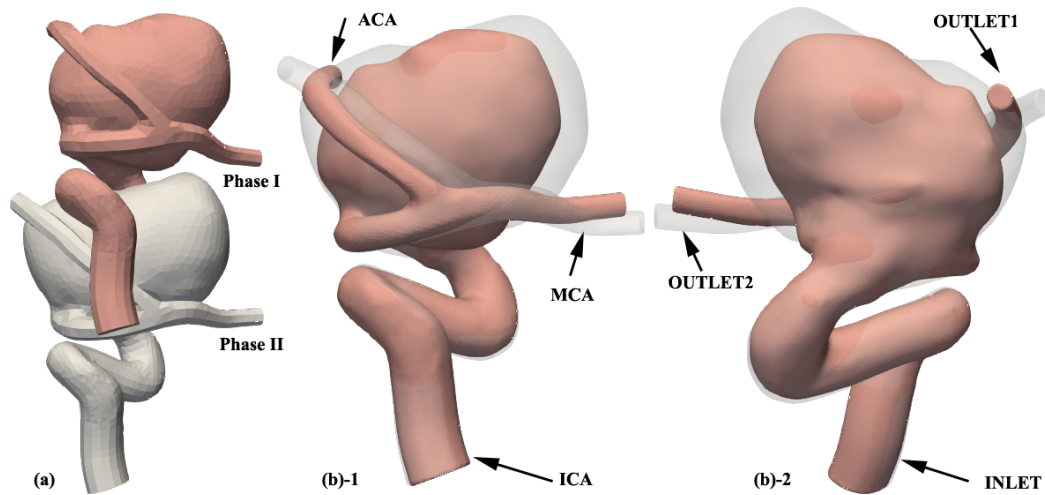


Figure 3.1: Schematic of the original physiological aneurysm geometries of ICA-1 MODEL in phase I and II (a) and corresponding aligned geometries from anterior ((b)-1) and posterior view ((b)-2). The vascular branches and boundaries :Inlet, Outlet1 and Outlet2, are indicated.

ogy analysis (Fig 3.1(a)). To solve this puzzle, the Geomagic Studio (Geomagic Inc.) was employed and a function called 'best-fit alignment' can automatically find the best fit position for the targeted separate geometries. The aligned geometries were posted in Fig3.1(b) from the anterior and posterior views. These two physiological geometries have rugged surface and the inlet and outlets are closed. Meanwhile, the surface of the geometry was smoothed in Geomagic Studio (Geomagic Inc.) generally to provide feasibility in meshing.

For the ICA-2 case, the patient was a male with the age of 27 years old and his aneurysm was discovered after a traumatic head injury incidentally. Specific clinical information was collected after getting the consent of the patient at the Allegheny General Hospital (Pittsburgh, US). This case is the same as a sample from a study which investigated the collagen fibre architecture from a group of clinical aneurysms (Robertson et al., 2015). The clinical data of specific items of this patient was summarised in Table3.1. This patient has no history of hypertension and diabetes and no signs of usage of medication. However, the patient has a family history of a cerebral aneurysm where both of his grandmother and mother had previous incidents of intracranial aneurysms.

As showed in Figure3.2(a), the manipulation of the closed boundaries and smoothing procedures was the same as the ICA-1 case. Specifically, due to the small diameter of the ophthalmic artery compared to other arteries in this ICA-2 geometry, removing the ophthalmic artery will make no remarkable influence to the CFD simulation results. Hence, the oph-

Table 3.1: General clinical information of the patient
 (adapted from (Robertson et al., 2015))

Location	Age	Gender	Symptomatic	SAH	Family history	IA	No. of IAs	Hypertension	Diabetic
ICA	27	M	Incidental	No	Yes	1	1	No	No

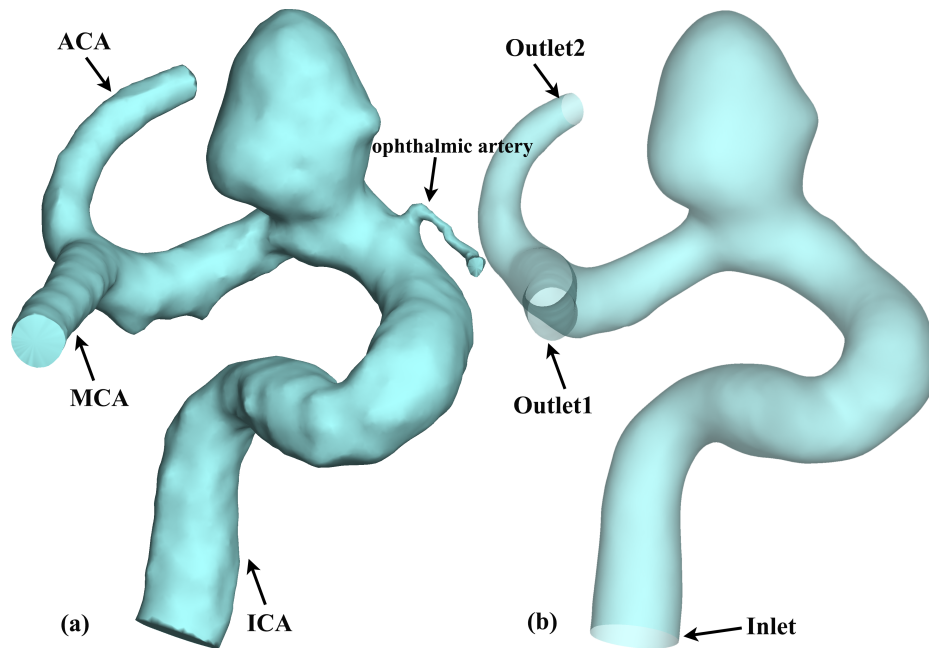


Figure 3.2: Schematic of the original physiological aneurysm geometry of ICA-2 model with anatomical structure names (a) and corresponding optimized geometry for modelling (b). The boundary Inlet, Outlet1 and Outlet2 utilized in CFD simulation are positioned in (b).

thalmic artery was removed from this physiological geometry, and the modified geometry is showed in Figure 3.2(b) as the fundamental model in the following research.

3.1.2.2 Morphology Analysis

The aneurysm sample of the ICA-2 case was retrieved after surgical intervention of this unruptured intracranial aneurysm. For further investigation, the harvested aneurysm tissue was taken to the University of Pittsburgh to conduct the mechanical and histological test. The morphology information of this aneurysm sample was summarized and morphology assessment indices were explained in Table 3.2.

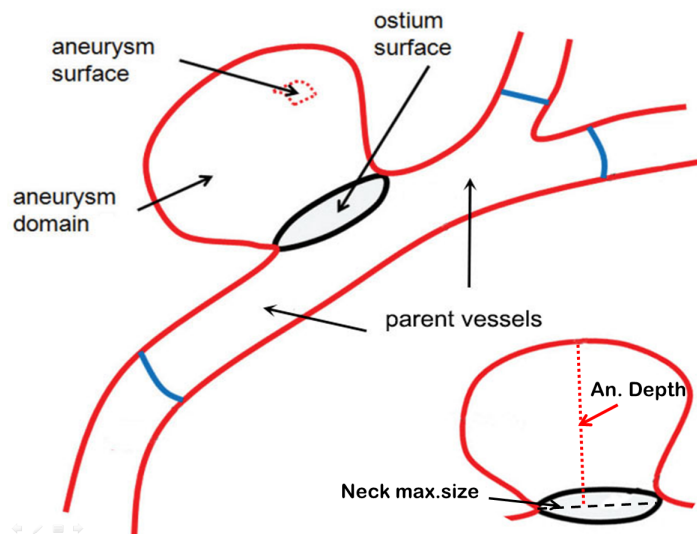


Figure 3.3: Subdivision of the vascular domain and quantitative terms for the morphology analysis of the aneurysm geometry (adapted from (Cebal et al., 2011))

To get a better understanding of the meaning of each index, the schematic of vascular subdivisions was presented in Fig. 3.3. According to this methodology of morphology analysis, several pertinent morphological indices for ICA-1 case could be measured through the reconstructed geometries. Compared to the ICA-2 case, this aneurysm was already a giant aneurysm in Phase I and it grew tremendously within two years. Aneurysm geometry in Phase II is served as a tool of the growth quantification which applied to the aneurysm in Phase I. And to quantify its growth, the index '**Volume**' and '**Surface Area**' is obviously the most significant factor from a more comprehensive perspective. Therefore, we can merely measure these two key indices for further investigation. The surface area and the volume of

this ICA-1 aneurysm is 1193.63 mm² and 3412.67 mm³ respectively. Even though the thickness of an aneurysm is also an important factor in the structural modelling, the medical imaging technique does not possess the capability of acquiring the information of non-uniform thickness distribution which limits the modelling in turn. The selection of the thickness for this model will be illustrated in the structural modelling section.

Table 3.2: Statistics of the morphology information of the aneurysm (adapted from (Robertson et al., 2015))

Volume (mm ³)	Surface Area (mm ²)	Equiv.diam. (mm)	Max.an.size (mm)	An.depth (mm)	Neck area (mm ²)	Neck max.size (mm)	Aspect ratio	Thickness (mm)
219	215	8.2	10.6	8.9	24.9	5.7	1.6	0.16
Volume	the volume of aneurysm above the ostium surface							
Surface Area	sum of area of all triangles on the aneurysm surface							
Equiv.diam.	equivalent sac diameter (equals to the diameter of a sphere converted from the aneurysm volume)							
Max. an. Size	the maximum distance measured within the aneurysm region between any two points							
An. Depth	the maximum height from the point on the aneurysm region to the ostium surface							
Neck area	area of the ostium surface							
Neck max.size	the maximum length of any two points on the edge of the ostium surface							
Aspect ratio	computed as the An. Depth divides the Neck max.size							
Wall thickness	averaged from the thickness on 5 random positions measured by micro-calipers							

3.1.3 Mesh Generation and Boundary Condition

3.1.3.1 Mesh: Spatial Discretization

The volumetric space of the reconstructed vascular geometry needs to be discretized to simulate the blood flow. The governing Navier-Stokes equations can be used to describe the motion of blood flow, and the velocity at every point in the flow domain and the shear stress on the boundary can be obtained. These solutions are not available in complex physical testing at this stage. Therefore, tetrahedral elements are usually produced to fill in the flow volume while layers of prism elements in the vicinity of flow boundary are extruded (Spiegel et al.,

2009; Janiga et al., 2013). There is a great significance in building these boundary elements to guarantee the accuracy in the estimation of the wall shear stress due to the risk from high-velocity radial gradients there. The methodology of mesh generation is vital to the simulation and the mesh dependency study is required to get reliable solutions (Hodis et al., 2012).

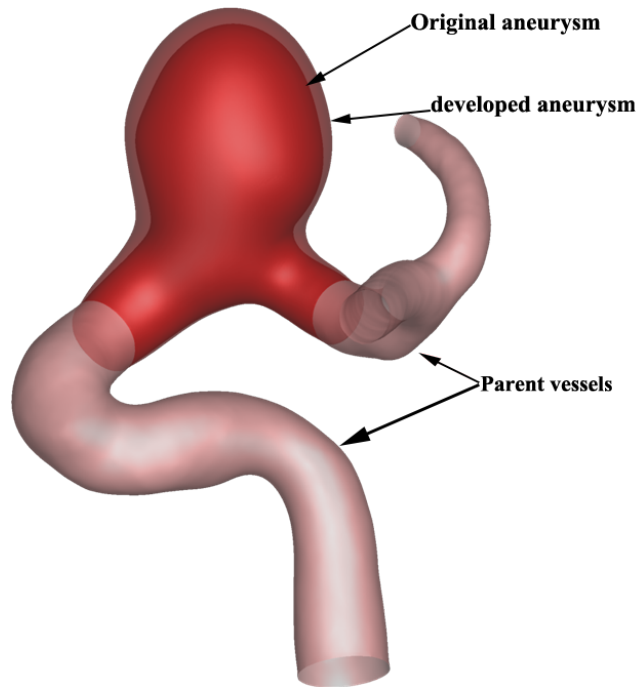


Figure 3.4: Translucent upstream and downstream parent vessels on the sides of aneurysm connect to the inserted aneurysm part to fulfil the mesh generation. The updated aneurysm replaces the original geometry constituting an integrated geometry.

In this study, two aneurysm models were meshed in ICEM CFD (ANSYS) in preparation for CFD simulations. ANSYS ICEM automatically integrates the aneurysmal section into the physiological geometrical domain, i.e. attaches the upstream and downstream extensions, and then automatically generates an unstructured tetrahedral mesh with prism layers lining the boundary. It is worth to note here that the aneurysm part is cut off individually to do the structural analysis which will be illustrated in the structural modelling part (Chapter 4) in detail. With respect to the CFD simulation, the updated inner-surface of the deformed aneurysm surface as the aneurysm evolving result is extracted after the structural modelling. This updating aneurysm geometry connects with the unchangeable upstream and downstream parent vessels composing an integrated geometry for further meshing. To illustrate this methodology, a growing aneurysm was built artificially of ICA-2 case is shown in Fig. 3.4.

Arise out of the complexity of the geometry, the unstructured tetrahedral volume meshes were generated using a top-down meshing approach where the computational domain is created by performing logical operations on primitive shapes. To achieve a more accurate solution, four prism layers were lining the boundary which enclosed the tetrahedra domain. The set up of specific parameters will be depicted elaborately in Section 3.1.5.1.

3.1.3.2 Boundary Conditions

The outlet of the middle cerebral artery and anterior cerebral artery are named as Outlet1 and Outlet2, of which the diameters are approximately 2.155 mm and 2.105 mm, 2.354 mm and 1.509 mm for ICA-1 and ICA-2 cases respectively. Similarly, the distal part of the internal carotid artery is denominated as Inlet with the diameter of around 5.348 mm and 4.154 mm for ICA-1 and ICA-2 cases respectively.

The boundary conditions adopted in this research are obtained from a one-dimensional model validated with in vivo measurements at the Geneva University Hospital (HUG) which can compensate the conditions when the patient-specific flow and pressure conditions are not available (Reymond et al., 2009). The artery tree in this 1-D model has network topology of 104 branches and each vessel has a pressure and flow rate attribute sampled along a beat cycle which has been integrated into Aneufuse software which is developed within the framework of the EU Project @neurIST (Villa-Uriol et al., 2011). Considering the segments of ICA-1 and ICA-2 are located at the nearly same positions in the arterial tree, the same inlet and outlets boundaries can be applied to both cases.

In the steady case, the overall reference pressure was set as 9000 Pa. Two relative pressure (3000 Pa) boundary conditions were applied on Outlet1 and Outlet2 while the inlet was given the mass flow rate (\dot{m}) boundary condition :

$$\dot{m} = \rho \cdot \dot{v} \quad (3.1.3)$$

where \dot{v} means volume flow rate which equals to $4.3e-06 \text{ m}^3/\text{s}$. This specific boundary condition was get from the software @neufuse which possesses the database of a 1D model of human vascular tree (Reymond et al., 2009). The ρ represents the constant density of blood flow which is $1066 \text{ kg}/\text{m}^3$. All these boundary conditions was stored in a file with the .ccl extension that will be further used in CFD simulation.

Apart from the steady flow, pulsatile flow type is more reliable in modelling the dynamic properties of blood flow. This research also includes this transient flow type and the boundary flow conditions were obtained in software @neufuse as well. In the pulsatile case, the overall reference pressure was set as 9194.01 Pa. Fig.3.5 illustrates the boundary conditions set in

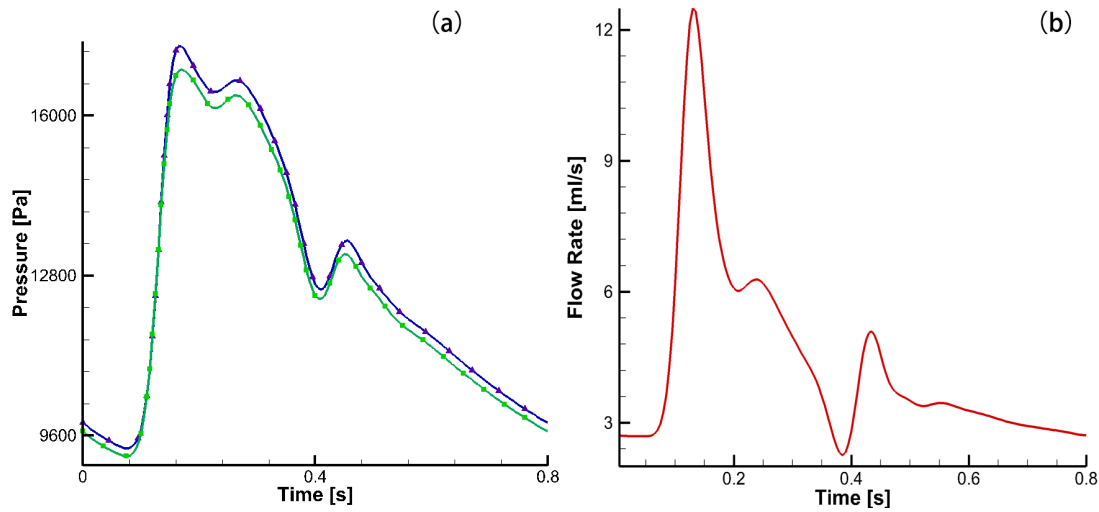


Figure 3.5: Pulsatile boundary conditions obtained through @neufuse in a full cardiac cycle.(a)Pressure curves of Outlet1 (green) and Outlet1 (blue); (b)flow rate boundary condition in Inlet

the Inlet, Outlet1 and Outlet2 with the flow rate and pressure indices. Note that the pressure magnitudes labelled in the figure stand for the absolute pressure which is equal to reference pressure plus relative pressure.

In terms of the arterial wall, it is presumed as the no-slip wall condition. The velocity of fluid immediately close to the wall assumes the velocity of the wall, which is zero. The blood flow is modelled as a Newtonian fluid with constant viscosity of $\mu = 0.0035 \text{ Pa} \cdot \text{s}$ and constant density of $\rho = 1066 \text{ kg} \cdot \text{m}^{-3}$.

3.1.4 Simulation Implementation

The mesh file and boundary conditions file produced by AneuFuse (with .ccl extension) were imported in the CFD solver (ANSYS CFX). The unsteady flow is simulated with 200 time steps per cardiac cycle (determined by a time independence study in Section 3.1.5.2) for 3 cycles with a fully implicit scheme and efficient solution algorithms. Computational results of the third cycle were adopted in the further hemodynamic characterization, especially in the interested aneurysm region, which is able to eliminate the adverse impact of initial transients.

Once solved, the ANSYS CFX offers the function of exporting statistics results for variables of interest, for example, the distribution of WSS vectors, OSI, potential aneurysm formation indicator (AFI) et al. The post-processing could be executed in CFX POST, another available option is Tecplot 360 which is widely used in academic researches. In most recent years,

Paraview is regarded as a magnificent visualization software to analyse large computational datasets. Hence, this research will make use of different post-processing instruments to illustrate the computational results for best effectiveness.

3.1.5 Spatial and Temporal Grid Independence Study

To balance the accuracy and the computational cost, the sensitive study of grid density was designed to determine an optimal mesh density. Meanwhile, the simulation results of pulsatile flow will be further linked to the growth & remodelling algorithm which inherently means that the time-step setup also plays a key role to guarantee the capability of capturing the flow feature precisely. The following two sections will elaborately depict the concrete investigation of grid density and time-step independence.

3.1.5.1 Grid Density Independence Study

The ICA-2 model was recruited here to investigate the mesh density study. A series of mesh density with different maximum element size was generated on this ICA-2 aneurysm model in ANSYS ICEM. The specific information, i.e., nodes number, element number, tetrahedron number and prism number, is listed in the Table 3.3 below.

Table 3.3: General mesh information of different study cases

	Case 1	Case 2	Case 3	Case 4
Nodes number	248241	446179	514067	704518
Element number	763634	1389746	1607385	2223870
Tetrahedron number	462522	854738	993317	1390198
Prism number	301112	535008	614068	833672

Four study cases were listed here as to determine an efficient and economic-computing mesh density. Regarding to the parameter setting, the global size of element height, prism height and prism layers (4) keep the same values for all study cases except the maximum of global element size index. This max element size controls the size of the largest element. For saving time, ANSYS ICEM provides the possibility of automatic replaying the meshing

process (.rpl replay file). The mesh quality is a significant factor which should be taken into consideration to guarantee the accuracy of the CFD simulation. ANSYS WORKBENCH has the function of evaluating the mesh quality for the mesh generated in ICEM CFD. The mesh metric has several evaluation criteria like element quality which provides a composite quality metric. For the 3D element, the calculation formula is described below:

$$Quality = C \left[\frac{volume}{\sqrt{\sum (Edgelenh^2)^3}} \right] \quad (3.1.4)$$

where C is a constant which is different for different element types. For tetrahedron and wedge/prism, the values of C are around 124 and 62 respectively provided by the ANSYS user manual. The element quality ranges between 0 and 1, from unacceptable to perfect. The value of 0 means that the element has a non-positive volume. In general, 0.2 is usually regarded as an acceptable threshold value (Lantz et al., 2012). The minimum values of element quality of all cases are above 0.2. In order to compare the element quality in a comprehensive way, the diagram which exhibits the statistics of element quality of case 1 and case 4 is plotted in Fig 3.6.

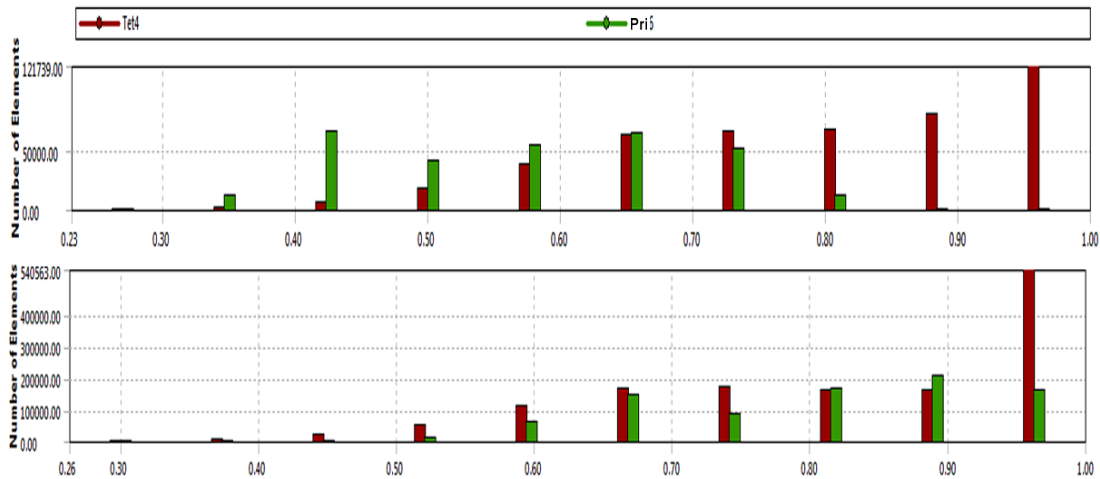


Figure 3.6: Distribution diagrams of statistics of element quality for case 1 (top) and case 4 (bottom). Red denotes the tetrahedron and green represents prism elements.

The above figure clearly shows that the element quality improved with the increase of mesh density. Especially for the prism elements, the green bars shift apparently from left to right in case 4 compared to that in case 1. In terms of tetrahedron elements, there is no significant change but the element numbers decrease within the range 0.5 to 0.9 which move to the last red bar. Additionally, the starting point in case 1 is 0.23 while that in case 4 is 0.26.

Hence, the element quality elevates with grid density undoubtedly, but even the coarsest case satisfies the standard of mesh quality.

Apart from the mesh quality, the more effective way of deciding the sufficient grid density to ensure the simulation accuracy is to compare the results between cases. Applying the same boundary conditions (steady flow) which would be introduced in detail in the next section, the simulation solutions are employed to evaluate the sufficient mesh density. Because the WSS is a crucial hemodynamic index extensively used in physiological simulations, this research uses WSS as the criterion to determine an optimal mesh density, specifying on the aneurysm region.

The original geometry was imported into Tecplot and all the parts except the aneurysm part were blanked which is shown as a semi-transparent (Fig 3.7 (a)). Then a plane was inserted in a proper position which can output the coordinates on the intersection of the plane and aneurysm geometry. To achieve the WSS distribution, only the contour of this intersection was extracted which is available shown in Fig 3.7 (b). There are 283 points in total mapping to this contour and the corresponding WSS magnitudes were the output of all study cases. The red curve represents the coarsest mesh while the blue curve displays the finest grids. The standard deviation between case 3 and case 4 is lowest (2.349%) which denotes that the solution is steady and efficient enough for the simulation in this research.

In order to conduct a more overall assessment, the WSS distributions of all 4 cases were plotted in Figure 3.8. To explicitly display the subtle difference of the WSS distribution among these cases, the colour map was restricted to 4 Pa as the maximal limit here. The prominent discrepancy regions were marked by rectangular boxes, one sit on the aneurysm and the other one was located in the upstream section. It is clear that case 3 and case 4 have nearly the indistinguishable distributions, which can indicate that the mesh in case 3 is fine enough for further investigations. Therefore, the setting of control parameters used in case 3 was used for all CFD simulations and further applications in this entire research.

In terms of ICA-1 model, we adopted the same setting up of mesh generation used in ICA-2 model. The final mesh was computed with 2,533,542 elements and 704,637 nodes for ICA-1 model, 1,607,385 elements and 514,067 nodes for ICA-2 model (Fig.3.9).

3.1.5.2 Time Steps Independence Study

The CFD simulation in this research provides the hemodynamic information of the blood flow, and more importantly, the mechanical stimuli on the arterial wall is given by the blood flow. The initial receptor of these stimuli is the endothelial layer, and the permeability of this monolayer plays a crucial role in vascular function. During the aneurysm inception and evolution, this permeability changes with the variation of the complex flow condition. To have

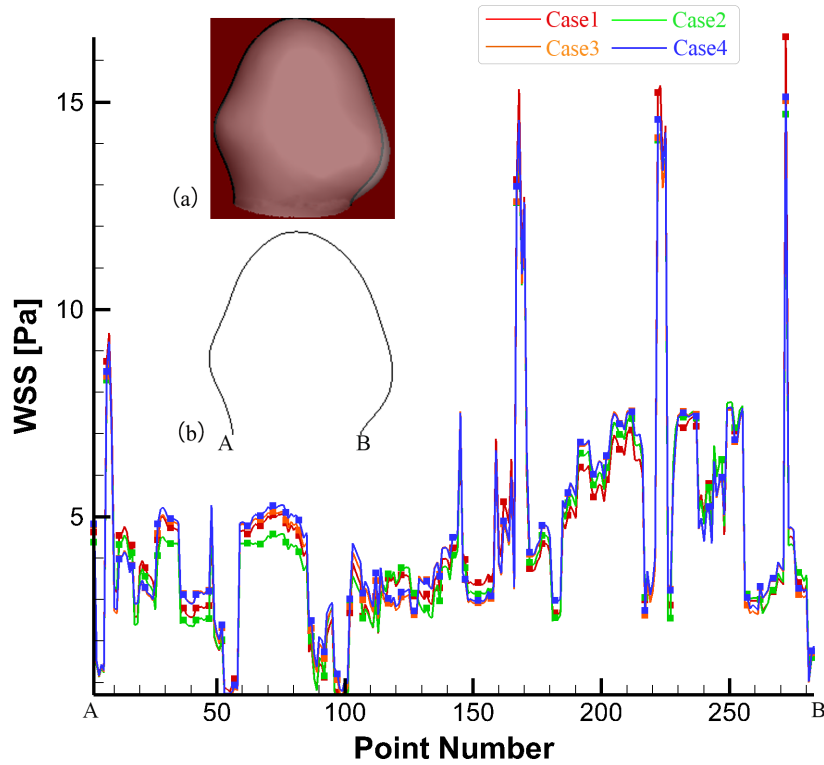


Figure 3.7: Grid independence study using the ICA-2 model: WSS magnitudes distribution on the same extracted profile from point A to point B on the aneurysm region of case 1-4.

a better understanding of this permeability, a novel hemodynamic index-Aspect Ratio (AR)-introduced by Krishna C. Vamsi was employed in this research to mimic the permeability of endothelium (Krishna et al., n.d.). This AR is a novel product to depict the wall shear stress variation over one cardiac cycle in the aspects of magnitude and orientation. In order to differentiate this AR from the AR which has been used in the morphology analysis, here we name it wall shear stress aspect ratio (WSSAR) instead. The explanation of the concrete calculation and understanding of this WSSAR will be explained in Section 3.2.1.6. Also because this WSSAR distribution is the vital investigation base of the endothelium permeability, which will be further linked to the study of aneurysm growth and stabilisation, we use this result to test the time-steps independence in the pulsatile flow simulation.

To reduce the simulation time, we adopted the steady flow to investigate the grid-density independence which is acceptable. For time-steps independence study, we set 5 scenarios of 50, 100, 200 400 and 800 time steps within one cardiac cycle (0.8 s) based on the above optimal grid density and applying the same pulsatile boundary conditions. The detailed setting up of

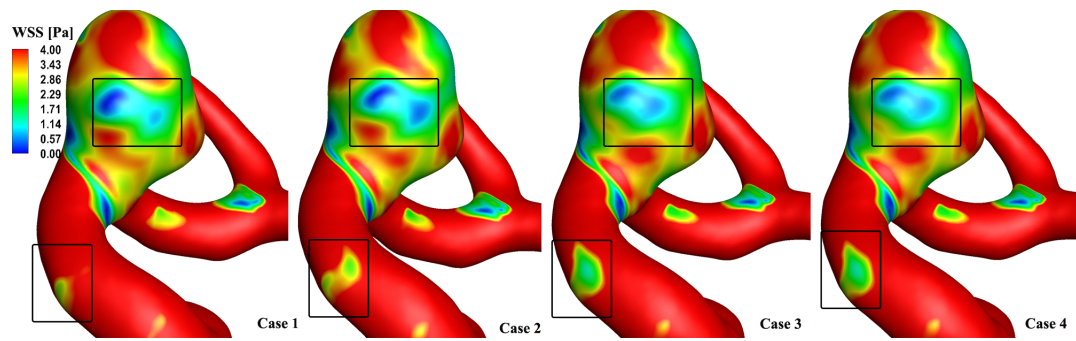


Figure 3.8: Grid independence study using the ICA-2 model: WSS distributions on the aneurysm geometry of case 1-4 are plotted and the specific locations with significant difference are marked by rectangles.

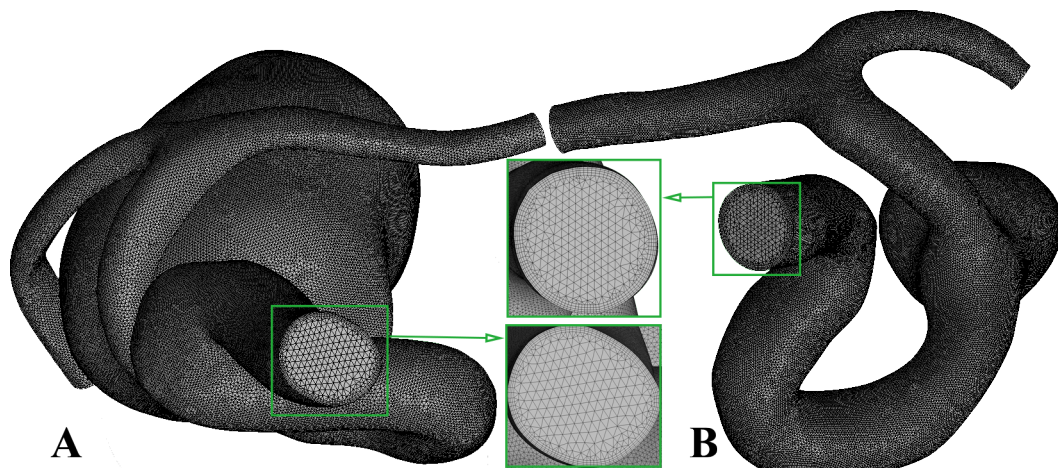


Figure 3.9: Unstructured tetrahedron mesh along with 4-layer prisms of ICA-1 (A) and ICA-2 (B) model

boundary conditions will be introduced in the next section. The Fig. 3.10 shows the WSSAR distributions of these five scenarios.

The WSSAR in Fig. 3.10 ranges from 0 to 1 and the legend color map was set to this range. The WSSAR distributions from left to right, from top to bottom represent the time steps of 50, 100, 200, 400 and 800 respectively. From the viewing angle shown in Fig 3.10, it is clear that the WSSAR distributions in all cases seem to like having no significant difference except the first scenario which has 50 time steps. However, in terms of the precise magnitude and local distribution, the high WSSAR area (red) in the TS-100 case is less than the other three cases on the top and anterior region of the aneurysm. In addition, the shape of high WSSAR region in the upstream in TS-100 is apparently different compared to the other three cases.

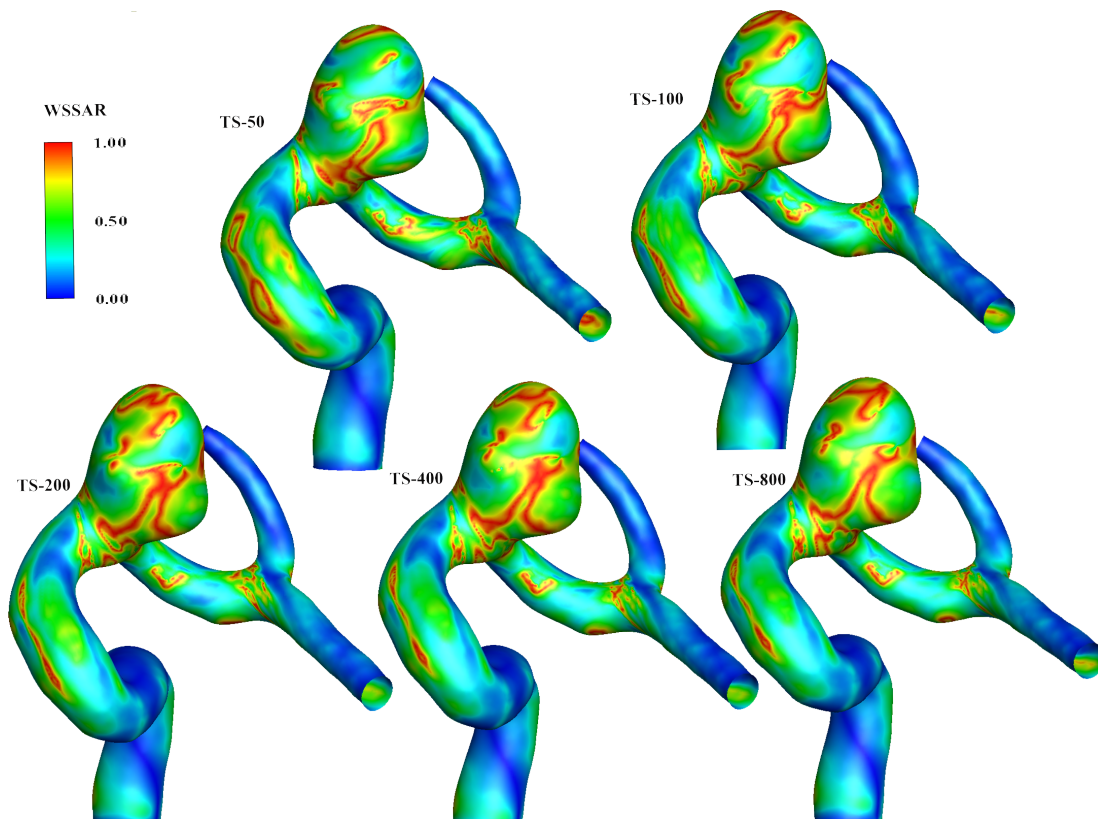


Figure 3.10: Time-step independence study using the ICA-2 model: WSSAR distributions on the aneurysm geometry of five scenarios. TS: Time-Steps

To be more precisely, we calculated the mean square error (MSE) between TS-800 case and TS-50 case, TS-100 case, TS-200 case, TS-400 case that were 10.19%, 2.66%, 0.84% and 0.37% respectively. Except the TS-50 case, the MSE in other cases were all located in the acceptable range for the simulation accuracy.

Even though there is still some slight difference among the TS-200 case to the TS-800 case, this subtle flaw can be omitted due to the economical efficiency of the computing time. The simulations consumed 20 h 13 min for the TS-200 case, 61h 02 min for the TS-400 case and 203 h 05 min for the TS-800 case. Considering this part of the simulation would be further integrated into the whole patient-specific FSG framework, the long-period computing time is indeed unnecessary to the insignificant accuracy difference to the finest scenario. Therefore, the optimal time steps in this research are 200 which will be used in further studies.

3.2 Hemodynamic Results

In the haemodynamic analysis, both steady and transient simulation play vital roles and specific-applied to different scenarios. A number of researches have indicated that low WSS and high WSS highly relate to the pathological progress in aneurysm evolution and rupture. According to this, our initial growth & remodelling theory linked low WSS to the elastinous constituents degradation as a single effect variable according to (Watton et al., 2011; Selimovic et al., 2014). As the research moves along, researchers found that the aneurysm growth is related to low WSS and high wall shear stress gradient. The sophisticated flow environment is expected to provide an insight into the pathological processing in aneurysm evolution, thus the pulsatile flow metric has been investigated extensively from multiple perspectives.

Velocity, pressure and other properties of blood flow are assumed constant at every time point in the flow domain, which could be considered as a steady flow. Obviously, the streamline of blood flow is a valuable analysis tool, in which the region with disturbed flow, secondary flow and circulating flow could be visualized clearly and used for further analysis of the biological response. The haemodynamic index WSS has attracted extensive attention in CFD simulation which is linked to biological behaviours of cells and tissue in most recent years. Close to a non-slip wall, there is a region where has large gradients in the dependent variables, i.e., velocity. The solution is needed to solve problems of accounting for viscous effects at the wall and the rapid variation of velocity here.

3.2.1 Haemodynamic indices for analysis

In a laminar flow, the wall shear stress is defined by the normal velocity gradient at the wall as

$$\tau_w = \mu \left(\frac{\partial u}{\partial y} \right)_{y=0} \quad (3.2.1)$$

where μ is the dynamic viscosity, u denotes the velocity of blood flow parallel to the wall and y is the distance to that wall.

The advantage of solving the fluid domain using steady flow is time-saving on condition that the properties varied over time is inferior to the spatial distribution. Basically, the most interested variables in the steady flow simulation are velocity, pressure and WSS distribution used in cardiovascular researches.

In the case of pulsatile flow, it can provide the real-time haemodynamic flow information in vivo. Apart from the aforementioned parameters, wall shear stress gradient (WSSG), oscillatory Sear Index (OSI), aneurysm Formation Indicator (AFI) and gradient oscillatory number (GON) are also available in pulsatile flow simulation.

3.2.1.1 Time-Averaged Wall Shear Stress (TAWSS)

As the name suggests, the TAWSS was used to assess the overall shear stress effect on the wall over a cardiac cycle, defined as

$$TAWSS = \frac{1}{T} \int_0^T \tau_t dt \quad (3.2.2)$$

where τ_t means the instantaneous wall shear stress and T is the period of one cardiac cycle. But many researchers only recruits the magnitude of TAWSS to analysis the mechanical state of their interested model which could be expressed in below:

$$TAWSS_{mag} = \frac{1}{T} \int_0^T |\tau_t| dt \quad (3.2.3)$$

3.2.1.2 Oscillatory Sear Index (OSI)

In addition, OSI, a more sensitive index to evaluate the flow dynamic properties proposed by Ku et al (Ku et al., 1985), indicates WSS fluctuations during a cardiac cycle. It is a nondimensional parameter ranged from 0 to 0.5 which defined as follows:

$$OSI = \frac{1}{2} \left\{ 1 - \frac{|TAWSS|}{TAWSS_{mag}} \right\} \quad (3.2.4)$$

The wss_i means the instantaneous WSS on a certain instant and T is the period of a cardiac cycle. The zero value indicates that the instantaneous WSS direction is aligned with the direction of the time-averaged WSS vector over the whole cardiac cycle. The other extreme (i.e. 0.5) shows that the instantaneous flow is by and large reversal to the direction of the time-averaged WSS vector, revealing a high oscillatory behaviour. The influence of OSI impacting on the pathology of aneurysm will be discussed in the forthcoming section.

3.2.1.3 Temporal and Spatial Wall Shear Stress Gradient (WSSG)

Temporal shear stress gradient is defined as the variation of wall shear stress between two neighbouring time steps at the same location. The expression formula is

$$WSSG_T = \frac{\partial \tau(x, t)}{\partial t} \approx \frac{\tau(x, t + \delta t) - \tau(x, t)}{\delta t} \quad (3.2.5)$$

where δt means the time interval. While the spatial wall shear stress was firstly proposed by M.Lei in 1996 (Lei et al., 1996), which is defined as

$$WSSG_S = \left(\frac{\partial \tau_{w,m}}{\partial m}, \frac{\partial \tau_{w,n}}{\partial n} \right) \quad (3.2.6)$$

where the wall shear stress (τ_w) parallel to the wall surface is decomposed into two components perpendicular to each other: $\tau_{w,m}, \tau_{w,n}$. Subscript m denotes the direction of time-averaged wall shear stress whilst the n indicates the in-plane perpendicular orientation. There is also a distinction of WSSG, positive and negative WSSG which represent the WSSG generated by the accelerating flow and decelerating flow respectively.

WSSG indicates the WSS derivation in the same direction with flow which is often accompanied with high WSS. Significantly, it is believed that high WSS and positive WSSG together play a vital role in the aneurysm initiation and evolution (Meng et al., 2007; Wang et al., 2009).

3.2.1.4 Aneurysm Formation Indicator (AFI)

The conception of AFI was proposed by A. Mantha et al. (Mantha et al., 2006) according to the fact that WSS direction varied greatly through the cardiac cycle based on the examination of where an aneurysm forms. To quantify this direction change, the angle θ between the transient WSS direction and the time-averaged WSS direction was employed, and the cosine of this angle is defined as the AFI. This index is also a nondimensional parameter and the magnitude changes from -1 to 1. The equation of the AFI definition is

$$AFI = \cos(\theta) = \frac{\tau_t \cdot TAWSS}{|\tau_t| \cdot |TAWSS|} \quad (3.2.7)$$

and it indicates the deviation of transient WSS direction on a certain timing where τ_t means the transient WSS and $TAWSS$ denotes the time-averaged WSS. The OSI represents the fluctuation of WSS over a cardiac cycle, while the AFI denotes the WSS fluctuation at some point. The threshold ranges from -1 to 1 which means that the instantaneous WSS direction is completely reversed to the time-averaged WSS and aligning with the reference direction respectively. Obviously, the value 0 is meant to have a 90° rotation of WSS.

Above mentioned TAWSS and OSI are the key factors in pathological process of aneurysm growth. However, a review made by Veronique Peiffer et al. (Peiffer et al., 2013) found that the low WSS and OSI is less robust than commonly used because of the unsuccessful mapping of shear and disease as the expected relation. The disturbed blood flow is usually considered

as the key research object to vascular diseases, but the above extensively-used flow metrics are unable to quantify the mechanical influence of the multi-directional flow. This multi-directionality should be taken into account for more specification on the positive correlation between hemodynamics and pathological involvement. Actually, the conception of multidirectional shear stress was introduced by Donald E. McMillan in 1985 (McMillan, 1985). Recently, studies have addressed the multi-directionality of the WSS over one cardiac cycle, the following sections will brief introduce several hemodynamic surrogates of multi-directional flow.

3.2.1.5 Gradient Oscillatory Number (GON)

In addition to these WSS-related indices, another parameter was dubbed as gradient oscillatory number (GON) was put forward by Yuji Shimogonya group who proved that GON can be an indicator for aneurysm inception (Shimogonya et al., 2009).

$$GON = \frac{1}{2} \left\{ 1 - \frac{\left| \int_0^T WSSG_S dt \right|}{\int_0^T |WSSG_S| dt} \right\} \quad (3.2.8)$$

This definition can evaluate the tension/compression force generated to endothelial cells (Lei et al., 2001). As expected, relatively higher GON magnitudes are gathered on the aneurysm surface which denotes the fluctuation of tension/compression forces squeezing on endothelial cells.

3.2.1.6 WSS Anisotropy Ratio - WSSAR

Combined the concepts of OSI and multi-directionality of flow, a novel quantitative index Wall Shear Stress Anisotropy Ratio (WSSAR) was developed which quantifies the combined influence of stress magnitude and bidirectionality (Krishna et al., n.d.). In the original publication, it was named as Anisotropy Ratio (AR). However, in order to differentiate this hemodynamic AR with the morphological Aspect Ratio, its abbreviation was nominated as WSSAR. First of all, a shear rosette was developed to record the wall shear stress vectors in a polar plot way at a fixed point during a cardiac cycle. Figure 3.11 illustrates two representative shear rosettes showing two distinct flow patterns: (a) laminar flow (b) disturbed flow with clear bidirectionality. In Figure 3.11 (a), the flow always along with the axial direction while the flow varies 150 degree over one cardiac cycle in Figure 3.11 (b). There are several dash circles in shear rosettes labelled with pink numbers indicating the magnitude of shear stress.

Hence, the shear rosette not only can track the WSS direction over one cardiac cycle, but also record the WSS magnitude at each time point.

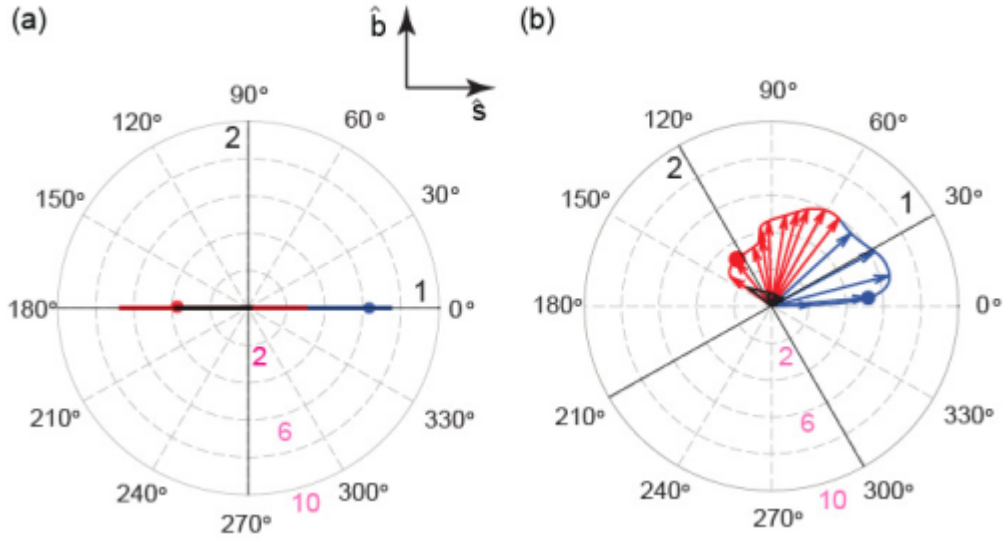


Figure 3.11: Representative shear rosettes show the WSS variation during one cardiac cycle including the accelerating phase (red) and decelerating phase (blue). \hat{s} denotes the axial direction while the \hat{b} indicates the secondary flow direction. The two perpendicular solid lines indicate the two principal directions of the rosette. (adapted from (Krishna et al., n.d.))

In the shear rosette, there are two orthogonal solid lines labelled with 1 and 2 indicating the two principal directions for the shear rosettes. The WSS components could be resolved along two arbitrary orthogonal directions represented by τ_x and τ_y . The principal directions are calculated by (Chakraborty et al., 2012):

$$\int_0^T \tau_x \tau_y dt = 0 \quad (3.2.9)$$

which means the two principal directions are solved by maximizing $\int_0^T \tau_x dt$ or minimising $\int_0^T \tau_y dt$, i.e. the direction of τ_1 and τ_2 . This which means the direction 1 and 2 are perpendicular to each other and detailed calculation method of deciding these two principal directions is explained thoroughly in Appendix A. The conception of this WSSAR could be represented by:

$$WSSAR = \frac{\tau_{2(max)} - \tau_{2(min)}}{\tau_{1(max)} - \tau_{1(min)}} \quad (3.2.10)$$

With the visualization through the shear rosette, the WSSAR is calculated by taking the ratio of projections of the shear rosette along the minor ('2' direction) to the major ('1' direction) axes. It is also could be depicted by the ratio of the width edge to the length edge of a rectangular box bounding to the shear rosette. Therefore, the WSSAR distribution on the arterial wall or aneurysm wall could be calculated.

We performed the CFD simulation on both ICA-1 and ICA-2 in ANSYS CFX and transferred the results to **Paraview**. For certain variables, the calculation algorithm was performed in **Matlab** from the WSS results from the ANSYS CFX simulation.

3.2.2 Results and Discussion: Representative Hemodynamic Distributions

Following the above CFD simulation procedures, the primary results were presented in Fig 3.12 of the steady flow simulation. Here only the ICA-2 model was used to illustrate the results of steady flow. Streamline distribution can reflect the flow trace inside the arterial wall and the low-speed flow concentrates in the aneurysm region (Fig 3.12 (a)). In Fig 3.12(b), the flow in the aneurysm was amplified to show the flow pattern more clearly. The figure legend was limited to the range of 0 to 0.5 m/s, and it obviously indicated the velocities in the aneurysm are almost below 0.5 m/s which shows the slow and helical flow in the aneurysm. The low velocity is often observed in recirculation region which has been suggested to be associated with aneurysm growth. In terms of the flow pattern, there were two groups of helical flow and the interior group presented lower flow velocities. Flow from the upstream part mostly went through the aneurysm spirally and the exterior group of the helix flow made a loop flowing to the downstream section. Pressure spike was located at the inlet and decreased gradually following the flow direction. Note that the pressure magnitudes in Fig 3.12(c) represented the relative pressure. The WSS distribution was illustrated in Fig3.12(d), and high WSS was gathered in a small region near the aneurysm neck in the downstream parent vessel. For the raised aneurysm surface, extremely low WSS distributed in the whole region due to the helical weak flow inside. WSS has been considered as one prominent pathogenic factor in the progress of an intracranial aneurysm developing. An experimental study of 35 rats indicated that the original formation site of saccular cerebral aneurysms is strikingly related to high WSS (Kondo et al., 1997). Masaaki Shojima developed 20 mathematical models of MCA aneurysms and suggested that high WSS was the pathogenic effect of aneurysm initiation while the low WSS might promote the growing with the degeneration within aneurysm wall and the rupture (Shojima et al., 2004). Moreover, the initiation region of intracranial aneurysms was observed in the contiguous area of flow acceleration where maladaptive wall

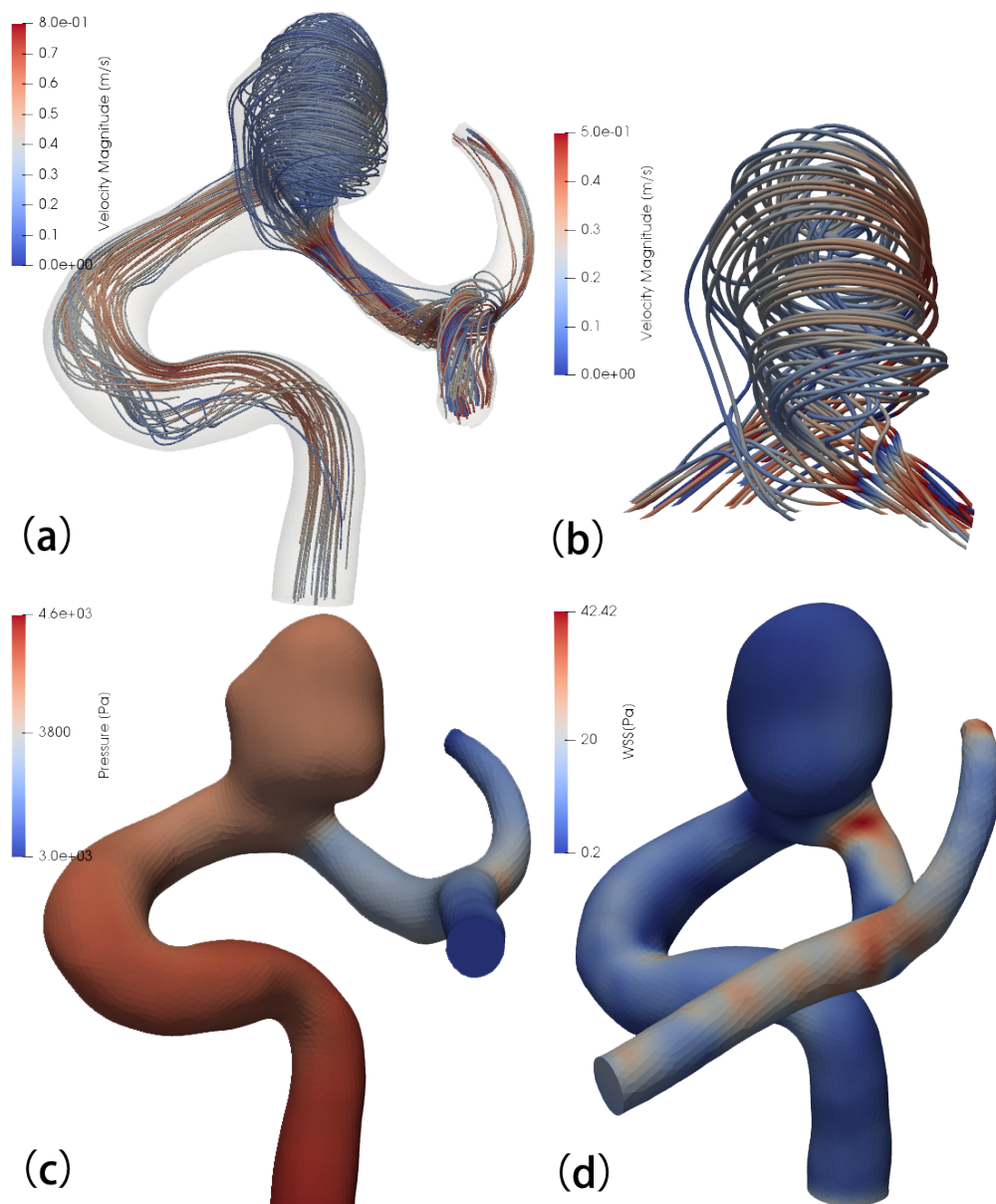


Figure 3.12: Primary haemodynamic results of steady flow condition using ICA-2 model as the representative model. (a) streamline distribution; (b) a zoomed-in version of flow in the aneurysm region; (c) relative pressure distribution; (d) WSS distribution

remodelling occurs. This suggested the combination of high WSS and a high gradient might trigger the inception of aneurysms (Meng et al., 2007).

For pulsatile flow simulation, TAWSS, OSI, WSSG, AFI, GON, WSSAR, these WSS-related

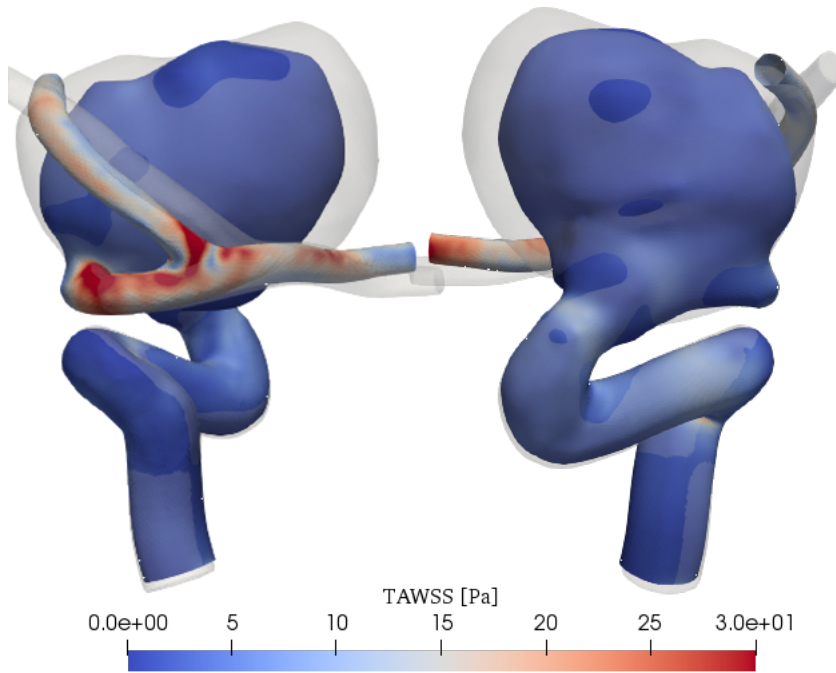


Figure 3.13: Counter plot of TAWSS distribution over one cardiac cycle with follow-up configuration of ICA-1 model (translucent).

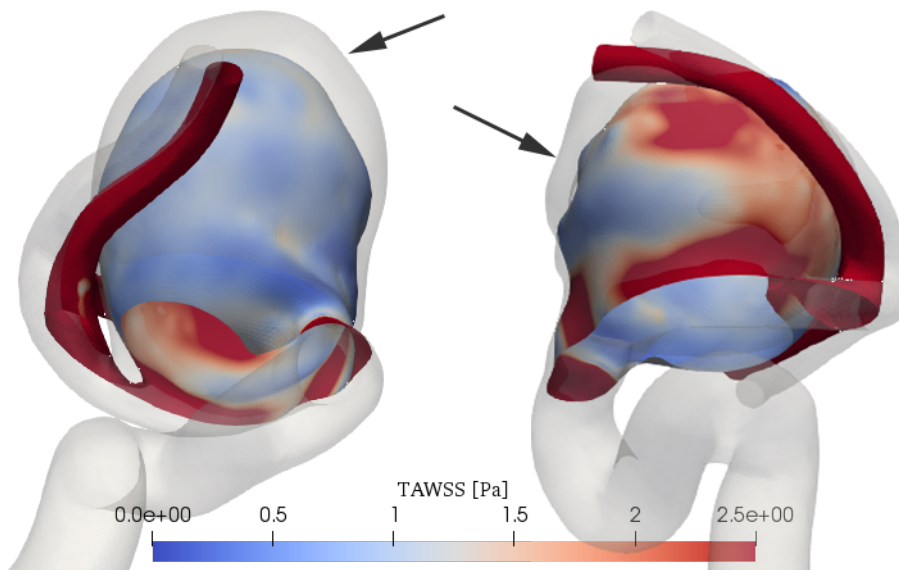


Figure 3.14: Counter plot of TAWSS distribution over one cardiac cycle with follow-up configuration of ICA-1 model (translucent). The color map is limited to 0-2.5 Pa.

variables are plotted for both ICA-1 and ICA-2 case. All these parameters are formulated based on WSS with different quantifying approaches. In the case of ICA-1, it has the follow up geometric configuration which can help to build the link between each haemodynamic variable and the aneurysm growth possibility.

Firstly, the TAWSS distribution of ICA-2 is analogous to the WSS distribution from the steady flow simulation. Hence, here only the TAWSS distribution of ICA-1 case is presented. Fig 3.13 shows the general TAWSS distribution which resembles with the WSS distribution of the case ICA-2. The high WSS ($>20\text{Pa}$) regions gather at the downstream of the aneurysm, i.e. near the neck and across the bifurcation. This is due to the remarkably narrowing down of the arterial diameter following the extremely large inflation of the aneurysm. In a similar manner, the overall aneurysm regions present low WSS in both ICA-1 and ICA-2 cases. To better investigate the impact of the low WSS on aneurysm evolution, the color map is restricted to 0-2.5 Pa showed in Fig 3.14. Significant growth regions are pointed out by the arrows accompanied with low WSS ($<1.5\text{Pa}$) distribution. Relative high WSS appear at the proximal part of the dome close to downstream. These results indicated that low WSS, lower than 1.5 Pa, has a positive relationship with aneurysm evolution. Even though this positive relationship is not explicit, i.e. there is no clear function between WSS magnitude and growth extend (displacement quantification), low WSS contributes to aneurysm growth which has been investigated by a large number of researches. This consequence might because the low WSS induce the dysfunction of endothelial cells which further leads to adverse pathological tissue remodelling in aneurysms. Moreover, the narrow-down WSS distribution suggests that the minimum WSS threshold could be set as 2.5 Pa as an instigator of aneurysm growth.

Secondly, the next haemodynamic parameter, OSI, is also a widely used haemodynamic parameter in CFD analysis. Fig 3.15 plotted the OSI distribution in anterior and posterior view. The physiological OSI threshold was suggested to be taken as 0.2 above which the damage of endothelial cells is triggered (Glor et al., 2004). The parent vessels of ICA-1 case shows a low OSI (0-0.2) distribution except for the tortuous region and the same to ICA-2 case which has been cut off. In the ICA-1 case, a relatively large region of high OSI is located at the posterior dome (0.3-0.5). Two isolated small areas with high OSI scatter in the anterior dome where the top one corresponds to an invaginated region in the follow-up geometry. For the ICA-2 case, the biggest high OSI gathering region (0.3-0.4) resides in the anterior dome. Moreover, three subtle regions with high OSI (0.35-0.5) are spotted at the little-protruded position, the posterior right side of the neck and the posterior dome respectively. On the large protruded side, there is no notable elevated OSI distribution.

Comparing the OSI distribution and the growth of ICA-1 aneurysm model, the region of highest OSI at the posterior dome seems to coincide with the marked growing region showed

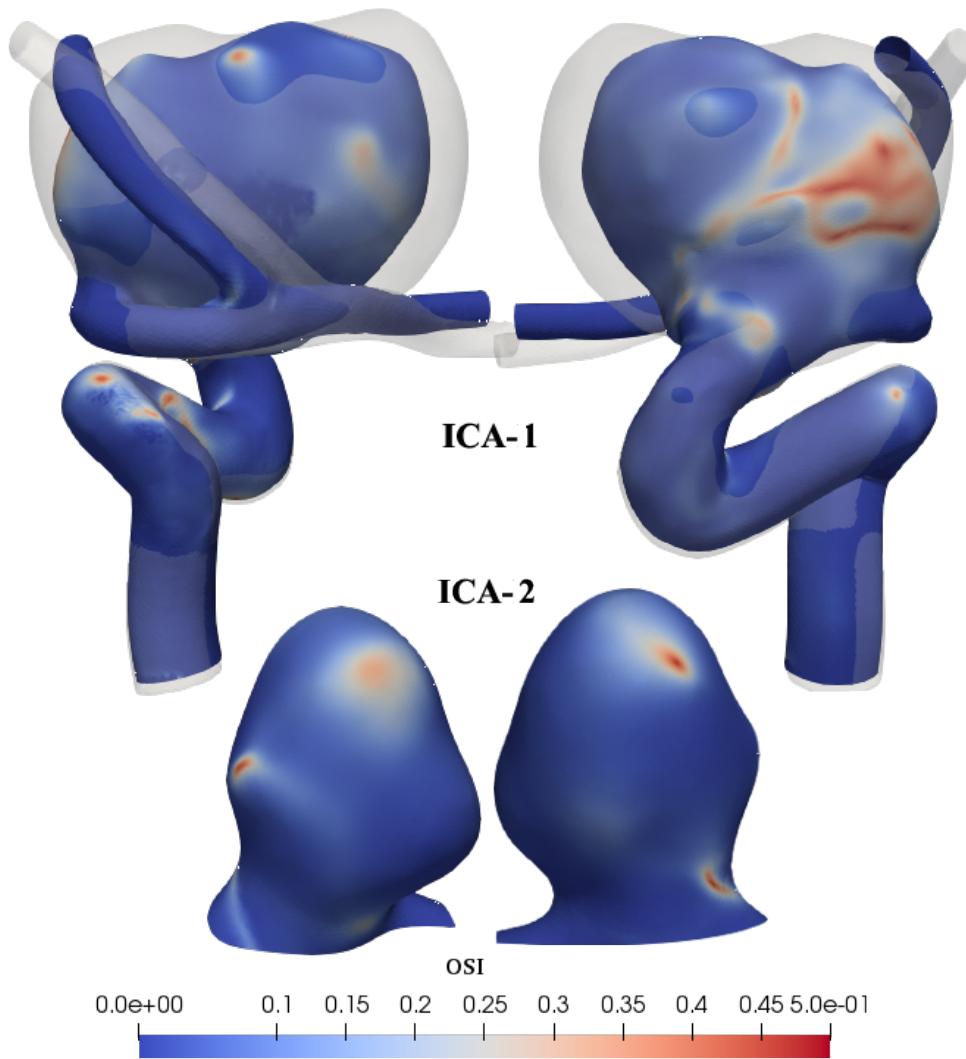


Figure 3.15: Counter plot of OSI distribution on the patient-specific geometries of ICA-1 and ICA-2 cases in anterior (left) and posterior (right) view

by the translucent geometry. However, the other two elevated OSI regions where has no outward growth feature which suggests it is unclear whether the high OSI has a positive relationship with aneurysm growth.

The third haemodynamic index, AFI, relates to the aneurysm formation. It defines the angle between the instantaneous WSS and the TAWSS direction at every time points. In the accelerating phase of systole, the secondary flow only plays as a supporting part with the axial component of flow dominating. Nevertheless, the magnitude of the axial component flow

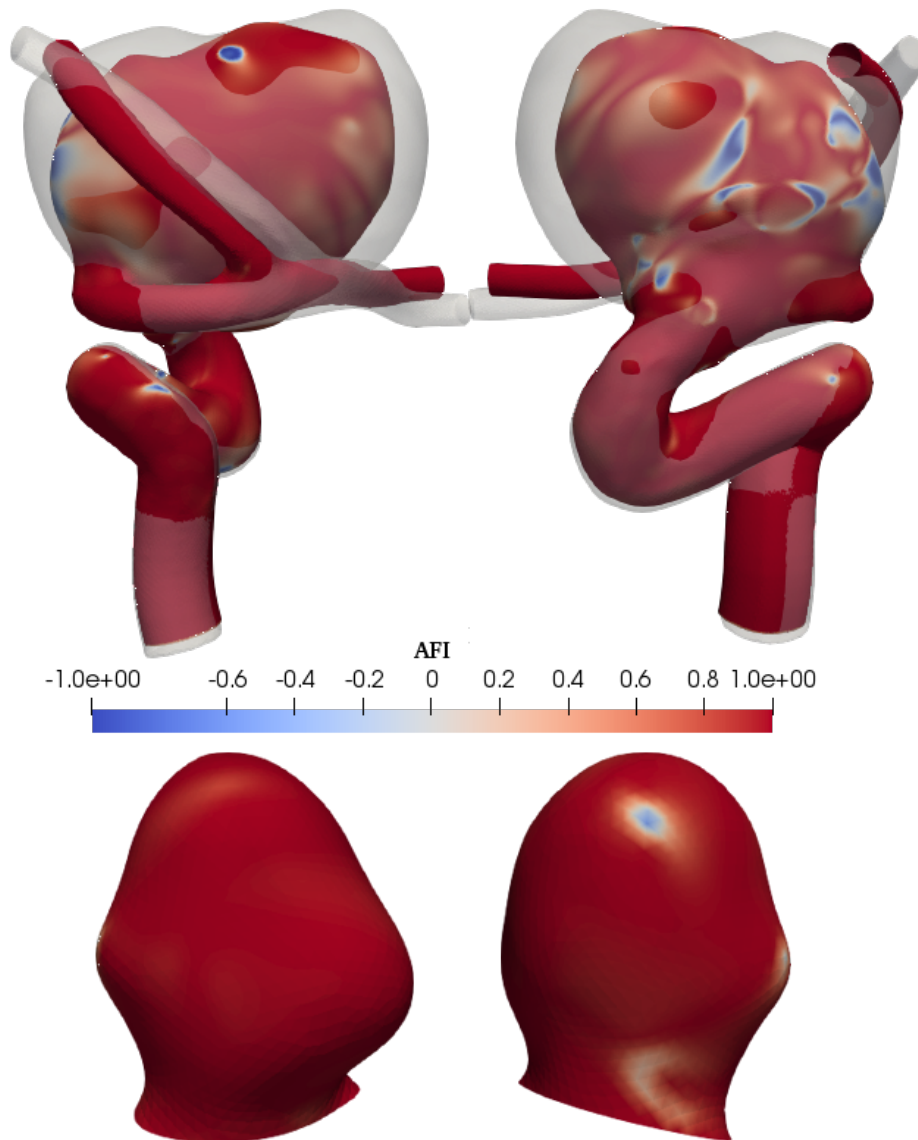


Figure 3.16: AFI contour plot at midsystolic deceleration (MSD) mapped on the patient-specific geometries of ICA-1 and ICA-2 cases in anterior (left) and posterior (right) view

drops remarkably during the decelerating phase, and the secondary flow component starts to lead the flow. Importantly, the secondary flow is often the preliminary and chief reason for endothelial cells dysfunction and subsequent vascular diseases. Hence, in terms of the time point, we choose the mid-systolic deceleration point to investigate the AFI distribution and

aneurysm growth, which is in accordance with the literature (Mantha et al., 2006). Here the AFI distribution at midsystolic deceleration was mapped on the surface in Fig 3.16. According to the definition of AFI, the red region (AFI=1) represents that the instantaneous WSS vector orients the same direction to the reference direction, i.e., TAWSS vector. And the blue colour (AFI=-1) denotes that the angle between instantaneous WSS vector and the TAWSS vector is 180 degree showing the complete reversal flow. If the AFI equals to 0, the transient WSS has a 90-degree rotation from the reference TAWSS direction.

In the AFI distribution of ICA-1 case, compared to the Fig 3.15, it is clear that the AFI and OSI distribution have a similar pattern. A visible low AFI region and high OSI region are both located at the posterior dome of the aneurysm where the aneurysm grows predominantly. However, it is also the same that no notable correlation between the aneurysm growth and AFI/OSI on the dome from the other side. But it could be seen from Fig 3.16 that there is a large region covered with white colour in the right dome from the anterior view and this phenomenon does not show in the OSI distribution. This comparison suggests that AFI is a more sensitive index to quantify the disturbed flow than OSI which could also exhibit in their definitions. OSI only has the clear definition on the ends of its range, completely align with or reversal to the TAWSS orientation, i.e. OSI equals to 0 and 0.5. But unfortunately, it is inexplicit about the values between 0 and 0.5. AFI clearly defined the angle between the transient WSS and TAWSS at any time point, but does not an overall effect over the cardiac cycle.

In the case of ICA-2, the distribution is also analogous to the OSI distribution except for the top region in the anterior view. The most unstable region with disturbed flow is located on the top of the aneurysm in the posterior view and there is also a tiny high AFI region on the back of the neck.

The tiny low AFI region with the aneurysm moves inward on the dome in the anterior view which suggests the possibility of aneurysm growth may not have to be in the outward direction. The small region of disturbed flow may induce the tissue growth and remodelling but not strong enough to lead to a marked outward growth, only contributing to the growth in the contiguous area. Hence, it can be speculated that the large region of low AFI (-1~0) could lead to the outward growth of the aneurysm. Based on this, there is only a small chance of growth for the aneurysm of ICA-2 case.

Concerning $WSSG_s$, a growing aneurysm on the anterior communicating artery was observed over 27 months which contained four stages of CT follow-up. After the CFD simulation performed on this case, they found that the WSSG in the nongrowth area was lower than 100 Pa/m while the larger WSSG (>1500 Pa/m) was observed adjacent to the enlarging area (Tanoue et al., 2011). Therefore, the color map of the spatial WSSG distribution on both

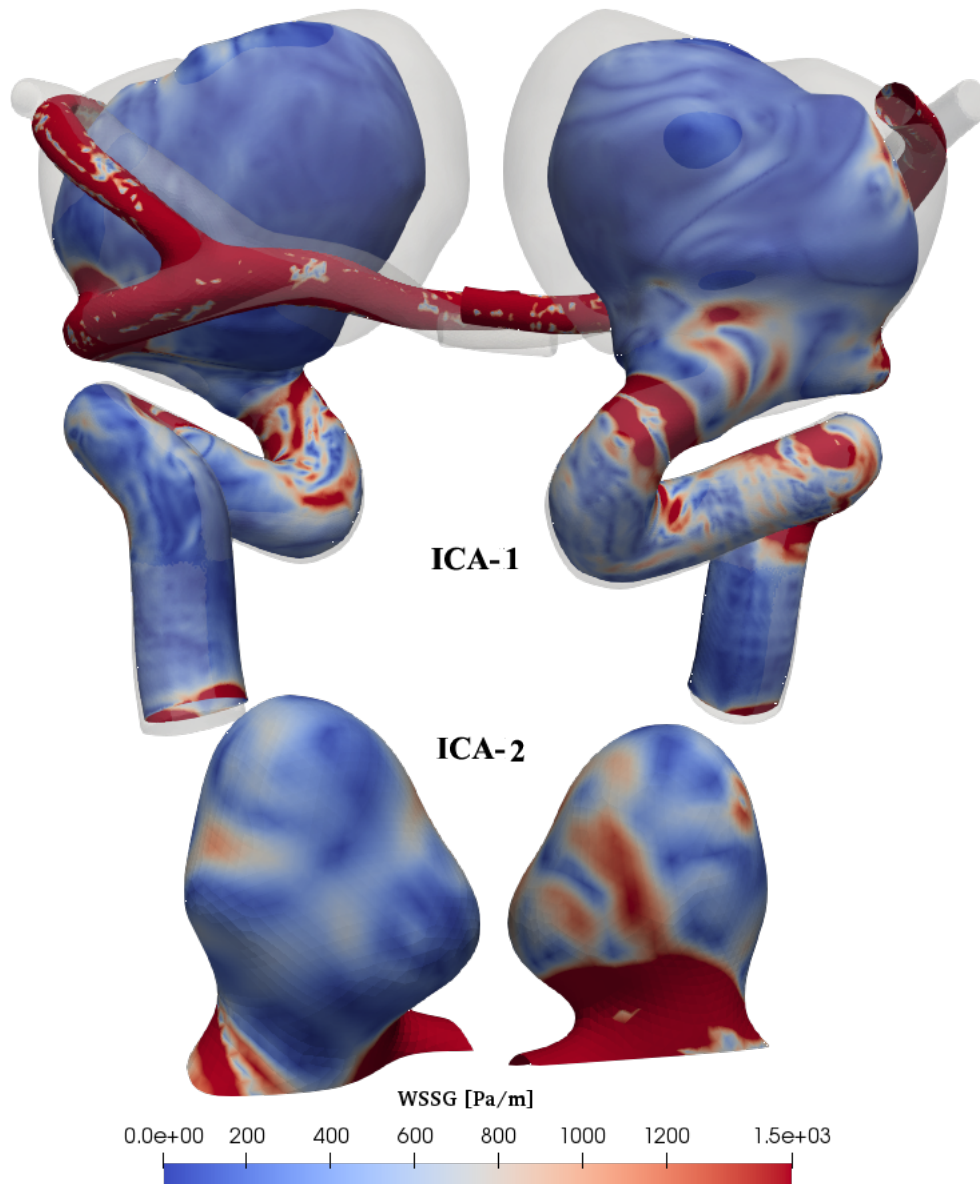


Figure 3.17: Counter plot of spatial WSSG distribution on the patient-specific geometries of ICA-1 and ICA-2 cases in anterior (left) and posterior (right) view

models were limited to 0-1500 Pa here (Figure 3.17). Figure 3.17 shows that the high $WSSG_s$ concentrates around the neck region on both models, the tortuous region in the upstream section and the entire downstream in ICA-1 model. Also, the highest $WSSG_s$ is up to 93510 Pa/m in the inner side of the junction connecting the aneurysm and the downstream section in this model. In the other ICA-2 model, the highest $WSSG_s$ magnitude achieved 18601 Pa/m and the high $WSSG_s$ also concentrated on the junction and the bifurcation of the downstream. These two models were applied the same boundary conditions but produced great difference on the magnitude of $WSSG_s$, which indicates that the geometric characteristics play a key role in the haemodynamic environment.

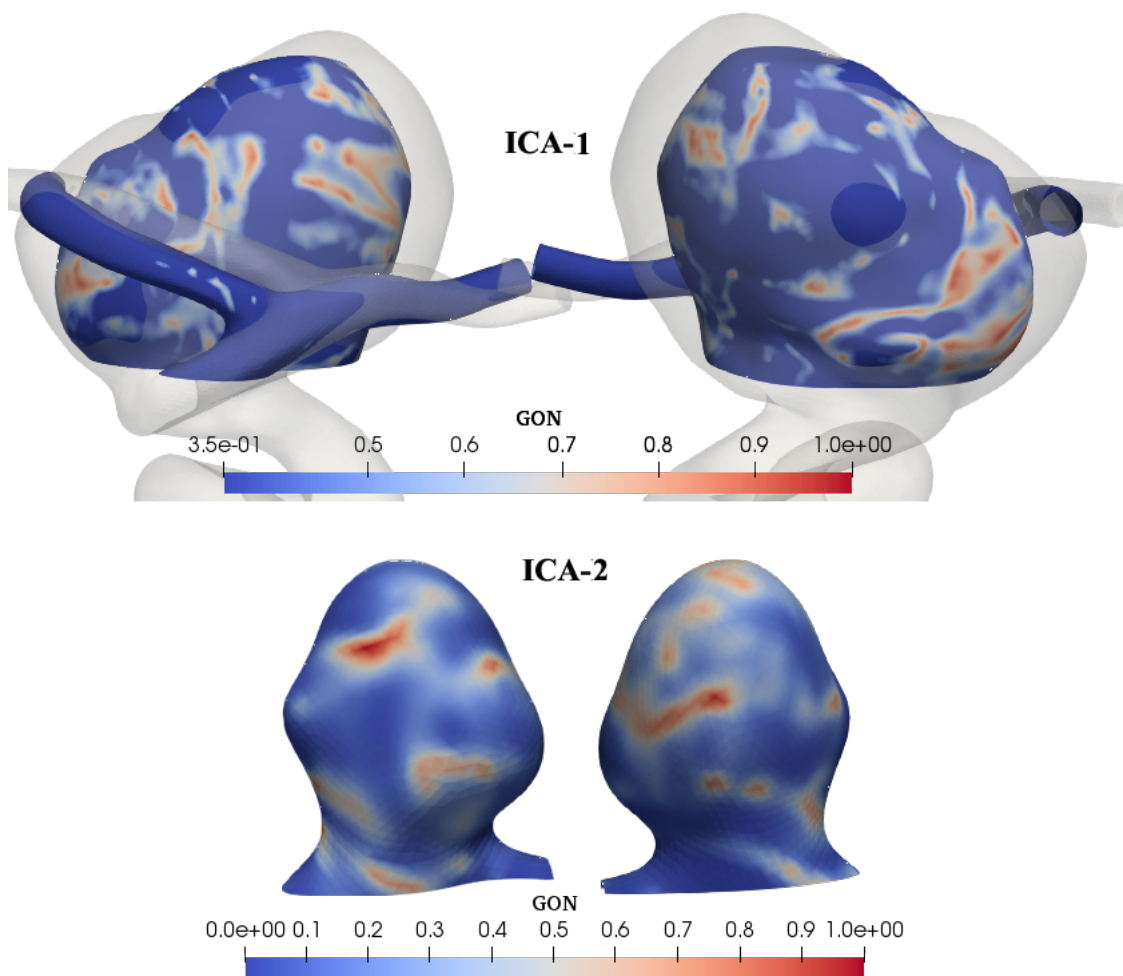


Figure 3.18: GON distribution mapped on the patient-specific geometries of ICA-1 and ICA-2 cases over the cardiac cycle in anterior (left) and posterior (right) view

AFI and GON are formulated to quantify the force exerted from the blood flow to endothelial cells but in different ways. On one hand, AFI is a function of WSS while GON is based on the $WSSG_s$. It can better represent the force on cells which have two opposite directions indicating the tension or compression. On the other hand, AFI only depicts the WSS fluctuation at a specific time point while GON is a comprehensive index representing the WSSG fluctuation over one cardiac cycle. This parameter is strongly correlated with the aneurysm inception showed in the research (Shimogonya et al., 2009) but not the subsequent growth. Figure 3.18 represents the GON distribution of ICA-1 and ICA-2 models and the maximum values are 0.9682 and 0.7439 for both models respectively. From the perspective of enlargement in the ICA-1 model, the high GON regions concentrate on the anterior and posterior side where have a relatively obvious enlargement. However, the overall high GON areas scatter on the geometry surface showed in both models. Hence, it is still unclear about whether the GON has a positive correlation with aneurysm growth.

Figure 3.19 shows the WSSAR map for the ICA-1 and ICA-2 models in anterior and posterior views. The WSSAR distribution on ICA-2 model is highly concentrated on the bottom of the bulge out regions from the geometric perspective. High WSSAR region represents the disturbed flow where the complex and abnormal haemodynamic environment would lead to adverse mechanical stimuli to vascular cells, especially to endothelial cells. Furthermore, this disadvantageous stimulation would induce different gene expressions and protein syntheses to respond to the mechanical signal and the subsequent tissue growth and remodelling. Therefore, this growth and remodelling will continue to accelerate the extrusion in the bulge position, leading to further enlargement of the aneurysm. To confirm this speculation, it is demanding a better understanding of how this WSSAR impact the vascular cells and the link to tissue growth and remodelling.

Above haemodynamic distributions on models ICA-1 and ICA-2 illustrate the different quantifications of WSS, magnitude or direction. The ICA-1 case which has the follow-up geometry is regarded as a reflection from the haemodynamic distribution to the aneurysm enlargement. But there are no predominantly positive correlations between haemodynamic distributions and aneurysm growth due to the unclear quantification of aneurysm growth. The next section will introduce the indices for capturing the aneurysm growth in the ICA-1 case in a more accurate way. The analysis of combining the aneurysm growth quantification and the haemodynamic distribution will be depicted in the next section to find a potential indicator for aneurysm growth.

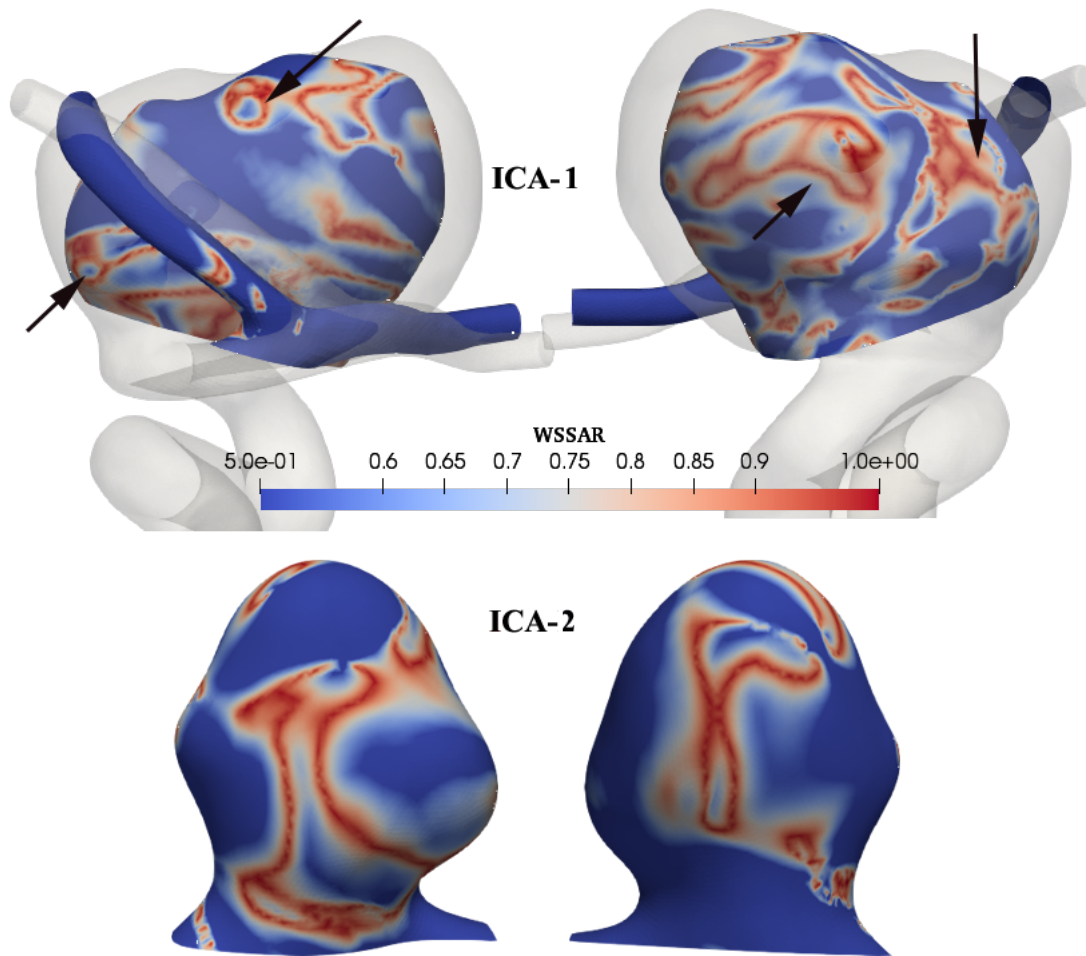


Figure 3.19: WSSAR distribution mapped on the patient-specific geometries of ICA-1 and ICA-2 cases over the cardiac cycle in anterior (left) and posterior (right) view

3.3 Correlation Analysis between Hemodynamics and Aneurysm Growth

3.3.1 Review: Hemodynamics and Aneurysm Growth

To study the association between hemodynamics and aneurysm growth, majority of researches performed the CFD simulation on the reconstructed aneurysm follow-up models aiming to find or develop an indicative haemodynamic index. Moreover, some studies also utilised patient-specific silicon models of aneurysms or in vitro experiments to investigate the haemo-

dynamic environment in aneurysms.

In general, high WSS is considered to be associated with aneurysm inception and rupture, while low WSS is more relevant with aneurysm growth. In a CFD study applied to 20 middle cerebral arteries, it found that higher WSS located around the neck region compared to healthy arteries, whilst lower WSS regions were observed at the aneurysm dome (Shojima et al., 2004). Through the analysis of a fusiform basilar aneurysm with two times follow up, there is a positive correlation between low WSS area where the magnitude is lower than 0.1 Pa and the highest enlargement region (Jou et al., 2005). Also, a larger low WSS region was observed in the process of aneurysm growth. One experimental study found that endothelium permeability is higher in low WSS region especially in the area having the higher WSSG (LaMack et al., 2005). Abnormal vascular remodelling coupled with inflammation is considered an important pathological variation in aneurysm growth. Low WSS under 0.4 Pa was suggested that has the effect of endothelial cells turn over thus leads to the infiltration of inflammatory cells (Boussel et al., 2008). It was noted that the residence time of inflammatory cells is prolonged by the disturbed flow which enhanced the interactions between circulating inflammatory cells and vascular endothelial cells, hence the monocytes are prone to adhere to endothelial cells in the high WSSG region (Hashimoto et al., 2006). Similarly, CFD simulations on the artificial bifurcation geometries have shown that the combined high WSS and positive WSSG_s is related to aneurysm initiation supported by histological analysis (Meng et al., 2006, 2007). Even though the low WSS has been illustrated leading to dysfunction of endothelial cells, the high WSSG was reported as a trigger to incur the destructive remodelling and inflammation and adjacent to growth region (Meng et al., 2007; LaMack, Friedman, 2007). In a univariate study, the ratio of the aneurysm to parent artery was artificially changed to do the CFD simulation which shows that the aneurysm growth is accompanied with the more disturbed flow, decreased WSS as well as the high WSSG (Tremmel et al., 2009). The same research group combined the CFD simulation with histology images derived from animal experiment, basilar terminus in rabbits, showing that the coexistence of high WSS and positive WSSG implied perilous hemodynamic stimuli was likely to generate aneurysmal remodelling (Metaxa et al., 2010). Haemodynamic study of a human cerebral aneurysm having four stages follows up over a 27 month period showed abnormal low WSS was located at the growing site while high WSSG was observed surrounding the growing region (Tanoue et al., 2011).

WSS has been considered to be impractical in quantifying aneurysm growth because it is hard to define a threshold or range of abnormal low WSS due to the large individual variation. Furthermore, it is unable to represent the complexity of the blood flow. Hence, researchers started moving the emphasis to develop novel indices to quantify the flow diversity derived

from the pulsatile movement, especially for complex geometries. A large dataset containing 119 intracranial aneurysms was analysed from two aspects, morphology and haemodynamics. Through the statistical study, WSS and oscillatory shear index were the only two independently significant variables in the assessment of aneurysm stability (Xiang et al., 2011). Daniel M Sforza et al. performed a longitudinal study of 33 unruptured intracranial aneurysms and divided into stable group and growing group. This study found there was no significant difference between these two groups in terms of mean wall shear stress but closely related to complex flow patterns, like vorticity ratios, viscous dissipation ratios (Sforza et al., 2016). As the deeper understanding of histological structure within aneurysm walls, the inflammation becomes a pivotal factor and a potential biomarker in the aneurysm stability study. Inflammation was associated with non-intact endothelium driven by higher vorticity, higher viscous dissipation and higher shear rate. And increased inflammation was correlated with degenerated and decellularized walls of cerebral aneurysms (Cebal et al., 2017).

Haemodynamic environment and stimuli do significantly impact the structure and biological response in the vascular/aneurysmal wall. However, many pieces of research on CFD analysis still can not find the direct reflection from WSS/WSSG to aneurysm growth. Recently, the aneurysm growth is associated with disturbed flow and inflammation within the wall tissue but still not clear about the underlying mechanisms. It is demanding to propose an index which can quantify the complexity of flow and at the same time can associate to aneurysm growth and stability.

3.3.2 Correlation Analysis

3.3.2.1 Quantification of Cerebral Aneurysm Growth

Alisa Selimovic investigated the same geometry of our ICA-1 model and devised two indices to quantify the extent of aneurysm growth, which are Displacement Index (**DI**) and Area Stretch Ratio (**ASR**) (Selimovic, 2013). These two indices could be served as a useful tool to correlate the hemodynamic environment to the aneurysm growth. Here we will give a brief description of the meaning of these two parameters, not the exact methodology.

Both indices were calculated depending on the two follow-up geometries which need to be aligned (3.1 (b)). The geometries reconstructed from the first and second stage were called G_1 and G_2 . The **DI** index quantifies the displacement from every point on G_1 geometry to the G_2 geometry in the normal direction with respect to the triangle on which the point located. This index is a relatively simple quantification which captures the Eulerian distance between two points. The following listed the key procedures of the algorithm implementation:

- ⊢ Calculates the centrepoint and normal vector (\hat{n}) of each triangular surface element of the G_1 dome;
- ⊢ Determines the point of intersection (if it exists) of the each \hat{n} with the G_2 surface;
- ⊢ For each element on G_1 , stores the nearest intersection point which lies within a triangle of the G_2 dome;
- ⊢ Computes the scalar distance between each centrepoint on the G_1 dome and the corresponding intersection point on the G_2 dome;
- ⊢ Interpolates the scalar distance from each centerpoint onto each node of the G_1 mesh a scalar distance, which is computed as the average of the scalar distances corresponding to all elements connected to that node.

Figure 3.20 shows the DI distribution on the G_1 geometry of ICA-1 model respective to the G_2 geometry.

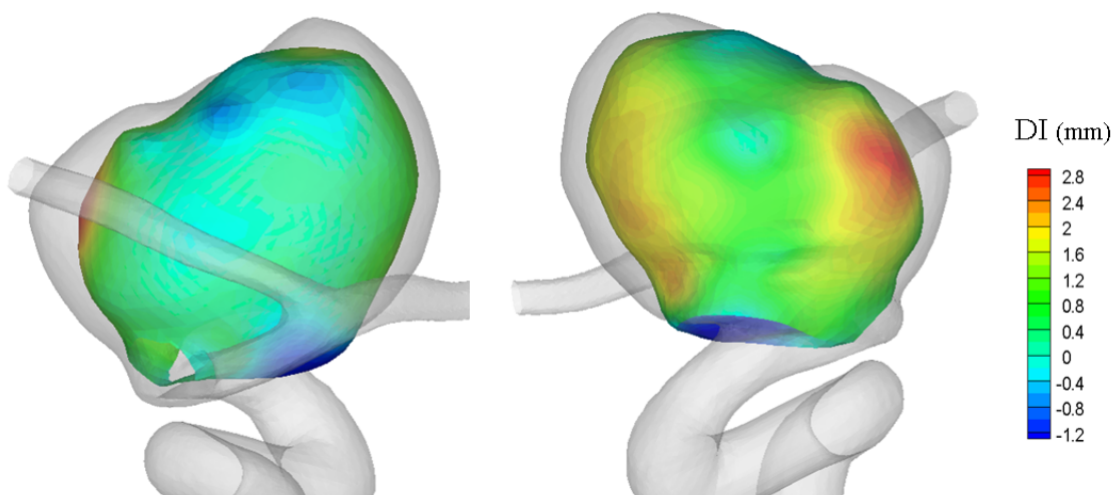


Figure 3.20: The DI index distribution plotted as a surface map of the G_1 geometry for the ICA-1 case in anterior (left) and posterior (right) view (adapted from (Selimovic, 2013))

To better characterize the growth of the aneurysm, the **ASR** is regarded as the stretch of G_1 surface over time, which is a function of DI. According to this definition, the growth could be represented as the ratio of the G_2 surface area to the related area in G_1 geometry. This is a more sophisticated description of aneurysm growth, and the larger ASR magnitude means the stronger growth within the aneurysm tissue in that region. Because this index was devised by (Selimovic, 2013) and its complexity, here we just simply exhibited the ASR distribution results (Fig. 3.21), the methodology of calculating this index could refer to (Selimovic, 2013).

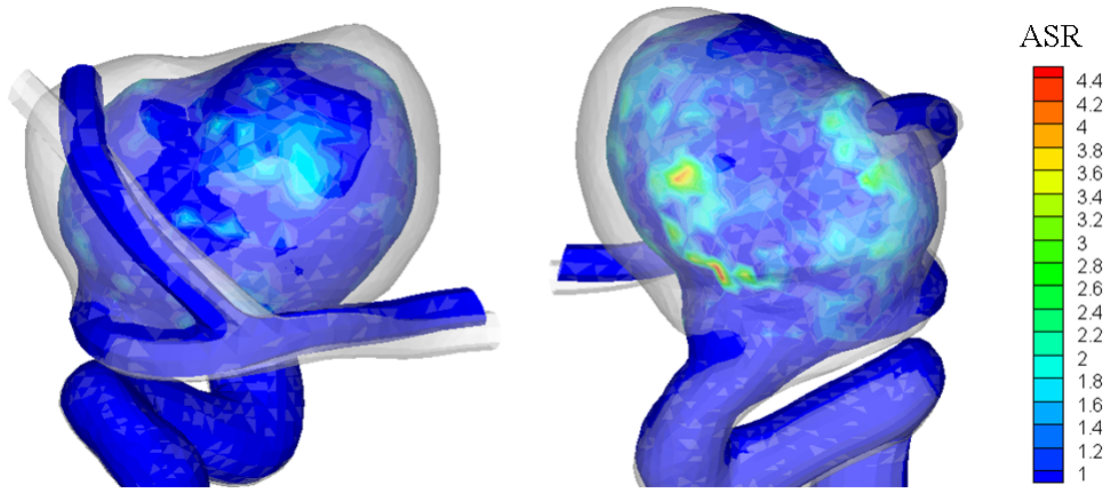


Figure 3.21: The ASR index distribution plotted as a surface map of the G_1 geometry for the ICA-1 case in anterior (left) and posterior (right) view (adapted from (Selimovic, 2013))

3.3.2.2 Correlation Result: WSSAR to Aneurysm Growth

Through the graphical and statistical analysis between the haemodynamic distributions of WSS, $WSSG_s$, OSI, AFI, GON and these two growth indices, the results suggest that the OSI and AFI correlate best with the high regions of both DI and ASR in ICA-1 the case, but this seems to be true only for the anterior part of the ICA dome (Selimovic, 2013). On the positive side, the OSI and AFI have a common sense which defined as a function of oscillatory flow, the deviation of instantaneous WSS direction to the time-averaged WSS vector. Hence, this assessment of the ICA-1 case suggests that large deviations of the instantaneous WSS vector probably is a driver for aneurysm growth.

From the negative perspective, even though there is some positive correlations exist, the correlations are still relatively weak and only effect on part of the geometry. This suggests the aneurysm growth is closely correlated with the capture of the oscillation of the flow more accurately and effectively. The OSI has a clear indication when the instantaneous WSS vector is consisted with or contrary to the time-averaged WSS direction, i.e. $OSI=0$ and $OSI=0.5$. However, it is unclear when the value is in the middle of 0 and 0.5 in defining the degree of the instantaneous WSS deviation. As to the AFI, it is able to characterize the angle between the instantaneous WSS vector and the time-averaged WSS vector by a cosine function. Analogously, it still has the drawback that this angle only represents an instantaneous time point rather than one cardiac cycle. Hence, WSSAR is a candidate parameter which can better quantify the flow oscillation over one cardiac cycle, capturing the bidirectionality of the

blood flow and suggests a preferred direction for endothelial cells alignment.

Compare this WSSAR distribution of ICA-1 model shown in Fig. 3.19 with the ASR distribution showed in Figure 3.21, there are four high WSSAR concentration regions located at similar sites in the high ASR regions. This suggests there are more clear positive correlations between the WSSAR and aneurysm growth compared to the previous haemodynamic parameters, i.e. OSI and AFI, which have been investigated correlates with aneurysm growth.

3.4 A Novel *G&R* Hypothesis: WSSAR-Endothelium Permeability-*G&R* function

One monolayer of endothelial cells constructs a permeability barrier between blood flow and the media layer of the arterial wall. Its morphology and function are regulated by the WSS given by the blood flow and the stretch on the vascular wall accompanying with the vasodilation and contraction which will elaborately be introduced in Chapter 7. In this section, we just focus on the mechanical stimuli given from the blood flow which is quantified by WSSAR to investigate its influence on the morphology and function of endothelial cells.

3.4.1 Morphology of Endothelial Cells in Aneurysm

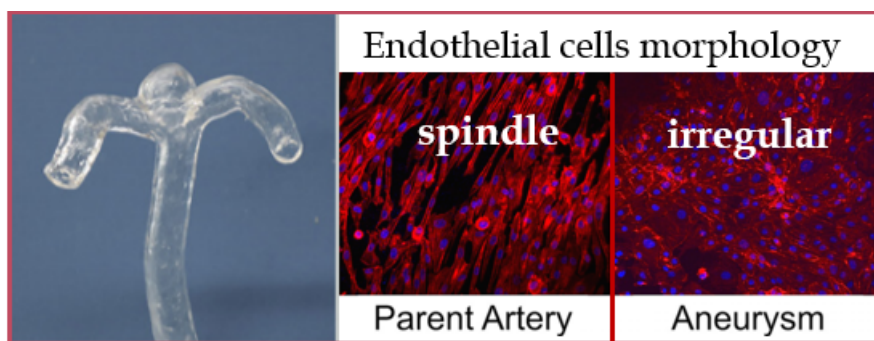


Figure 3.22: The polydimethylsiloxanes vessel is fabricated using 3D printing technology from vascular image data acquired by scanning images. Microscopy images of endothelial cells morphology and alignment on the parent artery and aneurysm apex with different haemodynamic conditions

(adapted from (Kaneko et al., 2017))

It has been verified by the experiment researches that the endothelial cells will align with the flow direction when the flow is uniform. Under the condition of complex flow like the

flow in an aneurysm, the laws of endothelial cells alignment responding to the flow stimuli is still unclear.

A research group in Japan induced cerebral aneurysms in 10 rats, and they observed the morphology of endothelial cells changed first in the course of aneurysm evolution (Jamous et al., 2005). This study illustrates the critical character of endothelial cells for aneurysm formation. One recent research developed an in vitro model with 3D printing technique, an aneurysm locating at the bifurcation of the basilar artery, cultured endothelial cells in growth medium. This research aims to investigate the biological impact of complex flow (aneurysm) on endothelial cells (Kaneko et al., 2017). Results showed that endothelial cells are spindle shape but randomly oriented under the static condition. After 24h culture with flow, endothelial cells elongate in the direction of flow in parent artery. Contrast to parent artery, most of the endothelial cells in the aneurysm had irregular shapes. This indicates that the endothelial cells are deeply sensitive to flow pattern which gives shear stress on top of cells.

3.4.2 Endothelial Cells Morphology Characterized by Flow Pattern

There is one research investigated whether the unsteadiness of flow or the WSS magnitude impacted the turnover of endothelial cells (Davies et al., 1986). In that in vitro experiment, endothelial cells were exposed to varied WSS amplitude in laminar flow or turbulence flow. Results show a substantial absence of endothelial cells alignment, cell turnover and cell loss stimulated by turbulence flow which indicated the unsteady flow character is much more influential on cell morphology and alignment. According to this, we picked three points on the ICA-2 model with similar magnitudes of WSS and plotted the corresponding shear rosettes to investigate the variation of flow over one cardiac cycle (Fig. 3.23). It shows strong distinction between A,B and C, i.e. on the aneurysm and the parent vessel. The shear stress rosette on point C indicates a nearly uniform flow and the flow direction is parallel to the axial direction of the arterial vessel (first principal direction pointing to 0°). But the flow direction varies to a wide range of degree on the aneurysm consistent with the complex haemodynamic condition inside the aneurysm. The mechanosensors on the top surface of endothelial cells enable the conversion of various mechanical stimuli given by the blood flow to different biochemical signals to the cytoskeleton fibres and nucleus. The cytoskeleton fibres are assumed to assemble themselves to respond to the mechanical stimuli thus reorient the stress fibres to resist the shear stress achieving an equilibrium status. Consequently, the interior structure of cytoskeleton fibres in endothelial cells is significantly related to the morphology and orientation of the cells.

Hence, this shear rosette is a clearer way to quantify the degree of WSS variation which

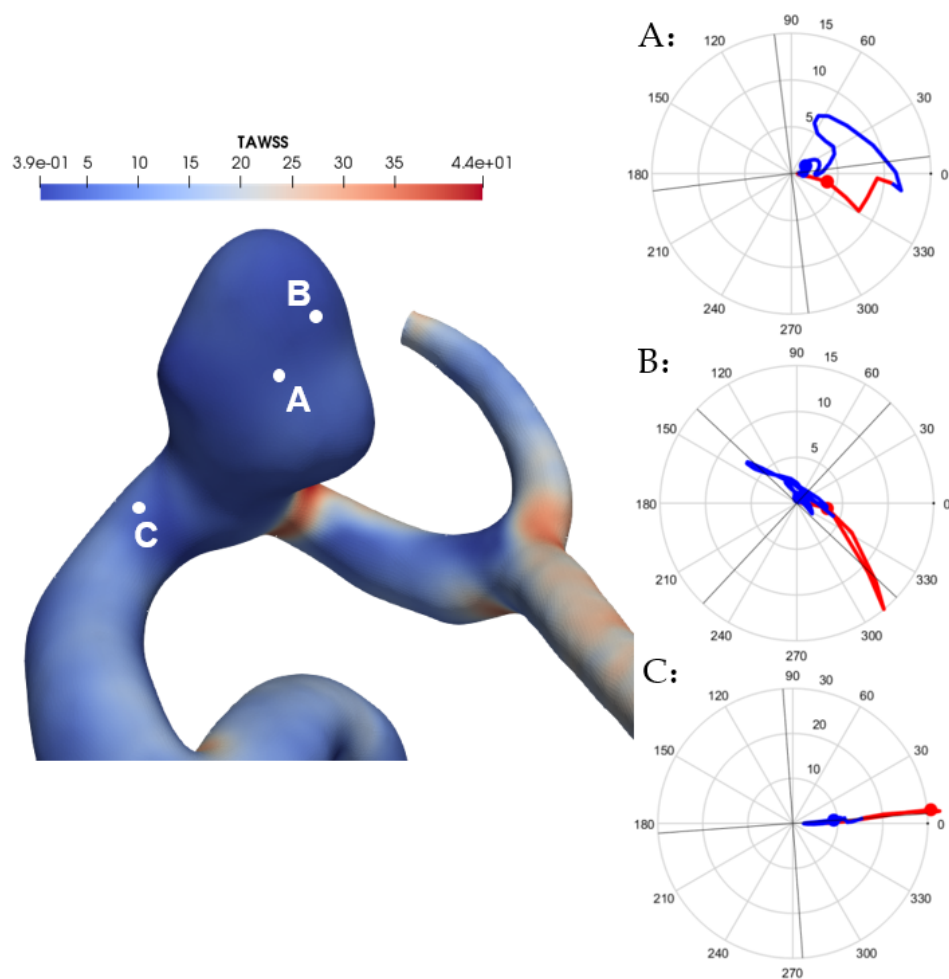


Figure 3.23: TAWSS distribution plotted on ICA-2 model and shear rosettes of 3 points (A, B, C) with similar TAWSS magnitude (A,B on the aneurysm and C on the parent vessel).

gives an insight into the orientation and morphology of endothelial cells. The first principle direction in the shear rosette provides an orientation indication for the long axis of endothelial cells (Krishna et al., n.d.). Combined with the in vitro experiment researches, the morphology mainly performs two types: spindle shape and irregular shape. Figure 3.25 plotted the WSSAR distribution on the ICA-2 model in the range of 0-1. As introduced in Section 3.2.1.6, when the WSSAR value is close to 0, it means the flow is well arranged along with the longitude axis of blood vessel. Whilst the WSSAR approaches to 1, the flow is unsteady and presents the clear secondary flows leading to bidirectionality in the flow and the exerting WSS. WSSAR correlates with regions in the aneurysm where cell mechanobiology, morphol-

ogy and alignment may be significantly altered with different extent of responses (Krishna et al., n.d.). Morphological changes of endothelial cells from spindle shape to irregular shape were observed sequentially at the cerebral artery bifurcation in response to hemodynamic shear stress indicated by an experimental study (Jamous et al., 2005). Figure 3.24 specifically shows the WSSAR distribution in the bifurcation and the following downstream sections.

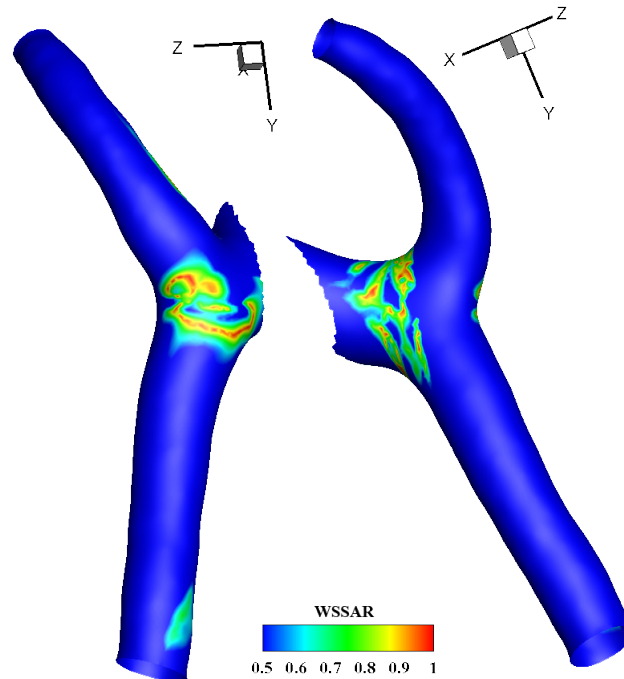


Figure 3.24: WSSAR distribution in the bifurcation region and the downstream sections with the colour map limited to 0.5 to 1

The colour map is limited to 0.5-1, almost all comparatively straight parts of the healthy artery has uniform colour distribution which implies that the endothelial cells in the range of 0-0.5 can maintain their physiological function. Explicit high WSSAR values are localized in the bifurcation area, these WSSAR values were extracted to calculate an averaged number which is 0.729. Hence, we assume that the endothelial cells with irregular shape are concentrated in the region where the WSSAR in the range of 0.75-1.

There are clear distinctions between red and blue colour in Figure 3.25 (left) which indicates there might be an abrupt change in flow patterns at the junctions. Moreover, the red region is highly concentrated within the range of 0.75-1. Therefore, we assume the endothelial cells in this area have the irregular shape showed in Figure 3.25 (right). In the rest region with the lower WSSAR magnitude, it is hypothesized that endothelial cells still can maintain

their spindle shape under the unidirectional flow or slightly disturbed flow.

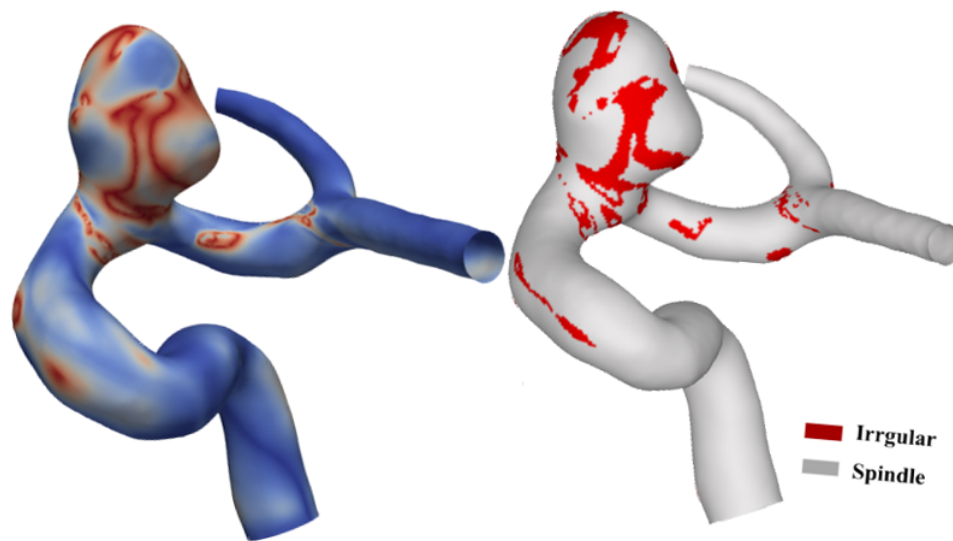


Figure 3.25: WSSAR distribution on the ICA-2 model and corresponding endothelial cells (ECs) morphology distribution over one cardiac cycle. The irregular shape is represented with red color while and spindle shape is showed by grey color.

This part of research can bridge the gap between the flow patterns and endothelial cells morphology mathematically in spite of the simplicity of the morphology quantification. The morphology of endothelial cells is closely related to the gap between cells which is a key factor in determining the permeability of the endothelium layer. Thus, the impact of endothelium permeability imposing on the tissue growth and remodelling in the course of aneurysm evolution will be summarised in the next section.

3.4.3 Hypothesis: Endothelium Permeability to Aneurysm Growth

Vascular permeability is regulated by endothelial cells which takes the responsibility of penetrating the small molecules or whole cells in the blood flow in and out of this endothelium layer. This permeability is pivotal and varies with different types and physiological state of the tissue. It was reported that two types of pathways allowing the molecules to traverse the arterial endothelium entering the underlying tissue: transcellular pathway (endothelial plasmalemmal vesicles) and paracellular pathway, observed through the electron microscopic technique (Chen et al., 1995). This layer of endothelial cells is permeable when the diameter of molecules is within the range from 0.1 nm to 11.5 nm (Pober, Sessa, 2007; Vogel, Malik,

2011). Molecules bigger than 3 nm transverse through the transcellular pathway while the smaller molecules (< 3 nm) is allowable to pass via the paracellular pathway (Vogel, Malik, 2011; Sukriti et al., 2014). These two pathways cooperatively maintain the normal function of the endothelial barrier.

In aneurysm wall, the presence of vascular endothelial growth factor (VEGF) has been observed (Kilic et al., 2005). VEGF leads to changes in endothelial cells increasing permeability at intercellular junctions in pathological status. The raised permeability further trigger the pathological pathways of the media layer and ECM, i.e. the accelerated transmigration and the tightened binding of inflammatory cells (Unemori et al., 1992). Mast cells increased predominately in the rat models with intracranial aneurysms and they have a higher number in the ruptured human aneurysm than unruptured aneurysms (Ishibashi et al., 2010; Hasan et al., 2012). Other inflammation cells, i.g. monocytes and macrophages, are also found in larger aneurysms and ruptured aneurysms which indicates that the high level of inflammation is significantly associated with aneurysm growth and rupture (Frosen et al., 2004; Amenta et al., 2015). Also, the wall histology of an intracranial aneurysm shows the main changes are apoptosis of endothelial cells, loss of collagen and the ECM remodelling. This enables the contrast agents to penetrate the surrounding cerebrospinal fluid which provides a possibility to assess the aneurysm instability from the permeability information on Dynamic Contrast-Enhanced MRI images (Vakil et al., 2015). Therefore, the endothelium permeability plays a nonnegligible role in the inflammation and tissue remodelling in an aneurysm, contributing to the aneurysm growth and rupture.

To develop our model, we hypothesise that the morphology of endothelial cells determines the regional permeability, which gives rise to different levels of inflammation and tissue remodelling. Specifically, the higher WSSAR indicates irregular shape of endothelial cells distributed in that region, which implies higher permeability and stronger wall remodelling. Consequently, it will induce the aneurysm to become larger.

3.5 Conclusion

Through the analysis of the widely-used haemodynamic indices and the aneurysm growth quantification (ICA-1 case), it is found that the oscillatory feature of the flow (OSI, AFI) has the high potential related to aneurysm growth. There is a recently devised flow metric, WSSAR, developed by Krishna et al. which is capable of effectively capturing the flow patterns both at the instantaneous time point and over one cardiac cycle. We assume the endothelial cells morphology is a function of WSSAR where the endothelium permeability is determined by the local distribution of endothelial cells morphology. Hence, we hypothesize that this WS-

SAR contributes to the aneurysm growth which also sheds light on a reasonable pathological pathway: oscillatory characteristic - WSSAR - endothelial cells morphology - endothelium permeability - aneurysm growth.



Structural modelling of Patient-Specific IA Models

4.1	Generation of the Thick-walled Aneurysm Model	85
4.2	Meshing and Boundary Conditions	87
4.3	Mechanical Parameters Study of Elastineous Constituents and Collagen Fibres	90
4.4	Collagen Fibres Alignment Distribution	102
4.5	Model Implementation with ANSYS	106
4.6	Results and Discussion	110

As mentioned in Section 2.3.1, with a simple cylindrical geometry as the model of a segment of healthy artery to develop an aneurysm, it is straightforward to generate the mesh of the model and simulate the subsequent large deformation of the mesh. But for a patient-specific geometry, commercial software such as ANSYS is more suitable for mesh generation and analysing the mechanical responses and deformation of the diseased artery under physiological loading condition. Given the complexity of the patient-specific aneurysm geometry, structural analysis and growth simulation become very challenging. Through the thickness of

the arterial wall, several layers of elements are created with unstructured grid cells to fit in the realistic geometry. One challenge is that the generation of the mesh for the patient-specific aneurysm is completely automatic leading to a mesh in which we are not able to identify the position of the element within the model. Meanwhile, to define the heterogeneous tissue properties to different elements, we need to know the position of each element within the model of the aneurysm. Hence, this automatically-generated mesh averts the possibility of assigning specific material property on each element in the aneurysm solid model. Even though the commercial software can widely extend the applicability of P-FSG framework, it also limits the functional implementation of the aneurysm growth algorithms. With the help of subroutine and users custom programmes, we successively develop a method which enables each element in this automatically generated mesh to be individually-controlled, leading to the aneurysm growth algorithms could be executed on our aneurysm model.

Furthermore, the greatest challenge is the multilayers mesh generated in the aneurysmal wall leading to the boundedness of large deformation which probably results in a smaller developed aneurysm compared to the real aneurysm progression. The non-convergence issue of the structural analyses is often attributed to the excessive distortion of one or more elements. This problem could lead to the unexpected termination of simulation not due to the G&R algorithm but the hyperelastic limitation of the solver.

This chapter will first describe the construction of a thick-walled aneurysm model from the ICA-2 model (Chapter 3, a membrane model) and the assignment of boundary conditions. Because of the limited experimental data on the mechanical behaviour of elastin and collagen in aneurysms, a parameter study is tested for the mechanical properties of elastin and collagen fibres in aneurysm part and healthy artery part respectively. To model collagen fibres mathematically, the method of calculating the alignment directions of them are clearly represented. Then, the key procedures to implement our aneurysm into ANSYS are introduced and the results of structural analyses are discussed.

4.1 Generation of the Thick-walled Aneurysm Model

To save computational time and resources, the structural modelling focuses on the aneurysm part which indicates that it is unnecessary to include all the geometry used in the CFD simulation. Obviously, the aneurysm part is crucial which is the field for the implementation of the G&R of the constituents in the arterial tissue. Given the clinical geometry introduced in Chapter [subsection 3.1.2](#), the aneurysm part was extracted in the @neufuse software.

The original geometry (Fig4.1(a)) was partitioned into three parts: the aneurysm section, upstream and downstream sections we call them parent artery. The cutoff aneurysm model,

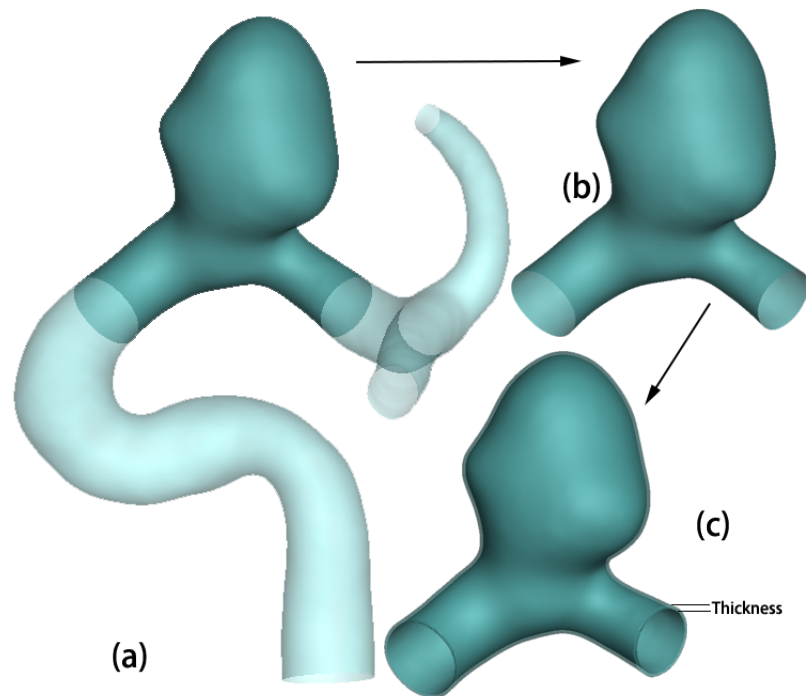


Figure 4.1: Extraction of the aneurysm segment and the generation of the thickness on the aneurysm model (a):original geometry; (b): extracted aneurysm segment; (c): aneurysm model with thickness

as an individual subject, was used in structural analysis. The diameters of two boundaries of the aneurysm model, connecting to the upstream and downstream sides respectively, are 3.617 mm and 3.070 mm measured in GEOMAGIC software. The thickness information of the unloaded aneurysmal wall was measured at five random positions by micro-calipers and the average thickness is 0.16 mm (Robertson et al., 2015). On the grounds that the technique of imaging is still limited, the outer contour of the aneurysm wall cannot be obtained clearly. So the thickness of this aneurysm wall was assumed as uniform in this research (Fig4.1(c)) which is consistent with other structural modelling of aneurysms (Brunel et al., 2017).

Once the inner surface of the aneurysm section was extracted, the Rhinoceros 5.0 software was employed to extend this surface outward and produced the entity of the thick-walled aneurysm model in the format of STL. However, the STL entity is not a readable format of the ANSYS solver. At this point, the software GEOMAGIC STUDIO 12.0, has powerful surface manipulation capabilities, was adopted here to construct grids and create a 3D solid model with an IGES format.

4.2 Meshing and Boundary Conditions

4.2.1 Meshing Methodology

As to the mesh generation, the build-in function in ANSYS ADPL was utilised and the element type we employed here was SOLID187. SOLID187 element is a 10-nodes tetrahedron, a higher order 3D element. This type of element is suitable for modelling irregular geometries (e.g. complex geometry produced in CAD system) which has a quadratic displacement behaviour. On each node, there are three degrees of freedom which are the translation in the directions of nodal x (UX), y (UY) and z (UZ). The construction of one individual SOLID187 element is shown in Fig4.2 and the nodes are located at each vertex and the midpoint of each edge. The reason for employing this element type is that it has great abilities in modelling plasticity, hyperelasticity, creep, stress stiffening, large deflection, and large strain. The pressure can be loaded on the surfaces: face J-I-K, face I-J-L, face J-K-L, face K-I-L (Fig4.2).

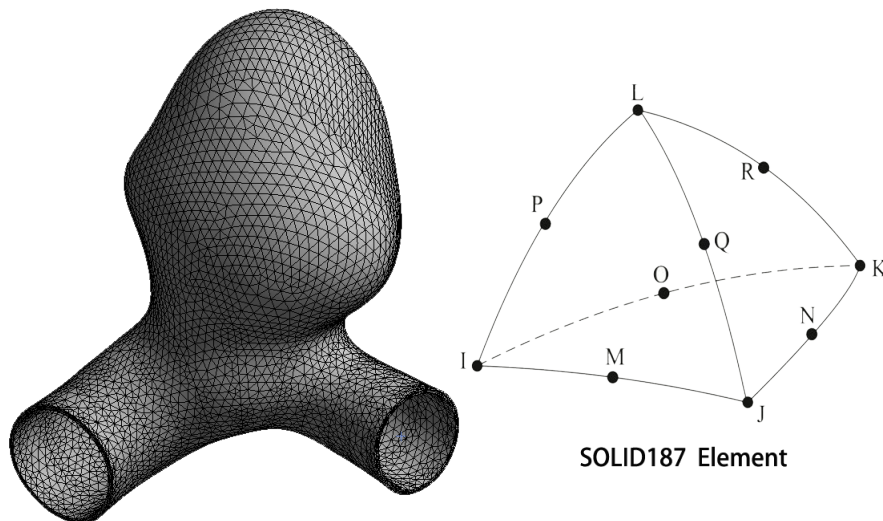


Figure 4.2: Mesh of our aneurysm model and the shape of its constitutional unit: SOLID187 element type which has hyperelastic property

The meshing method is free mesh in ANSYS APDL which is usually restricted to tetrahedral elements with the merit of the capability of being applied to any complex geometry.

4.2.2 Imposition of Boundary Conditions

To save the computing resource and time, the aneurysm part and a short segment of the contiguous parent vessels were extracted showed in the above section. We named them as an 'aneurysm model' in the rest of this study. It is unclear about the actual traction on the edge of the parent vessels at the beginning of the structural modelling. Therefore, the boundaries on both side edges were presumed to be fixed as a zero displacement constraints (Lu et al., 2008). The constraints on the boundary was applied on the patches on the two sides of aneurysm (Fig4.3, red). A uniform pressure of 120 mmHg (16kPa), at systole, was applied to the inner surface (luminal wall) with the neglect of the cerebrospinal fluid pressure outside the aneurysm. Similarly, this pressure was applied in the normal direction to each patch on the inner surface of this model.

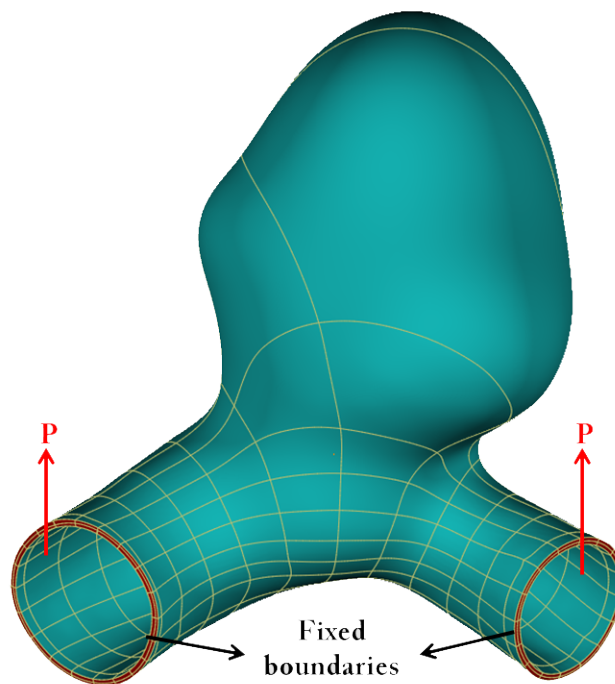


Figure 4.3: Boundaries condition applied on the thick-wall aneurysm model consisting of pressure on the inner surface and fixed constraints on the connection surfaces (red patches)

4.2.3 Grid Independence Study in Structural Modelling

Similar to the CFD simulation, the grid independence study was performed before the structural modelling for the sake of the reliability and accurateness of produced results.

Table 4.1: Mesh statistic information and key results of four study scenarios

	Scenario 1	Scenario 2	Scenario 3	Scenario 4
Global element size	0.4	0.3	0.2	0.15
Node number	40207	62442	122773	210162
Element number	20059	31176	61335	105222
Element Quality (Average Value)	0.6549	0.7304	0.7998	0.7730
Maximum Displacement(mm)	0.4768	0.47723	0.47741	0.47746

The global element size in Table 4.1 is the essential control of the mesh density which indicates the element edge length. The displacement result was picked out for the assessment in this grid-independence study. The mesh effectiveness evaluation was addressed in terms of the element quality, the consuming time for computation and the displacement distribution deviation among results. The mesh density increases from scenario 1 to scenario 4 which have coarsest and finest grids respectively. It has been mentioned in the grid-independence study in the CFD simulation that 0.2 is usually regarded as an acceptable threshold value for mesh quality (Lantz et al., 2012). In total, more than 99.85% of the elements had a quality above 0.2 and most of them amassed in the range of 0.75-1. Moreover, the average value of element quality in scenario 3 is the highest (0.7998). Hence, based on the point of the mesh quality, the scenario 3 is the optimal case and the scenario 1 should be expelled as a result of the relatively poor element quality which is below 0.7.

Applying the aforementioned boundary conditions and assigning the same hyperelastic material properties which will be elucidated in the next section, the structural modelling results are attained for different cases. With respect to the displacement distribution, the four scenarios have inappreciable difference which is shown in Fig 4.4. Due to the infinitesimal divergence, only scenario 1 and scenario 4 are employed to exemplify the displacement

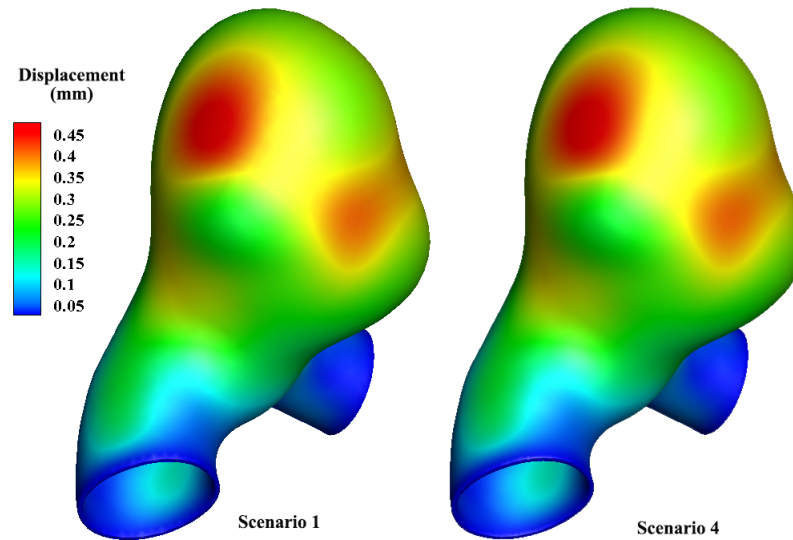


Figure 4.4: Displacement distributions on aneurysm after the structural modelling of Scenario 1 and Scenario 4

distribution difference here. Table 4.1 lists the maximum displacement values of these four scenarios. The margin-of-error is 0.138% of scenario 1 where the precondition is using result of the scenario 4 as the standard, and the margin-of-errors in other two scenarios are even less.

The computational time is also a significant component which needs to be considered carefully, which highly impacts the overall simulation time of our patient-specific FSG framework. The analysis of element quality and results deviation suggest that the current determination should be made between scenario 2 and 3. The computational time in scenario 2 saves in excess of 55% compared to scenario 3. However, the margin-of-errors of the displacement results are $4.84e-04$ and $1.05e-04$ in scenario 2 and 3 respectively, where the differences could be dismissed. Given all this consideration, the mesh density of scenario 2 is chosen to take part in the whole computational FSG framework for the aneurysm growth analysis.

4.3 Mechanical Parameters Study of Elastineous Constituents and Collagen Fibres

After the mesh generation and boundary conditions application, the most significant procedure is to assign the proper material parameters on each element according to the various constituents within the arterial wall. The following sections will center on the investigation

and implementation of specific hyperelastic properties in the model of the aneurysm wall and parent arterial wall.

The biomechanical properties of the passive arterial wall are chiefly dominated by collagen and elastin fibres, as well as the ground matrix. This ground matrix includes passive SMCs and all other constituents with the exclusion of elastin and collagen fibres, representing the elastic mechanical properties resemble elastin fibres.

In healthy arteries, the elastin fibres act a predominant function in bearing the load from the blood pressure. Especially, in intracranial arteries, there is only one fenestrated sheet of elastin fibres, named the internal elastic lamina (IEL) with the absence of external elastic lamina (EEL). The collagen fibres stay as the crimped state in lower pressure giving no contribution to the load bearing. J.T.C. Schrauwen and his colleagues investigated the 3D configuration of collagen fibres in response to the pressure in carotid artery (Schrauwen et al., 2012). They found the biggest configuration change mainly occurred between 40 to 80 mmHg which means that the collagen fibres starts bearing the load from 40 mmHg. Fig 4.5 also showed that most collagen fibers were stretched to straight configurations under the pressure of 80 mmHg.

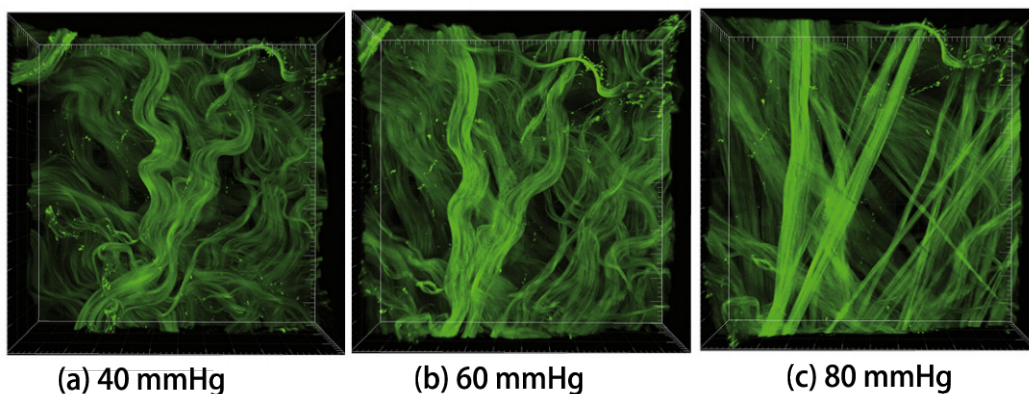


Figure 4.5: Collagen fibers configuration in the adventitia of the carotid artery at different pressures
(adapted from (Schrauwen et al., 2012))

Soft tissue adaption occurs during the aneurysm inception and evolution all along, in which collagen fibres struggle to self-regulate towards the homeostatic mechanical state. It is clear that the assembly of arterial components is remarkably distinct between the healthy arterial wall and the aneurysm wall.

In arterial walls, elastin performs as the main load-bearing component under normal pressure. As the pressure goes up, the physiological wavy form of collagen changes to straight-

ened which means the collagen is mechanically recruited. Collagen fibres, mainly the type I collagen, are primarily in charge of the load-carrying under higher blood pressure.

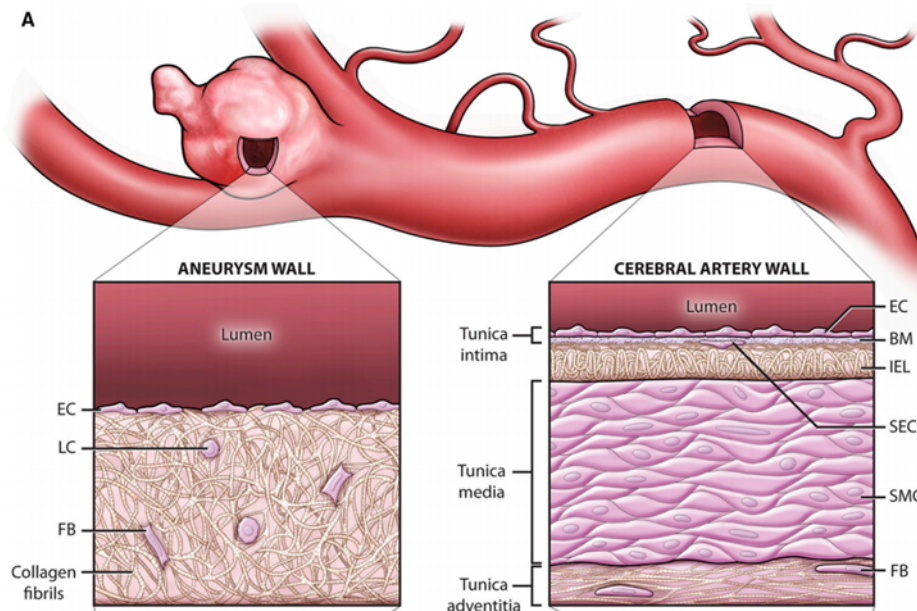


Figure 4.6: Constituents difference between cerebral arterial wall and aneurysm wall (adapted from (Etmnan et al., 2014)). BM, basal membrane; EC, endothelial cells; FB, fibroblasts; ICA, internal carotid artery; ICA-E, extracranial ICA; LC, lymphocytes; MCA, middle cerebral artery; SEC, subendothelial cells; and SMC, smooth muscle cells

Mechanical behaviour of each component part and their corresponding proportions in arterial wall change greatly during the aneurysm evolution. The two key components, collagen and elastin, are the dominant constituents in the progress of the aneurysm evolution and governs the mechanical response of the aneurysm wall. Hence, for the aneurysmal wall and the healthy arterial wall, they possess different proportions of elastin and collagen material constitutes. In healthy cerebral arteries, one integral internal elastic lamina (IEL) and smooth muscle cells (SMC) are filled in the media layer and the collagenous tissue mainly constitutes the adventitia layer as a protective sheet (Etmnan et al., 2014) showed in Fig 4.6. But along with the aneurysm evolution, the elastinous constituents degrades and it only remains some isolated fragments of elastin in the aneurysmal wall. Meanwhile, collagen fibres in the adventitia layer start growing and remodelling to withstand the pressure from the blood flow. The collagen fibres start to act as the main load-bearing component through the aneurysm wall.

4.3.1 Constitutive Models

4.3.1.1 Neo-hooken Model for Elastinous Constituents Modelling

It is supposed that the mechanical response of the non-collagenous matrix (elastin) in the arterial wall associated with isotropic deformations (Holzapfel et al., 2000). The classic Neo-Hookean model is adopted here to model the isotropic response of elastinous constituents. The strain energy function (SEF) can be expressed as

$$\Psi_E = c^E (I_1 - 3) \quad (4.3.1)$$

where $c^E > 0$ is a stress-like material parameter and we defined it as

$$c^E = \frac{1}{2} m^E \times k^E \quad (4.3.2)$$

In the above equation, m^E denotes the elastin concentration, a dimensionless and normalized variable, which is assumed to be 1 in the normal artery. Besides, I_1 is defined as

$$I_1 = tr(\mathbf{C}) = tr(\mathbf{F}^T \mathbf{F}) \quad (4.3.3)$$

in which the \mathbf{F} is the deformation gradient tensor and \mathbf{C} represents the right Cauchy deformation tensor. Along with the elastin degradation, m^E decreases and the prescribed minimum is 0 which means no elastinous constituents exists within the arterial wall. Also, the k^E denotes the shear modulus of elastinous constituents. The specific value of m^E and k^E used in this model will be introduced in the next section.

4.3.1.2 Anisotropic Model of Collagen Fibers

As mentioned in Section 1.2, the arterial wall has three layers acting different functions. The elasticity of arterial wall is mainly given by the elastic fibres at low strains and collagenous tissue performs anisotropic behaviour at high strains located in the media and adventitia layer. In terms of the intima layer composed of one monolayer of endothelial cells, the collagen (basically of Type I and Type III) is only related to intima hyperplasia and arteriosclerosis which produced by the proliferation of intimal cells (mainly myofibroblasts)(Canham et al., 1989). Therefore, in healthy arteries, the collagen in the media and adventitia layer is taken into consideration in the constitutive model of the arterial wall. On account of the anisotropic behaviour of collagen with the strong stiffening effect at higher pressures which could be represented by an exponential function, the anisotropic hyperelastic model with the SEF expression of collagen fibres:

$$\Psi_C(a_{01}, a_{02}) = \frac{k_1}{2k_2} \sum_{i=4,6} \{exp[k_2(I_i - 1)^2] - 1\} \quad (4.3.4)$$

where a_{01}, a_{02} are two vectors indicating the directions of two families of collagenous fibres, and here $|a_{01}| = |a_{02}| = 1$. In addition, the invariants I_4 and I_6 are the squares of the stretch in the direction of a_{01} and a_{02} , respectively (Holzapfel et al., 2000). Considering the cylindrical morphology of arterial wall, the a_{01}, a_{02} could be expressed as:

$$[a_{01j}] = \begin{bmatrix} 0 \\ \cos\beta_j \\ \sin\beta_j \end{bmatrix}, \quad [a_{02j}] = \begin{bmatrix} 0 \\ \cos\beta_j \\ -\sin\beta_j \end{bmatrix}, \quad j = M, A \quad (4.3.5)$$

M, A donate the media layer and adventitia layer respectively. And β_j represents the angles between two families of collagen fibers embedding in the wall tissue helically.

$$A_{1j} = a_{01j} \otimes a_{01j}, \quad A_{2j} = a_{02j} \otimes a_{02j}, \quad j = M, A. \quad (4.3.6)$$

The above function characterizes the structure of media and adventitia tissue which comprised of collagen fibers and represented by tensors A_{1j} and A_{2j} . The definitions of invariants I_4 and I_6 are

$$I_{4j} = A_{1j} : C, \quad I_{6j} = A_{2j} : C, \quad j = M, A. \quad (4.3.7)$$

where C is the Right Cauchy-Green deformation tensor related to the deformation matrix. When modelling the anisotropic mechanical behaviour of collagen, invariants I_{4j} and I_{6j} should be greater than 1. On the grounds that the wavy structure of collagen fibers can only contribute in the extension condition, which means they are unable to be activated in the circumstance of compression. In other words, the behaviour of collagen fibers would be isotropic when I_{4j} and I_{6j} equal or less than 1.

Arterial wall is simplified as one layer without the distinction of the media and adventitia layer in this research. The parameters $k_1 > 0$ and $k_2 > 0$ are linear constant and exponential constant (dimensionless) of collagen respectively. The method of getting the orientations of the two collagen fibres on aneurysm model will be introduced in Section 4.4. Once we got the orientation information of collagen fibres, the specific expression of a_{01} and a_{02} here can be applied to the SEF function to represent the mechanical behaviour of collagen fibres in the aneurysm model. Values of two quantitative parameters k_1 and k_2 in this research need to be investigated by analytical solutions with the detailed description below.

4.3.2 Parametric Study of the Mechanical Properties for Elastin and Collagen Fibres

Mechanical behaviour of collagen fibres and elastin can be represented by strain energy functions (SEFs). According to the similarities of geometric features, the aneurysm and parent vessels were tested by a spherical model and a cylindrical model to get the analytical solution respectively.

It is worth to mention that this study compacts the media layer and adventitia layer into one combined layer. Even though the two-layer modelling of aneurysm growth and remodelling has been used for decades, a patient-specific geometry (i.e. complicated morphology) as the specimen is firstly used to investigate the aneurysm growth and remodelling in this research. The complicity of the geometry also incurs the manipulative difficulties in the establishment of geometry and the following fulfilment of the methods. Importantly, there is no obvious boundary between the media and adventitia layer in the aneurysms. Here we simplified the structure of arterial tissue (both the aneurysm section and the parent vessel section) as one layer in modelling the aneurysm growth and remodelling. In spite of the existing mechanical experiments on arterial tissue (Sommer et al., 2009), the question is most specimen harvested from elderly people which can not be directly used in our model (27 years old) because the passive mechanical properties of artery tissue are obviously different with ages (Cox, 1977; Hansen et al., 1995). Therefore, to match the mathematical model in this research, we put forward the hypothesis that testing the material properties of elastin and collagen in one-layer vascular tissue to quantify their different mechanical behaviours in healthy artery and aneurysm respectively.

4.3.2.1 Cylindrical Model of Healthy Artery Wall

There is scarcely available experimental tests of the mechanical behaviour of healthy arterial tissue could be applied to this research. Gerhard Sommer et al. detected the biaxial mechanical properties of intact human carotid arteries harvested from a set of specimens with an average age of 77.6 years old (Sommer et al., 2009). However, the patient sample in this research is 27 years old, the great disagreement of ages leads to the absence of available experimental data that could be used for the case in this research. Since the passive mechanical properties of artery tissue varies with age remarkably (Cox, 1977; Hansen et al., 1995). For example, the dilation extent of carotid artery over the cardiac cycle declines with age. One research indicated that the diameter changes about 13%, 10% and 5% in the groups aged 15, 30, 70 years old respectively (Hansen et al., 1995). Therefore, it is necessary to perform a parameter study to find suitable values for related parameters which control the mechanical behaviour

of vascular arteries.

The vascular system is made up of vessels with the basic cylindrical shape with bends and bifurcations. In the study of mathematical models, the arteries could be regarded as the connection of oodles of tube segments. Hence, to investigate the mechanical behaviour of the healthy arterial wall, the cylindrical model could be used here to test proper material parameters.

Characteristic parameters of a cylindrical model, unloaded configuration, are length (L), radius (R) and height of the thickness (H). After applying an axial stretch on the ends and a uniform pressure normal to the inner surface, the corresponding changed characteristic parameters on the loaded configuration are shown in Fig 4.7.

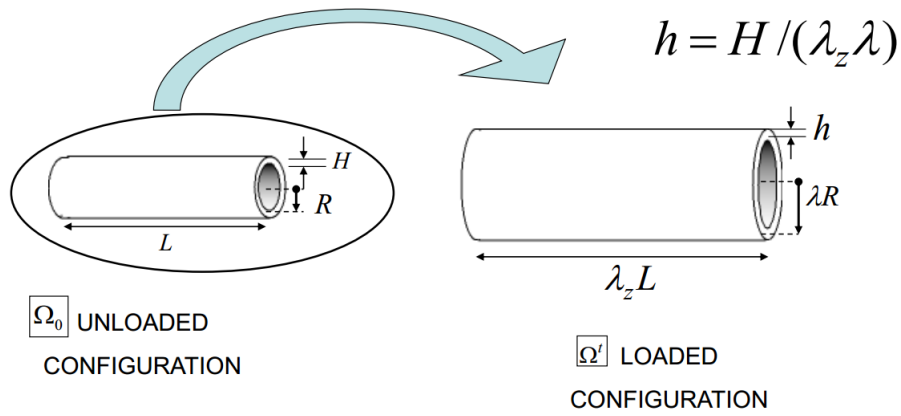


Figure 4.7: Unloaded and loaded configurations of the analytical model of a cylinder. L , length; R , radius; H : height of thickness on unloaded configuration; h , height of thickness on loaded configuration; λ_z , axial stretch; λ , circumferential stretch

In the cylindrical polar coordinates system, it can be shown that

$$\mathbf{F} = \begin{bmatrix} \lambda_r & 0 & 0 \\ 0 & \lambda_\theta & 0 \\ 0 & 0 & \lambda_z \end{bmatrix}, \quad \mathbf{C} = \begin{bmatrix} 1/(\lambda\lambda_z)^2 & 0 & 0 \\ 0 & \lambda_\theta^2 & 0 \\ 0 & 0 & \lambda_z^2 \end{bmatrix} \quad (4.3.8)$$

where λ_r , λ_θ , λ_z represent the radial stretch, circumferential stretch and axial stretch respectively. Because arterial wall is set as an incompressible tissue, then we have $\lambda_r \lambda_\theta \lambda_z = 1$ and λ_θ is named as λ in a simple way. Hence the expression of first invariant of \mathbf{C} could be deduced as:

$$I_1 = \text{trace}\mathbf{C} = \lambda^2 + \lambda_z^2 + \frac{1}{(\lambda\lambda_z)^2} \quad (4.3.9)$$

Then the force balance governing equation for the mechanical equilibrium of this elasti-

nous and collagenous cylindrical model could be expressed as:

$$P = \frac{1}{\lambda \lambda_z} \frac{H}{R} \frac{\partial \Psi_E + \partial \Psi_C}{\partial \lambda} \quad (4.3.10)$$

here P denotes the blood pressure. With the combination of equation 4.3.1 and 6.3.4, the differential part in above question could be formulated as follows:

$$\frac{\partial \Psi_E + \partial \Psi_C}{\partial \lambda} = \frac{k^E m^E (\bar{I}_1 - 3)}{2\partial \lambda} + \frac{k_1 \Sigma(i=4,6) \exp[k_2(\bar{I}_i - 1)^2 - 1]}{2k_2 \partial \lambda} \quad (4.3.11)$$

Because the I_4 and I_6 in the above equations are highly dependent on the collagen fibre orientations, so the alignment of collagen fibres also need to be determined here. It is well known that two families of collagen fibres are arranged in symmetrical spirals. The alignment of collagen fibres embedded in the media layer and the adventitia layer is illustrated in Fig 4.8. The representable angles to qualify these collagen fibres which helically lying in the tangent plane of the media layer and the adventitia layer are $2\beta_M$ and $2\beta_A$ respectively. This means the angle β_j denotes the angle between the fibre direction (one family) and the circumferential direction in each individual layer.

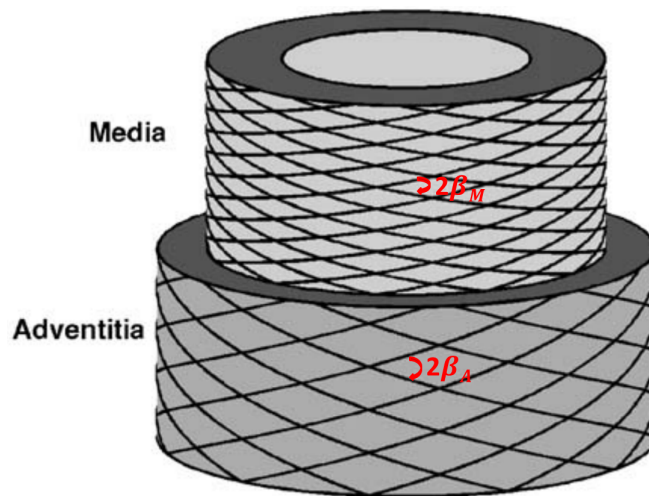


Figure 4.8: Collagen fiber architecture in the media and the adventitia layer of arterial wall (adapted from (Driessen et al., 2004))

Fig. 4.8 shows clearly that the angles between the two families of collagen fibres are distinct in media and adventitia layer. The β_M and β_A are defined 29.0° and 62.0° according to the experiment data for a carotid artery from a rabbit model (Chuong, Fung, 1983; Wuyts

et al., 1995; Xie et al., 1995). In a number of mathematical models, the definitions of β_M and β_A are 30.0° and 60.0° respectively (Watton et al., 2011; Grytsan et al., 2015). However, this type of setting of the arterial wall does not coincide with the scenario of our modelling. In this research, the constitutive model is built on one intact layer of an arterial wall, neither the angle information of the media layer nor that of the adventitia layer are available. There is one experimental study of a dataset of human carotid arteries recently which provides the statistic data of the β in the intact wall - adventitia, media, intima which are 20.4° , 25.9° (100KPa domian) and 6.9° respectively (Sommer et al., 2009; Sommer, Holzapfel, 2012). In this 1D analytical analysis, the angle β of the intact wall is considered as 20.4° which follows the experimental data.

Hence, after combining the Equation 4.3.5 and 4.3.6, the A_1 and A_2 could be formulated as:

$$A_1 = \begin{bmatrix} 0 & 0 & 0 \\ 0 & \cos^2\beta & \cos\beta\sin\beta \\ 0 & \cos\beta\sin\beta & \sin^2\beta \end{bmatrix}, \quad A_2 = \begin{bmatrix} 0 & 0 & 0 \\ 0 & \cos^2\beta & -\cos\beta\sin\beta \\ 0 & -\cos\beta\sin\beta & \sin^2\beta \end{bmatrix} \quad (4.3.12)$$

where the angle β is set to 20.4° . Through the processing of Equation 4.3.7, the expression of I_4 and I_6 can be calculated straightforward:

$$I_{4,6} = tr(C^T A_i) = \cos^2\beta\lambda^2 + \sin^2\beta\lambda_z^2, \quad i = 1, 2 \quad (4.3.13)$$

Taking consideration of the patient-specific model in this research (the geometrical information introduced in Section 3.1.2), the R is set as the mean value of inlet and outlet of the parent vessel in this aneurysm model which equals to 1.67mm. The thickness is uniform as 0.16 mm and the concentration of elastin (m^E) in the healthy artery should be 1. Because the zero displacement constraint was applied to two boundaries of the model in 3D simulation, the λ_z here we set as 1. Given the above information, the relationship between pressure (P) and the circumferential stretch (λ) could be built with the involving of parameters k^E , k_1 , k_2 as well as the orientations of collagen fibres (i.e. β_j in Equation 4.3.5).

4.3.2.2 Numerical Result of Key Parameters in SEFs

Force balance equation 4.3.2.1, the basement of this 1D analytical study, was calculated in Matlab and the subsequent relationship between **Pressure** and **Circumferential Stretch** was obtained (Fig 4.9).

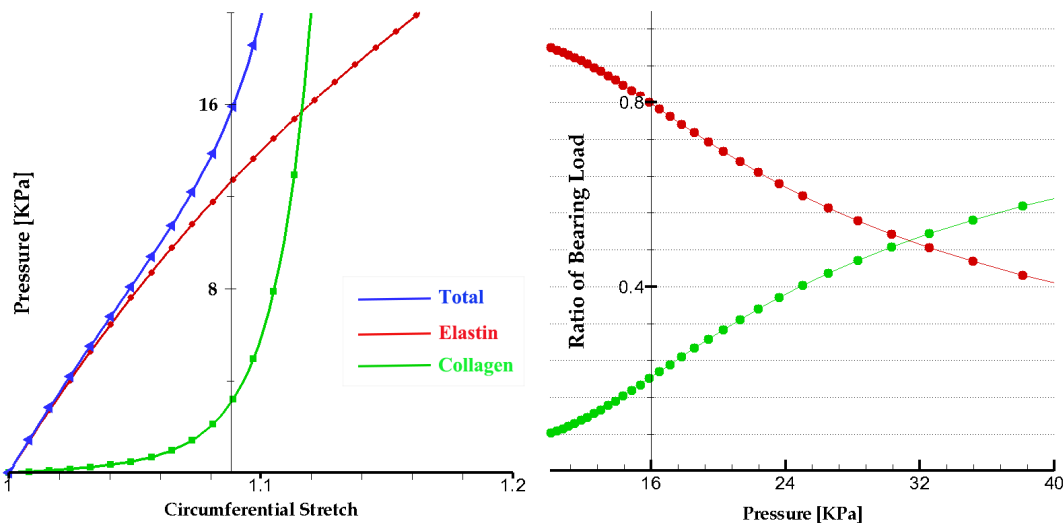


Figure 4.9: L: Mechanical behaviours of elastin, collagen and the total arterial wall in the healthy artery. R: Load bearing ratio of elastin and collagen under various pressures for healthy artery (red: elastin; green: collagen)

The principal criteria of quantifying the mechanical behaviour are:

1. The configuration of collagen fibres changes considerably from 40 to 80 mmHg and nearly all collagen fibres are stretched to straight configuration under 80 mmHg (Fig 4.5) (Schrauwen et al., 2012).
2. Elastineous constituents bear 80% of the blood pressure load at systole (Watton, Hill, 2009).

As mentioned before, elastin is in charge of the load bearing under lower pressure and the collagen starts to be recruited after a certain threshold of strain. The material property of collagen tested in this research (green line, Fig 4.9, L) shows steep stiffening within the pressure span (40-80 mmHg) which indicates that the configuration of collagen fibres changes to straight gradually from the crimped morphology. This result reflects the reasonable mechanical behaviour of collagen which agrees with the experimental observation. And under lower pressure, it is obvious that the elastin plays a key role in bearing the load in a nearly linear way. In order to explain the division and cooperation of the elastin and collagen more explicitly, the percentage for load bearing of elastin and collagen under various pressures is plotted in Fig 4.9 (R). The total load bearing was set as 1, i.e. the sum of the collagen bearing ratio and elastin bearing ratio is equal to 1. Under systolic pressure, the elastin bears approximate 80% load and as the pressure increases, more collagen participates in bearing the load. When the pressure surges to a high value, the collagen starts dominating, which indicates its function of a protective sheet.

4.3.2.3 Sphere Model of Intracranial Aneurysm Wall

It is well known that the internal elastic lamina (IEL) in the cerebral arteries takes the dominant role in bearing the load from the lower blood pressure and collagen constituents provide the tensile resistance required at high pressures.

As early in 1961, Hassler has put forward that the bulk of the wall of intracranial aneurysms is comprised of collagen fibres and the remnant of isolated fragments of elastin (Hassler, 1961). Therefore, the primary variation from a healthy artery to an aneurysm is owing to the fragmentation of the elastinous constituents. This was confirmed by Hassler and Nyström using a histological experiment which indicated that the aneurysms only form in the condition that the internal elastic membrane is broken (Hassler, 1961; Nyström, 1963). So in aneurysms, the collagen constituents take the dominant role in withstanding the pressure derived from the pulsatile blood flow. Collagen has the anisotropic mechanical behaviour and when it starts to be recruited, it becomes much stiffer which coincides with the fact that aneurysms are less distensible than intracranial arteries (Scott et al., 1972).

In the light of the geometric feature of saccular aneurysms, an analytical sphere model was employed to investigate the mechanical behaviour of this partitioned aneurysm model in this study. Hence, we implemented the simulation of the inflation of the incompressible spherical membrane. The initial spherical configuration which is the unloaded configuration (Ω_0) with the radius R and thickness H . In the wake of pressurising, the radius and thickness in the loaded configuration turn to λR and H/λ^2 respectively, shown in Fig 4.10.

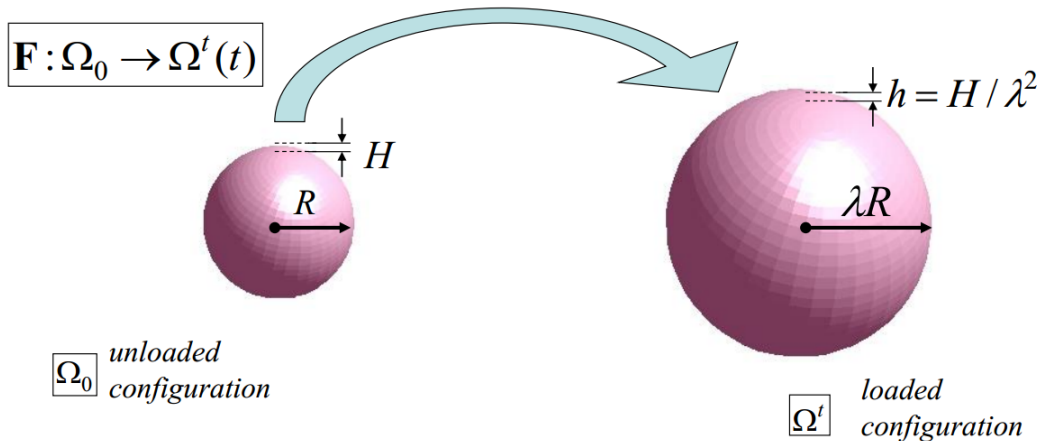


Figure 4.10: Unloaded and loaded configurations of the analytical model of sphere. R , radius; H : height of thickness on unloaded configuration; h , height of thickness on loaded configuration; λ , stretch

In the spherical polar coordinates system, it can be shown that

$$\mathbf{F} = \begin{bmatrix} \lambda_r & 0 & 0 \\ 0 & \lambda_\theta & 0 \\ 0 & 0 & \lambda_z \end{bmatrix}, \quad \mathbf{C} = \begin{bmatrix} 1/\lambda^4 & 0 & 0 \\ 0 & \lambda^2 & 0 \\ 0 & 0 & \lambda^2 \end{bmatrix} \quad (4.3.14)$$

where $\lambda_r = \lambda_\theta = \lambda_z$. Because the aneurysm wall is set as incompressible tissue, then we have $\lambda_r \lambda_\theta \lambda_z = 1$. Hence the expression of first invariant of \mathbf{C} could be deduced as:

$$I_1 = \text{trace} \mathbf{C} = 2\lambda^2 + \frac{1}{\lambda^4} \quad (4.3.15)$$

Then the governing equation for the mechanical equilibrium could be expressed as:

$$P = \frac{1}{\lambda^2} \frac{2H}{R} \frac{\partial \Psi_E + \partial \Psi_C}{\partial \lambda} \quad (4.3.16)$$

here P denotes the blood pressure. Considering the real condition of the patient-specific model in this research, the R (4.12mm) is calculated from the volume (219mm³) which has been measured in the lab. The thickness is uniform of aneurysm model which equals to 0.16 mm and the concentration of elastin (m^E) should be much less than 1. The specific concentration need to be tested further in the next step. Given the above information, the relationship between pressure (P) and the stretch (λ) could be built with the involving of parameters m^E, k_1, k_2 .

4.3.2.4 Numerical Result of Key Parameters in SEFs

The structural difference between the normal artery and the aneurysm has already introduced in the beginning of this section. The aneurysm in this research is a developed aneurysm which infers that only some elastin fragments scattered in the aneurysmal tissue. Similarly, the mechanical behaviour of collagen and elastin in the aneurysm was tested based on the variables: k^E, m^E, k_1, k_2 . Referring to the equation 4.3.2.3, the representing relationship of circumferential stretch varied with the pressure showed in Fig 4.11 L.

Here we suppose that in the course of aneurysm developing, the mechanical property of each elastin fiber is constant while the concentration of elastin is decreasing. Contribution of elastin for bearing load is negligible and nearly all mechanical behaviour of total tissue is controlled by collagen constituents under all levels of pressure. In the same way, the load bearing ratio-pressure curve was plotted to indicating the role of elastin and collagen more clearly in Figure 4.11 R.

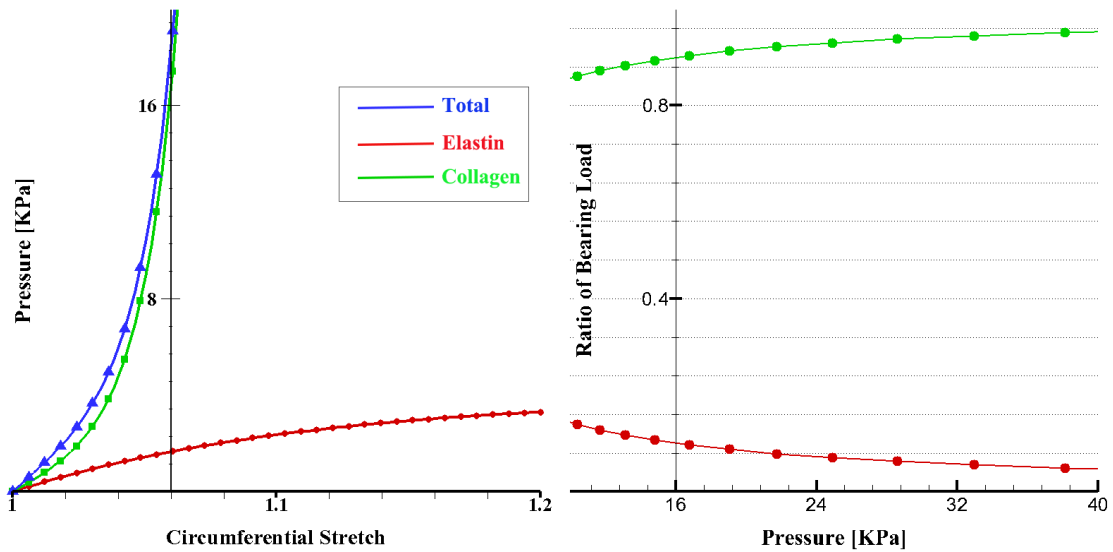


Figure 4.11: L: Mechanical behaviours of elastin, collagen and the total arterial wall in the healthy artery. R: Load bearing ratio of elastin and collagen under various pressures for aneurysm (red: elastin; green: collagen)

As the pressure goes higher, the collagen constituents undertake increasing responsibility in bearing the load given by the blood pressure. This indicates the significance of collagen in aneurysms and its growth and remodelling mechanism is the crucial issue in the aneurysm evolution process.

4.4 Collagen Fibres Alignment Distribution

Principal curvature has been extensively used in various academic researches and engineering fields. As the 3D reconstruction technique develops rapidly and more practically, 3D models are remarkably becoming the core research subject which leads to high requirements on the characterization of the topology of those models.

Related to this research, the alignment of two families of collagen fibres is correlated to the principal curvatures distribution (Ma et al., 2004). And the arrangement of collagen fibres is a key component in the structural modelling of both the healthy artery and the aneurysm model. Since the collagen fibres in arterial tissue are non-verifiable, it is necessary to employ some simple and regular models to validate the correctness of the methodology for calculating principal curvature distributions.

4.4.1 Methodology of Principal Curvature Acquisition on Irregular Geometries

The principal curvatures at a certain point on a differentiable surface can capture the maximum and minimum degree of the surface bends, which are named as first and second principal curvatures respectively. To explicitly demonstrate the process of acquiring these principal curvatures, an illustrative schematic diagram is shown in Fig4.12.

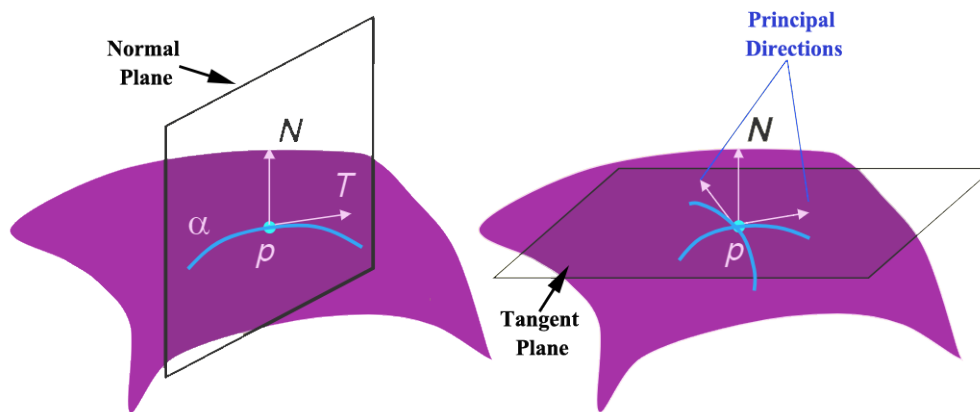


Figure 4.12: Schematic diagram of the definition of principal curvatures and the calculation procedures

(<http://slideplayer.com/slide/8564902/>)

Firstly, at one point p on a surface, the normal vector (\mathbf{N}) could be determined, consequently producing countless normal planes which incorporate the normal vector. Each normal plane will cut the surface in a plane curve named as α with a certain curvature which is defined as the reciprocal of the radius of the osculating circle. At the same time, a corresponding tangent direction (\mathbf{T}) is also generated. If the curvature has the same direction with the normal vector (\mathbf{N}) at that point, the curvature is taken to positive, or else negative. The directions of two principal curvatures in the tangent plane with the maximal and minimal curvatures values are always perpendicular to each other. In general, the first and second principal curvatures are denoted by k_1 and k_2 , as showed in Fig 4.13.

In this research, the principal curvature direction is the crucial subject which can represent the collagen fibres arrangement in the arterial tissue. The methodology to achieve the principal curvature directions is required to be available to anatomical geometries, i.e. complex 3D geometry. The cardinal mathematical algorithms demonstrated here are according to (Ma et al., 2004) and (Rusinkiewicz, 2004). The aneurysm model in this research is mapped

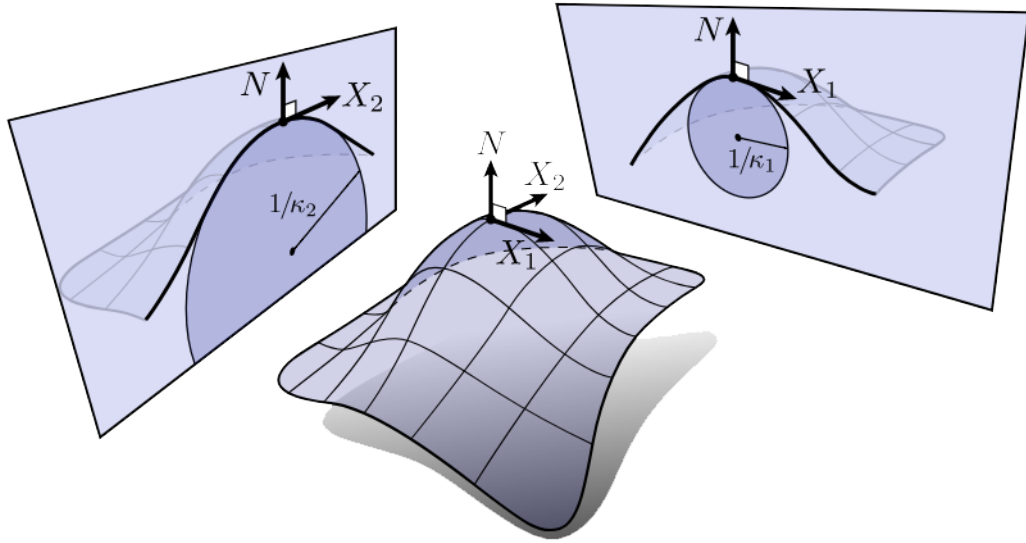


Figure 4.13: Schematic diagram of the first and second principal curvatures (k_1, k_2) and principal directions represented by unit vectors X_1, X_2 .
(<http://brickisland.net/cs177/?p=144>)

with triangular mesh, and the target is to acquire the principal curvature directions on each vertex. Because several triangle faces are shearing one vertex, hence the voronoi areas at each vertex are also calculated (Voronoi Diagram). In the calculation of the normal vector on each triangle facade and at each vertex, we also introduced the methods in (Max, 1999; Meyer et al., 2002). Concrete implementation procedures are described as follows:

1) Local coordinate system establishment

Build local orthogonal coordinate systems on each vertex p of triangle facets which denoted as $(\mathbf{P}, \mathbf{Q}, \mathbf{N})$. A tangent plane at vertex p is established and \mathbf{P}, \mathbf{Q} are unit vectors within this plan. \mathbf{N} is also a unit vector normal to that tangent plane.

2) Curvature calculation

Vertex p and its three adjacent vertices are fit in to a quadratic surface patch which could be integrated into a bivariate polynomial $f(u, v)$ in the local coordinate system, the surface could be formulated as :

$$f(u, v) = au^2 + buv + cv^2 \quad (4.4.1)$$

The Gauss-Weingarten map for this quadratic surface is

$$A = \begin{pmatrix} 2a & 2b \\ 2b & 2c \end{pmatrix} \quad (4.4.2)$$

Given this matrix \mathbf{A} , the eigenvalues (k_1, k_2) present the principal curvatures while the eigenvectors $(\mathbf{v}_1, \mathbf{v}_2)$ are principal curvature directions. The lucid mathematical expressions are

$$\begin{aligned} k_1 &= a + c + \sqrt{(a - c)^2 + 4b^2} \\ k_2 &= a + c - \sqrt{(a - c)^2 + 4b^2} \\ \mathbf{v}_1 &= (2b, a - c + (a - c)^2 + 4b^2) \\ \mathbf{v}_2 &= (2b, a - c - (a - c)^2 + 4b^2) \end{aligned} \quad (4.4.3)$$

and $\mathbf{v}_1, \mathbf{v}_2$ need to be normalized which are denoted as $\bar{\mathbf{v}}_1, \bar{\mathbf{v}}_2$.

3) Conversion to global coordinate system

Conversion function is given below from the local coordinate system to the global coordinate system:

$$V_j = \begin{pmatrix} P_x & Q_x & N_x \\ P_y & Q_y & N_y \\ P_z & Q_z & N_z \end{pmatrix} \begin{pmatrix} \bar{v}_{j1} \\ \bar{v}_{j2} \\ 0 \end{pmatrix}, j = 1, 2 \quad (4.4.4)$$

Note that P_x, P_y, P_z are direction cosines of \mathbf{P} in the global coordinate system, the same to \mathbf{Q} and \mathbf{N} . Meanwhile, \bar{v}_{j1} and \bar{v}_{j2} represent the coordinates of $\bar{\mathbf{v}}_j$ in local coordinate system.

4.4.2 Collagen Fibres Distribution on Patient-Specific IA Models

Above mentioned approach is the core segment to acquire the principal curvature directions on a given 3D model. The Appendix 2 employed a series of simple models including the original healthy artery model in order to illustrate and validate this approach for the calculation of principle directions. Here we will introduce the application on our complex aneurysm model, the research subject in this research.

Figure 4.14 plotted the first and second principle directions on this aneurysm model with green and grey colour respectively. It is clearly shown that they are perpendicular to each other in Fig 4.14 (C). In the region of the parent artery, the first principle directions align with the circumferential direction which proves that the results are correct. The normalized the directions as a_{01} and a_{02} could be further participated in the SEFs for collagen fibres.

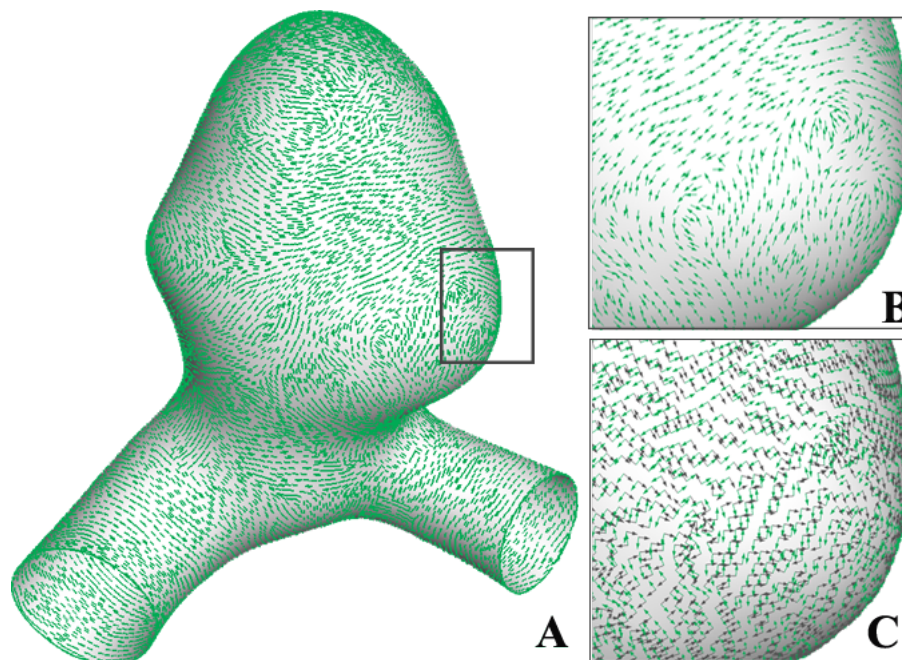


Figure 4.14: Distribution of first principal curvature direction on aneurysm surface (A). A locally magnified first principal curvature direction distribution within the rectangular region(B) and the second principal curvature direction distribution(C, grey arrows)

4.5 Model Implementation with ANSYS

4.5.1 Partition of the Structural Model

The cut-off part used in this structural analysis consists of not only the aneurysm section but also the parent vessels. According to the above material parameter study, aneurysms and healthy arteries have extremely different mechanical behaviours. Based on this, it is necessary to partition this model into the aneurysm section and the parent vessel section. Hence, the patient-specific model for structural analysis was divided into three parts: the aneurysm, parent vessels and a transitional region (Fig.4.15). Combined with the previous analytical solution of the cylinder model and the sphere model for parent vessel and the aneurysm respectively, different mechanical behaviours were taken into account and determined by the underpinning of the knowledge from the biomechanical researches in recent years.

As to the transitional region around the neck, a simple linear algorithm was utilized here

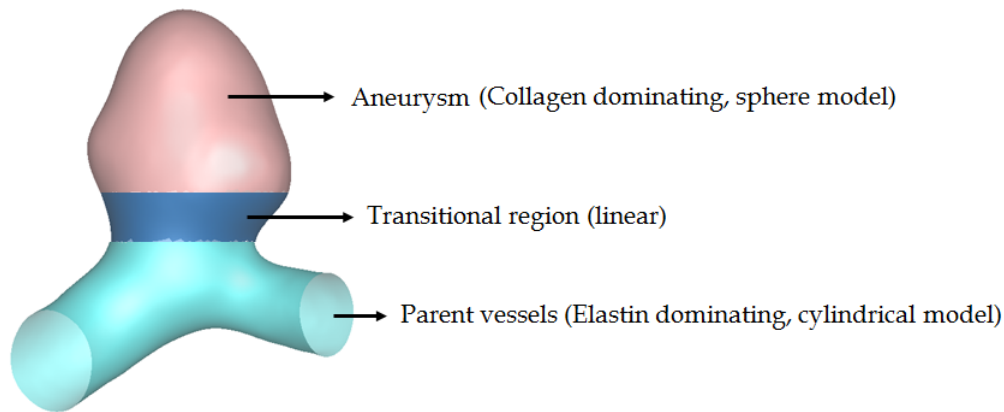


Figure 4.15: Segments of the structural model: aneurysm(pink), parent vessel(cyan), transitional region (blue)

in helping to solve the convergence problem. On the basis of the above analytical methods (equation 4.3.2.1), the pressure-circumferential stretch relationship is presented in Fig 4.9 and Fig 4.11 integrating the appropriate values for the variables : k^E , m^E , k_1 , k_2 . The specific values for of geometrical parameters and mechanical parameters for both arterial wall and aneurysmal wall are summarized in Table 4.2.

Table 4.2: Summary of geometrical parameters and mechanical parameters of elastin and collagen constituents for arterial wall and aneurysmal wall

	R (mm)	H (mm)	λ_z	β ($^\circ$)	m^E	k^E (kPa)	k_1 (kPa)	k_2
Arterial wall	1.67	0.16	1	20	1	460	10	65
Aneurysmal wall	4.12	0.16	-	-	0.083	460	100	100

4.5.2 Transformation of Global Coordinate System

The origin of global coordinates locates at a point on the downstream part of parent vessel showed in Fig4.16 (blue). A tremendous quantity of experimental researches has revealed that there is a remarkable difference of hyperelastic properties between an aneurysm and normal arteries. To more precisely model the mechanical response of the aneurysm model which referred in the preceding section, the model was segmented into three parts (i.e. the

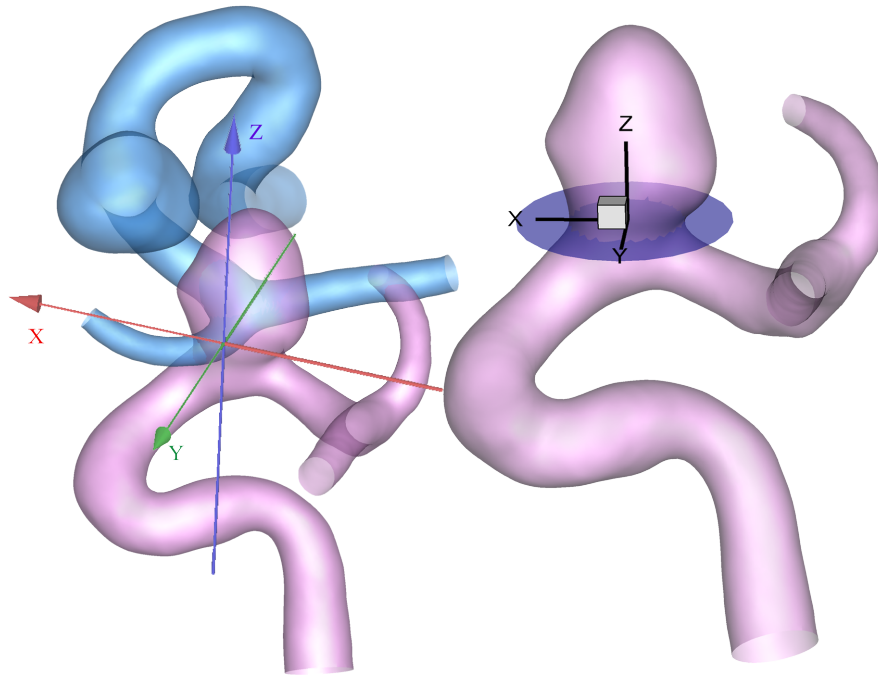


Figure 4.16: Coordinate system transformation for entire geometry.
blue: original; pink: transformed geometry

aneurysm, parent vessels and a transitional region in between). Considering it is difficult to partition the geometry according to the incipient coordinates locates, the solution is selecting a plane going through the neck which can produce a slice that is nearly a circle. Then the 'centre' of the plan was calculated which was defined as the origin of the new global coordinates. Z axis was perpendicular to this slice plane with the positive direction toward the dome of the aneurysm. Y-axis is approximate in the middle of the acute angle between parent vessels on the two sides. Meanwhile, X-axis is definitely orthogonal to Y and Z direction and positive to upstream part. Then the partition work could be easily operated according to the Z coordinates. When the z coordinate is greater than 1, then the point belongs to the aneurysm section. Likewise, when z coordinate is lower than -1, it is assigned to parent vessels. The left points between -1 and 1 belong to the transitional part.

The reason why the whole geometry has to be transformed is two boundaries of the aneurysm in the structural analysis have to connect with the remain parent vessels and then execute the CFD simulation. The coordinate transformation procedure is the initial step and the CFD simulation and structural modelling are based on the transformed geometry (Fig4.16 (pink)) in the new coordinate system.

4.5.3 ANSYS Implementation

We use ANSYS Mechanical 15.0 to model the artery and the aneurysm on the basis of solid mechanics, APDL classic module. The hyperelasticity of our model is achieved by the **Anisotropic Hyperelasticity** model. The anisotropic constitutive strain-energy density function W is:

$$W = W_V(J) + W_d(\bar{\mathbf{C}}, \mathbf{A} \otimes \mathbf{A}, \mathbf{B} \otimes \mathbf{B}) \quad (4.5.1)$$

where:

$W_V(J)$: volumetric part of the strain energy

W_d : isochoric part of the strain energy

Note that the volumetric part is totally independent of the isochoric part. The exponential-function-based strain energy potential is given by:

$$\begin{aligned} W_d(\bar{\mathbf{C}}, \mathbf{A} \otimes \mathbf{A}, \mathbf{B} \otimes \mathbf{B}) &= \sum_{i=1}^3 a_i (I_1 - 3)^i + \sum_{i=1}^3 b_i (I_2 - 3)^i \\ &+ \frac{c_1}{2c_2} \{ \exp[c_2 (I_4 - 1)^2] - 1 \} \\ &+ \frac{e_1}{2e_2} \{ \exp[e_2 (I_6 - 1)^2] - 1 \} \end{aligned} \quad (4.5.2)$$

Compared to our constitutive models of elastineous constituents and collagen fibres, only the items I_1, I_4 and I_6 are related to our model. The c_1, c_2, e_1, e_2 represent the k_1, k_2 in the SEF of collagen fibres in Equation 6.3.4 for two families of collagen fibres respectively. Here we assume the mechanical behaviour for two families of collagen fibres are identical. Hence, we have $c_1 = e_1 = k_1$ and $c_2 = e_2 = k_2$, which is according to the EXP item. And the A_1 in the **EXP** item represents the c^E in Equation 4.3.1 to quantify the Neo-Hookean behaviour of elastineous constituents.

The AVEC and BVEC in Fig 4.17 denotes the orientations of collagen fibres, say family A and family B. This orientation could be obtained from the method in the Section 4.4.2. the key word **PVOL** represents the volumetric potential and its value D equals $1/k$, where k is the bulk modulus. As Mohammed Yahya reported, the value of initial bulk modulus k is 34.7 MPa (Yahya, 2010). The D value is a very low number which could be neglected, indicating that the material is nearly incompressible. Consequently, the volumetric potential have been determined.

TBOPT	Purpose	Input Format
POLY	Anisotropic strain energy potential	TB,AHYPER,,POLY TBDATA,,A1,A2,A3,B1...
EXP	Exponential anisotropic strain energy potential	TB,AHYPER,,EXPO TBDATA,1,A1,A2,A3,B1,B2,B3 TBDATA,7,C1,C2,E1,E2
AVEC	Material direction constants	TB,AHYPER,,AVEC TBDATA,,A1,A2,A3
BVEC	Material direction constants	TB,AHYPER,,BVEC TBDATA,,B1,B2,B3
PVOL	Volumetric potential	TB,AHYPER,,PVOL TBDATA,,D

Figure 4.17: TB table which defines the input format for anisotropic hyperelasticity model.

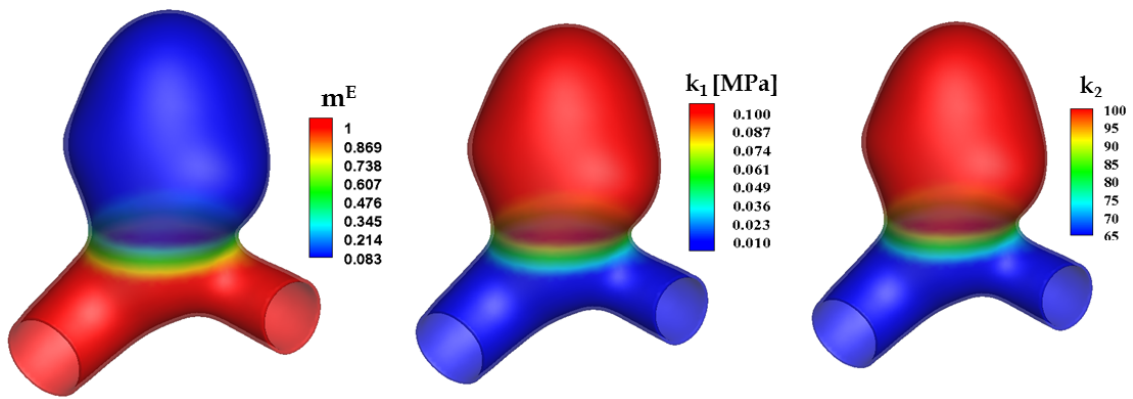


Figure 4.18: Initial distributions of mass density of elastineous constituents, k_1 and k_2 distributions on the aneurysm model

4.6 Results and Discussion

After the implementation of material properties assignment and the boundary conditions, the structural modelling could be enabled to capture the mechanical state of our model. Consequently, the basic displacement, stress, strain distribution could be achieved for further analysis.

4.6.1 Displacement Distribution

Figure 5.5 plots distributions of the key material parameters in the SEF of elastineous constituents and collagen fibres on the aneurysm part, parent vessels and the transitional region, according to the parameter study above. This m^E , k_1 and k_2 distributions are the initial quantification of the mechanical state of the aneurysm model. The elastineous constituents

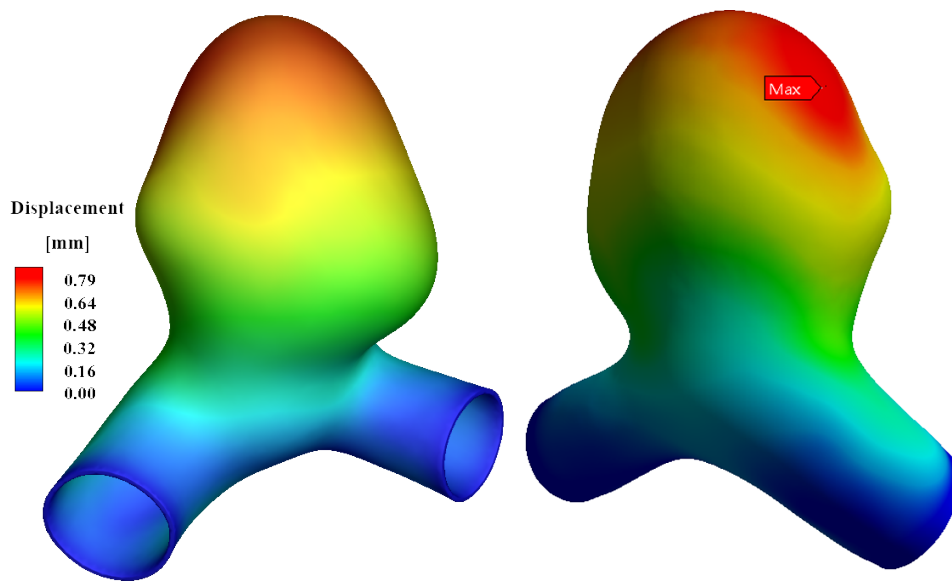


Figure 4.19: Color coded imaging of aneurismal wall displacement at peak systole. The color codes range from no displacement (blue) to maximum displacement of 0.79 mm (red). The largest wall displacement (arrow) occurred close to the dome of the aneurysm. Left: front view; Right: back view

in aneurysm only remain less than 1% compared to the normal healthy artery which due to the ripping of the internal elastin lamina from the neck. As the aneurysm growing and remodelling, the mechanical behaviour of collagenous constituents changes dramatically with the increase of the stress. The values of k_1 and k_2 in aneurysm region are larger than that in parent artery which denotes that they are much stiffer with lower distensibility.

Figure 4.19 shows the displacement distribution after applying the systolic pressure on the inner surface. The maximum displacement occurs on the side of the dome top which is in agreement with other studies (Isaksen et al., 2008; Ivanov et al., 2016). Alvaro Valencia et al. modelled 7 cerebral aneurysms using the fully coupled fluid-solid interaction method. They found that the displacement on the aneurysm fundus ranges from 0.16 mm to 0.74 mm which indicates that the displacement varies with the morphology, size and position of arteries and aneurysms (Valencia et al., 2008). They also pointed out that the maximum displacement located on the wall where the jet impinges at that position for the centred aneurysms on arterial bifurcation.

4.6.2 Distribution of Equivalent Strain

Besides the displacement distribution, researchers have significantly stronger interests in the stress and strain distribution on aneurysm wall which has been reportedly related to the aneurysm rupture risk.

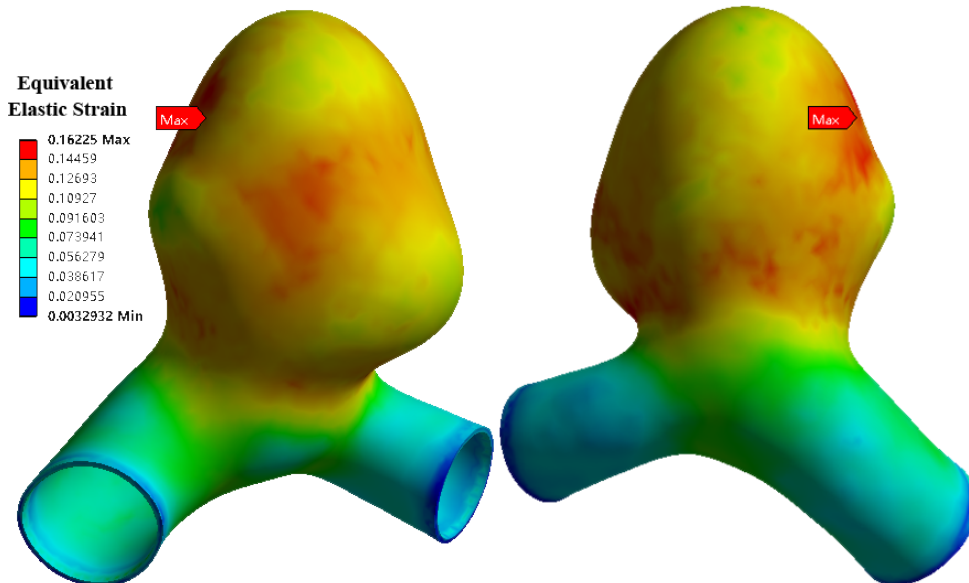


Figure 4.20: Distribution of the von-Mises elastic strain on the aneurysm model. The strain ranges from 0.0033 to 0.16225 and the maximum strain shows around the upper left region where is around the maximum displacement position. Left: front view; Right: back view

Fig 4.20 shows the distribution of the von-Mises elastic strain on the aneurysm model. On the boundaries, the strain is close to zero which is owing to the fixed restriction. Equivalent elastic strain in the aneurysm segment is larger than that in parent arteries. The position of maximum strain (around 0.16225) is sitting on the approximately same place with the maximum displacement. The relative large strain occurs in the aneurysm centre region in the front view and around the neck in the back view. In an FSI study of a giant intracranial aneurysm, the equivalent strain value is similar to this study which is 0.16085 (Khe et al., 2016). Apart from the equivalent strain, each component of the elastic strain tensor is also available in the ANSYS output file which is useful in computing the right Cauchy - Green deformation tensor.

4.6.3 Distribution of Equivalent Stress

Most aneurysms rupture when the wall strength cannot bear the load from the blood pressure due to the mechanical damage in the wall, that is to say, the stress on the wall exceeds the holding strength itself. In structural analysis, von-Mises stress is generally used for the characterization of the mechanical state of the material. It could be calculated via the stress tensor (Khe et al., 2016), here denoted as σ_{von} :

$$\sigma_{von} = \sqrt{\frac{(\sigma_{11} - \sigma_{22})^2 + (\sigma_{22} - \sigma_{33})^2 + (\sigma_{33} - \sigma_{11})^2}{2}} \quad (4.6.1)$$

Figure 4.21 plots the von-Mises (equivalent) stress distribution on our aneurysm model. In the bulge region, the magnitude of von-Mises stress is relatively low showed with blue colour. The highest stress around 1.46 MPa is located at the aneurysm neck (red arrow). Jørgen Gjernes Isaksen et al. modelled an aneurysm with a Fung-Type strain energy function and isotropic nonlinear hyperelastic material and found that highest equivalent stress was close to 5×10^5 Pa. The high-stress concentration region was located at the dome and the neck region and impingement forces from the blood flow on the aneurismal wall were found to be largest in the neck (Isaksen et al., 2008). A K Khe et al. compared the stress distributions of one-way and two-way FSI models and results showed that the von-Mises stresses are higher in the one-way FSI model than that in the two-way FSI model (Khe et al., 2016). The maximum von-Mises stress is about 1.59 MPa in the one-way FSI model which is close to the maximum value in our model. However, in the two-way FSI model, the maximum value only half of the that in the one-way FSI model with the similar distribution. This indicates that the modelling method used in this research might overestimate the stress level. Dmiry Ivanov et al. compared the effective stress distribution of large and small aneurysms and the results showed that the stress reached 50000 Pa in the stress concentration region which is 3-4 times higher than that in small aneurysms using the hyperelastic Mooney-Rivlin model (Ivanov et al., 2016).

The stress distributes are similar among varies aneurysm models with different definitions of elastic material properties. However, the magnitudes of the equivalent stress are differently impacted by the material properties. This indicates that in order to achieve a more accurate stress distribution, a better solution is applying the relatively realistic material properties of an aneurysm which depends on the more advanced and specific experimental studies.

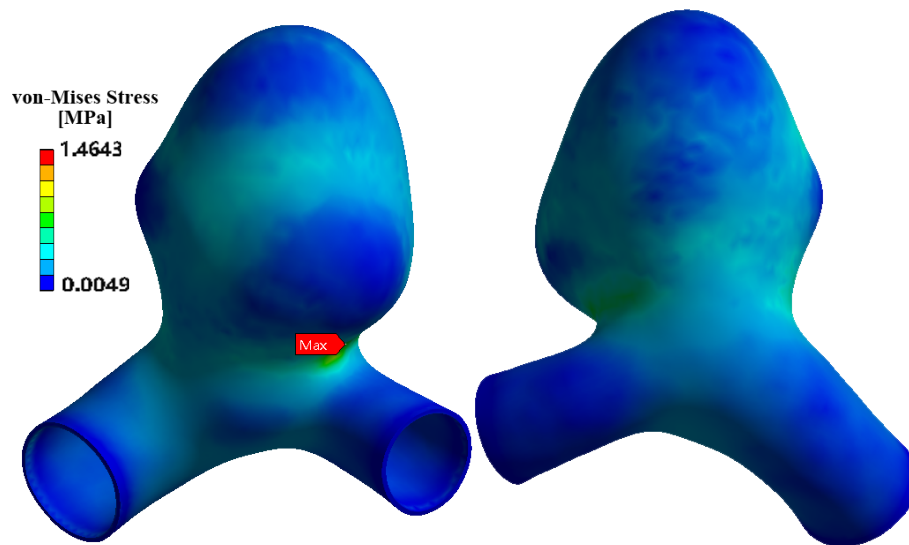


Figure 4.21: Distribution of the von-Mises stress on the aneurysm model. The stress ranges from 0.0049 MPa to 1.4643 MPa and the maximum stress shows around the neck region where has high curvature. Left: front view; Right: back view

4.6.4 Conclusion

In conclusion, this chapter mainly introduced the structural modelling of this intracranial aneurysm model. The first section depicted that the aneurysm part was extracted from the whole geometry and then added thickness to construct a thick-wall model. In the second section, we employed ANSYS to mesh it with the hyperelastic material properties which allow large deformation on each element and applied the boundary conditions. The kernel of this chapter is the third section which focused on the appropriate material properties based on the SEF proposed by Holzapfel in 2000. We did the parameter studies of aneurysm wall and healthy artery wall respectively and defined a transitional region in between to avoid the gigantic gap which could lead to the fast failure of the computational solving process. In terms of the collagen fibres, the SEF to quantify their mechanical behaviour requires the information of collagen alignment, that is to say, the collagen fibre orientation specific on each element. Therefore, the fourth section mainly gave a description of the calculation of the collagen fibre directions following the assumption in the literature. After all the preparation work has been done, we need to implement our modelling setting into ANSYS software and utilize the ANSYS solver to execute the simulation (section 5). In the last section, we plotted and discussed the key results. The single structural modelling of the initial state in our aneurysm model is only one component of the framework in this research, so here we just

discussed the basic displacement, equivalent strain and equivalent stress distribution on our model. The FSG framework of aneurysm G&R will be described in detail in the next chapter which is the key integration content of this thesis.



Aneurysm Evolution Modelling using the p-FSG Framework

5.1 Development of the Patient-Specific FSG (p-FSG) framework	117
5.2 Key Hypotheses in Aneurysm Growth and Remodelling	122
5.3 Illustrative Model: p-FSG linking with steady flow - low WSS	126
5.4 Renovated p-FSG with A Pulsatile Flow Metric - WSSAR	133

Complementary experimental studies and computational modelling are critical methodologies to exploit the sophisticated biomechanical progress of arterial disease which is not able to be achieved in vivo especially for human beings. Physiological condition changes dynamically, the limited experimental technique is in urgent need of assistance in the aspect of computational models. In this research, to simulate the remodelling and growth of intracranial aneurysms, the framework which includes blood flow simulation, hyperelastic modelling of the aneurysm and arterial wall, the variation in aneurysm wall induced by the influence of blood flow and the mechanical regulation of the constituents within the wall, three interactional parts, is designed to mimic the dynamic aneurysm evolution.

Regards to the modelling of aneurysm growth and remodelling, a Fluid-Solid-Growth (FSG) framework applied to a membrane model has already been proposed and modelled the aneurysm growth successfully (Watton, Hill, 2009; Watton et al., 2011). The methodology in this FSG framework is the basement of the novel patient-specific FSG framework developed in this research. This research employed some primary methods in previous FSG model, furthermore, it improves the whole framework via using patient-specific geometry and simulating more biomechanical reactions which will be introduced in detail in the following sections. In clinical perspective, it is difficult to diagnose the aneurysm evolution on the ground that most intracranial aneurysms are asymptomatic and stable. On the other hand, the experimental histological analysis of the aneurysm tissue only can be manipulated after surgeries, which also sets obstacles in verification of computational simulation results as aneurysm evolves. Hence, this research employ clinical patient-specific aneurysm as the original geometry which might be able to provide more practical application to clinicians side. This framework aims to quantify the biomechanical status of the existing aneurysm more accurately and get more understanding of the stability of existing aneurysm: whether it is stable or has the high possibility to rupture.

This chapter will firstly introduce the novel contributions, the work flow of the patient-specific FSG framework as well as the detgrowth and remodelling Then this enhanced patient-specific FSG was implemented and the key results will be presented. Apart from this, we also employed a new pulsatile flow metric-WSSAR which was already introduced in Chapter 3 to improve the growth and remodelling (G& R) algorithm. The novel hypotheses in the current FSG framework might be able to provide more accurate insight to the pathological aneurysm development in reality and to provide more reasonable criteria for diagnositic decisions.

5.1 Development of the Patient-Specific FSG (p-FSG) framework

The rupture of intracranial aneurysms can give rise to severe consequence (e.g. disability or death), but the asymptomatic feature of this disease brings great challenges to clinical detection and treatment. Surgeons mainly rely on the medical images (e.g. CT, MRI) to determine the pathological condition of patients and the following therapy protocols. Meanwhile, people generally will choose to remove the aneurysm in consideration of safety which accompanies with the extremely high cost. An increasing number of intracranial aneurysms is detected with the development of imaging technology, and the annual risk of rupture is around 0.7% (Rinkel et al., 1998). Therefore, the accurate prediction of aneurysm rupture be-

comes a vital issue for both clinicians and patients from the perspective of economics and efficient management. Toward this objective, an enriched and goal-directed patient-specific FSG framework is developed.

Previous studies have modelled the aneurysm growth and remodelling on the basis of healthy arteries using a mathematical membrane model (Watton et al., 2004; Baek et al., 2006; Kroon, Holzapfel, 2008). But membrane models are unable to capture the transmural variation along the radial direction of the walls which elicits the requirement of a more elaborate model with thickness. The patient-specific thick-walled model in this research can shed light on a more detailed and integrated understanding of the intricate changes within the wall during the aneurysm evolution. The aneurysm growth and remodelling mechanisms also focus on two principal parts, elastin and collagen, but also incorporated the degeneration of collagen and more cellular mechanobiological mechanisms.

5.1.1 Improvements in contrast to FSG framework

To differentiate the previous FSG framework, here the novel patient-specific FSG framework is dubbed simply as p-FSG framework. After having a clear understanding of the previous FSG framework, specific to which, this p-FSG framework develops a cascade of improvements in several aspects as follows:

- In the technical application aspect, the structural solver in this p-FSG framework is replaced by the commercial software ANSYS APDL, replacing the previous academic sophisticated scripts. This commercial software has been developed for decades of years and has been used by academics extensively, which offers high possibility and practicality to apply our mathematical model with the help of inbuilt tutorials and the development group.
- As mentioned before, the original aneurysm model in FSG framework is a cylindrical membrane which stands for a healthy artery. But taking into consideration the clinical significance, it is more reasonable to model the aneurysm evolution from the pathological state of the aneurysms in patients. So the foundational aneurysm geometry in the novel p-FSG model is the patient-specific 3D aneurysm which is more conform to the clinical requirements and applications.
- This p-FSG framework compensates for the lack of the endothelium layer in FSG framework which is the most sensitive and functional part in interacting with blood flow. The participation of this significant layer not merely enables the simulations of the complete vascular constitutes, more importantly, provides a pathogenic factor of aneurysm evolution which is as important as the constituents remodelling with the media and adventitia layers. Besides, we use the pulsatile flow metric WSSAR to quantify the mechanical stimuli to endothelial

cells, also link this to collagen degradation function which is not included in the previous FSG framework. The comprehensive methodology will be narrated in Section 5.4.1.

- Finally, to overcome the downsides of the membrane-based FSG framework, the aneurysm in this research is generated as a thick-walled solid model which could provide the possibility of modelling the sophisticated and subtle biological reactions. Based on this perspective, the simulation of molecule transmural transport (e.g. oxygen) could be the further investigation direction.

5.1.2 Workflow of the p-FSG framework

FSG framework has succeeded in integrating the blood flow, structural remodelling and constituents reactions and variations within the arterial wall into a mutually influenced system, transferring the mechanical stimuli to biological responses in a computational aneurysm growth system. Based on ideas and methodologies in the previous FSG framework, the workflow of this p-FSG framework is presented in Fig.5.1, which is similar to the FSG framework. Once we got the surface geometry and the thick-walled model of aneurysm section, the CFD simulation and structural modelling could be solved in ANSYS CFX and ANSYS APDL, respectively. These two components could provide the flow stimuli to endothelial cells and mechanical stimuli to fibroblasts separately, quantifying the mechanical state of vascular cells. Then the biomechanical response of vascular cells were integrated into the G&R algorithm to generate the updated constitutive models for aneurysmal wall. As the update of the tissue properties of the aneurysmal wall, the aneurysm was able to enlarge according to the response to mechanical stimuli. Apart from this, one novelty of this research is we firstly integrated the endothelial mechanobiology into the growth function associated with flow feature. All programs were controlled by Perl which made the framework started with one click and then run automatically.

Fig.5.2 shows a more sophisticated workflow of operating steps and the coupling relationship between different components explicitly.

First of all, the clinical geometry is divided into the aneurysm section and the parent vessels section. The aneurysm section is specifically designed for structural modelling module. And the parent vessel is prepared for connecting with growing aneurysm to run the CFD simulation. This computational cycle begins with a quasi-static structural analysis, representing the equilibrium status under the systolic pressure. Given the pressure as the initial boundary condition, the constitutive models of the aneurysm and the artery have been introduced elaborately in Chapter 4 depicting the Neo-Hookean behaviour of elastineous constituents and nonlinearity and anisotropy of two families of collagen fibres. Through the algorithmic

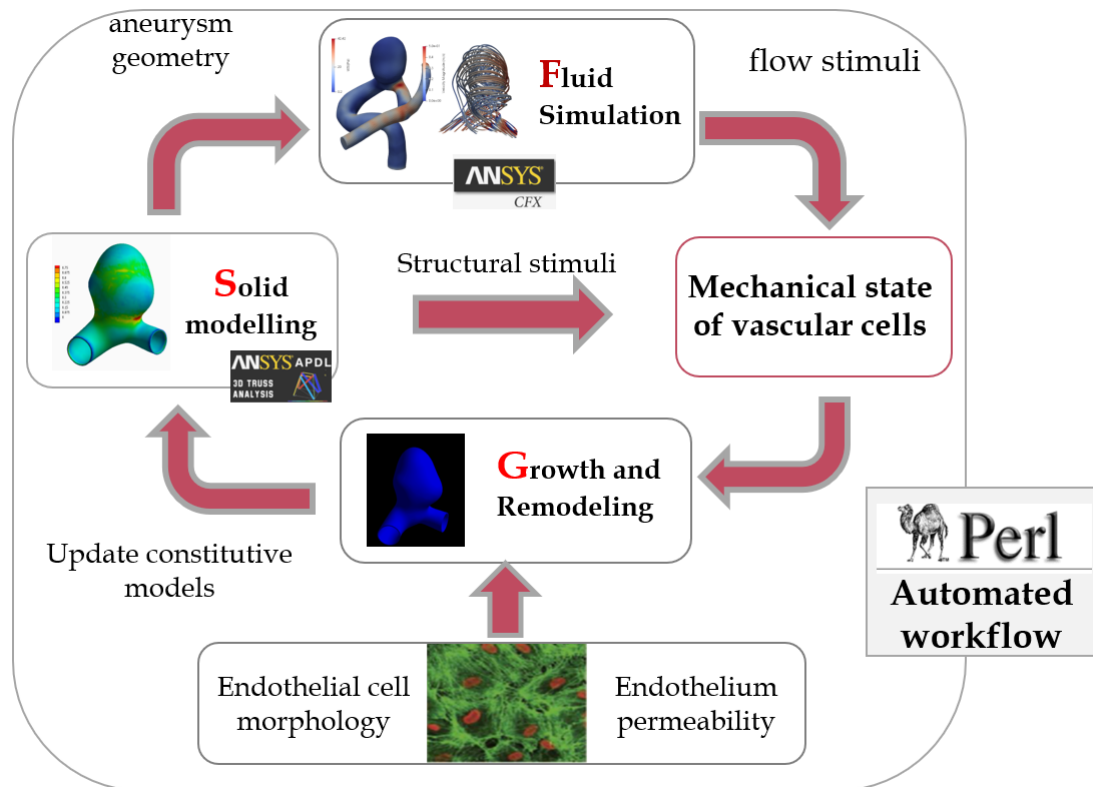


Figure 5.1: Schematic diagram of the p-FSG framework showing the relationship of different components

executant ANSYS APDL, deformation, stress and stretch distribution can be calculated. It is worth to note that the mesh of this thick-walled aneurysm model was kept and the only updates are values of key parameters in the constitutive models over the iterations in the framework. The boundary transections of the aneurysm model are strictly restrained so that the inner surface of the deformed aneurysm geometry precisely connected to boundaries of parent vessels. Based on the displacement result after structural modelling, the inner surface of the aneurysm section could be reconstructed with constant boundaries. Therefore, an integrated arterial geometry with the updated growing aneurysm is imported into ICEM CFD to generate the mesh. In the fluid section, remeshing the geometry is necessary due to the continuously enlarged aneurysm. Then the computational fluid dynamics analysis is conducted in ANSYS CFX with the boundary conditions which are pressure and mass flow rate. The quantitative parameters of haemodynamic environment represented mechanical stimuli to endothelial cells. These stimuli are consolidated into the algorithmic representation of endothelial cells dysfunction and the permeability of the endothelium layer. This could

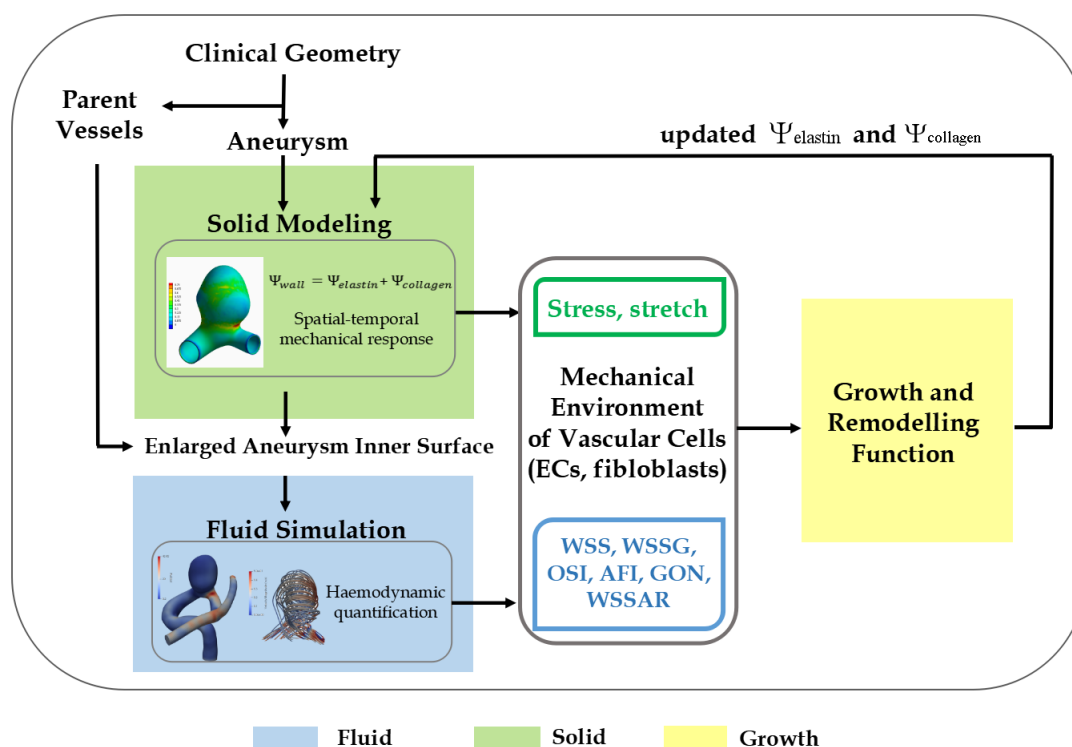


Figure 5.2: Illustrative workflow of the p-FSG framework. Three key components: **solid modelling, Fluid simulation and Growth and Remodelling** are marked with green, blue and yellow boxes.

further impact the elastinous and collagenous constituents and then updates the constitutive models as a result. The solid modelling algorithm then grasps this updated constitutive models to do the structural analysis. Therefore, a computational p-FSG loop is established to develop the growth of an aneurysm.

This p-FSG framework takes the advantages of the previous FSG framework and develops a number of novel techniques and hypotheses as well. This novel p-FSG framework is able to combine the biology and mechanics, realising the connectivity of blood flow, constituents variation within the arterial wall and the mechanical influence of the biomechanical environment of vascular cells. It attempts to characterise the mechanical state of aneurysm wall more accurately and provides the likelihood that predicting the aneurysm development on the basis of the current status of aneurysms in patients. With this application, the clinicians could be given more reliable and quantitative information in diagnosis and treatment planning.

5.2 Key Hypotheses in Aneurysm Growth and Remodelling

Fluid simulation and structural analysis sections have been introduced in Chapter 3 and Chapter 4 respectively. Hence, this section is focusing on the G&R module which consists of the degradation of elastin and the remodelling of collagen. So the next two subsections will introduce the methodology of degradation and remodelling function, which influenced by haemodynamic stimuli and regulated by the deviation of Cauchy stress in the direction of collagen fibres respectively.

5.2.1 Elastin Degradation

In intracranial arteries, only the internal elastic lamina is embedded in the media layer with the disappearance of external elastic lamina (Stehbens, 1972). The half-life of elastin is extremely long (approximately 50 years), which indicates the loss of elastin in aneurysms is owing to tremendous elastolysis rather than inadequate synthesis (Shimizu et al., 2006). During the evolution of intracranial aneurysms, extensive elastin fragmentation and degeneration had been found by histological evidence (the volume fraction of elastin was decreased from 22.7% to 2.4% in aneurysms) (He, Roach, 1994). In spite of the deficit of the remaining elastin in an aneurysm, the degradation function should be still taken into account in the developing of aneurysms. The m^E in healthy parent artery is defined as a normalized value which equals 1. In according to the parameter study in Section 4.3.2, the initial m^E in an aneurysm is set as 0.083. This is in accordance with the study which found that the dry weight of elastin dropped from $12\% \pm 7\%$ to $1\% \pm 1\%$ (Rizzo et al., 1989). After normalized the elastin concentration in healthy artery to 1, the elastin concentration in aneurysms was 0.083 by calculation ($1\%/12\%$). It is worth to note that the m^E represents the elastineous constituents which still have the Neo-Hookean function. This suggests that most broken elastin sheets and fibres segments have lost their mechanical function in bearing the loads, only left a minor proportion still have the Neo-Hookean properties.

To simulate the elastin degradation, the key equation is recalled from Section 2.3.3:

$$m^E(t + \Delta t) = m^E(t)[1 - \mathcal{F}_D \cdot D_{max}^{\Delta t}] \quad (5.2.1)$$

$D_{max}^{\Delta t}$ denotes the maximum degradation rate in each time increment Δt . According to (Watton et al., 2011), $D_{max}^{\Delta t} = 0.75$ which means that at most 75% of the existing elastineous constituents are degraded per year. The \mathcal{F}_D is a function of haemodynamic stimuli characteriz-

ing the degradation rate. The specific definition of \mathcal{F}_D is dependent on the haemodynamic parameter chosen to link with the elastin degradation which will be depicted in detail in the next two sections.

5.2.2 Collagen Remodelling

Wall stress includes the stress on elastineous constituents and on collagen fibres. In accordance to Laplace's Law, which is

$$T = PR \quad (5.2.2)$$

where the T denotes the wall tension, P and R represent the pressure and the radius of the tube respectively. This equation indicates that the wall tension increases with the enlargement of the cylindrical vessel radius to withstand a given internal fluid pressure. Hence in our model, the total stress would continuously increase over the continual enlargement of the aneurysm volume which leads to the inability of the stress going back to and further maintains at the homeostatic level. Hence, the responsibility of maintaining the wall stability is taken by the collagen.

For arteries in the healthy state, the collagen in the adventitia layer performs as the crimple morphology remaining unstretched under the physiological pressure which plays as a protective role. Given an existing aneurysm, the remnant elastin fibres do play a negligible role in bearing the load. Collagen fibres currently undertake the work for maintaining the stress in the aneurysm wall in the way of remodelling. The strain energy function for qualifying the mechanical behaviour of collagen is the central issue in the remodelling process. In healthy arteries, two families of collagen fibres align along preferred directions orderly and helically. Along with the aneurysm growth, the collagen fibres remodel their properties in the aspects of collagen volume, fibre orientation and thickness, as well as the type of fibres. To simulate the fibre orientation in irregular geometry here refers to an aneurysm, the effective collagen fibre direction is postulated highly correlating with the local stress rather than strain (Carver et al., 1991; Taber, Humphrey, 2001). Earlier mentioned in Chapter 4, two families of collagen fibres align with the principal curvature directions (Ma et al., 2007). Baek et al. proposed that the collagen turnover rate is appeared to be modulated by the stress (Baek et al., 2006). The assumption in growth models of arteries is the artery tissue attempts to restore the wall stress to homeostatic (i.e. stable) state via remodelling its stiffness (Hariton et al., 2007). We hypothesise that the mechanical properties of collagen adapt to maintain the stress while the collagen fibres do not re-orientate at this stage.

5.2.2.1 k_2 Remodelling

The collagen remodelling in this p-FSG framework is achieved by updating the constitutive model to adapt the changing mechanical environment, i.e. remodel the k_2 value which used for quantifying the mechanical properties of collagen fibres during aneurysm evolution.

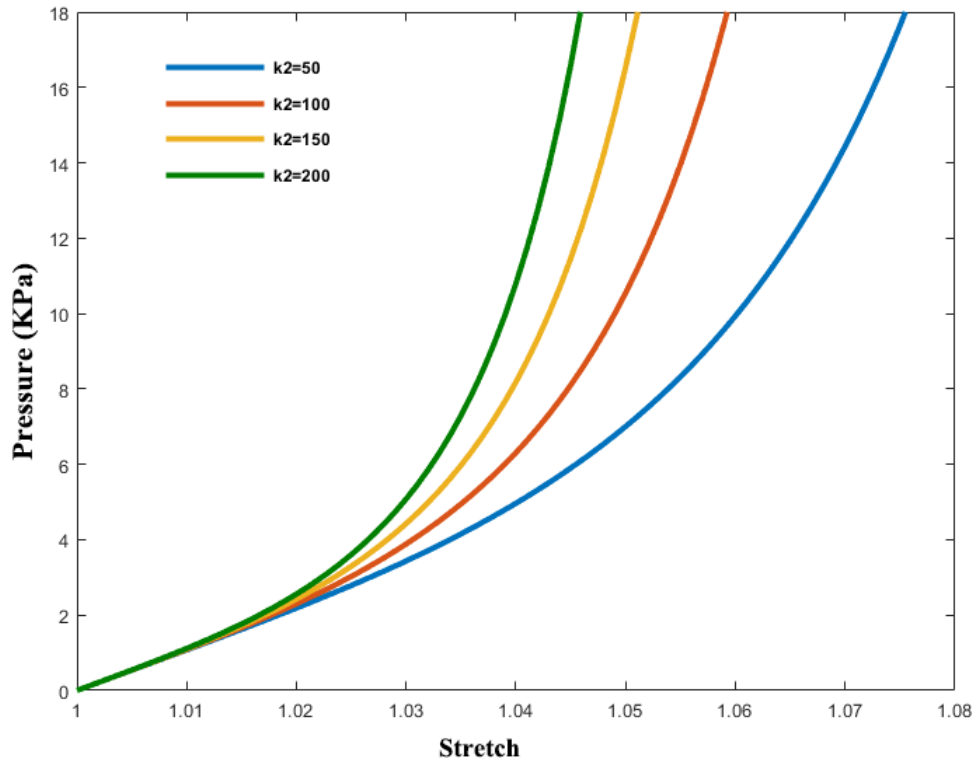


Figure 5.3: Illustration of the influence of k_2 magnitude on pressure-stretch relationship on aneurysm model

As illustrated in Figure 5.3, we investigated the relationship between pressure and stretch through a series of different k_2 values. By reducing the collagen parameter k_2 , the stresses in the collagen fibres would be reduced for a given pressure without changing the reference configuration and the material modulus k_1 of the constituents. Hence, collagen constituents can drag the stress to the homeostatic level through this remodelling process.

The homeostatic stresses from a balanced condition were defined as the stress distribution from the initial structural modelling, which is the stress level for the collagen to maintain through remodelling. Triggered by the elastin degradation, each structural simulation with updated constitutive models can produce different stress distribution which can trigger the collagen remodelling regime. Detailed remodelling mechanism could be expressed as:

$$\frac{dk_2}{dt} = -\gamma \left(\frac{\sigma_C(t) - \sigma_{Ch}}{\sigma_{Ch}} \right) k_2 \quad (5.2.3)$$

$$k_2(t + \delta t) = k_2(t) + \frac{dk_2}{dt} \delta t \quad (5.2.4)$$

where $\sigma_C(t)$ is the current Cauchy stress field; σ_{Ch} is defined as the initial Cauchy stress distribution at homeostatic state ($t=0$). Time increment δt implies a time period relating to the aneurysm growth rate which needs to be confirmed by clinical observation and analysis in the future. Through this remodelling process, the updated k_2 in each element could be incorporated in the next G&R cycle.

5.2.2.2 Implementation of Cauchy Stress with ANSYS

For elements which have large strain capability, it requires the computational ability in terms of the large deformation of elements where the deformation can no longer be neglected. The strain quantity output from Ansys solver is the Hencky (logarithmic) strains in the global coordinate system. A logarithmic or Hencky strain measure is defined as:

$$[\varepsilon] = \ln[U] \quad (5.2.5)$$

where U denotes the right stretch (shape change) matrix. The right Cauchy-Green deformation tensor (Green's deformation tensor) is defined as:

$$[C] = [F]^T [F] \quad (5.2.6)$$

F is the deformation gradient tensor which could be separated into a rotation and a shape change using the right polar decomposition theorem:

$$[F] = [R][U] \quad (5.2.7)$$

Because $[R]^T [R] = [I]$ and $[U]$ is a symmetric tensor, then we can achieve:

$$[C] = [U]^T [R]^T [R] [U] = [U]^2 \quad (5.2.8)$$

But this is only applicable to the non hyperelastic materials. The mesh type we used in this study is SOLID187 and our constitutive model is hyperelastic material. Given the hyperelastic definition of the aneurysm and arterial wall model here, the strain output from ANSYS

is Green-Lagrangian or St.Venant-Lagrangian (E). Hence, right Cauchy-Green deformation tensor could be directly calculated by:

$$[C] = 2[E] + [I] \quad (5.2.9)$$

According to this, the right Cauchy-Green deformation tensor could be calculated from the strain tensor output by ANSYS. Therefore, with the collagen fibre direction matrix calculated in the Section 4.4, invariants I_4 and I_6 can be easily calculated.

$$I_{4,6} = [C] : A_{1,2} = [C] : (a_{01,02} \otimes a_{01,02}) \quad (5.2.10)$$

where a_{01}, a_{02} are unit vectors in the directions of two families of collagen fibres. Note that the invariants I_4 and I_6 are the squares of the stretches (λ^C) in the directions of the two families of collagen fibers and therefore have a clear physical interpretation, i.e. $\lambda_{4,6}^C = \sqrt{I_{4,6}}$ (Holzapfel et al., 2000). Then the Cauchy Stress can be expressed by $I_{4,6}$:

$$\sigma_C = \lambda_C \frac{\partial \Psi_C}{\partial \lambda_C} = 2I_{4,6} \cdot (I_{4,6} - 1) \cdot k_1 \cdot \exp[k_2 \cdot (I_{4,6} - 1)^2] \quad (5.2.11)$$

5.3 Illustrative Model: p-FSG linking with steady flow - low WSS

To fulfil the p-FSG framework, we firstly built up an illustrative model following the idea in the previous FSG model. The haemodynamic environment is a significant factor in the course of aneurysm evolution which has been discussed in Section 3.3.1. Also, referring to the G&R mechanism in FSG framework, the elastin degradation is triggered by the low WSS which induce the further collagen growth and remodelling. Following this idea, the first step of implementing this p-FSG framework is the adoption of low WSS as the haemodynamic stimuli. As to the collagen remodelling part, it has been elaborately introduced in the last section, so here we just specified the specific definition of \mathcal{F}_D in terms of WSS.

5.3.1 Contribution of low WSS to Aneurysm Growth

Hemodynamics studies have found that growing regions occurred in regions with low WSS (Boussel et al., 2008; Acevedo-Bolton et al., 2006). For implementation of the degradation function with low WSS, and the WSS-related function \mathcal{F}_D as a weight factor, the definition has been introduced in equation 2.3.3.

Elastin degrades at a maximal speed at a lower WSS scope which is defined as 0 to τ_X . When WSS magnitude larger than τ_{Crit} , the location has no elastin degradation ($\mathcal{F}_D = 0$). In between, the degradation function was presumed a quadratic form showed in the above equation. And when the spatial WSS is lower than τ_X , it indicated this region has the maximum degradation rate ($\mathcal{F}_D = 1$). The definition of low WSS has not achieved a well acceptable value no matter in the CFD analysis and experimental studies. Moreover, the value of τ_X and τ_{Crit} in different studies employed different levels ranging from 0.5 Pa to 4.59 Pa and 2 Pa to 9.2 Pa respectively (Watton et al., 2011; Selimovic et al., 2014). The magnitudes of τ_X and τ_{Crit} should be specified by the spatial WSS distribution on patient-specific geometry in this case. Referring to the WSS distribution showed in the CFD simulation results, here τ_X and τ_{Crit} were set as 0.5 Pa and 4 Pa respectively. The functional relationship between the $\mathcal{F}_D(\tau)$ and WSS was illustrated in Figure 5.4.

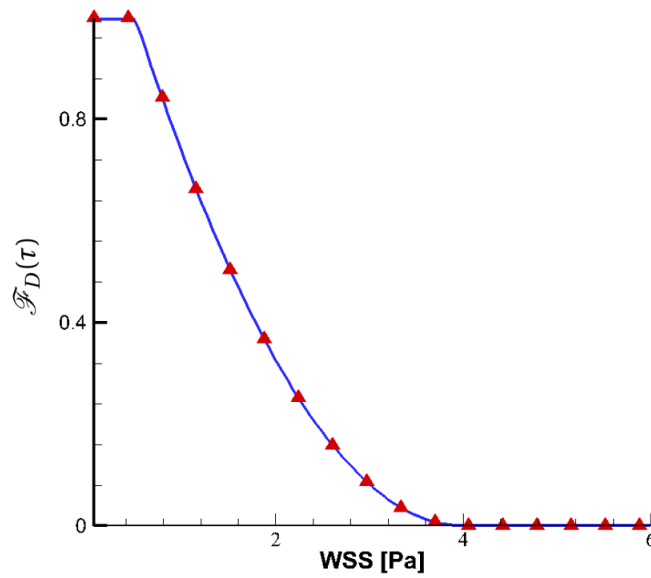


Figure 5.4: Elastin degradation function $\mathcal{F}_D(\tau)$ utilising the values $\tau_{Crit} = 4$ Pa and $\tau_X = 0.5$ Pa

Related to the mass density of elastineous constituents, the Equation 5.2.1 could be written as:

$$m^E(t + \Delta t) = m^E(t)[1 - \mathcal{F}_D(\tau(t)) \cdot D_{max}^{\Delta t}] \quad (5.3.1)$$

Hence, the function between the haemodynamic environment and the elastineous constituents changing is formulated which enables the aneurysm to further develop in our model.

5.3.2 Results and Discussion

Fluid simulation, structural remodelling and G&R functions have been depicted above, this section integrates these three parts and focuses on the implementation of our framework on a patient-specific aneurysm.

First of all, the clinical geometry was constructed from the screening information. Then it was partitioned into two parts: parent vessel and aneurysm which used to do the CFD and structural simulation respectively. The aneurysm model was given a thickness and corresponding boundary condition with justified material parameters, the stress, strain, deformation distribution could be output for further analysis. Due to the deformation, the inner surface of the aneurysm model changed. Hence, the updated geometry of the aneurysm inner surface was adopted to do the CFD simulation. The relative index, i.e. WSS, could be linked to the mechanism of elastin degradation. This function adjusted the total strain energy function of the tissue by changing the concentration of elastin (m^E) which induce a different spatial stress distribution on the second loop. The variation of the stress leads to the occurrence of collagen remodelling, in other words, the collagen remodelling began at the third loop until the model reached an equilibrium state.

Figure 5.5 picturized the material parameters of elastin (m^E) and collagen (k_1, k_E) in the initial state listed in Table 4.2 which has verified in Section 4.3.2.

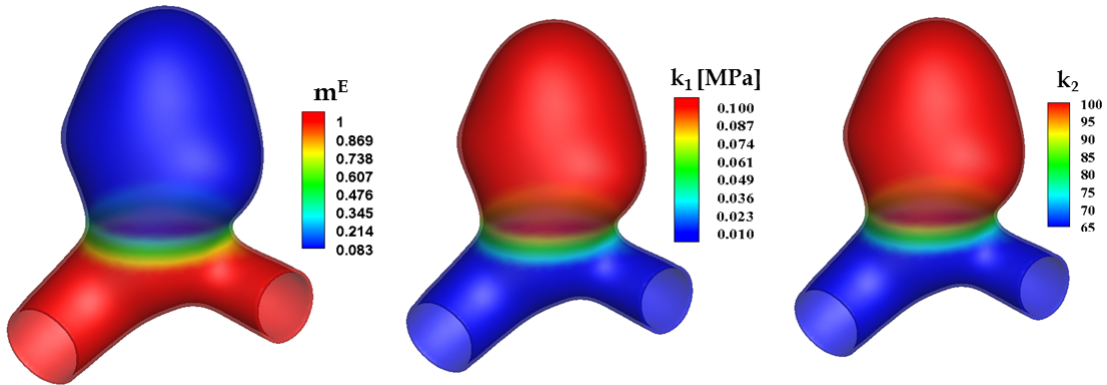


Figure 5.5: Initial distributions of material parameters of the structural model

The total strain energy function is the sum of strain energy function of elastin and collagen (Equation 4.3.1, 6.3.4), expressed as

$$\begin{aligned}\Psi &= \Psi_E + \Psi_C \\ &= \frac{1}{2} m^E \times k^E (I_1 - 3) + \frac{k_1}{2k_2} \sum_{i=4,6} \{ \exp[k_2 (I_i - 1)^2] - 1 \}\end{aligned}\quad (5.3.2)$$

The elastin concentration in an aneurysm is much lower than in normal artery, and the linear transition locates on the neck region. Similarity, the collagen in an aneurysm is remarkably stiffer which could be paraphrased as the values of k_1 , k_2 should be larger than that in parent vessel. The physiological time domain for the aneurysm evolution is simulated for 18 time steps ($t=0 \sim 18$).

5.3.2.1 Deformation as Aneurysm Growth

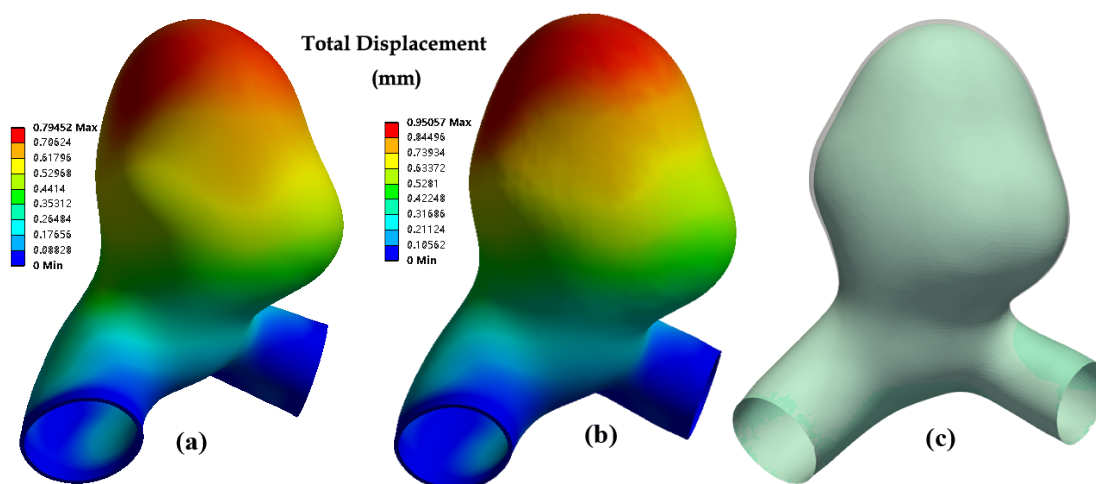


Figure 5.6: Displacement distribution through the thickness of aneurysm model (a-b) and the corresponding inner surfaces of the growing aneurysms (c) at $t=0$ and $t=18$ (green: $t=0$; transparent: $t=18$)

The original aneurysm model deformed derived from pressurization at systolic peak we applied at $t=0$. Because of the fixation of two boundaries, i.e. displacement=0, which are aiming for connecting the parent vessels, the displacement is gradually increasing from two boundaries to the top. Figure 5.6 represents the displacement distribution on aneurysm geometries at $t=0$ (a) and $t=18$ (b). As shown in the legends, the maximum displacement is 0.79452 mm at $t=0$ while it reaches 0.95057 mm at the final time step, approximate 1.2 fold higher but keeps the same distributional characteristic.

To clearly show the aneurysm growth, we also plotted the inner surface of the enlarged aneurysm at $t=0$ and $t=18$ respectively in Figure 5.13(c) where shows a slight difference regarding the enlargement extent. More specifically, the volume of our aneurysm models at different time steps was calculated. The volume of the original aneurysm geometry is 406.77 mm^3 (V_0); at $t=0$, the model is enlarged to 496.765 mm^3 due to the pressurization (V_1); at $t=18$, the volume grows to 514.92 mm^3 resulted from the growth and remodelling of the aneurysm wall (V_2). Hence, the actual growth volume should exclude the enlargement from pressurization, i.e. $V_2 - V_1$, is 18.15 mm^3 .

5.3.2.2 Variation of WSS Distribution

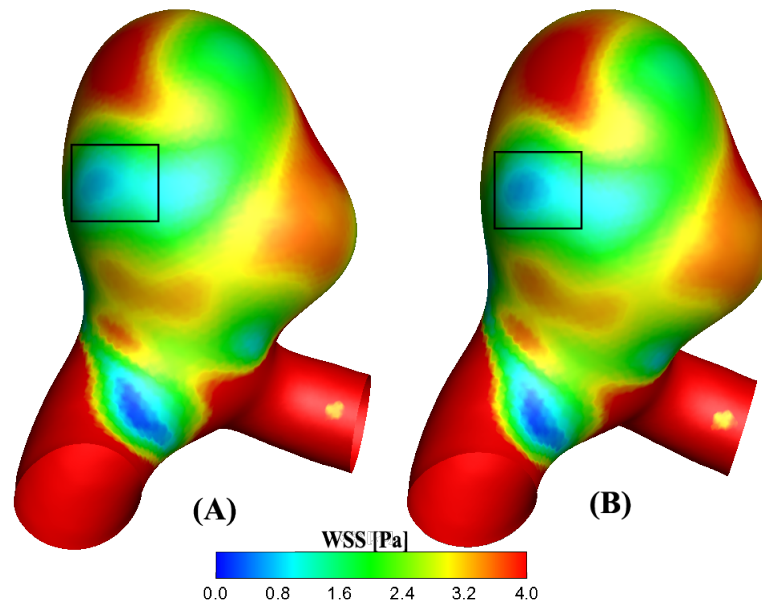


Figure 5.7: WSS spatial distribution on the inner surface of aneurysm model at $t=0$ (A) and $t=18$ (B).

Figure 5.7 shows the spatial WSS distribution localised on aneurysm model where relates to the G&R algorithm. It shows hardly a noticeable difference between the initial and final equilibrium state, which caused by the subtle enlargement after the growth and remodelling mechanism. The colour map was limited to 0-4 Pa to visualize the low WSS location. As Figure 5.7 showed, the distribution of WSS in the last state is analogous to that at the beginning. Only a small region showing noticeable decreasing WSS is presented in the aneurysm which is labelled with a rectangular box. This WSS decline is owing to the enlarged aneurysm which

generated a further dilation at that site. Low WSS is generally derived from the adverse flow condition which implies there is a high possibility of further growth in that region.

5.3.2.3 Evolution of WSS and m^E

Recall the elastin degradation function in equation 5.2.1 and 2.3.3, τ_X and τ_{Crit} was set as 0.5 and 4 Pa respectively. In the region of WSS lower than 0.5 Pa, elastin degrades at the highest speed while if WSS magnitude is larger than 4 Pa, there is no elastin degradation occurs. Within this scope, elastin degrades abiding the algorithm expressed in equation 2.3.3. The consequent elastin concentration distribution is plotted in Figure 5.8 below. Note that the elastin degradation only occurs in the aneurysm and transitional region. The colour map is restricted to the maximum number equals to 0.083 which is the initial mass density in the aneurysm, in order to explicitly present the change in the aneurysm part.

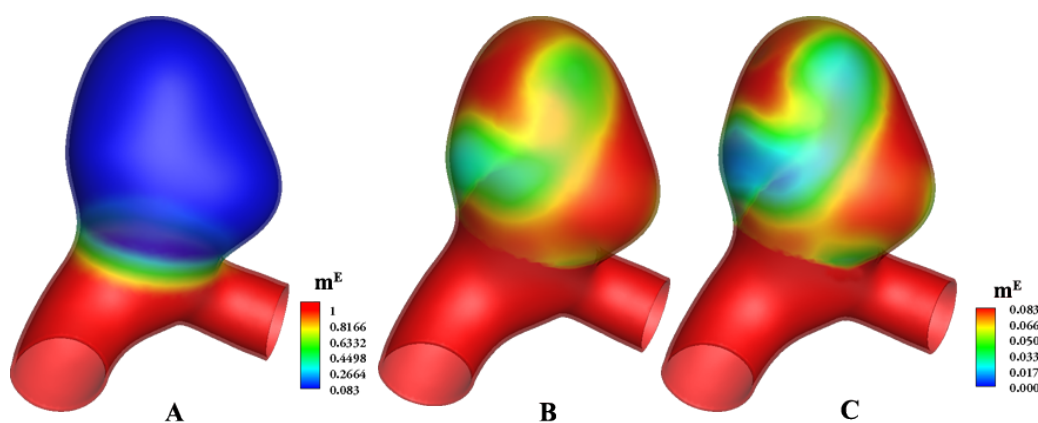


Figure 5.8: Spatial evolution of normalised mass density of elastin in the aneurysm model at $t = 0, 9, 18$. (A, B, C)

Compared to the WSS distribution, it is clear that lower WSS region leads to less elastin mass density which is consistent with the elastin degradation function we proposed. Even though the existing elastin mass density is already indeed low, it can degrade obviously with the influence of low WSS (Figure 5.9) which reach up to 95.63% at the final state. This result could provide a more accurate elastin distribution to structural analysis, which helps the quantification of aneurysm state more precisely.

5.3.2.4 Evolution of k_2

Figure 5.10 illustrates the evolution of k_2 distribution in the aneurysm geometry at $t = 0, 9, 18$. In section 5.2.2, we propose that the k_2 remodelling is linked to local mechanical response

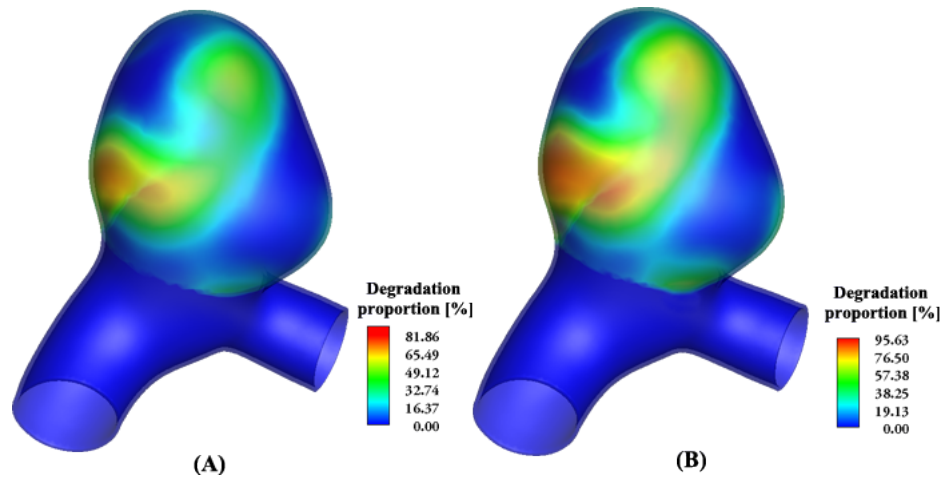


Figure 5.9: Elastin degradation proportion distributes on aneurysm model at t=9 (A) and t=18 (B)

(i.e. Cauchy stress in the direction of collagen fibres) of each element. During k_2 remodelling process, the non-uniform response in aneurysm region is more explicit. Considering the low WSS region showed in Figure 5.7, more collagen adaption happened in the corresponding region which reveals the collaboration of elastin and collagen to maintain the stability of the aneurysm wall.

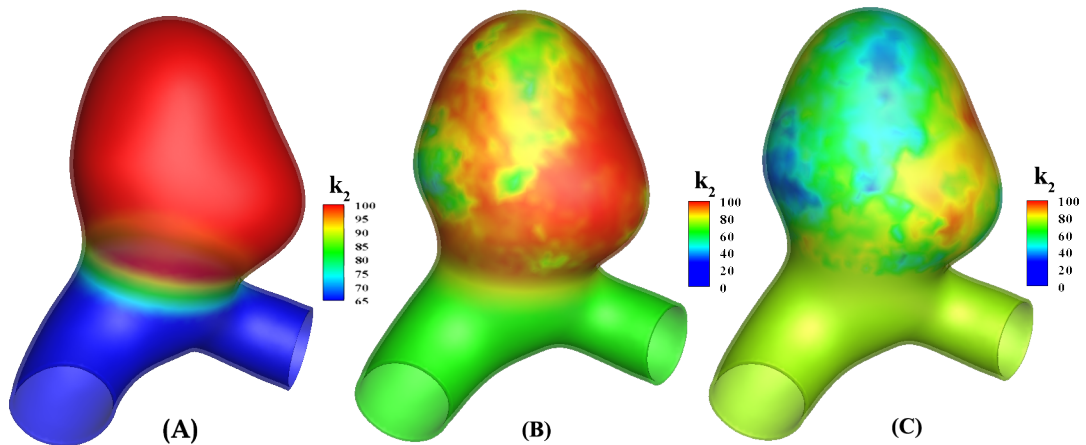


Figure 5.10: Spatial evolution of collagen parameter k_2 in the aneurysm geometry at t = 0, 9, 18. (A, B, C)

5.4 Renovated p-FSG with A Pulsatile Flow Metric - WSSAR

5.4.1 Motivation: Key Pathological Contributions to Aneurysm Continuous Growth and Rupture

Enormous histological evidence has shown that the elastin sheet is broken into fractured fragments and the number of collagen fibres increases with higher stiffness in the aneurysms. This means that the structure of aneurysms mainly consists collagen which performs high stiffness leading to low distensibility of the aneurysm. How can this stiff aneurysm continue to enlarge and rupture eventually? The answer to this question is the main investigation point in this research. This section will focus on the pathological process in the period of aneurysm enlargement and rupture which could provide insight into our growth and remodelling mechanism.

In order to understand the function of elastineous constituents and collagen respectively in the period of aneurysm inception, further growth and rupture, the elastase and collagenase have been extensively used in experimental researches. In 1984, Philip B. Dobrin et al. conducted an experiment study using the purified elastase and collagenase in cylindrical segments of different types of arteries, including carotid arteries and iliac arteries (Dobrin et al., 1984). When they only imposed the purified elastase, arteries only produced slight dilation and no rupture occurred. But all specimen arteries treated with pure collagenase ruptured. In the course of the elastase treatment, the vessels exhibited decreased compliance which due to the elastin degradation and the gradual recruitment of collagen fibres. In the collagenase case, in contrast, the slope of pressure-diameter curve elevated after the treatment which indicated that the compliance of vessels increased. Moreover, all vessels leaked without control or ruptured bluntly. Then they treated the vessels with elastase and collagenous sequentially and then produced marked dilation compared to the isolate treatments and all ruptured as well. This combined treatment imitated the principal pathological process of aneurysm production which indicates that the further dilation and rupture of aneurysms is attributed to collagen rather than elastin. Suzanne Menashi et al. also pointed out that in the unruptured aneurysms, there was no sign of increased collagenase activities but it showed in the ruptured aneurysms (Menashi et al., 1987). In 1994, the research group of Philip B. Dobrin imposing the elastase and collagenase on the autopsy aneurysms and healthy arteries as control indicated that the degradation of arterial elastin only produced moderate dilation (6%-10% at 100 mmHg) accompanied with declined distensibility. And the elongation and

tortuosity of the aneurysm were also regarded as a result from elastin degradation (Dobrin, Mrkvicka, 1994). Moreover, the treatment of collagenase produced the larger dilation (10%-23% at 100 mmHg) and ruptured with elevated distensibility. This research suggested the increased collagenolytic activity or the decreased inhibition to this activity which provided an insight into the association between collagen degradation and aneurysm growth.

In the Section 3.4, we have investigated the contribution of endothelium permeability which is quantified by WSSAR to aneurysm evolution. More specifically, here we will focus on the mechanism of how permeability impact the collagen properties and the related biological activities because collageneous constituents are the determinative reason for an aneurysm further enlargement and rupture, which has been proved by experimental studies aforementioned above. Even though the intricate pathological mechanisms of intracranial aneurysm growth and rupture have not been completely elucidated, the intensified inflammation activities are resulting in the acceleration of the ECM remodelling and protein degeneration by the elevated endothelium dysfunction and permeability (Chalouhi et al., 2012). From the perspective of collagen distribution, type I collagen is confined in tunica adventitia and fibronectin is restricted in tunica media in the healthy arterial wall. Nevertheless, they disperse through the wall of aneurysm (Austin et al., 1993). The type III and IV collagen expressed less in aneurysm wall compared to healthy arteries (Kilic et al., 2005). The collagen mass is regulated by two pathways: degradation and biosynthesis, the former activity is primarily executed by collagenases. The matrix metalloproteinases (MMP) family is the main mediators of ECM remodelling, especially the ruin of collageneous and elastinous constituents (Matrisian, 1990). In an aneurysm, levels of collagenases and elastases were found increased predominantly, and the major collagenase types seem to be MMP-2 and MMP-9 firstly proposed by Kim et al. (Gaetani et al., 1999; Bruno et al., 1998; Kim et al., 1997). These two types of MMP are produced by vascular cells, including smooth muscle cells, endothelial cells and fibroblasts, and inflammatory cells, like lymphocytes, lymphocyte and especially macrophages (Penn et al., 2014). Leukocyte and macrophage infiltration are likely to associate with the loss or destroy of smooth muscle cells and collagen, and it was observed in both unruptured and much more in ruptured aneurysms (Kataoka et al., 1999; Frosen et al., 2004). Studies showed that macrophage infiltration results in the secretion of both MMP-2 and MMP-9 in an aneurysmal wall which demonstrated that the increased inflammatory activities are contributing to the intracranial aneurysm progression (Aoki et al., 2007a; Ishibashi et al., 2010). As to the other pathway, collagen biosynthesis, it was reportedly downregulated at the transcriptional level by the inflammatory cytokines, i.e. tumour necrosis factor- α (TNF- α) and interleukin-1 β (IL-1 β) (Aoki et al., 2009c). Takemura et al. also found the overexpression of MMP-1 besides the MMP-2 and MMP-9 in aneurysm walls

(Takemura et al., 2010). MMP-1, also known as an interstitial collagenase, involves the ECM remodelling and precisely, the degeneration of types I, II, and III collagen. MMP-1 expression is intensified by the NF- κ B with the subsequent macrophage infiltration and decreased collagen biosynthesis (Aoki et al., 2011a). NF- κ B is activated in endothelial cells and was also observed overexpressed in intracranial aneurysm walls (Aoki et al., 2007c). Therefore, there is another pathway to downregulate the biosynthesis of collagen from the aspect of inflammation.

5.4.2 Hypothesis of Aneurysm Growth with Respect to WSSAR

According to the above knowledge and research results, it is reasonable to propose the hypothesis: High permeability of endothelial layer contributes to the inflammatory cells infiltration, which leads to varies of signal pathways and a cascade of biological reactions resulting in the intensification of collagen degradation and weakening of collagen biosynthesis. The endothelium permeability is determined by the localized morphology of endothelial cells closely related and sensitive to flow patterns which could be quantified by a novel flow metric - WSSAR.

5.4.2.1 Elastineous Constituents Degradation with High WSSAR

Even though only a few elastineous constituents remain in the aneurysm tissue, they still contribute to the elasticity of the aneurysm wall. With the evolving of aneurysms, these constituents continuously degrade under the haemodynamic influence. Similar to degradation with low WSS, here we also defined two thresholds representing the degradation levels, i.e. $WSSAR_{crit}$ and $WSSAR_{max}$. The degradation level factor, denoted as $\mathcal{F}_{D(WSSAR)}^E$ is defined as:

$$\mathcal{F}_{D(WSSAR)}^E(t) = \begin{cases} 0, & WSSAR(t) \leq WSSAR_{crit} \\ \left(\frac{WSSAR(t) - WSSAR_{crit}}{WSSAR_{max} - WSSAR_{crit}} \right)^2, & WSSAR_{crit} < WSSAR(t) < WSSAR_{max} \\ 1, & WSSAR(t) \geq WSSAR_{max} \end{cases} \quad (5.4.1)$$

The numerical choice of $WSSAR_{crit}$ and $WSSAR_{max}$ is highly dependent on the endothelial cells morphology. As mentioned in Section 3.4.2, the endothelial cells were assumed as irregular shape in the range of 0.75-1. Therefore, the remarked high WSSAR region (above 0.75) hypothesized representing irregular morphology of endothelial cells is defined as having the highest degradation level. Then the $WSSAR_{max}$ is supposed to be 0.75 and when

WSSAR is above 0.75, the $\mathcal{F}_{D(WSSAR)}^E = 1$. Figure 3.24 clearly showed that the WSSAR in the healthy artery is below 0.5. So in the range of WSSAR between 0-0.5 where the $\mathcal{F}_{D(WSSAR)}^E = 0$, we assume there is no degradation of elastine constituents occurs. Endothelial cells could be regarded as having the ability to maintain their normal functions in this relatively slight disturbed flow within this range. Hence the $WSSAR_{crit}$ is defined as 0.5. Between these two key thresholds (i.e. 0.5-0.75), we assume a linear relationship to quantify the degradation level concerning the WSSAR value between 0.5 and 0.75 ($0 < \mathcal{F}_{D(WSSAR)}^E < 1$).

To demonstrate this $\mathcal{F}_{D(WSSAR)}^E$ more visually explicit, an illustrative curve showed in Fig5.11 represents the relationship between $\mathcal{F}_{D(WSSAR)}^E$ and WSSAR value.

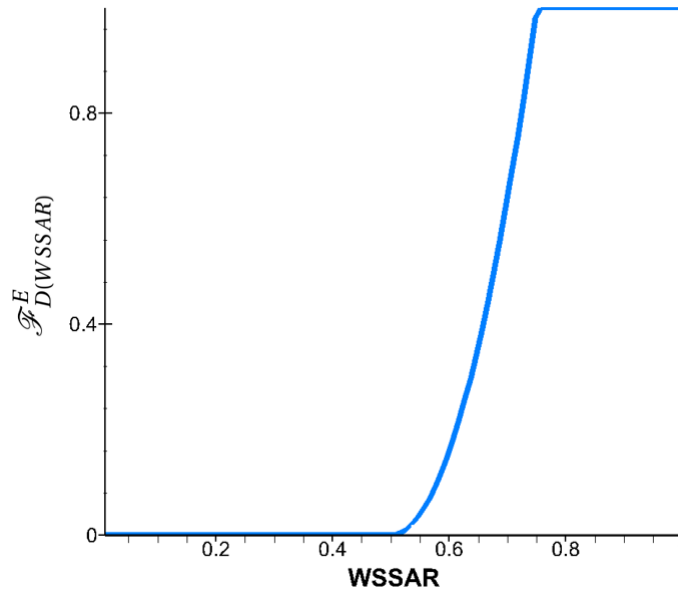


Figure 5.11: Elastine constituents degradation function $\mathcal{F}_{D(WSSAR)}^E$ varies with WSSAR ($WSSAR_{crit} = 0.5$ and $WSSAR_{max} = 0.75$).

The mass density m^E , which could also be named as concentration, is a function of $\mathcal{F}_{D(WSSAR)}^E$. The definition of m^E is the same as the m^E in Section 5.3.1. When the elastine constituents degrade in the aneurysm, the mass density will vary following the below function:

$$m^E(t + \Delta t) = m^E(t)[1 - \mathcal{F}_{D(WSSAR)}^E D_{max}^{\Delta t}] \quad (5.4.2)$$

in which the $D_{max}^{\Delta t}$ means the maximum degrading proportion of elastine constituents for each time and the Δt denotes the time increment between each elastine degradation with the unit year. Here the $D_{max}^{\Delta t} = 0.25$ indicates that at most 25% of the elastine can be

degraded per year.

5.4.2.2 Collagen Degradation

Besides the degradation of elastineous constitutes which only plays a tiny role in aneurysm growth, the main pathological evolution is collagen adaptation. Compared to the p-FSG linking with low WSS, the collagen adaptation here also considered the collagen degradation process regulated by the mechanical stimuli from blood flow. The contents below will introduce the implementation of collagen degradation and remodelling in order.

5.4.2.2.1 Collagen Degradation Linking to High WSSAR

Based on the hypothesis introduced in above sections, we also incorporated the collagen degradation into our G&R mechanism. In the collagen degradation function, we associate the m_C to WSSAR which is analogous to elastineous constituents degradation. The important issue in this section is how to define the initial mass density of collagen in the aneurysm. The concentration of collagen was reported decreased compared with the normal artery (Sumner, 1970). One research found that the collagen proportion elevated in the media layer of the aneurysmal aorta from 62% to 84% as the result of elastin degradation (Menashi et al., 1987). Another study stated that the collagen in abdominal aneurysms increased from $24\% \pm 5\%$ to $37\% \pm 16\%$, but pointed out that collagen type I and III as well as their ratio did not show a deficiency in the aneurysms (Rizzo et al., 1989). Hence, the collagen concentration in aneurysms might be decreased, unchanged or raised which leads to a dilemma in the determination of initial collagen concentration of our aneurysm model. The rational explanation for this phenomenon could be the collagen increased with the elastin degradation in the early stage of aneurysm formation. As the aneurysm further evolves, the collagen fibres start to degrade leading to a lower concentration. So in this research, we suppose the concentration of collagen fibres in aneurysm part is the same as that in parent arteries which in a middle stage of the variation during the aneurysm development. The more accurate definition of this concentration needs the help from the corresponding experiment studies in the future.

Here we presume a maximum degradation portion of collagen per year, named as D_{max}^C to distinguish the degradation factor of elastineous constituents which is denoted as D_{max} . And we assume the maximum degradation proportion $D_{max}^C = 0.1$ which means the greatest degradation of existing collagen fibres is 10% per year. So the updated collagen concentration could be expressed as follows:

$$m^C(t + \Delta t) = m^C(t)[1 - \mathcal{F}_{D(WSSAR)}^C D_{max}^C \Delta t] \quad (5.4.3)$$

where the $\mathcal{F}_{D(WSSAR)}^C$ is analogous to the one used in the degradation of elastineous constituents ($\mathcal{F}_{D(WSSAR)}^E$) with a slight difference.

$$\mathcal{F}_{D(WSSAR)}^C(t) = \begin{cases} 0, & WSSAR(t) \leq WSSAR_{crit} \\ \left(\frac{WSSAR(t) - WSSAR_{crit}}{WSSAR_{max} - WSSAR_{crit}} \right), & WSSAR_{crit} < WSSAR(t) < WSSAR_{max} \\ 1, & WSSAR(t) \geq WSSAR_{max} \end{cases} \quad (5.4.4)$$

Here we specify the changing rate of m^C within the range from $WSSAR_{crit}$ to $WSSAR_{max}$ is linear showed in the Figure 5.12 (pink).

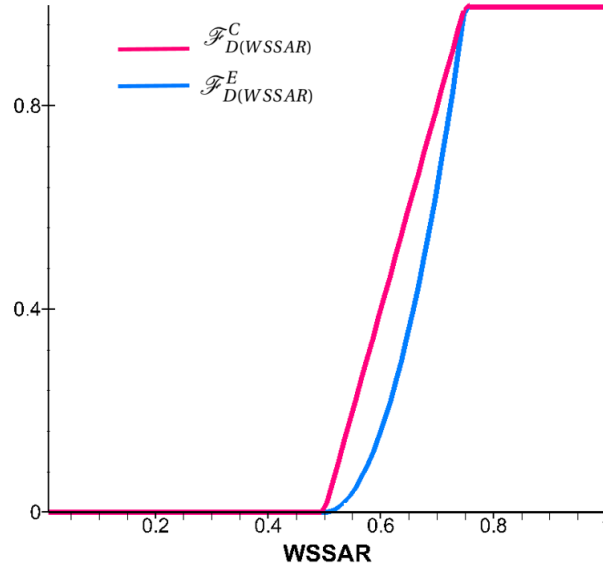


Figure 5.12: Comparison of elastineous constituents degradation function $\mathcal{F}_{D(WSSAR)}^E$ and $\mathcal{F}_{D(WSSAR)}^C$ varies with WSSAR ($WSSAR_{crit} = 0.5$ and $WSSAR_{max} = 0.75$).

5.4.3 Results

Compared to the p-FSG linking with low WSS, the G&R in this section also introduced a novel flow metric, i.e. WSSAR, which is able to quantify the flow bidirectionality via the consideration of both WSS magnitude and direction. The elastineous degradation was linked with

WSSAR to replace the low WSS and the collagen degradation mechanism was also included in the G&R algorithm. The key variations over the G&R process are the mass density of elastin constituents (m^E), collagen constituents (m^C) and the mechanical behaviour of collagen fibres (k_2).

To the end of this p-FSG framework, the structural modelling, fluid simulation and the G&R algorithm were iterated 46 time steps where one time step indicates a certain period of time. As to the specific time for each interval, it is dependent on the verification from the large-scale clinical follow-up data to define a reasonable and applicable time period. Hence, in the following sections, we just use t to indicate the number of the time step.

5.4.3.1 Deformation as the Aneurysm Growth

The original aneurysm model deformed derived from pressurization at systolic peak we applied at $t=0$. Because of the fixation of two boundaries, i.e. displacement=0, which are aiming for connecting the parent vessels, the displacement is gradually increasing from two boundaries to the top. Figure 5.13 represents the displacement distribution on aneurysm geometries at $t=0$ (a) and $t=46$ (b). As shown in the legends, the maximum displacement is 0.79452 mm at $t=0$ while it reaches 1.2339 mm at the final time step, approximate 1.55 fold higher but keeps the same distributional characteristic.

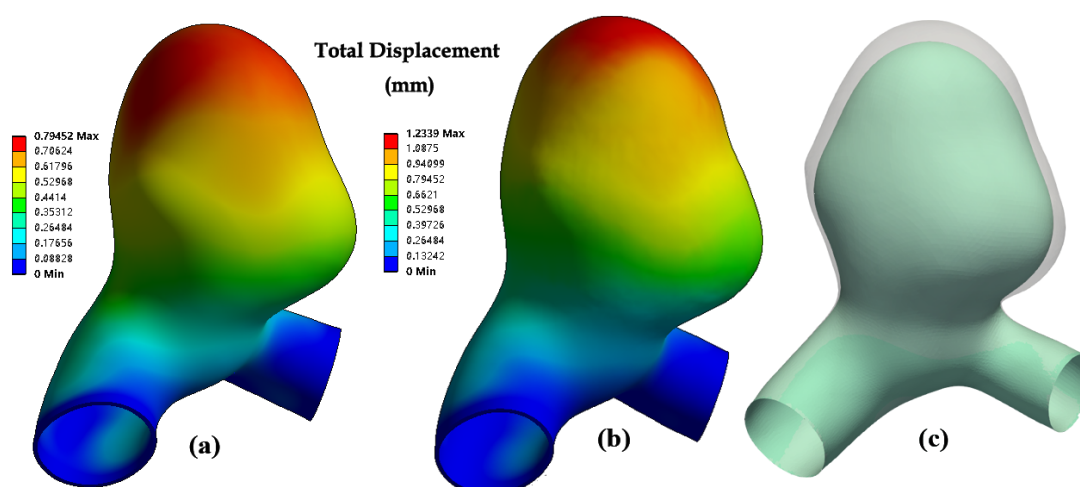


Figure 5.13: Total displacement distributions on the aneurysm model (a,b) and the corresponding enlarged inner surface showed with translucent contour (c) at $t=0$ and $t=46$ respectively. Green: $t=0$; Transparent: $t=46$.

To clearly show the aneurysm growth, we also plotted the inner surface of the enlarged aneurysm at $t=0$ (a) and $t=46$ (b) respectively in Figure 5.13 where shows distinctive difference

in terms of the enlargement extent. More specifically, the volume of our aneurysm models at different time steps were calculated. The volume of the original aneurysm geometry is 406.77 mm^3 (V_0); at $t=0$, the model is enlarged to 496.765 mm^3 due to the pressurization (V_1); at $t=46$, the volume grows to 542.92 mm^3 resulted from the growth and remodelling of the aneurysm wall (V_2). Hence, the actual growth volume should exclude the enlargement from pressurization, i.e. V_2-V_1 , is 46.15 mm^3 .

5.4.3.2 Variation of WSSAR distribution

The haemodynamic environment in an aneurysm varies with the enlargement of aneurysm geometry. Figure 5.14 plotted the WSSAR distribution at $t=0$ (A) and $t=46$ (B) representing the similar distributions. The colour map is limited to 0.75 to 1 because we hypothesised that the endothelial cells transform to irregular shape leading to a diverse permeability condition.

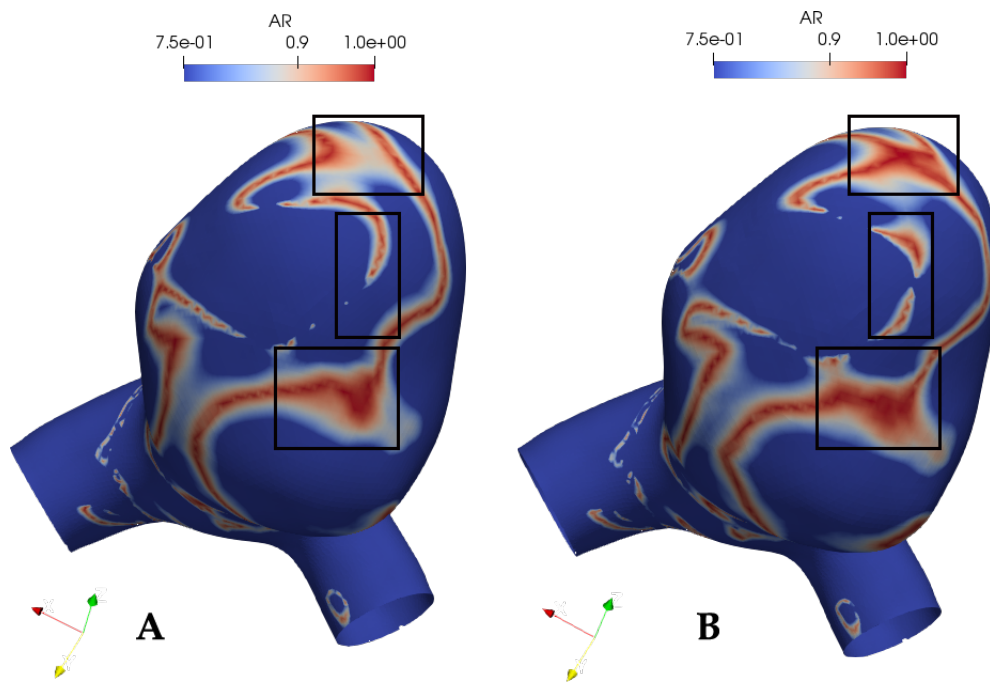


Figure 5.14: WSSAR distribution on aneurysm models at $t=0$ (A) and $t=46$ (B) with rectangular boxes where shows relatively recognizable variation.

The distribution of WSSAR between the initial state and the final aneurysm state is generally similar. However, they still show a recognisable difference and three regions with relatively apparent variation were picked out by rectangular boxes. It seems that the high WSSAR region within the boxes moves to a more concentrated area especially on the top region.

Moreover, we calculated the points number in different WSSAR levels listed in Table 5.1 to compare the haemodynamic environment in more detail.

Table 5.1: Summery of WSSAR in different levels at t=0 and t=46

WSSAR	0.5-0.6	0.6-0.7	0.7-0.8	0.8-0.9	0.9-1	sum
T=0	1986	1798	1640	1475	1192	8091
T=23	1809	1799	1646	1511	1216	7981
T=46	1820	1719	1655	1414	1219	7827

The adverse WSSAR was defined to start from 0.5 in the G&R algorithm, and the span from 0.5 to 0.75 represented a transitional section of endothelial cells from elongated morphology to an irregular shape. Therefore, here we analysed the WSSAR above 0.5 and set five levels from 0.5 to 1. As the aneurysm growth in our model, the nodes number of high WSSAR in the level of 0.5-0.6, 0.6-0.7, 0.8-0.9 decreased and that in the level of 0.7-0.8, 0.9-1 increased in spite of the small amount. In the level from 0.5-0.7, the nodes numbers were 3781 and 3539 at t=0 and t=46 respectively. Between 0.7-1, the nodes numbers were 4307 and 4288 at the two time points respectively. This indicated that the nodes number decreased either in the lower WSSAR level or the higher WSSAR level and leads to the total nodes number declined (5.1 sum).

5.4.3.3 Evolution of WSSAR and m^E

The degradation rate of elastineous constituents is dependent on the WSSAR distribution, and we defined a function called $\mathcal{F}_{D(WSSAR)}^E$ in the methodology section. Figure 6.4 (A) shows the $\mathcal{F}_{D(WSSAR)}^E$ distribution where the red region indicates the maximum degradation rate. No elastin degradation happens to the blue area in which has a relatively favourable flow condition. Figure 6.4 (B-1,B-2) plots the normalized elastin mass density at t=23 and t=46 over the aneurysm revolution. The colourmap was limited to 0-0.083 which is the initial mass density of elastin in the aneurysm region. The m^E in the parent artery is 1, and the transitional region ranges from 0.083 to 1, hence these two regions are covered with the red colour.

Comparing the 6.4 (A) and 6.4 (B), it is clear that the region has higher $\mathcal{F}_{D(WSSAR)}^E$ leads to the lower mass density of elastineous constituents and vice verse. As the aneurysm growth, the m^E degrades according to the distribution of $\mathcal{F}_{D(WSSAR)}^E$ and achieve the heterogeneity

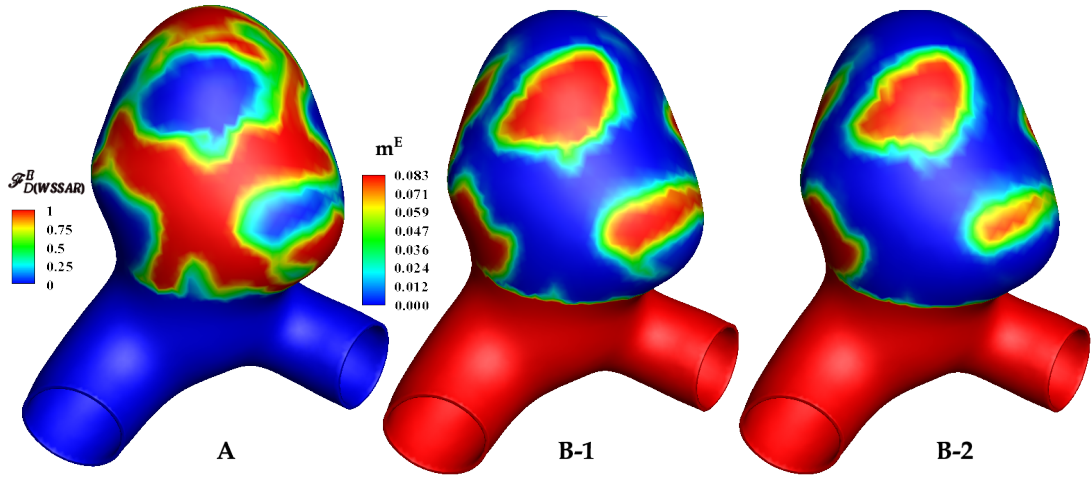


Figure 5.15: The $\mathcal{F}_{D(WSSAR)}^E$ distribution dependent on the WSSAR calculated from the fluid simulation (A) and the subsequent m^E evolution at $t=23$ and $T=46$.

of the mass density distribution.

5.4.3.4 Evolution of WSSAR and m^C

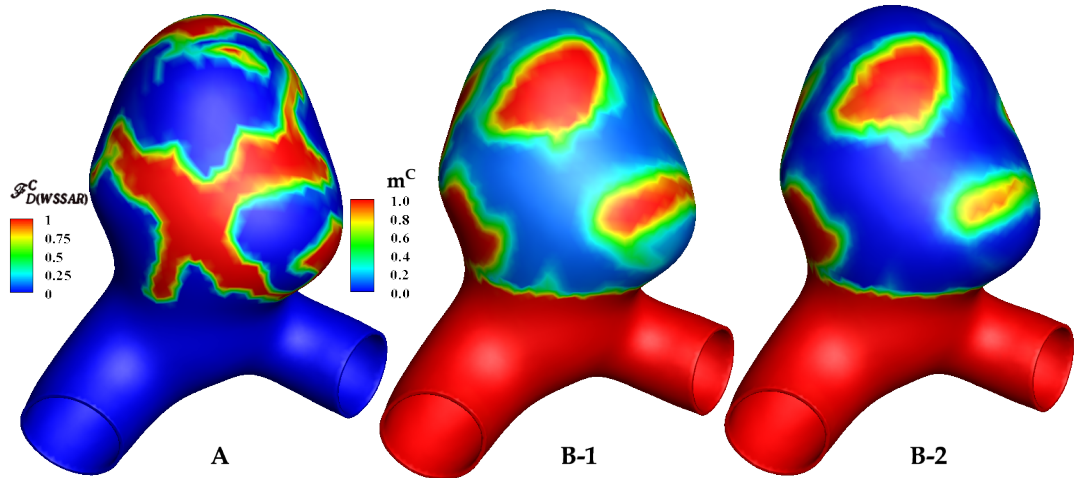


Figure 5.16: The $\mathcal{F}_{D(WSSAR)}^C$ distribution dependent on the WSSAR calculated from the fluid simulation (A) and the subsequent m^E evolution at $t=23$ and $T=46$.

Similar to the elastin degradation, the degradation of collagen fibres is also related to the mechanical stimuli from the blood flow which has been demonstrated carefully in Section 5.4.1. The distribution of $\mathcal{F}_{D(WSSAR)}^C$ is similar to the $\mathcal{F}_{D(WSSAR)}^E$ distribution but has smaller

degradation area with slight difference due to the linear function in Equation 5.4.4. The collagen concentration was assumed as the same in both the aneurysm and healthy artery, and they are normalised to 1 indicating the initial collagen concentration. The same, the higher $\mathcal{F}_{D(WSSAR)}^E$ results in the lower concentration of collagen fibres with stronger degradation activities.

5.4.3.5 Evolution of WSSAR and k_2

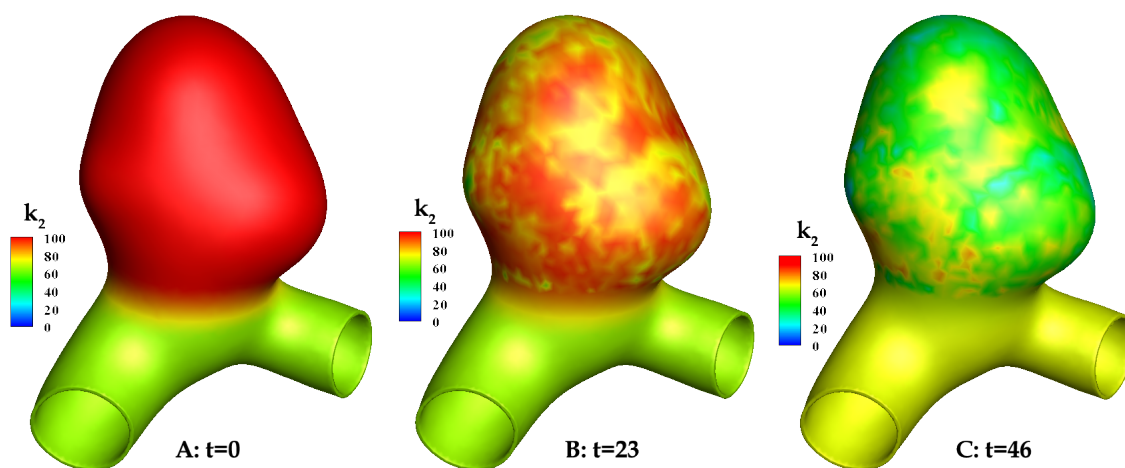


Figure 5.17: Spatial distribution of k_2 at $t=0, 23, 46$ indicates mechanical behaviour changing of collagen fibres as the aneurysm evolution.

According to the SEF function of collagen fibres, k_2 is a dimensionless parameter which is mainly in charge of the non-linear properties. As the aneurysm growth, the stiffness of collagen fibres needs to decrease to maintain the stress restored to homeostatic level. Figure 5.17 shows the non-uniform distribution of k_2 which is remodelled based on the stress deviation. At the initial state, the k_2 is uniform in the aneurysm as the assumption. Accompanied with collagen remodelling, k_2 declines from 100 to lower magnitudes and eventually the k_2 values in most regions are lower than the k_2 in the healthy artery.

5.4.4 Discussion and Conclusion

This p-FSG framework introduced a novel flow metric (WSSAR) which could better quantify the flow patterns based on the 3D complex clinical geometry. Since the WSSAR is associated with the endothelial cells morphology and function, we linked the endothelial cells permeability to the inflammatory activities. Hence, besides the elastin degradation and collagen

remodelling, the collagen degradation was also added which is highly related to the inflammation pathway in our G&R algorithm.

The maximum of total displacement is 1.2339 mm at the final time step increased from 0.79452 mm, which is due to the first pressurisation. The quantification of aneurysm enlargement is not accurate only by displacement, so we also calculated the volume of the aneurysm over its development. The volume increased 136.15 mm^3 , which is approximately 33.4% compared to its original geometry. The relatively limited enlargement is because of the complexity of the geometry itself on one side, especially the topography around the neck with high curvature. This high curvature easily gives rise to the highly localised distortion leading to the diversity of the whole simulation.

As to elastin degradation, it could be neglected on account of the small amount remained in the aneurysm part (8.3%). But based on the reality that there is still part of elastin fragments left, the G&R always considered the degradation of elastin in spite of the minor effect of this process. Owing to the relative small geometric variation, the flow environment in the aneurysm has a similar distribution compared to the initial condition. WSSAR distribution only showed a slight difference in the top region and around the base of the larger bulge on the aneurysm model. Through the statistical analysis, the number of high WSSAR points (0.5-1) decreased 264 at $t=46$, but the number of higher WSSAR (0.9-1) elevated slightly. Interestingly, the high WSSAR region is highly correlated with the high maximum principal stress region and high Von-mises stress area (Figure 4.21) which indicates the strong pathological activities occurs in that region.

The elastin degradation was linked to low WSS in previous researches (Grytsan et al., 2017b; Watton et al., 2011), but the elastin degrades by the MMPs which is correlated with the permeability of endothelium. Compared to the WSS, WSSAR can better capture the oscillatory of the flow thus the permeability could be a function of WSSAR. So in this research, the elastin degrades with the WSSAR replacing the low WSS so that it can model the mechanobiology pathway, mechanical stimuli - biological activities (inflammation) - tissue constituents reaction.

On the basis of the WSSAR, the elastin and collagen fibres degraded with certain rates. Regions with high WSSAR has a stronger degradation rate leading to a lower mass density of elastin and collagen fibres. Regarding the mass density of collagen fibres, the concentration increases at the beginning of aneurysm formation to compensate the loss the elastin to bear the blood pressure (Watton et al., 2004). As mentioned before, the collagen could be higher/lower or equal to the control healthy artery, indicating the collagen mass density varies dynamically in different stages of aneurysm evolution. We assumed that the concentration of collagen fibres is the same to the connected artery which is a limitation in this

study. The further improvement in radiology technique might help to provide a quantitative evaluation of the mass and arrangement of collagen fibres in arterial tissue. Another key pathological process is the remodelling of collagen fibres, contains their turnover and configuration variation. The SEF of collagen fibres we adopted here is the classic constitutive model (Holzapfel et al., 2000) where k_2 is the key parameter in quantifying the non-linear behaviour of collagen fibres. Hence, in our remodelling functions, the k_2 remodels with the stress deviation trying to restore the stress to homeostatic level. Results showed that the k_2 decreased spatially in the aneurysm implying that the stiffness of collagen fibres are decreasing. This is consistent with the experimental study which analysed 42 aneurysms and showed the softer aneurysms have a higher rupture risk (Brunel et al., 2017). And the comparison of stress distribution between the initial state and the final state indicated that the collagen fibres are able to maintain the stress around the homeostatic level with a slight increase (6%) of the maximum value via the remodelling algorithm in this research.

In conclusion, this chapter depicted two p-FSG models that linked the elastin degradation to low WSS and high WSSAR respectively, the later also incorporated the collagen degradation through the inflammation pathway. They both achieved the spatial distribution of arterial constituents and mechanical behaviour and aneurysm growth. Our p-FSG framework is able to model the aneurysm evolution from the clinical state under an automatically computational platform and provide more insight into understanding and predicting the rupture of an aneurysm.



An integrated P-FSG Framework Incorporating Collagen Growth Function

6.1	Collagen Growth Function Represented by Fibroblasts	147
6.2	Summary: An integrated P-FSG framework	152
6.3	Two Comparative Cases with Collagen Growth Function Turning on/off	154
6.4	Illustrative Results Link with Flow Metric with An Updated Prismatic Mesh	167
6.5	Discussion	172
6.6	Concluding Remarks	174

The P-FSG framework described in the preceding chapter focused on the mechanical stimuli from the haemodynamic environment, which is closely correlated with the endothelial cells. We proposed a hypothesis that utilising a function of flow metric to quantify the endothelium permeability which is strongly associated with the inflammatory activities and aneurysm growth. Then the degradation of elastinous and collagenous constituents could be

modelled through this pathway. The collagen growth plays a pivotal role during the aneurysm growth, compensating the mechanical loss from the elastinous constituents degradation. Even though the collagen synthesis and degeneration of collagen fibres might achieve a balanced state in maintaining the equilibrium state of an aneurysm, the collagen degradation activities with a much stronger level should be the reason for inducing the further development and the rupture of an aneurysm. Therefore, the dynamic growth/atrophy of the collagen fabric regulated by fibroblasts need to be considered into our P-FSG framework. This chapter will propose a more sophisticated P-FSG framework with the presentation of fibroblasts mechanobiology.

A brief review on mechanisms of fibroblasts secreting, depositing and degenerating collagen fibres will be given in the first section. Upon this, mathematical modelling of the recruitment configuration of fibroblasts and the growth/atrophy of collagen fabric mediated by the fibroblasts stretch deviation from the attachment stretch level are carefully described with equations. After adding the implementation of collagen growth function, an integrated P-FSG framework is constructed and a flow diagram of the full framework is shown in the second section. To explicitly present the influence of collagen growth function, two comparative models are made, one has the normal collagen growth function and the growth function is muted in the other model. Results of geometric growth, stress and strain distribution, fibroblasts stretch, collagen mass density distribution, etc. are comprehensively analysed and discussed. In the end, we utilize a prismatic mesh to replace the original tetrahedron one generated in ANSYS APDL automatically to test its ability of large deformation. With this mesh, we linked the WSSAR flow metric to p-FSG as a comparison for the same simulation in Chapter 5. Based upon this, we linked the aneurysm G&R function to OSI to model the condition of irregular enlargement or a secondary aneurysm growth.

6.1 Collagen Growth Function Represented by Fibroblasts

The adaptive behaviour of collagen fibres is comprised of the mass density variation and the changing of their mechanical properties. In the preceding chapter, these two adaptive activities were both taken into consideration but only contained collagen degradation. No matter in healthy arteries or an aneurysm, the continuous synthesis and atrophy of collagen fibres both exist. These two processes keep a balanced status to maintain the equilibrium in arteries or aneurysms. However, in the course of aneurysm evolution, the unbalance between the deposition and degradation would contribute to the development of an aneurysm. Hence,

the following sections will introduce the function of fibroblast cells secreting and degrading collagen fibres under the regulation by mechanical stimuli.

6.1.1 Mechanisms Between Fibroblasts and Collagenous Constituents

As mentioned in Section 1.2.5.4, the leading collagen type in vascular wall is type I and III produced with a high level over the development of an aneurysm, which is mainly attributed to an enhanced activity of fibroblasts. Procollagen precursors, the earlier pattern to polymerize into collagen fibrils that bound together to form collagen fibres, are primarily produced by fibroblasts (Alberts et al., 1994). Birk and Trelstad proposed that fibroblasts control the formation of collagen fibrils on the deep recesses which reside on the cell surface and thus control the structure of the collagen matrix (Birk, Trelstad, 1986). This suggests a direct link between fibroblasts and the collagen arrangement. In a pre-strained condition, when fibroblasts contract the surrounding matrix which triggers the deposition of newly produced matrix collagen fibres (Huang et al., 1993). Fibroblasts synthesize collagen molecules in minutes and secrete them in no more than one hour. These collagen molecules are assembled to the fibrils form in the extracellular matrix and eventually form the cross-linked fibres. The continual maintenance of the ECM by fibroblasts requires a continuous turnover of collagen fibres except for the synthesis and secretion. The half-life of collagen fibres is reportedly between 60 to 70 days in the normotensive states and 17 days in hypertensive conditions in the rat aorta models (Nissen et al., 1978). Another study also reported that the turnover of collagen in various tissue with a half-life of 3–90 days which is rather rapid (Humphrey, 1999). Moreover, the turnover rate of collagen could increase many folds under the mechanical or biological stimuli (Nissen et al., 1978).

These cells not only can synthesize and deposit collagen fibres but also able to secrete proteases to degrade the collagenous material, which interdependently keeps the equilibrium within the tissue. Hence, fibroblasts have abilities in the production, organization and clearance of collagen fibres in the extracellular matrix. And all these functions are also regulated by the mechanical microenvironment of the extracellular matrix. The adherence of fibroblasts to the extracellular matrix mainly relies on integrins, which is a type of mechanical receptors transducing the signals from the extracellular matrix to the cytoskeleton inside the cells (Wang, Thampatty, 2006; Gupta, Grande-Allen, 2006). It is reported that these integrins enable fibroblasts to reorient as a result of responding to the variation of the mechanical microenvironment playing as stretch sensors (Chiquet et al., 2003). Therefore, the variation of collagen orientation leads to the mechanical microenvironment changing, further influences the orientation of fibroblasts and their ability to move (Dallon, Sherratt, 1998). It has

been observed that fibroblasts in the aneurysmal wall tend to be elongated, and they often show a parallel alignment (Kroon, Holzapfel, 2007).

6.1.2 Remodelling the Recruitment Configuration of Fibroblasts

An experimental study cultured fibroblasts growing in the reconstituted collagen gels and results proved that the fibroblasts do align the flexible collagen meshwork around themselves. Moreover, this study also found that these sprays of collagen fibres aligned parallel to the long axis of the cell (Harris et al., 1981). Meanwhile, according to the growth/atrophy model of the collagen fabric in (Watton et al., 2011), the stretch sensed by the fibroblasts is assumed to be equal to the stretch on collagen fibres, i.e. $\lambda^F \equiv \lambda^C$. F and C denote fibroblasts and collagen fibres respectively. However, in this research, we can only achieve the stretch on the directions of collagen fibres which is not the exact stretch acting on the collagen fibres. Therefore, the stretch in the orientation of collagen fibres is denoted as $\bar{\lambda}^C$ to differentiate with λ^C .

The definition of an attachment stretch is that fibroblasts or collagen fibres have distinct natural reference configurations. The attachment stretch of collagen fibres is defined as the stretch on the collagen fibres at systole at $t = 0$. Similarly, the attachment stretch of fibroblasts is regarded as the stretch in the fibroblasts at systolic at $t=0$, i.e. $\lambda_{AT}^F = \lambda_{(t=0)}^F = \lambda_{(t=0)}^C$. However, the current structural model is unable to directly extract the stretch on collagen fibres or on fibroblasts, therefore, here we assume the attachment stretch as 1.05 at homeostatic state ($\lambda_{AT}^F = 1.05$).

Given the increased stretch in the mechanical environment, fibroblasts restructure their cytoskeleton and ECM contacts, i.e. fibroblasts reconfigure their natural reference configurations, in order to reduce the stretch and reach a new equilibrium by restructuring their cytoskeleton and ECM contacts. The gross stretch in the direction of fibroblasts is the product of the recruitment stretch of fibroblasts and the stretch of fibroblasts, and the recruitment stretch could be expressed as:

$$\lambda_R^F = \frac{\bar{\lambda}^C}{\lambda^F} \quad (6.1.1)$$

At homeostatic state ($t = 0$), we specify that the fibroblast stretch $\lambda^F = \lambda_{AT}^F$, hence

$$\lambda_R^F(t = 0) = \frac{\bar{\lambda}^C(t = 0)}{\lambda_{AT}^F} \quad (6.1.2)$$

The λ_R^F is remodelled to maintain the fibroblast stretch λ^F to go back to the attachment

stretch (λ_{AT}^F). This process could be expressed as

$$\frac{d\lambda_R^F}{dt} = \alpha \frac{\lambda^F - \lambda_{AT}^F}{\lambda_{AT}^F} \quad (6.1.3)$$

where the α is a non-dimensional parameter relating to a mechanical feedback factor from the ECM environment, which influences the loading state of fibroblasts. For the analysis in this research, $\alpha = 0.1$. As the aneurysm enlarging, the overall stretch in the direction of collagen fibre will alter, i.e. $\bar{\lambda}^C$. Through the remodelling of recruitment stretch operated in the Equation. 6.1.3, the fibroblast stretch will consequently update from the stretch $\bar{\lambda}^C$ at current time step and the recruitment stretch of fibroblast remodelled from the last time step:

$$\lambda^F(t) = \frac{\bar{\lambda}^C(t_n)}{\lambda_R^E(t_n - 1)} \quad (6.1.4)$$

Through manipulating above equations, the recruitment stretch of fibroblasts and the stretch on fibroblasts could be calculated at each iteration. Consequently, the mechanobiological phenomenon that the force exerted from fibroblasts acting on the ECM, here mainly focuses on the collagen fibres, is able to be described mathematically.

6.1.3 Growth/Atrophy of the Collagen Fabric

At homeostatic state, it is regarded that the deposition and atrophy of collagen fabric have achieved a dynamically balanced system. The fibroblasts act the function of synthesizing collagen material and degrading collagen fibres which implies that there is a relationship between the mass density of fibroblasts and collagen fibres. We assume that the mass density changing rate of collagenous constituents relies on the concentration of fibroblasts (m^F) in the arterial wall. This concentration (m^F) indicates that the ratio of the density of fibroblasts at time t to that at homeostatic state ($t=0$). Moreover, the concentration of fibroblasts is assumed to be proportional to the mass density of collagenous constituents (m^C), which can be expressed as $m^F = \xi_0 m^C, \xi_0 > 0$ (Wattton et al., 2011).

It is impractical to quantify the individual collagen production and degradation respectively, but the net variation of the mass density of collagen fibres is achievable to represent clearly. Here we define the net variation of collagen fibres acted by individual fibroblast is a function of the stretch on fibroblast ($\mathcal{F}(\lambda^F)$).

$$\frac{dm^C}{dt} = m^F \mathcal{F}(\lambda^F) = \xi_0 m^C \mathcal{F}(\lambda^F) \quad (6.1.5)$$

Here we use a new function $\mathcal{F}_G(\lambda^F) = \xi_0 \mathcal{F}(\lambda^F)$ to simplify the above equation and build

an explicit function to quantify the concentration changing of collagen fibres. However, the exact function of $\mathcal{F}_G(\lambda^F)$ is unknown. Even though, the understanding of the interaction between mechanical stimuli and biological response could help to characterize the mass density changing of collagen fibres mediated by the stretch on fibroblasts. Increased mechanical loading is known to increase the proliferation and collagen production of fibroblasts (Aumailley et al., 1982; Bishop, Lindahl, 1999; Butt et al., 1995). Chiquet et al. also reported that the stretch of ECM will generate a positive force on fibroblasts resulting an up-regulation of collagen fibres deposition and inhibition of collagenase expression through the signal transferring. On the contrary, the relaxation of ECM will trigger a distinct signalling pathway which leads to a reversed effect of protein expression (Chiquet et al., 2003; Watton et al., 2011). Based on this, the function $\mathcal{F}_G(\lambda^F)$ could be defined as:

$$\mathcal{F}_G(\lambda^F) = \beta \left(\frac{\lambda^F - \lambda_{AT}^F}{\lambda_{AT}^F} \right) \quad (6.1.6)$$

The β is a phenomenological growth parameter that relates to the increasing or decreasing rate of the mass of the collagenous constituents under the regulation of fibroblasts in response to deviations of stretch on fibroblasts from homeostatic levels. For the analysis in this paper, $\beta = 0.8$ (Watton et al., 2011). The full formula representing the collagen growth and atrophy influenced by the fibroblasts could be summarized as:

$$\frac{dm^C}{dt} = \beta m^C \left(\frac{\lambda^F - \lambda_{AT}^F}{\lambda_{AT}^F} \right) \quad (6.1.7)$$

This equation indicates that when the fibroblast stretch is larger than the attachment stretch, a net positive force will act on fibroblast promoting the cells secrete or deposit more collagen fibres. While the stretch level on fibroblasts is lower than the λ_{AT}^F , the net up-regulation effect of collagenase expression would result in the decline of collagen mass.

6.1.4 Implementation with ANSYS

To implement above equations that formulate the mass density of collagen fibres regulated by the mechanical stimuli sensed by fibroblast, it is essential to calculate the variable $\bar{\lambda}^C$. This key parameter could be post-calculated from the strain tensor output by ANSYS software.

As explained in Section 5.2.2, the invariants $I_{4,6}$ is the function of Green-Lagrange strains. Note that the invariants I_4 and I_6 are the squares of the stretches ($\bar{\lambda}^C$) in the directions of the two families of collagen fibres and therefore have a clear physical interpretation, i.e. $\bar{\lambda}_{4,6}^C = \sqrt{I_{4,6}}$ (Holzapfel et al., 2000). The anisotropic behaviour of collagen fibres only con-

tributes when the fibres are stretched, i.e. the I_4 or I_6 has to be larger than 1. If I_4 or I_6 is less than or equal to 1, the mechanical behaviour of aneurysm wall is isotropic given rise by the elastinous constituents. That is to say, collagen fibres are not under stretch or get compressed conversely.

Once the $\bar{\lambda}_{4,6}^C$ is calculated from the Green-Lagrange strain (ANSYS), then the recruitment stretch of fibroblasts (λ_R^F) and the fibroblasts stretch (λ^F) are deduced via Equation 6.1.1-6.1.3. The recruitment stretch of fibroblasts (λ_R^F) remodels in terms of the stretch deviation from the attachment stretch. As the remodelling of recruitment stretch of fibroblasts (λ_R^F), the fibroblasts stretch (λ^F) is updated at each time step. Through the Equation 6.1.7, the amount of collagen fibres concentration changing with the regulation of the stretch on fibroblast could be modelled in the course of aneurysm evolution.

6.2 Summary: An integrated P-FSG framework

Mechanisms of collagen growth mediated through fibroblasts were introduced and mathematically modelled in the last section. Hence, the destructive progress and the self-protective behaviour in an aneurysm were both included in our G&R function. The consequence of an aneurysm evolution, i.e. growth or stabilization, is determined by the interplay between these two mechanisms.

Figure 6.1 illustrates the integrated workflow of the P-FSG framework with clear identification of three key components showed by different colours (Fluid simulation-blue, Solid modelling-orange, G&R algorithm-green). This framework utilizes the medical images as the input data to reconstruct patient-specific aneurysm model, which is divided into the aneurysm section and the parent artery section. The aneurysm section is specialized in the solid modelling while the parent artery only serves to the haemodynamic simulation. In the fluid simulation part, the mechanical stimuli applied on endothelial cells is characterized and associated to endothelial cells morphology. Endothelium permeability is hypothesized as a function of endothelial cells morphology which is quantified by a novel flow metric (WS-SAR). At the same time, the possibility of modelling the endothelium permeability allows the mathematical model to mimic the inflammatory pathway which can lead to the elastin and collagen degradation pathological process (G&R).

On the aspect of solid modelling, this structural model was assigned with the material properties through a parameter study which tested the appropriate values of the mass density and mechanical behaviour of elastin and collagen fibres in the aneurysm part and the healthy artery. After the structural solving, we can achieve the displacement, stress and strain distribution information, etc. The displacement information was implemented into the aneurysm

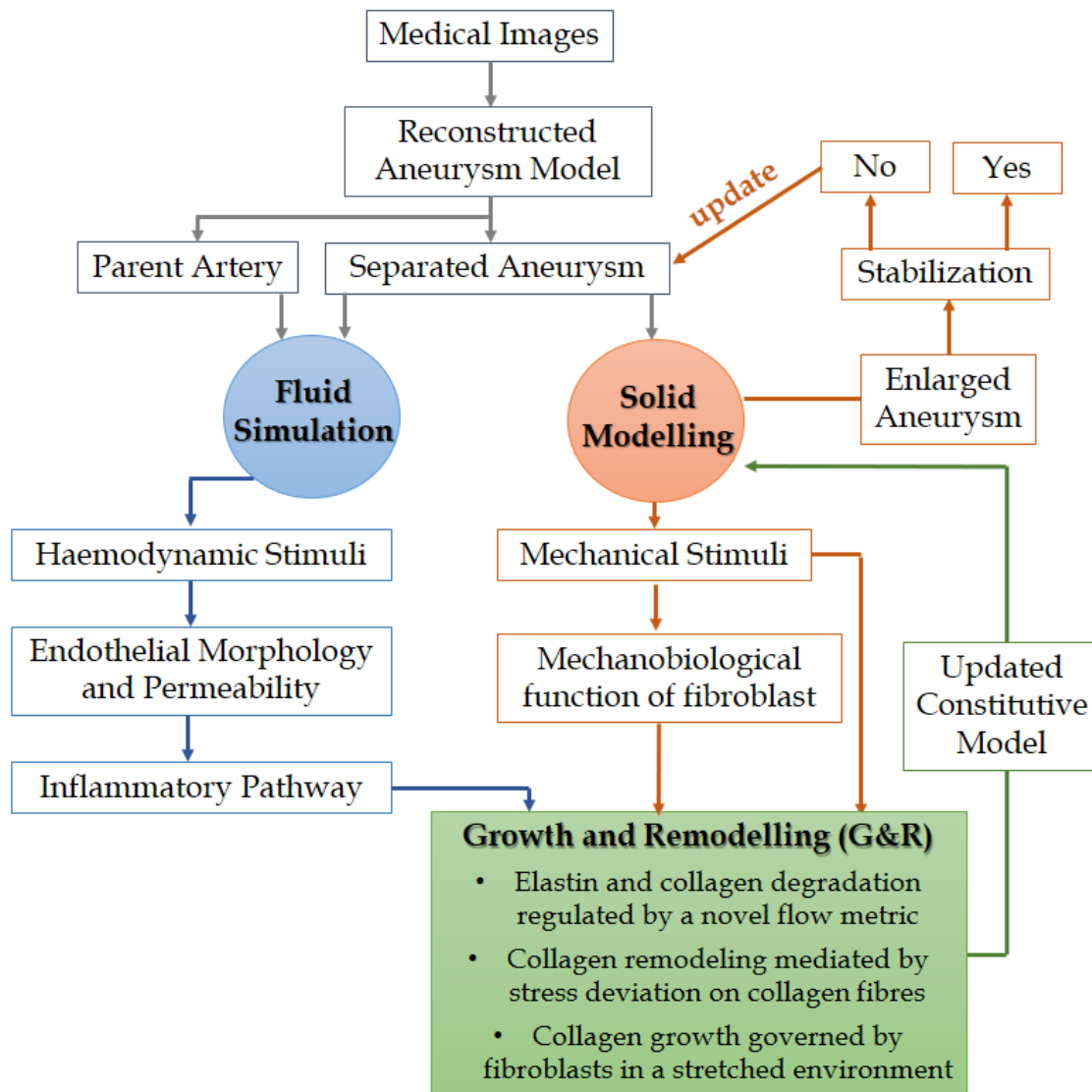


Figure 6.1: Detailed design of the whole P-FSG framework shows the key hypotheses and the workflow from the medical images to achieve the stability of the aneurysm model. The primary parts, fluid simulation, solid modelling and G&R function, are represented by blue, orange and green color respectively.

geometry reconstruction which indicated the enlarged aneurysm. This updated aneurysm model combined with the parent vessel was imported into the fluid solver to further capture the updated haemodynamic environment. The basic idea of collagen remodelling is to restore the stress to the homeostatic level, so here stress-mediated remodelling method was

adopted in this research (G&R). In this collagen remodelling section, the mechanical stimuli (stress) as a functional input to govern the collagen remodelling. The other pathway we also incorporated is the fibroblasts mechanobiology which associates with the growth/atrophy of collagen fibres (G&R). The mechanobiology of fibroblasts is mediated by the stretch sensed by cells, and the mechanical stimuli are calculated from the structural modelling.

After the G&R algorithm, the updated constitutive model was imported into the structural solver to do the structural analysis. Through iterations of this F-S-G cycle, the aneurysm model is able to keep enlarging until it achieves a stable state. In this integrated P-FSG framework, it made several improvements on the novelty:

1. Started with a patient-specific aneurysm reconstructed model which replaced the cylindrical membrane model or thick-wall tube model made in other researches;
2. Employed a novel flow metric which can characterize the feature of oscillatory flow in a more explicit and accurate way;
3. Represented the endothelium layer from the perspectives of the morphology of endothelial cells and the endothelium permeability and further incorporated in G&R function;
4. The idea of collagen remodelling and the collagen growth/atrophy mediated by fibroblasts was basically followed (Watton et al., 2004), but this is the first time we applied these hypotheses to a 3D patient-specific model;
5. The commercial software ANSYS provides a strong solver for our complex structural model. We also achieved the individual control of elements in the automatically-generated mesh.

6.3 Two Comparative Cases with Collagen Growth Function Turning on/off

This chapter we incorporated the collagen growth function as a self-protective mechanism of an aneurysm by representing the fibroblasts mechanobiology. To investigate the influence of this function to aneurysm stability which has been introduced in the first section, here we build two sets of models with different collagen growth rates to see the influence of collagen growth to aneurysm development.

6.3.1 Models Setting Up

First of all, these two models are illustrative models in order to investigate the influence of the growth function of collagen fibres. Therefore, the degradation of elastinous and collagenous constituents is set as a prescribed function aiming to save the computational time. Moreover, from the geometric perspective of our aneurysm model, it seems like a secondary aneurysm was being developed showed by the larger bulb. Aiming to mimic a second aneurysm evolution in this case, the degradation region was localized around the larger bulb through a sphere model shown in Figure 6.2. The centre $([x_0, y_0, z_0])$ of the sphere is located at $[-2, 4, 4]$ in Cartesian coordinates system with a radius of 8 mm. The boundary lines of the intersection from left and right sides are clearly showed between the green aneurysm model and the translucent sphere model.

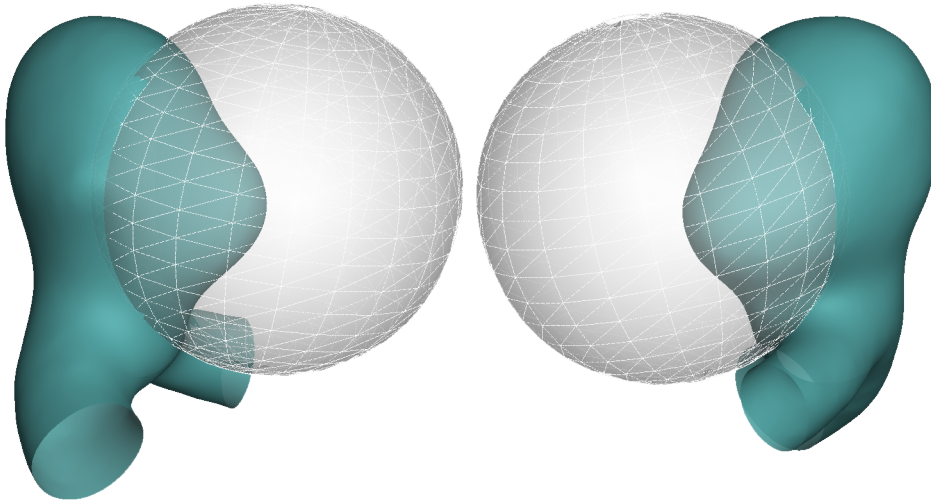


Figure 6.2: A sphere model is located at the larger bulb of the aneurysm model, which restricts the degradation region for elastin and collagen fibres

The same mesh and boundary conditions introduced in Chapter 4 were used in the structural modelling here. Degradation of elastin and collagen fibres is a destructive mechanism leading to the further enlargement of the aneurysm model in the localized region. Here in contrast to the degradation function linked with haemodynamic environment showed in the last chapter, we utilized another prescribed degradation function for elastin and collagen explained by equations below:

$$deg = \left(\frac{r-D}{r}\right)^n \quad (6.3.1)$$

where the **deg** denotes the degradation intensity and **r** means the radius of the sphere. **n** is a regulation parameter to mediate the degradation rate, **n** = 4 in this analysis. As to **D**, it means the distance between a point on the aneurysm model and the sphere centre. This point should be located within the region limited by the sphere, i.e. **D** should smaller than **r**, otherwise **deg** equals to 0. The mass density of elastin and collagen fibres could be achieved by the equation below:

$$m^{E,C}(t + \Delta t) = m^{E,C}(t)[1 - deg \cdot D_{max}^{\Delta t}] \quad (6.3.2)$$

Note that elastin and collagen degraded as an identical rate but with different initial values, $m^E(t = 0) = 0.05$ and $m^C(t = 0) = 1$ on the aneurysm sac. $D_{max}^{\Delta t}$ is the maximum degradation percentage per year which is also the same to elastinous and collagenous constituents ($D_{max}^{\Delta t} = 0.2$). Specific parameter settings and the implementation codes are listed in Appendix 3 about the degradation rate and degradation regions for elastin and collagen fibres.

The idea of collagen remodelling still follows the hypothesis that collagen fibres remodel to drag the stress returning back to the homeostatic level. It is notable that the k_2 in the remodelling function is modified to k_1 here:

$$\frac{dk_1}{dt} = -\gamma \left(\frac{\sigma_C(t) - \sigma_{Ch}}{\sigma_{Ch}} \right) k_1 \quad (6.3.3)$$

Here we recall the SEF for collagen fibres :

$$\Psi_C(a_{01}, a_{02}) = \frac{k_1}{2k_2} \sum_{i=4,6} \{exp[k_2(I_i - 1)^2] - 1\} \quad (6.3.4)$$

Reason for replacing k_2 to k_1 is that k_2 participates in the exponential term which could easily cause the termination of the simulation with a non-converged solution. Owing to the high non-linearity of the exponential function, the linear variation of k_1 would decrease the possibility of the solution divergence.

In terms of collagen growth function mediated by fibroblasts remodelling, here we designed two scenarios named as **case 1** and **case 2**. The collagen growth function is applied to **case 1** and muted in **case 2** for investigating the collagen growth influence to the aneurysm evolution. For the analysis of this study, the α we defined here is 0.1. According to (Watton et al., 2011), β is related to the fibroblasts function regulating the mass density change of collagenous constituents as a response to the stretch deviation from the homeostatic level. It equals to 0.8 year^{-1} in **case 1** and which is set as zero ($\beta = 0$) due to the shutting down of

collagen growth function in **case 2**.

6.3.2 Results of Two comparative Cases

Modelling results on the aspects of geometric comparison, prescribed degradation and G&R of arterial tissue will be exhibited in the following sections. On the perspective of geometric comparison, the final inner surface profiles of enlarged aneurysm geometries in contrast to original aneurysm surface from **case 1** and **case 2** are compared. The mass density distributions of elastinous and collagenous constituents are illustrated, especially in the localised region where the degradation occurs. This chapter also includes collagen remodelling and collagen growth function which are mediated by stress deviation and represented by the recruitment stretch remodelling of fibroblasts respectively. Therefore, the homeostatic stress of collagen fibres, stress deviation between the stress at the ending time point and this homeostatic status as well as the k_1 distribution after remodelling will be plotted to represent the collagen remodelling results. Then the variation of collagen mass density mediated by the stretch deviation from the attachment stretch level of fibroblasts and stretch distribution of fibroblasts are illustrated for the **case 1** model. In the end, the effective stiffness of collagen fibres, i.e. the product of mass density and k_1 , will be compared to investigate the effectiveness of overall G&R function to the aneurysm stability in this P-FSG framework.

6.3.2.1 Comparison of the Total Deformation

In order to compare the enlargement of the aneurysm model quantitatively, volumes of the original aneurysm model, pressurized aneurysm geometry and enlarged aneurysm geometries due to the growth function in **case 1** and **case 2** are summarized in Table 6.1.

Table 6.1: Summary of geometric information of aneurysms models at different stages

	Original Geometry	Pressurized Geometry	Case 1	Case 2
Volume (mm^3)	406.77	513.389	517.008	542.206

For both two cases, the volume of the initial aneurysm geometry is the same which equals to 406.77 mm^3 and it increases to 513.389 mm^3 due to the pressurization. To investigate the effective growth of the aneurysm model, here the increased volume is calculated by utilizing the final volume to minus the pressurized volume. In Table 6.1, we just listed the consequent

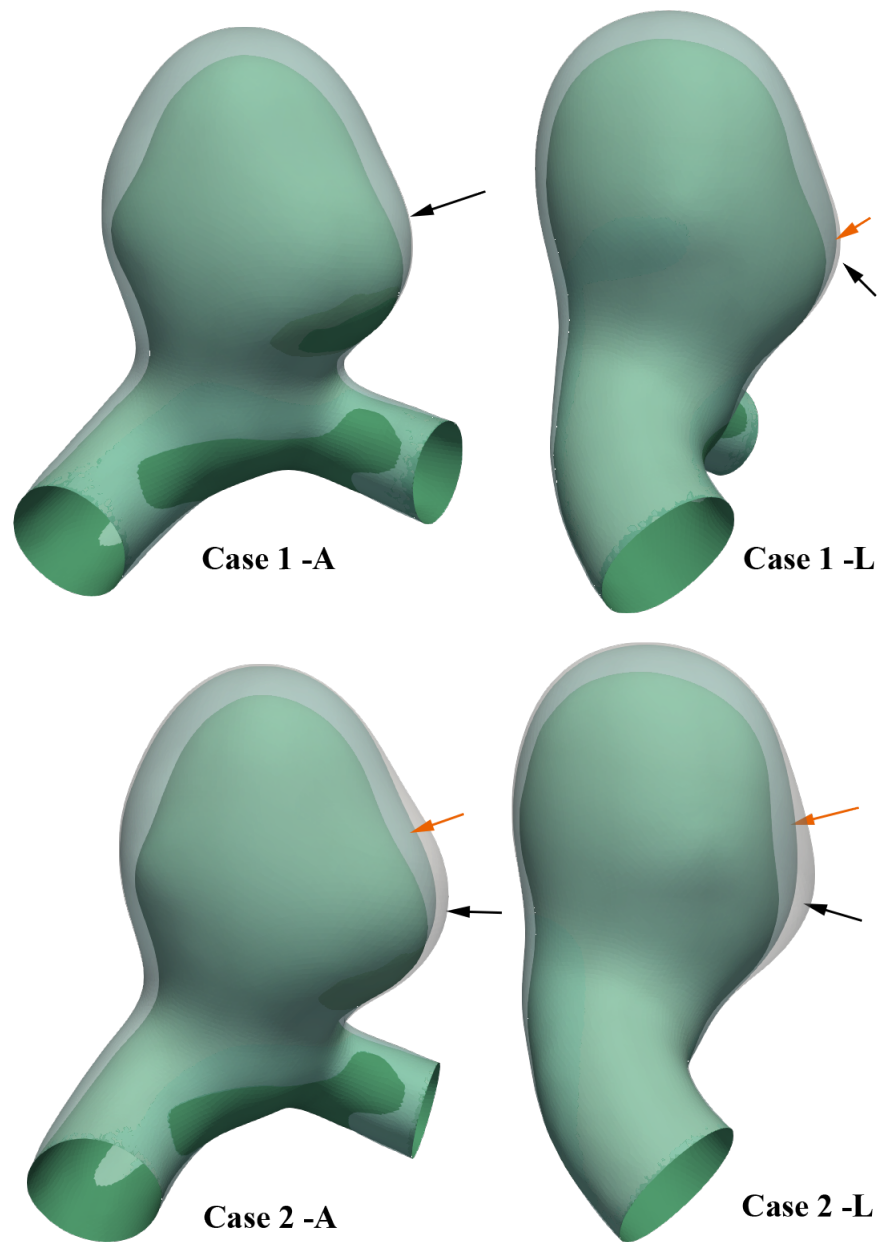


Figure 6.3: Comparison of deformations from the original state of aneurysm between Case 1 and Case 2 from the anterior view (A) and lateral view (L).

volume of **case 1** and **case 2**. For **case 1** which implemented the collagen growth function, the final volume of the aneurysm model is 517.008 mm^3 . The increased amount of the volume is less than 4 mm^3 which is negligible in contrast to the original 'huge' volume. As a comparison of **case 1**, the volume increased to 542.206 mm^3 in **case 2**, which is about 5.6% dilation, and

the enlargement region was clearly shown in Figure 6.3 (Case 2-A, L).

The final states after deformation in contrast to original geometry and pressurized geometry of the aneurysm model for **case 1** and **case 2** are plotted in Figure 6.3. The original aneurysm geometry was represented by green colour, pressurized geometry was plotted as a translucent profile pointed by orange arrows and the final enlarged aneurysm geometries were exhibited by more translucent profiles denoted by black arrows at the outer most layer. On the ground that the degradation region was localized by a sphere model where the destructive process could lead to the enlargement, there is no dilation occurs on the remaining regions. In **case 1**, only a slight dilation showed in the lateral view (Figure 6.3) but hardly see any dilation from the front view. A much larger dilation explicitly showed in **case 2** both from the front and the lateral view implying a secondary aneurysm evolution.

6.3.2.2 Elastinous and Collagenous Constituents Degradation

Degradation hypotheses of elastinous and collagenous constituents have been elaborately introduced in the preceding chapter, and the only difference is that the degradation function is prescribed (see Equation 6.3.1 and the 'spatialdeg' function in Appendix 3) using a sphere model rather than linking to flow metric here. According to the prescribed degradation rule, the mass density distributions of elastinous and collagenous constituents evolution will be presented below.

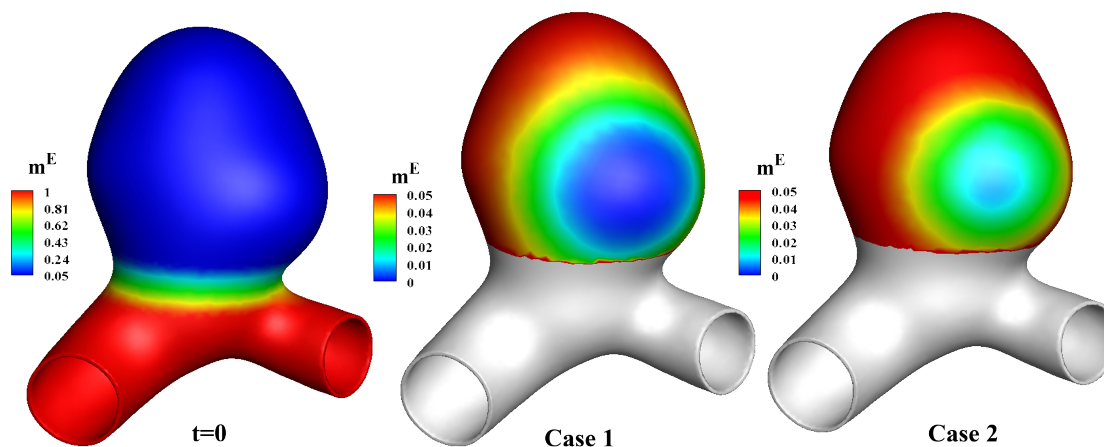


Figure 6.4: Initial mass density distribution of elastin from 0.05 in aneurysm sac to 1 in healthy artery and there is a transitional region in between; the ending states of m^E for case 1 and case 2 respectively.

Figure 6.4 shows the mass density distribution of elastin at the beginning status and at the

end of the aneurysm evolution **case 1** and **case 2**. The colour maps of the final mass density of elastin in **case 1** and **case 2** were limited from 0 to 0.05 which is the initial mass density in the aneurysm section. Because there is no elastin degradation occurs in the parent vessel/the transitional region and there is a wide gap of the elastin mass density between the aneurysm section and the parent vessel part, we covered these two parts with white color to signify there is no variation of the mass density. First of all, the degradation rule was revealed clearly by both mass density distributions of case 1 and case 2. Regions, where are closer to the sphere centre, have higher degradation rates. It is easy to notice that the lower mass density region in case 1 is larger than that in case 2, and the lowest mass density value in case 1 is much lower than that in case 2. As mentioned before, the elastin degrades with the same rate in these two cases. Reason for producing such different distributions is the case 1 ended at time step 40 while case 2 stopped at time step 16. This earlier termination of the simulation is due to the turning off of the collagen growth function.

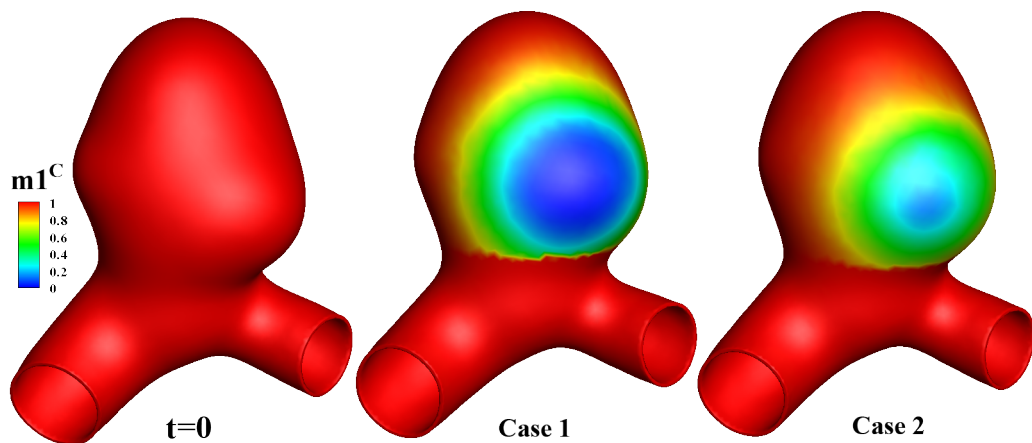


Figure 6.5: Initial mass density distribution of collagen which is 1 throughout the model and the ending states of $m1^C$ for case 1 and case 2 respectively.

Similar to elastin degradation, the rule for collagen degradation is the same but with distinct initial mass density distribution of collagenous constituent. Mass density of collagen fibres is 1 throughout the model hypothesized in this research showed in Figure 6.5. The remnants of collagenous constituents within the degradation area in case 1 are lower than that in case 2, which is similar to elastin degradation for the same reason. Here we use $m1^C$ to denote the collagen mass density inducing by the degradation mechanism to differentiate the mass density variation due to the growth function.

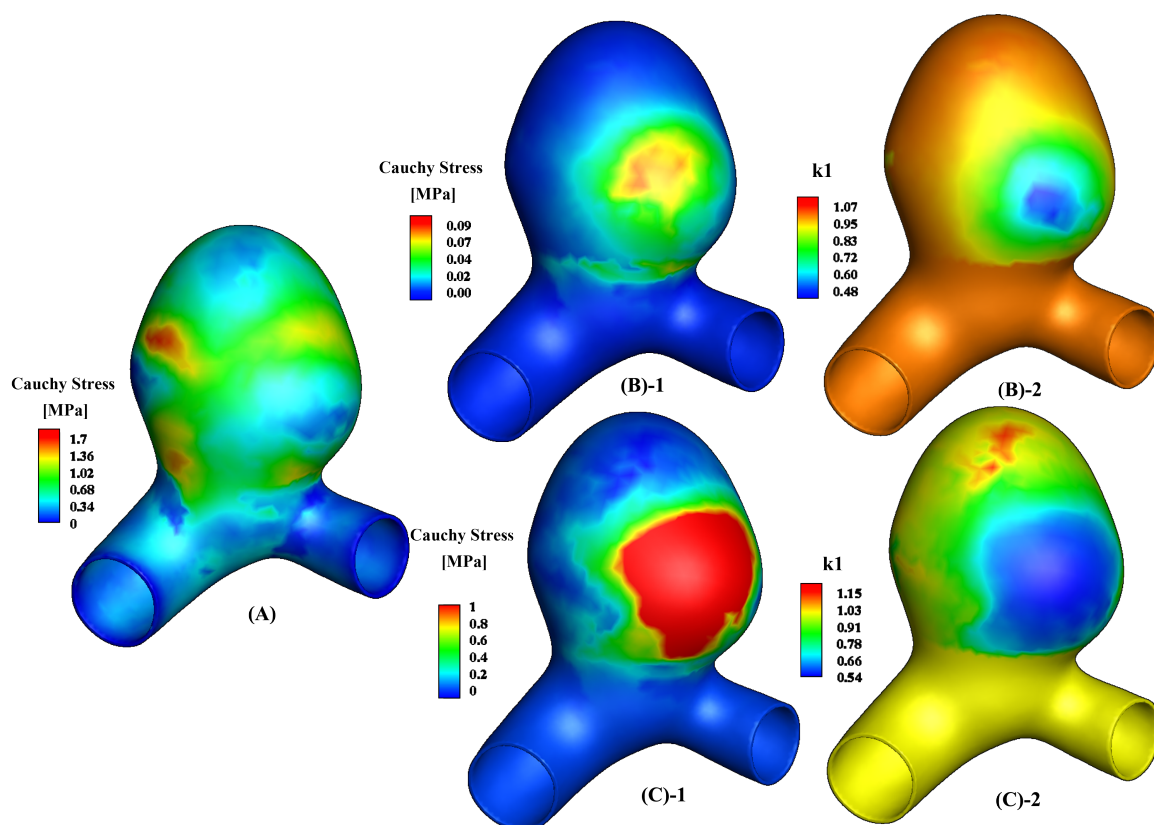


Figure 6.6: (A) Cauchy stress distribution at homeostasis. (B)-1 illustrates the Cauchy stress difference between the final state and the homeostatic level and (B)-2 shows the consequent k_1 remodelling result for case 1. (C)-1 and (C)-2 present the corresponding distributions showed in (B) for case 2. All pictures indicate the first family of collagen fibres, i.e. I_4 .

6.3.3 Collagen Remodelling

Collagen remodelling signifies that collagen fibres alter their mechanical behaviour, i.e. stiffness, in response to the mechanical loss and the increased stress in the tissue, and the former is derived from the destructive degradation in this research. This is a protective action to prevent the occurrence of the final rupture of an aneurysm. Collagen fibres remodel attempting to return the stress back to homeostatic level and the equation was formulated in Equ. 6.3.1. Given that the collagen remodelling is dependent on the stress deviation from the homeostasis, here we also plot the Cauchy stress distributions at homeostasis for both families of collagen fibres showed in Figure 6.6 (A) and Figure 6.7 (A) respectively, which are the same for case 1 and case 2.

Figure 6.6 introduces the k_1 evolution results of the first collagen family for case 1 and case 2 in (B) and (C). Homeostatic Cauchy stress distribution of the aneurysm model is shown in Figure 6.6 (A); maximum Cauchy stress is approximate 1.7 MPa and higher Cauchy stress presents in the margin regions of two dilations on the left and right side of the aneurysm model. Lower Cauchy stress shows on the dome of the aneurysm model and two small dilations. For case 1 with the collagen growth function, the maximal value of the Cauchy stress deviation is 0.09 MPa at the ending point of the simulation which is small enough to indicate that the stress is successfully dragged back to the homeostatic level. When switched off the growth function, the stress deviation is continuously increasing which reaches as high as 9.9 MPa. The color map is limited to 0-1 for the sake of showing the fully remodelling region. Generally, higher stress deviation would lead to lower magnitude of k_1 , but it seems that these two type of regions are not totally matched between (B)-1 and (B)-2, (C)-1 and (C)-2. It should be explicitly noted that the stress deviation is just determined by one time point while the k_1 remodelling is a cumulating consequence, this explains why the highest stress deviation area does not appear at the lowest k_1 region.

For the other family of collagen fibres (I_6), Cauchy stress distribution at homeostasis, stress deviation from homeostatic level and the consequent k_1 remodelling result for case 1 and case 2 are presented in Figure 6.7. A higher Cauchy stress region (up to 2 MPa) occurs around the right neck of the aneurysm model. Analogous to collagen family I_4 , higher Cauchy stress (0.8 ~ 1.2 MPa) is located around the root of two small bulbs and on the top of the whole aneurysm while two small dilations exhibit relative low Cauchy stress (0.4 ~ 0.8 MPa). For case 1, the maximum stress deviation is 0.08 MPa which means the stress level was dragged back to homeostatic level and k_1 remodelled to 0.42 at the final time point in response to the stress deviation. However, after turning off the growth function in case 2, the stress deviation keeps increasing up to 9.59 MPa but the color map is limited to 0-1 MPa for the same reason showed in Fig 6.6. This high stress deviation promoted the k_1 remodelled to 0.54 with a larger low k_1 region compared to case 1.

It is the same for collagen family I_4 and I_6 that the minimum value of remodelled k_1 in case 2 is lower than the minimum k_1 in case 1. Even though the high stress deviation will give rise to faster decline of k_1 in case 2, the F, S, G&R algorithm iterations stop earlier leading to a shortage of 24 times k_1 remodelling iterations due to the turning off of collagen growth function. This reveals the remodelling speed of k_1 in case 1 is slower than that in case 2, which is in agreement of the smaller stress deviation in case 1.

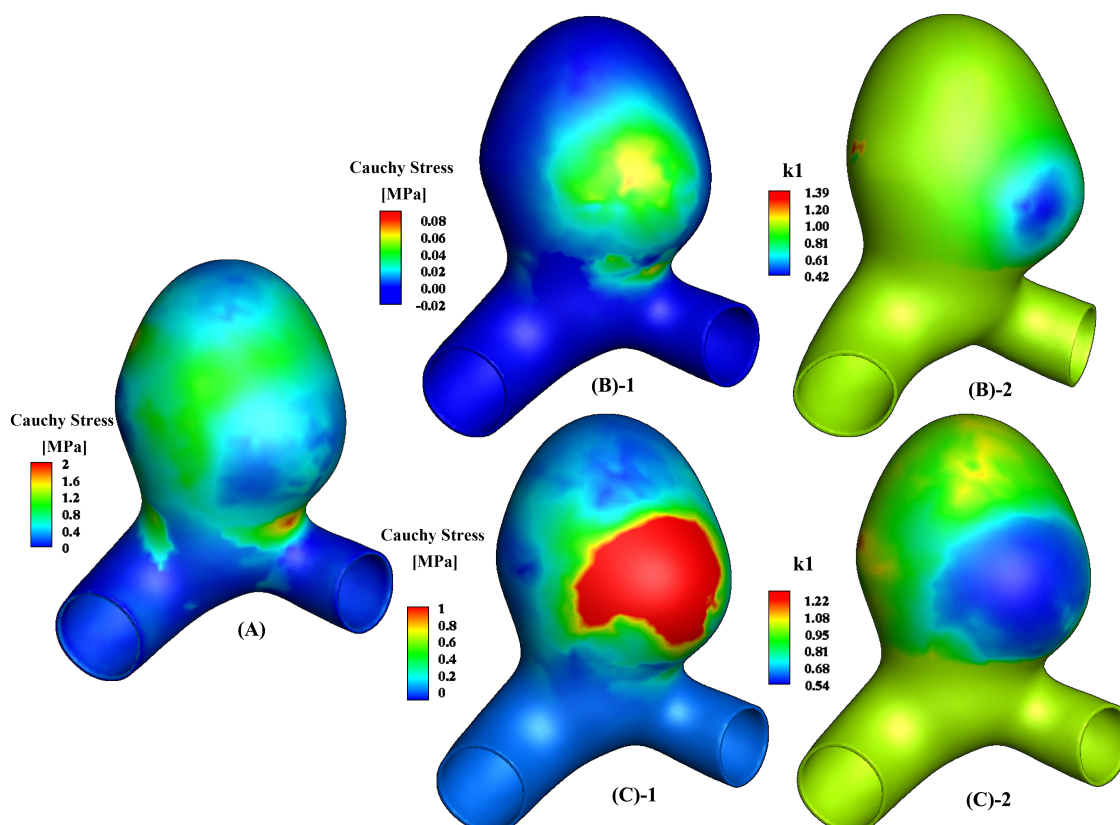


Figure 6.7: (A) Cauchy stress distribution at homeostasis. (B)-1 illustrates the Cauchy stress difference between the final state and the homeostatic level and (B)-2 shows the consequent k_1 remodelling result for case 1. (C)-1 and (C)-2 present the corresponding distributions showed in (B) for case 2. All pictures indicate the second family of collagen fibres, i.e. I_6 .

6.3.4 Adaption of Collagen Mass

As mentioned before, in face of the increased stretch along with the destructive degradation, fibroblasts remodels their recruitment stretch attempting to return the stretch on fibroblasts to the attachment stretch level. Through this recruitment stretch remodelling, function of fibroblasts is also regulated relating to the secreting and degenerating collagen fibres.

According to the hypothesis represented by Equ. 6.1.7, the mass density variation of collagen fibres is dependent on the stretch deviation of fibroblasts from the attachment stretch level through the fibroblasts remodelling pathway. Figure 6.9 (A)-(B) shows the stretch distribution of fibroblasts for collagen family I_4 and I_6 respectively. Fibroblasts stretch elevates to 1.069, which is approximate 1.8%, for both collagen families and region of high stretch is

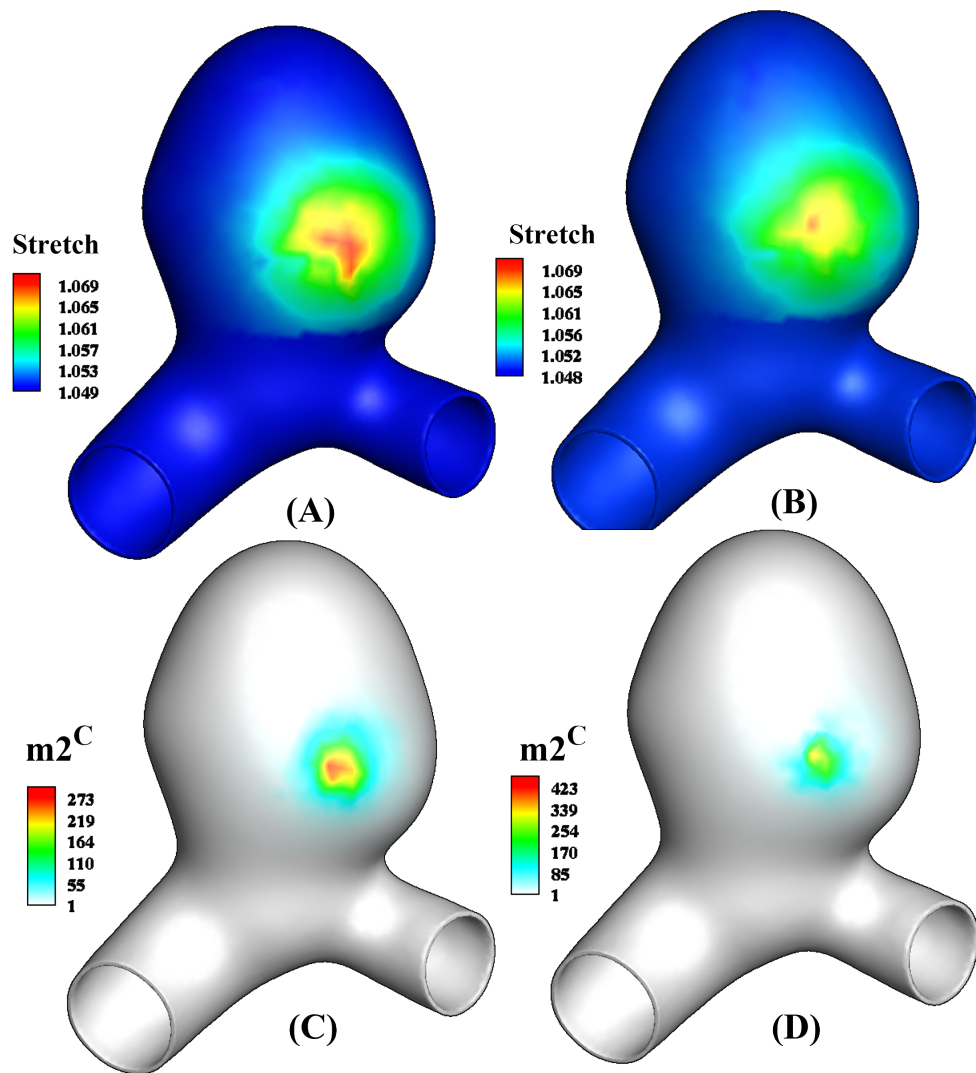


Figure 6.8: (A)-(B) show the stretch of fibroblasts at the ending time point in the direction of collagen family I_4 and I_6 respectively in case 1. Corresponding mass density distributions of collagen fibres mediated by fibroblasts mechanism are plotted in (C)-(D).

larger for collagen family I_4 . Mass density distributions of collagen are plotted in Figure 6.9 (C)-(D) for collagen family I_4 and I_6 respectively and we use white color to denote the original level of collagen mass density. The mass density variation owing to the atrophy/growth mechanism here is signified by $m2^C$. Correspondingly, the higher stretch leads to higher mass density distribution in the same region on the larger bulb. Mass density elevates to maximal level which is 273 folds compared to the collagen mass density in healthy artery for collagen

family I_4 and 423 folds for collagen family I_6 .

6.3.5 Collective Variation from Collagen Degradation and Adaption

To explicitly reveal the distinct variation of collagen mass density due to degradation via the inflammatory pathway and atrophy/growth mediated by fibroblasts, we introduce the related results separately by $m1^C$ and $m2^C$ distribution. In this section, the collective mass density variation of collagen fibres and the overall mechanical properties will be introduced as a representation of collagen fibres status after G&R. The collective mass density of collagen fibres can be formulated as:

$$m^C = m1^C * m2^C \quad (6.3.5)$$

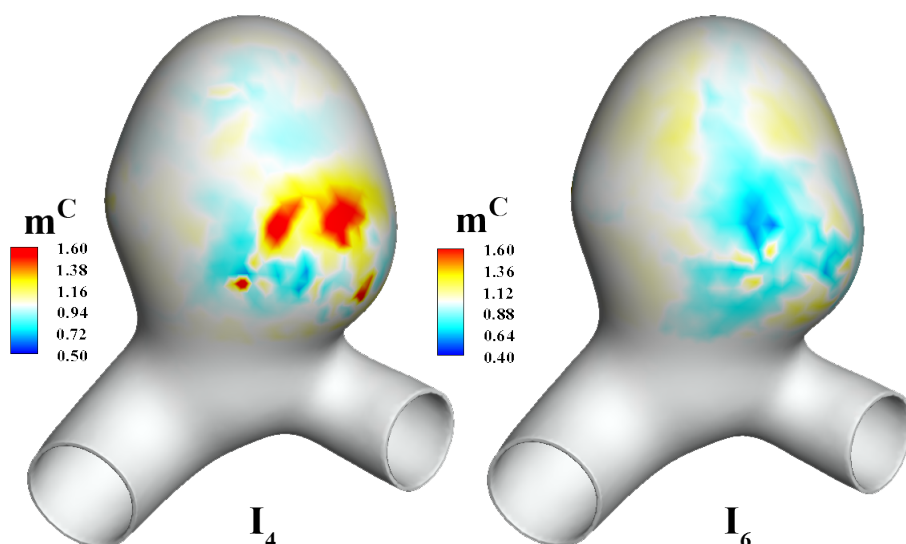


Figure 6.9: Collective mass density of two families of collagen fibres from the destructive degradation and growth function in case 1.

For case 2, there is no collagen growth function, hence the collective mass density m^C is the same to the resulting mass density of collagen from the degradation activities $m1^C$ in Figure 6.5. In case 1, in the prescribed region limited by the sphere model, the highest (about 2.04) and lowest (about 0.56) mass density of collagen family I_4 are concentrated here (Figure 6.9). But for collagen family I_6 , a largely concentrated low mass density region is presented on the larger bulb with a slightly higher mass density distribution surrounded sparsely (lower than 1.2).

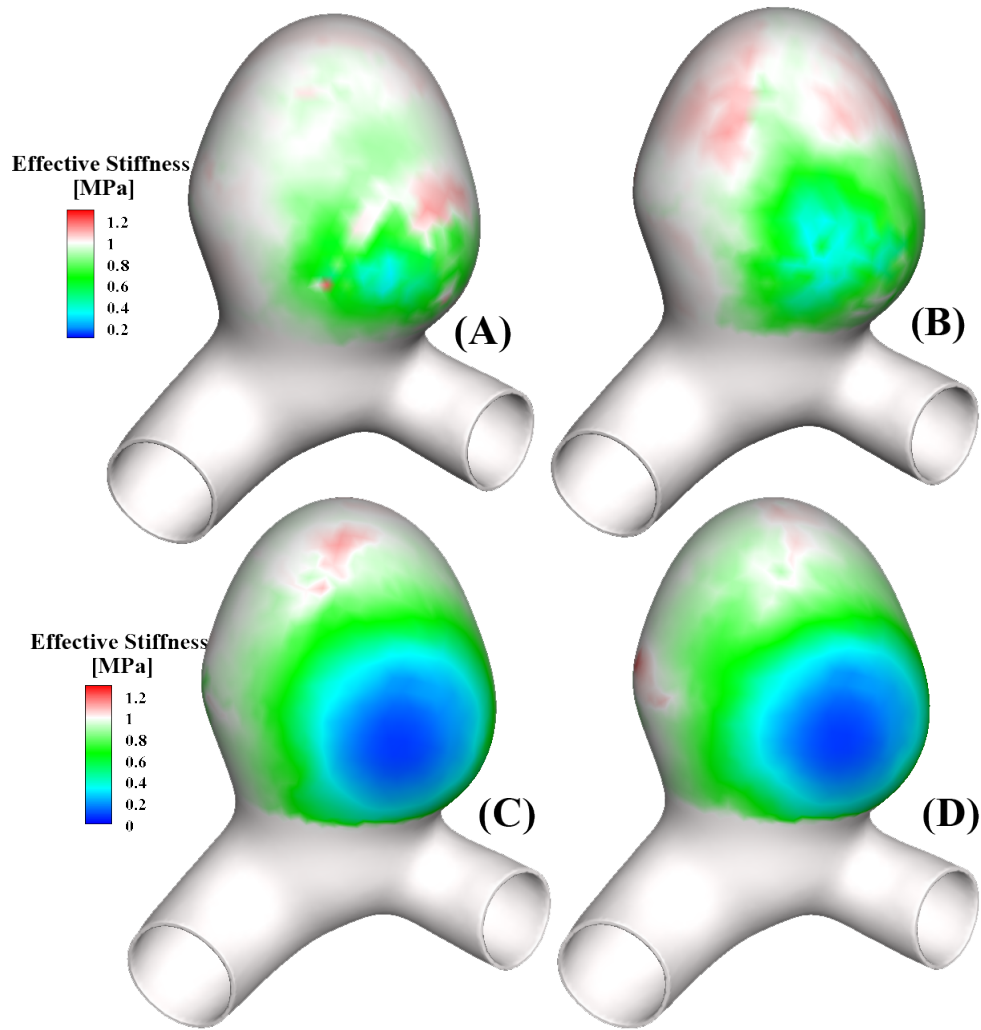


Figure 6.10: Effective stiffness distribution of two families of collagen fibres for case 1 (A-B) and case 2 (C-D).
 (A),(C): first family group, I_4 ; (B),(D): second family group, I_6 ;

Since the gross mass density of collagen fibres could be obtained, the overall mechanical behaviour of them could also be presented. k_1 and k_2 jointly determine the mechanical behaviour of collagen fibres while the k_2 in the modelling in this chapter was defined as a constant parameter. Therefore, the mechanical property of collagen fibres is only dependent on the k_1 value. Effective stiffness here is defined as the production of mass density and the stress-like material parameter k_1 which can represent the total mechanical condition of collagen fibres in the aneurysm model. Figure 6.10 illustrates the effective stiffness of collagen

fibres for case 1 (top) and case 2 (bottom). To clearly see the variation from the initial state that the effective stiffness is 1 everywhere, the color map was adjusted to show the unchanged region with white color. Remarkable low effective stiffness is presented in the second bulb region in case 2 which has no auxiliary collagen growth function (Figure 6.10 (C-D)). For case 1, most effective stiffness values range from 0.4 to 0.8 around the second bulb with a very small low effective stiffness region (below 0.4) for both I_4 and I_6 . Stiffer collagen fibres, i.e. higher than 1, are located on the boundary of decreased stiffness region and the area is larger for collagen family I_6 compared to I_4 (Figure 6.10 (A-B)).

6.4 Illustrative Results Link with Flow Metric with An Updated Prismatic Mesh

This section we developed a new prismatic mesh based on the same aneurysm geometry in order to improve the deformation ability and expand the extent of aneurysm enlargement. Two flow metrics, WSSAR and OSI, were linked to the aneurysm G&R algorithm here where the WSSAR case can as an comparison to the results showed in Chapter 5 to see whether this new prismatic mesh has stronger deformation capability. High OSI region was presented in a localized region, thus the OSI-linked case could as an illustrative model to simulate the irregular aneurysm evolution or secondary aneurysm growth.

6.4.1 Prismatic Mesh Generation

In the structural modelling section, we used tetrahedral elements which is highly automated. Tetrahedral elements can fit the complex geometry better with their simple computations but with a compensation with a weaker ability of large deformation. Through the above simulations, one possibility of the relative small growth of the aneurysm might be the mesh texture. Hexahedron elements have been reported superior than tetrahedral elements in the aspects of accuracy and deforming freedom but with excessive effort on mapping to arbitrary geometries. In this study, it is challenging to generate hexahedron mesh on the aneurysm geometry. Hence, here we employ the prismatic elements with 3 layers shown in Figure 6.11, following the method of generating boundary layers in CFD simulation.

In chapter 5, we linked two types of flow metric, WSS and WSSAR, to our R&G algorithm but without the collagen growth function. In the current chapter, to explicitly show the impact of collagen growth regulated by fibroblasts, we muted the hemodynamic linking and use the prescribed degradation function instead. Due to numerical problems with convergence

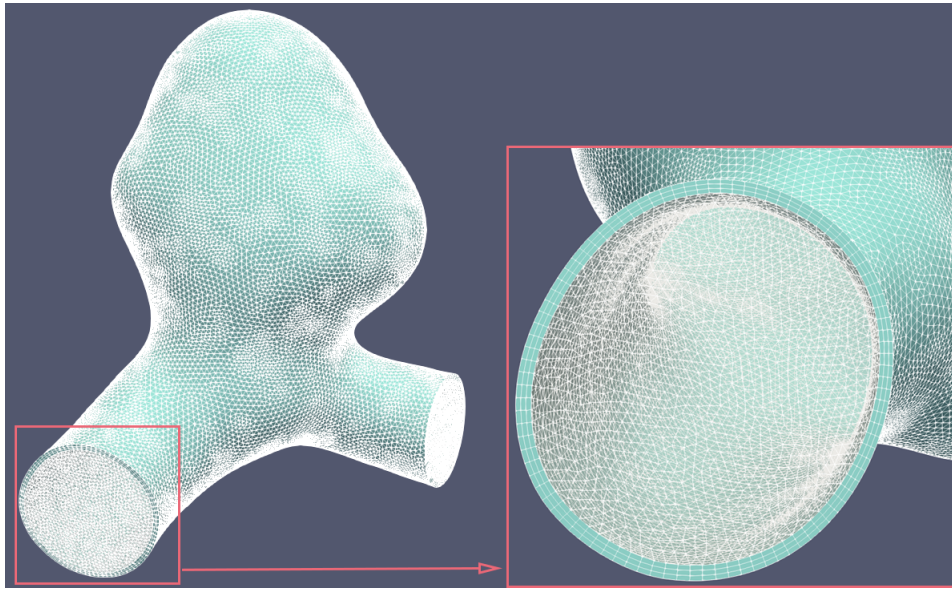


Figure 6.11: Prismatic mesh on the aneurysm model

caused by the highly nonlinear exponential of collagen fibres, the collagen growth function was turned off for the following simulations. On basis of the preceding two chapters, here we use two illustrative integrated p-FSG cases linking with flow stimuli, WSSAR and OSI, to show the full results.

6.4.2 p-FSG link with WSSAR

In this section, we employed the degradation method associated to WSSAR flow metric showed in chapter 5 and deactivated the collagen growth function to make a comparison with the results presented in chapter 5. Because the specific methods has been introduced elaborately, so here we just show the modelling results of the aneurysm growth and the anisotropic distribution of collagen fibres as representative results. Core correlation functions between WSSAR and the normalized mass density of collagen fibres were formulated in Equation 5.4.3 and Equation 5.4.4.

According to this degradation rule, the degradation given when linking to AR in figure 6.12 shows a large area affected, mainly across the anterior surface of the aneurysm sac. Generally, higher WSSAR region led to stronger degradation, resulting in lower mass density presented on the aneurysm. The white region in WSSAR distribution means the values are below 0.6 while it means the undegraded collagen fibres. At $t=3$, the normalized collagen mass density is reduced to a value of approximately 0.6 shown in green and there is some growth of the

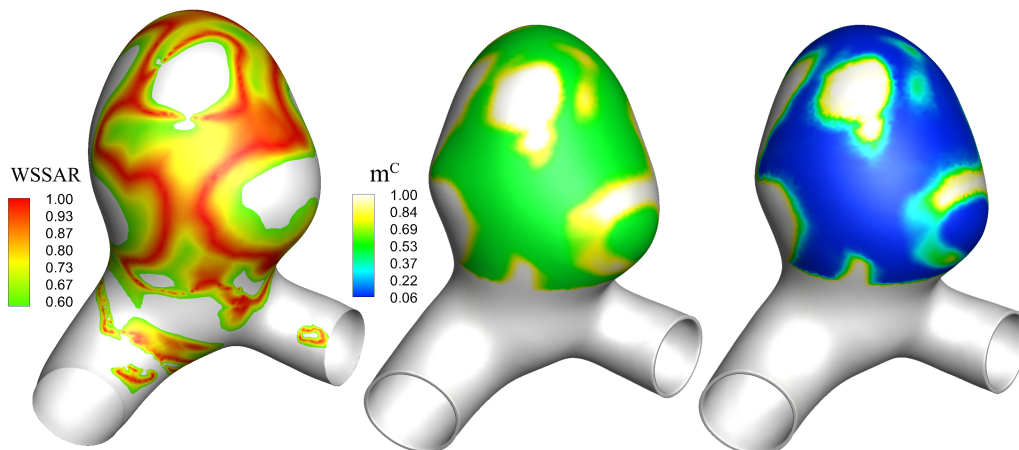


Figure 6.12: Spatial distribution of WSSAR at initial state and normalised mass density of collagen fibres as aneurysm evolves with degradation linked to WSSAR from left to right at $t=3$ and $t=6$.

aneurysm sac noticeable. There is significant growth of the aneurysm sac visible at the final time step and further degradation of collagen fibres, reduced to 0.1; meaning that less than 10% of the initial collagen mass remains.

To test the deformation ability of this new prismatic mesh, we plotted the comparison of aneurysm geometries between the initial state ($t=0$) and the final geometrical state ($t=6$) in Figure 6.13.

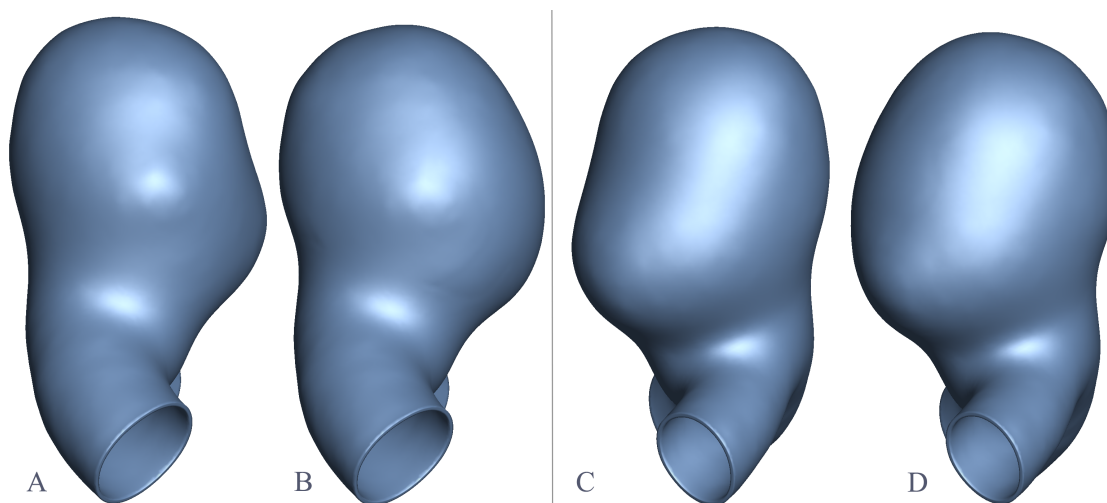


Figure 6.13: Left (A-B) and right (C-D) lateral views of pressurized aneurysm and the final state of the aneurysm growth.

This comparison indicates an obvious bulge out region where has high WSSAR distribution (Figure 6.13(B, D)). In Chapter 5, to quantify the aneurysm growth, we calculated difference of aneurysm volumes from the initial state to final state. However, due to the locally enlargement here, it is not reasonable to quantify the growth by the overall volume increase-ment. Aneurysm growth showed in Figure 5.13(c) is more likely an overall growth, which is hardly to notice the correspondence between the high WSSAR region and the larger growth area. However, the p-FSG framework with this new prismatic mesh can clearly represent this mapping relationship. Results indicates that this prismatic mesh is able to perform a better deformation in simulating the aneurysm evolution.

6.4.3 p-FSG link with OSI

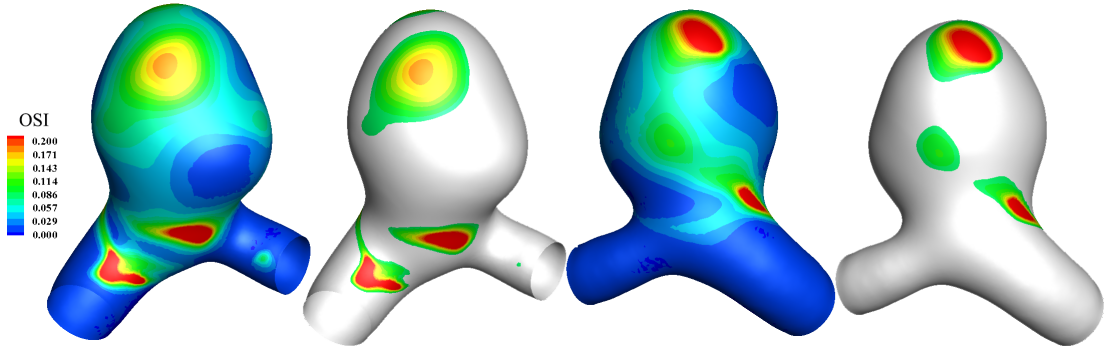


Figure 6.14: Left (A-B) and right (C-D) lateral views of pressurized aneurysm and the final state of the aneurysm growth.

Most aneurysms are irregular and part of them can grow a secondary aneurysm based on the original one. This requires a demand for locally enlargement when models the aneurysm evolution. Through the analysis of hemodynamic indices presented in Chapter 3, here we use OSI as an effective hemodynamic stimulus from the blood flow. Follow the degradation rules, it is necessary to define the threshold of OSI_{Crit} and OSI_{max} in the Equation below:

$$\mathcal{F}_{D(OSI)}^C(t) = \begin{cases} 0, & OSI(t) \leq OSI_{Crit} \\ \left(\frac{OSI(t) - OSI_{Crit}}{OSI_{max} - OSI_{Crit}} \right), & OSI_{Crit} < OSI(t) < OSI_{max} \\ 1, & OSI(t) \geq OSI_{max} \end{cases} \quad (6.4.1)$$

The physiological OSI threshold was suggested to be taken as 0.2 above which the damage of endothelial cells is triggered (Glor et al., 2004). To determine an appropriate threshold for

OSI_{Crit} and OSI_{max} , we plotted the OSI distribution where the color bar was limited to 0 to 0.2 (Figure 6.14).

The OSI distribution in Figure 6.14 appears to have areas of high oscillatory nature at the top of dome on both posterior and anterior sides of the aneurysm, around the neck of the aneurysm and more towards the upstream side of the aneurysm. A maximum value of 0.2 is reached for this patient specific model shown in red. OSI value below 0.075 was cut off and represented by the white color, from which the high OSI region was basically captured. Hence, the OSI_{Crit} here was defined as 0.075. In terms of OSI_{max} , we selected the boundary between the green and yellow color where the OSI value is around 0.1 as the threshold value.

Like the results represented in the last section, here we only plot the OSI distribution and the mass density of collagen fibres, to show the degradation function, and the aneurysm configuration comparison as representative results.

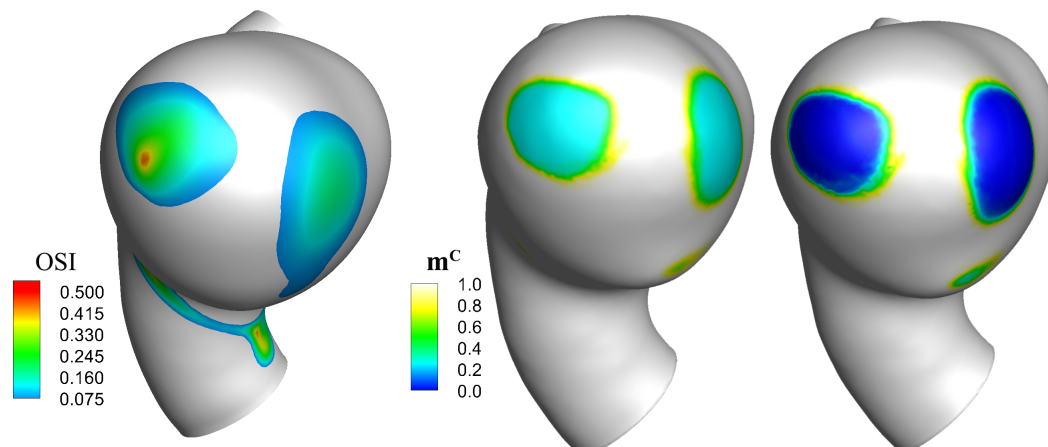


Figure 6.15: Spatial distribution of OSI at initial state and normalised mass density of collagen fibres as aneurysm evolves with degradation linked to WSSAR from left to right at $t=4$ and $t=7$.

The degradation linked to OSI in Figure 6.15 above shows high rates of degradation with significant aneurysm growth localised at the areas of high OSI easy to see by the aneurysm wall bulging, where the normalised mass density of collagen fibres decreases below 0.05; shown in blue. There are also areas of lower degradation identified with normalized mass density of collagen fibres at approximately 0.5 shown in green. There is clearly deformation shown in Figure 6.16, but it is restricted to small areas causing meshing issues and the simulation to stop. The geometry produced has become irregular with two prominently protruding areas of growth near the top of the aneurysm sac, this simulation only considers the OSI at $t=0$ however the irregular geometry produced would likely have an effect on the flow dynamics

so would be recommended that this simulation is repeated with flow solving at each step.

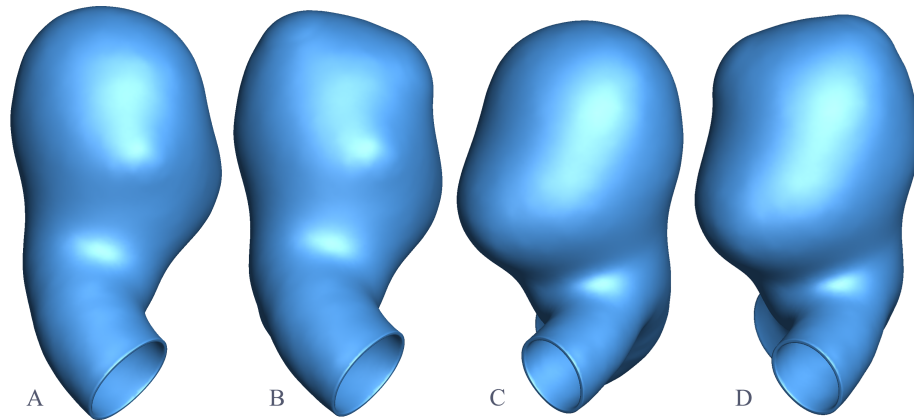


Figure 6.16: Left (A-B) and right (C-D) lateral views of pressurized aneurysm ($t=0$) and the final state ($t=7$) of the aneurysm growth mediated by OSI.

Overall, in this section we utilize a prismatic mesh to replace the original tetrahedron one generated in ANSYS APDL automatically. With the linking with flow metrics, WSSAR and OSI, results show that this new mesh has a stronger ability in dealing with large deformation (WSSAR case) compared to the same p-FSG presented in Chapter 5. Meanwhile, the OSI case successfully simulated the condition of irregular enlargement or a secondary aneurysm growth.

6.5 Discussion

The motivation behind this illustrative study is investigating the impact of collagen growth function on the aneurysm stability. For the sake of explicitly showing the difference between turning on and turning off the collagen growth function, the degradation should be limited to a noticeable and localized region. An obvious geometric feature of our aneurysm model is that there is a larger bulb on the right side, which implies a possibility of a second aneurysm development, which is a very common phenomenon in the aneurysm disease. To mimic a secondary aneurysm evolution, we use a sphere model to localize the destructive degradation scope close to the larger bulb in this model rather than link to the flow environment shown in Chapter 5.

Firstly, we compared the further enlargement of the aneurysm model and results showed that the model with collagen growth function only dilated a neglected extent. As a comparison, the model without collagen growth function presented a remarkable growth in the lo-

calized region. A stable aneurysm is generally defined as remaining unchanged or growing at a creeping speed for a long time which is safe for staying in the brain. Taken in this sense, the enlarged model in case 1 after 40 times F-S-G&R iterations could be regarded as a stable aneurysm. For saving the solving time from the haemodynamic analysis, here we use a prescribed degradation algorithm with an exponential function in the prescribed region. The mass density of elastin and collagen both decreased in this region as the degradation results. In response to the elevated stress induced by the enlargement, collagen fibres remodel themselves via k_1 aiming to maintain the stress level at homeostasis. Results showed that the case 1 model with collagen growth implementation had successively maintained the Cauchy stress at the homeostatic level but the Cauchy stress in case 2 was continuously increasing until the final failure of the simulation even there was a much larger region of low k_1 distribution. Key hypothesis in this chapter is the recruitment stretch remodelling of fibroblasts and the collagen atrophy/growth function mediated by fibroblasts, hence we analysed the mass density variation of collagen fibres through this pathway. The higher stretch deviation regions presented more collagen growth which is consistent with the hypothesis that stretch deviation (decrease/increase) of fibroblasts from the attachment level drives the collagen atrophy/growth. Because the collagen mass density variation derived from two processes: degradation and fibroblasts mediation, the gross variation was also investigated to show the consequent collagen mass and their mechanical properties distributions. Collagen mass density distributed unevenly of collagen family I_4 around the larger bulb with crossed high and low mass density distribution in Case 1. For I_6 , a larger region with lower mass density was shown at the same site but the collective collagen mass density was still higher than that in case 2 due to the growth function. It has been proved by histological studies that the quantity of collagen fibres was lower in ruptured aneurysm (Gaetani et al., 1998; Vanrossomme et al., 2015). Aneurysm stability relies on a dynamic balance kept by the competition between aneurysm wall repair and destruction, i.e. collagen degradation and G&R function (Etminkan, Rinkel, 2016). This is in agreement with our study in case 1, the incorporation of the collagen growth function enables the aneurysm geometry to keep as original profile or only enlarge a small extent. The effective stiffness showed a slightly lower region in case 1 while an extremely low effective stiffness with a large region presented in case 2. One recent experimental study analysed 42 aneurysms and results showed that softer aneurysms have a higher rupture risk (Brunel et al., 2017). Several mechanical studies also indicated that the stiffer wall presented a lower rupture risk in contrast to softer aneurysms (Costalat et al., 2011; Sanchez et al., 2013; Brunel et al., 2018). According to this, results of effective stiffness in this research also suggested that the aneurysm model in case 1 is a stable aneurysm. Through the analysis of all results, the geometric analysis, mass density and effective stiffness distributions of collagen

fibres are supported mutually and collaboratively indicate that the collagen growth is a pivotal function in the stabilization of aneurysms.

Degradation of elastin and collagen linked to flow metric has been elaborately introduced in the last chapter and practically employed in the P-FSG framework. Here we utilized the prescribed degradation function was aiming to compare the influence of collagen growth clearly and save the computational time. It is straightforward to integrated the flow-mediated degradation and fibroblasts-mediated growth into one P-FSG framework, which is an integrated P-FSG framework.

6.6 Concluding Remarks

As has been mentioned throughout this thesis, for the sake of modelling aneurysm evolution to become more sophisticated, more explicit descriptions of arterial mecha-nobiology needed to incorporated in our P-FSG framework. In this chapter, two comparative aneurysm models were investigated with the collagen growth function turning on and turning off. Although the degradation function here was prescribed rather than linked to flow metric, the correct representation of related hypotheses have been proved by the mass density results of elastin and collagen in this chapter and the flow-mediated degradation has been validated in the last chapter. The geometric analysis, mass density and effective stiffness distributions of collagen fibres were analysed and these results indicated that modelling the collagen growth mediated by fibroblasts is necessary which is an effective self-protective mechanism for the stabilization of an aneurysm. Moreover, through the test of a new prismatic mesh, aneurysm growth results compared to Chapter 5 indicate that this mesh can produce a larger growth and can mimic an secondary aneurysm growth based on the existing one.



Conclusion: Summaries and Considerations for Future Development

7.1 Summaries and Contributions	177
7.2 Limitations	180
7.3 Potential Improving Points in Future Work	181
7.4 Concluding Remarks	184

A novel patient-specific fluid-solid-growth framework was developed in this research involving the clinical screening image data, mechanobiological behaviour of load bearing fibres and the representation of mechanotransduction between force stimuli and cellular response. This framework was designed to investigate the aneurysm stability by mathematically modelling the biomechanical responses of main components within the aneurysmal tissue, i.g. elastin, collagen fibres, endothelial cells and fibroblasts. This chapter will give a brief summary firstly to conclude the study of each chapter and further to extract the main points of

contributions of this research. Undoubtedly, there are a few limitations exist in this thesis which will be explicitly declared in the second section. According to the current limitations, a few potential improving points are proposed in order to realize the final application in assisting clinical diagnosis.

7.1 Summaries and Contributions

7.1.1 Brief Summaries for Preceding Chapters

Chapter 2 introduced the general concepts of FSG framework and chapter 3-5 basically decomposes this FSG framework into fluid simulation, solid modelling and G&R implementation to comprise this full framework. While chapter 6 made a sophistication with the consideration of the collagen atrophy/growth mechanism driven by fibroblasts forming an integrated P-FSG framework.

Structural-mediated model for vascular wall has been reviewed in Chapter 2 and the model in (Holzapfel et al., 2000) was employed in this research with the mechanical representation of elastin and collagen fibres. This model requires the clear information on collagen fibres direction which is the component of the SEF for collagen. For a cylindrical tube, it could be easily represented by angles while for complex geometries, it was reported that the collagen fibres align with the principal curvature directions (Section 4.4.2). On the grounds that there is no available experimental data about the mechanical properties could be used for the intracranial aneurysm in this research, hence the mechanical behaviour of the aneurysm section and the parent artery section were both determined by a sphere model and a cylindrical model respectively according to the load bearing proportional allocation (Section 4.3.2).

On the haemodynamic side, we employed another aneurysm model which has the follow-up data to investigate the relationship between the aneurysm growth and haemodynamic features. Aneurysm growth was quantified by two indices (growth quantification): Displacement Index (DI) and Area Stretch Ratio (ASR) (Selimovic, 2013). Analysis results suggested that the aneurysm growth was associated with large deviations of the instantaneous WSS vector which probably is a driver for the aneurysm growth. A novel flow metric named WSSAR, clearly captured the magnitude and direction of every instantaneous WSS over one cardiac cycle, thus the oscillatory flow is better captured compared to OSI and AFI. WSSAR has been suggested to signify the preferable alignment direction of endothelial cells (Krishna et al., n.d.) and it was adopted in this research to characterise the morphology of endothelial cells. We proposed a hypothesis that the aneurysm growth is linking to the endothelial permeability which is associated to morphology of endothelial cells (Section 3.4).

Vascular mechanical homeostasis is significant to the function and dysfunction of the arterial wall and it is necessary to be explicitly linked to the G&R hypotheses. The arterial or aneurysmal wall has a remarkable capability of adapting relative tissues to varying mechanical conditions. This adaptation capacity was represented by a fundamental hypothesis that the G&R mechanisms aim to drive the arterial mechanical system to homeostatic states. Definitions of vascular mechanical homeostasis employed throughout this thesis are listed as follows:

- stretch homeostasis for fibroblasts
- stress homeostasis for collagen fibres

Collagen remodelling process is collagen fibres remodel their mechanical properties to drag the stress on fibres to homeostatic level (Section 5.2.2). While fibroblasts are responsible for the atrophy/growth of collagen fibres as well as the deposition and their function is determined by the stretch they sensed. The mass density of collagen fibres was regulated by fibroblasts which mediated by the stretch. This follows the hypothesis that fibroblasts aim to retain or return the stretch to the homeostatic level through the stretch remodelling which drives the collagen growth function (Section 6.1). In chapter 5, collagen remodelling was achieved by the decreasing of k_2 which is a control parameter in the SEF of collagen fibres. Results showed that the higher stress deviation on collagen fibres led to lower k_2 distribution but the whole deformation was relatively small. In chapter 6, we replaced the k_2 with k_1 owing to the high non-linearity of k_2 in the exponential term which easily drove the divergence of the solution. Meanwhile, to test the collagen growth function implemented in chapter 6 and to mimic the formation of a second bleb, a sphere model was applied on the aneurysm model to localize the functional region with G&R. Two scenarios were built up with and without the growth function, and results showed that the growth function was the key mechanism to aneurysm stabilization. However, the elastin and collagen degradation was prescribed which needs to link the flow in further development.

7.1.2 Main Contributions

This p-FSG framework is built upon a previous FSG framework developed by the research group lead by Paul Watton. Novel sophistications to current mathematical models, including the representation of the mechanobiology of endothelial cells and thick-walled patient-

specific aneurysm model, were motivated from the important mechanobiological notions and clinical applications:

- **Growth from Clinical State: Patient-specific Aneurysm Model**

This P-FSG framework applies the growth and remodelling function on a patient-specific aneurysm, i.e. modelling the aneurysm growth based on the clinical state. Existing aneurysm growth models are all derived from a cylindrical membrane or thick-walled tube, even though a part of researches with the word 'patient-specific' in the title, the patient-specific segments actually mean the parent artery connected to the aneurysm section which was still replaced by a cylindrical tube.

- **Representation of Endothelium in G&R Function by Implementing a Novel Flow Metric**

G&R function has been investigated for decades and in this research we related mechanobiology of the endothelium layer to the G&R function. Here a novel flow metric, WSSAR, was employed to represent the endothelial cells morphology, which formulates a function of endothelial permeability. Recently, the inflammatory activities within the aneurysm wall has been highly emphasized to the aneurysm growth and rupture. Endothelial permeability plays a pivotal role associated with the inflammation which enables this inflammatory pathway can be numerically modelled.

- **Endothelial Response to Pulsatile Flow instead of Steady Flow**

In previous FSG framework, the elastin degradation was linking to the flow metric, WSS, calculated by the steady flow condition. Oscillatory flow characteristics can significantly influence the mechanobiological response of cells, like OSI and AR, and the cell responses play critical roles in the G&R process. Hence, in this p-FSG framework, we started linking the pulsatile flow as the hemodynamic stimuli to endothelial cells response, further impact the tissue growth and remodelling function.

- **Commercial Software ANSYS was Employed to be Fully Adapted with G&R in (Watton et al., 2004)**

Compared to the previous FSG framework, we utilized a thick-walled model generated in ANSYS APDL to replace the membrane model. For a complex geometry with automatically generated mesh by the commercial software ANSYS, we defined a new coordinate system which provides a clear boundary to differentiate the aneurysm section and healthy artery section, then apply the G&R methods in (Watton et al., 2004) successfully to the aneurysm section for modelling the further evolution of an aneurysm. More importantly, most aneurysms

are accompanied with thrombosis and this thick-walled aneurysm model provides a platform to simulate the oxygen transportation which is highly impacted by the thrombosis. A leading hypothesis is that the observed locations of low WSS related to wall hypoxia, which could lead to increased endothelium permeability. As proposed in this study, the endothelium permeability plays a significant role in the aneurysm progression.

7.2 Limitations

• Absence of Unloaded Geometry

In the structural modelling section, the inner surface of the reconstructed model was applied the systolic pressure as the boundary condition. However, the aneurysm model we utilized here was reconstructed by the screening images indicating that it was already under a certain load from the pulsatile blood flow. Specifically, the volume of the original aneurysm model was 406.77 mm^3 and grew to 496.765 mm^3 after the pressurization process, indicating that the geometry undergoes a change of approximately 22%. In this research, we regarded this loaded geometry as a unloaded one which may bring some deviation in contrast to the reality state, like in the case of quantification of growth volume.

• Uniform Wall Thickness of Aneurysm Model

In terms of our structural modelling, uniform thickness of the aneurysm was set due to the limitation from current scan technique but this thickness was based on the experimental test. The G&R function, i.e. collagen remodels with the Cauchy stress deviation from that at the homeostatic condition while the collagen growth is driven by the fibroblasts function mediated by the stretch stimuli, is also influenced by the thickness which contributes to the stress distribution which could further impact the accuracy of the structural modelling. Hence, the uniform thickness of the aneurysm setting is one limitation in our p-FSG framework which could be improved from two aspects: improving with the imaging technology until it can capture the wall outlines and considering the volumetric growth into the G&R function (Grytsan et al., 2017a), i.e. model the thickness development based on mechanical environment.

• Representation of Endothelial Cells only Considered the WSS Influence

As to the CFD simulation module, here we just defined two WSSAR thresholds to differentiate the endothelial cells morphology which has not been validated by corresponding experiments. Moreover, endothelial morphology in this research is dependent on the fluid stimuli without the consideration of cyclic stretch which also highly impacts on the align-

ment and function of endothelial cells. With respect to this, we have investigated a 1D model of endothelial cells alignment under the influence of combined WSS and cyclic stretch reciprocally which has been investigated and will be introduced in the Appendix C with some preliminary results. However, this is still a premature study, which needs more research before its application.

- **Growth Extent of Aneurysm Model is Limited**

This is a major shortcoming of this study where the aneurysm model has only limited deformation. Final termination of all G&R simulations are owing to the excessive distortion of certain elements rather than the stabilization of the aneurysm itself. This is probably the problem from the ANSYS solver where the solving ability for hyperelastic material deformation is not strong enough or our G&R function still needs to refine at some points, which needs further investigation. The other possible reason is the mesh generated by ANSYS is unstructured with a relatively disordered distribution, a more structured mesh would be helpful to generate a larger deformation.

7.3 Potential Improving Points in Future Work

Mathematical models inevitably need to make certain simplifications compared to the real targeted subject with complex constituents and structure. With the knowledge of the limitations of our model, there are a few refinements can be made in future work. Firstly, our solid model is relatively simple, i.e. one layer with the same material property everywhere, the initial heterogeneity of aneurysm wall and the volumetric growth should be considered into the sophistication of the solid model. A majority of aneurysms are accompanied with thrombosis remarkably influence the molecule transportation across the aneurysm wall. Therefore, our structural model embedded with a thrombus layer cooperated with transport function could be considered as a direction for further investigation in the assessment of aneurysm stability.

7.3.1 Sophistication of the Structural Model

Due to the complexity of the aneurysm geometry, the model in P-FSG framework is simplified the media and adventitia layers as one mixed monolayer. In the future work, two distinctive media and adventitia layers could be implemented in a patient-specific model to simulate the aneurysm evolution more specifically. Simultaneously, with the rapid development of medical imaging technology, the uniform thickness of our aneurysm model could be replaced by

the localized thickness through the aneurysm wall, which will also benefit the computational model to achieve more realistic simulation results.

In the presented P-FSG framework, we assume the models is isochoric, i.e. non-volume changing, during the aneurysm progression, while mass density variation of the elastin and collagen constituents existed. As mentioned before, the thickness is associated with the stress distribution which involves the collagen remodelling function in G&R. The volumetric adaption has been highlighted the importance for the modelling of aneurysm evolution (Humphrey, Holzapfel, 2012). The formulation of volumetric change as a consequence of the local mass change of certain constitutes was proposed (Schmid et al., 2012; Eriksson et al., 2014) where the mass changed could lead to volume or density change with the other one constant:

- Constant individual density (CID): individual density is constant while the individual volume changes;
- Adaptive individual density (AID): individual density is adaptive while the individual volume is constant.

Results made by (Eriksson et al., 2014) suggested that the modelling of elastin degradation is suitable for the AID approach because the CID could changes the natural reference configuration of the elastin fibres, thus leading to the shirk of the arterial wall. As the elastin loses, the reduction in elastin mass is compensated by increased mass of proteoglycans and other connective tissues. While for collagen growth, the CID approach can depict the position with the largest volume increase in the aneurysm dome is just where the mass of collagen is largest. And the density change is much lower than the mass change for collagen. Applying these two approaches to our P-FSG framework, the wall thickness could be predicted by achieving the volumetric changes as a consequence of G&R accurately. In contrast to isotropic growth, a AAA aneurysm growth model with anisotropic volumetric change has been investigated (Grytsan et al., 2017a).

7.3.2 Modelling Endothelium Permeability Mechanobiologically

Not only intracranial aneurysms, but other cardiovascular diseases are also all highly related to endothelial cells function. Most cardiovascular diseases are first driven by the dysfunction of endothelial cells which means that the first defence layer diminishes its normal function. The gathering effect of this dysfunction is the changing permeability of this location, which gives the large fenestration to micro molecules allowing them to break into the media and adventitia layer. The cell alignment information can provide insight into the angles between cells, via which the gap among cells could be quantified. The input parameters in the mod-

elling of endothelial cells alignment are WSS and cyclic stretch which could be obtained from the haemodynamic simulation and structural modelling of specific vascular geometries, a preliminary study will be shown in Appendix C (1D model). This leads to the high practicalness to further apply to 3D modelling. Once this alignment of endothelial cells is modelled, the permeability of this endothelium layer could be further investigated in a more specific way. In the following research, if we can mimic the morphology and alignment of endothelial cells, the gap among cells would be calculated more accurately. Then the permeability could be quantified using this gap information, and link to other pathological processes to simulate the development of sorts of cardiovascular diseases, i.g., aneurysms. Moreover, the endothelial cells modelling of their mechanobiology properties represents an inflammation pathway, and the screening technique with high-contrast agents can indicate the inflammation activities on images, which is also an essential factor for aneurysm revolution and rupture.

7.3.3 Transport Model with Thrombosis

The primary purpose of building the thrombus layer (Figure 7.1) is to understand the pathological process of oxygen transport to aneurysm evolution, and possibly mimic the changing environment of oxygen levels with propagating thrombus and cellular adaptive response during aneurysm evolution.

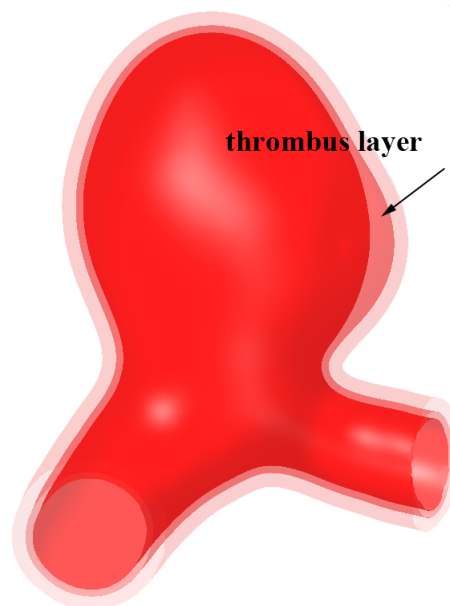


Figure 7.1: A conceptual model of aneurysm with a thrombus layer embedded

In future modelling, the disturbance of the chemical environment on cellular function-

ality, here we focus on oxygen concentration, will be cooperated into our P-FSG framework to link to the G&R function contributing to aneurysm evolution. As showed in Figure 7.1, the thrombus layer with non-uniform thickness could be integrated into our aneurysm model while it is just a conceptual model at this stage. Thrombus will impede the oxygen transport to the wall driving a distinct cellular composition and decomposition as well as the function expression which belongs to the G&R modulus.

The transport model of a healthy artery and an aneurysm with thrombus has been built in my research group. Hence it would be straight forward to combine that transport model to this P-FSG framework forming a more sophisticated model.

7.3.4 Model Validation by Clinical Follow-up Data

All researches related to aneurysm evolution, no matter the clinical/experimental investigation or mathematical models are aiming to interpret the known information to underline pathological mechanisms and ultimately develops as a clinical tool for guiding the diagnosis and treatment. For any research, the eventual target should always be in the direction of clinical application with the investigation in basic science. The rupture risk assessment of intracranial aneurysms, i.e. aneurysm stability, has been extensively investigated (reviewed in 1.4) but there is still no reliable criteria could indicate the rupture risk accurately.

The current P-FSG framework is able to model the aneurysm growth based on the clinical state. Theoretically, the stability could be determined by the final growing degree. However, parameters like collagen growth and remodelling need to be optimized by clinical follow-up images representing different stages of aneurysm growth, then generalized P-FSG framework could serve as a clinical tool in differentiating the stability of aneurysms. Investigations on virtual stent deployments coupling with reliable mechanobiological modelling of the arterial and aneurysm wall could also apply to help on clinical intervention.

7.4 Concluding Remarks

A novel patient-specific FSG framework presented in this thesis is built up to investigate the intracranial aneurysm stability with the representation of the mechanobiological function of cells and structural constituents under mechanical stimuli (structural/haemodynamic). Even though the understanding of intracranial aneurysm inception, enlargement and rupture are still not clear, models of mechanobiology are significant for the understanding of physiological and pathophysiological arterial processes. Our multiscale and multiphysics simulation for modelling aneurysm evolution involves the representation of arterial con-

stituents with the G&R capacity, i.e. the synthesis and adaptation of the cells (fibroblast, ECs) and mechanobiology regulation of structural components (elastin and collagen fibres) . Although the further application of this study still requires additional biological research, the coupling between this modelling framework and experimental study could enhance our current understanding of aneurysm progression and the rupture risk assessment.

References

- Acevedo-Bolton Gabriel, Jou Liang-Der, Dispensa Bradley P, Lawton Michael T, Higashida Randall T, Martin Alastair J, Young William L, Saloner David.* Estimating the hemodynamic impact of interventional treatments of aneurysms: numerical simulation with experimental validation: technical case report // *Neurosurgery*. 2006. 59, 2. E429–E430.
- Alberts B, Dennis B, Lewis J, Raff M, Roberts K, , Watson JD.* Localization of atherosclerotic lesions in the human basilar artery // *Molecular Biology of the Cell*, 3 edn. 1994. 978–986.
- Amenta Peter, Valle Edison, Dumont Aaron, Medel Ricky.* Inflammation and intracranial aneurysms: mechanisms of initiation, growth, and rupture // *Neuroimmunology and Neuroinflammation*. 2015. 2, 2. 68–68.
- Anwar MA, Shalhoub J, Lim CS, Gohel MS, Davies AH.* The effect of pressure-induced mechanical stretch on vascular wall differential gene expression // *Journal of vascular research*. 2012. 49, 6. 463–478.
- Aoki Tomohiro, Kataoka Hiroharu, Ishibashi Ryota, Nozaki Kazuhiko, Morishita Ryuichi, Hashimoto Nobuo.* Reduced collagen biosynthesis is the hallmark of cerebral aneurysm: contribution of interleukin-1 β and nuclear factor- κ B // *Arteriosclerosis, thrombosis, and vascular biology*. 2009c. 29, 7. 1080–1086.
- Aoki Tomohiro, Kataoka Hiroharu, Morimoto Masafumi, Nozaki Kazuhiko, Hashimoto Nobuo.* Macrophage-derived matrix metalloproteinase-2 and-9 promote the progression of cerebral aneurysms in rats // *Stroke*. 2007a. 38, 1. 162–169.
- Aoki Tomohiro, Kataoka Hiroharu, Nishimura Masaki, Ishibashi Ryota, Morishita Ryuichi, Miyamoto Susumu.* Regression of intracranial aneurysms by simultaneous inhibition of nuclear factor- κ B and Ets with chimeric decoy oligodeoxynucleotide treatment // *Neurosurgery*. 2011a. 70, 6. 1534–1543.
- Aoki Tomohiro, Kataoka Hiroharu, Shimamura Munehisa, Nakagami Hironori, Wakayama Kouji, Moriwaki Takuya, Ishibashi Ryota, Nozaki Kazuhiko, Morishita Ryuichi, Hashimoto Nobuo.* NF- κ B is a key mediator of cerebral aneurysm formation // *Circulation*. 2007c. 116, 24. 2830–2840.

- Aparício Pedro, Thompson Mark S, Watton Paul N.* A novel chemo-mechano-biological model of arterial tissue growth and remodelling // *Journal of biomechanics*. 2016. 49, 12. 2321–2330.
- Arrese Ignacio, Sarabia Rosario, Pintado Rebeca, Delgado-Rodriguez Miguel.* Flow-diverter devices for intracranial aneurysms: systematic review and meta-analysis // *Neurosurgery*. 2013. 73, 2. 193–200.
- Aumailley M, Krieg T, Razaka G, Müller PK, Bricaud H.* Influence of cell density on collagen biosynthesis in fibroblast cultures // *Biochemical Journal*. 1982. 206, 3. 505–510.
- Austin G, Fisher S, Dickson D, Anderson D, Richardson S.* The significance of the extracellular matrix in intracranial aneurysms // *Annals of Clinical & Laboratory Science*. 1993. 23, 2. 97–105.
- Baek S, Rajagopal KR, Humphrey JD.* Competition between radial expansion and thickening in the enlargement of an intracranial saccular aneurysm // *Journal of Elasticity*. 2005. 80, 1-3. 13–31.
- Baek S, Rajagopal KR, Humphrey JD.* A theoretical model of enlarging intracranial fusiform aneurysms // *Journal of biomechanical engineering*. 2006. 128, 1. 142–149.
- Bederson Joshua B, Awad Issam A, Wiebers David O, Piepgras David, Haley Jr E Clarke, Brott Thomas, Hademenos George, Chyatte Douglas, Rosenwasser Robert, Caroselli Cynthia.* Recommendations for the management of patients with unruptured intracranial aneurysms: a statement for healthcare professionals from the Stroke Council of the American Heart Association // *Circulation*. 2000. 102, 18. 2300–2308.
- Birk David E, Trelstad Robert L.* Extracellular compartments in tendon morphogenesis: collagen fibril, bundle, and macroaggregate formation. // *The Journal of cell biology*. 1986. 103, 1. 231–240.
- Birukov Konstantin G, Jacobson Jeffrey R, Flores Alejandro A, Ye Shui Q, Birukova Anna A, Verin Alexander D, Garcia Joe GN.* Magnitude-dependent regulation of pulmonary endothelial cell barrier function by cyclic stretch // *American Journal of Physiology-Lung Cellular and Molecular Physiology*. 2003. 285, 4. L785–L797.
- Bishop Jill E, Lindahl Gisela.* Regulation of cardiovascular collagen synthesis by mechanical load // *Cardiovascular research*. 1999. 42, 1. 27–44.
- Borel JP, Bellon G.* Vascular collagens. General review // *Pathologie-biologie*. 1985. 33, 4. 254–260.
- Boussel Loic, Rayz Vitaliy, McCulloch Charles, Martin Alastair, Acevedo-Bolton Gabriel, Lawton Michael, Higashida Randall, Smith Wade S, Young William L, Saloner David.* Aneurysm growth occurs at region

- of low wall shear stress // *Stroke*. 2008. 39, 11. 2997–3002.
- Boutouyrie Pierre, Laurent Stéphane, Benetos Athanase, Girerd Xavier J, Hoeks Arnold Pg, Safar Michel E.* Opposing effects of ageing on distal and proximal large arteries in hypertensives. // *Journal of hypertension. Supplement: official journal of the International Society of Hypertension*. 1992. 10, 6. S87–91.
- Brembeck Felix H, Rosário Marta, Birchmeier Walter.* Balancing cell adhesion and Wnt signaling, the key role of β -catenin // *Current opinion in genetics & development*. 2006. 16, 1. 51–59.
- Brinjikji W, Zhu Y-Q, Lanzino G, Cloft HJ, Murad MH, Wang Z, Kallmes DF.* Risk factors for growth of intracranial aneurysms: a systematic review and meta-analysis // *American Journal of Neuroradiology*. 2016. 37, 4. 615–620.
- Brisman Jonathan L, Song Joon K, Newell David W.* Cerebral aneurysms // *New England journal of medicine*. 2006. 355, 9. 928–939.
- Brunel Hervé, Ambard Dominique, Dufour H, Roche PH, Costalat Vincent, Jourdan Franck.* Relationship between cerebral aneurysm wall stiffness and rupture risk // *Computer methods in biomechanics and biomedical engineering*. 2017. 20, sup1. 33–34.
- Brunel Hervé, Ambard Dominique, Dufour H, Roche PH, Costalat Vincent, Jourdan Franck.* Rupture limit evaluation of human cerebral aneurysms wall: Experimental study // *Journal of biomechanics*. 2018. 77. 76–82.
- Bruno Gerard, Todor Roxanne, Lewis Isabel, Chyatte Douglas.* Vascular extracellular matrix remodeling in cerebral aneurysms // *Journal of neurosurgery*. 1998. 89, 3. 431–440.
- Buck Robert C.* Reorientation response of cells to repeated stretch and recoil of the substratum // *Experimental Cell Research*. 1980. 127, 2. 470–474.
- Buckley MJ, Banes AJ, Levin LG, Sumpio BE, Sato M, Jordan R, Gilbert J, Link GW, Tran R Son Tay.* Osteoblasts increase their rate of division and align in response to cyclic, mechanical tension in vitro. // *Bone and mineral*. 1988. 4, 3. 225–236.
- Butt Richard P, Laurent Geoffrey J, Bishop Jill E.* Mechanical load and polypeptide growth factors stimulate cardiac fibroblast activity // *Annals of the New York Academy of Sciences*. 1995. 752, 1. 387–393.
- Canham Peter B, Finlay Helen M, Dixon Jan G, Boughner Derek R, Chen Andrew.* Measurements from light and polarised light microscopy of human coronary arteries fixed at distending pressure // *Cardiovascular research*. 1989. 23, 11. 973–982.

- Carver Wayne, Nagpal Madan L, Nachtigal Maurice, Borg Thomas K, Terracio Louis.* Collagen expression in mechanically stimulated cardiac fibroblasts. // *Circulation research.* 1991. 69, 1. 116–122.
- Cebral Juan, Ollikainen Eliisa, Chung Bong Jae, Mut Fernando, Sippola Visa, Jahromi Behnam Rezai, Tulamo Riikka, Hernesniemi Juha, Niemelä Mika, Robertson Anne, others .* Flow conditions in the intracranial aneurysm lumen are associated with inflammation and degenerative changes of the aneurysm wall // *American Journal of Neuroradiology.* 2017. 38, 1. 119–126.
- Cebral Juan R, Duan Xinjie, Chung Bong Jae, Putman Christopher, Aziz Khaled, Robertson AM.* Wall mechanical properties and hemodynamics of unruptured intracranial aneurysms // *American Journal of Neuroradiology.* 2015. 36, 9. 1695–1703.
- Cebral Juan R, Mut Fernando, Weir Jane, Putman Christopher.* Quantitative characterization of the hemodynamic environment in ruptured and unruptured brain aneurysms // *American Journal of Neuroradiology.* 2011. 32, 1. 145–151.
- Chakraborty Amlan, Chakraborty Sutirtha, Jala Venkatakrishna R, Haribabu Bodduluri, Sharp M Keith, Berson R Eric.* Effects of biaxial oscillatory shear stress on endothelial cell proliferation and morphology // *Biotechnology and bioengineering.* 2012. 109, 3. 695–707.
- Chalouhi Nohra, Ali Muhammad S, Jabbour Pascal M, Tjoumakaris Stavropoula I, Gonzalez L Fernando, Rosenwasser Robert H, Koch Walter J, Dumont Aaron S.* Biology of intracranial aneurysms: role of inflammation // *Journal of Cerebral Blood Flow & Metabolism.* 2012. 32, 9. 1659–1676.
- Chalouhi Nohra, Hoh Brian L, Hasan David.* Review of cerebral aneurysm formation, growth, and rupture // *Stroke.* 2013. 44, 12. 3613–3622.
- Chen Yuh-Lien, Jan Kung-Ming, Lin Huai-San, Chien Shu.* Ultrastructural studies on macromolecular permeability in relation to endothelial cell turnover // *Atherosclerosis.* 1995. 118, 1. 89–104.
- Chien Shu.* Mechanotransduction and endothelial cell homeostasis: the wisdom of the cell // *American Journal of Physiology-Heart and Circulatory Physiology.* 2007. 292, 3. H1209–H1224.
- Chiquet Matthias, Gelman Laurent, Lutz Roman, Maier Silke.* From mechanotransduction to extracellular matrix gene expression in fibroblasts // *Biochimica et Biophysica Acta (BBA)-Molecular Cell Research.* 2009. 1793, 5. 911–920.
- Chiquet Matthias, Renedo Ana Sarasa, Huber François, Flück Martin.* How do fibroblasts translate mechanical signals into changes in extracellular matrix production? // *Matrix biology.* 2003. 22, 1. 73–80.

- Chuong CJ, Fung YC.* Three-dimensional stress distribution in arteries // *Journal of biomechanical engineering.* 1983. 105, 3. 268–274.
- Civelekoglu G, Tardy Y, Meister J-J.* Modeling actin filament reorganization in endothelial cells subjected to cyclic stretch // *Bulletin of mathematical biology.* 1998. 60, 6. 1017–1037.
- Claiborne Johnston S, Wilson Charles B, Halbach Van V, Higashida Randall T, Dowd Christopher F, McDermott Michael W, Applebury Carol B, Farley Thomas L, Gress Daryl R.* Endovascular and surgical treatment of unruptured cerebral aneurysms: comparison of risks // *Annals of neurology.* 2000. 48, 1. 11–19.
- Costalat Vincent, Sanchez Mathieu, Ambarb Dominique, Thines L, Lonjon Nicolas, Nicoud Franck, Brunel H, Lejeune JP, Dufour Henri, Bouillot P, others.* Biomechanical wall properties of human intracranial aneurysms resected following surgical clipping (IRRAs Project) // *Journal of biomechanics.* 2011. 44, 15. 2685–2691.
- Cox ROBERT H.* Effects of age on the mechanical properties of rat carotid artery // *American Journal of Physiology-Heart and Circulatory Physiology.* 1977. 233, 2. H256–H263.
- Crompton MR.* Mechanism of growth and rupture in cerebral berry aneurysms // *British medical journal.* 1966. 1, 5496. 1138.
- Dallon John C, Sherratt Jonathan A.* A mathematical model for fibroblast and collagen orientation // *Bulletin of mathematical biology.* 1998. 60, 1. 101–129.
- Darnell James E, Lodish Harvey F, Baltimore David, others.* *Molecular cell biology.* 2. 1990. book.
- Dartsch PC, Hämmerle H.* Orientation response of arterial smooth muscle cells to mechanical stimulation. // *European journal of cell biology.* 1986. 41, 2. 339–346.
- Davies Peter F, Remuzzi Andrea, Gordon Ethel J, Dewey C Forbes, Gimbrone Michael A.* Turbulent fluid shear stress induces vascular endothelial cell turnover in vitro // *Proceedings of the National Academy of Sciences.* 1986. 83, 7. 2114–2117.
- Dhar Sujan, Tremmel Markus, Mocco J, Kim Minsuok, Yamamoto Junichi, Siddiqui Adnan H, Hopkins L Nelson, Meng Hui.* Morphology parameters for intracranial aneurysm rupture risk assessment // *Neurosurgery.* 2008. 63, 2. 185–197.
- Di Achille Paolo, Humphrey Jay D.* Toward large-scale computational fluid-solid-growth models of intracranial aneurysms // *The Yale journal of biology and medicine.* 2012. 85, 2. 217.
- Diagbouga Mannekomba R, Morel Sandrine, Bijlenga Philippe, Kwak Brenda R.* Role of

- hemodynamics in initiation/growth of intracranial aneurysms // *European journal of clinical investigation*. 2018. 48, 9. e12992.
- Dobrin PB, Mrkvicka R.* Failure of elastin or collagen as possible critical connective tissue alterations underlying aneurysmal dilatation // *Cardiovascular Surgery*. 1994. 2, 4. 484–488.
- Dobrin Philip B, Baker William H, Gley William C.* Elastolytic and collagenolytic studies of arteries: implications for the mechanical properties of aneurysms // *Archives of Surgery*. 1984. 119, 4. 405–409.
- Doenitz Christian, Schebesch Karl-Michael, Zoepfel Roland, Brawanski Alexander.* A mechanism for the rapid development of intracranial aneurysms: a case study // *Neurosurgery*. 2010. 67, 5. 1213–1221.
- Driessen NJB, Wilson W, Bouten CVC, Baaijens FPT.* A computational model for collagen fibre remodelling in the arterial wall // *Journal of theoretical biology*. 2004. 226, 1. 53–64.
- Erhart Philipp, Grond-Ginsbach Caspar, Hakimi Maani, Lasitschka Felix, Dihlmann Susanne, Böckler Dittmar, Hyhlik-DÜrr Alexander.* Finite element analysis of abdominal aortic aneurysms: predicted rupture risk correlates with aortic wall histology in individual patients // *Journal of endovascular therapy*. 2014. 21, 4. 556–564.
- Eriksson TSE, Watton PN, Luo XY, Ventikos Y.* Modelling volumetric growth in a thick walled fibre reinforced artery // *Journal of the Mechanics and Physics of Solids*. 2014. 73. 134–150.
- Eroschenko Victor P, Di Fiore Mariano SH.* Di-Fiore's atlas of histology with functional correlations. 2013. book.
- Etminan Nima, Dreier Rita, Buchholz Bruce A, Beseoglu Kerim, Bruckner Peter, Matzenauer Christian, Torner James C, Brown Robert D, Steiger Hans-Jakob, Hänggi Daniel, others .* Age of collagen in intracranial saccular aneurysms // *Stroke*. 2014. 45, 6. 1757–1763.
- Etminan Nima, Rinkel Gabriel J.* Unruptured intracranial aneurysms: development, rupture and preventive management // *Nature Reviews Neurology*. 2016. 12, 12. 699.
- Feng Yixiang, Wada Shigeo, Tsubota Ken-Ichi, Yamaguchi Takami.* Growth of Intracranial Aneurysms Arised from Curved Vessels under the Influence of Elevated Wall Shear Stress-A Computer Simulation Study // *JSME International Journal Series C Mechanical Systems, Machine Elements and Manufacturing*. 2004. 47, 4. 1035–1042.
- Figueroa C Alberto, Baek Seungik, Taylor Charles A, Humphrey Jay D.* A computational framework for fluid–solid-growth modeling in cardiovascular simulations // *Computer methods in applied mechanics*

- and engineering. 2009. 198, 45-46. 3583–3602.
- Fillinger Mark F, Marra Steven P, Raghavan Madhavan L, Kennedy Francis E.* Prediction of rupture risk in abdominal aortic aneurysm during observation: wall stress versus diameter // *Journal of vascular surgery.* 2003. 37, 4. 724–732.
- Finlay Helen M, Whittaker Peter, Canham Peter B.* Collagen organization in the branching region of human brain arteries // *Stroke.* 1998. 29, 8. 1595–1601.
- Fogelholm Rainer, Hernesniemi Juha, Vapalahti Matti.* Impact of early surgery on outcome after aneurysmal subarachnoid hemorrhage. A population-based study. // *Stroke.* 1993. 24, 11. 1649–1654.
- Forsting M, Wanke I.* Intracranial Vascular Malformations and Aneurysms: From Diagnostic Work-Up to Endovascular Therapy. 2009.
- Frosen Juhana, Piippo Anna, Paetau Anders, Kangasniemi Marko, Niemela Mika, Hernesniemi Juha, Jaaskelainen Juha.* Remodeling of saccular cerebral artery aneurysm wall is associated with rupture: histological analysis of 24 unruptured and 42 ruptured cases // *Stroke.* 2004. 35, 10. 2287–2293.
- Fu Bingmei M, Tarbell John M.* Mechano-sensing and transduction by endothelial surface glycocalyx: composition, structure, and function // *Wiley Interdisciplinary Reviews: Systems Biology and Medicine.* 2013. 5, 3. 381–390.
- Fujiwara Keigi, Masuda Michitaka, Osawa Masaki, Kano Yumiko, Katoh Kazuo.* Is PECAM-1 a mechanoresponsive molecule? // *Cell structure and function.* 2001. 26, 1. 11–17.
- Fung YC, Fronek K, Patitucci P.* Pseudoelasticity of arteries and the choice of its mathematical expression // *American Journal of Physiology-Heart and Circulatory Physiology.* 1979. 237, 5. H620–H631.
- Gaetani Paolo, Tartara Fulvio, Grazioli Vittorio, Tancioni Flavio, Infuso Lodovico, Baena Riccardo Rodriguez y.* Collagen cross-linkage, elastolytic and collagenolytic activities in cerebral aneurysms: a preliminary investigation // *Life sciences.* 1998. 63, 4. 285–292.
- Gaetani Paolo G, Baena Riccardo Rodriguez y, Tartara Fulvio, Luca Messina Alberto, Tancioni Flavio, Schiavo Roberta, Grazioli Vittorio.* Metalloproteases and intracranial vascular lesions // *Neurological research.* 1999. 21, 4. 385–390.
- Gasser T Christian, Auer Martin, Labruto F, Swedenborg J, Roy J.* Biomechanical rupture risk assessment of abdominal aortic aneurysms: model complexity versus predictability of finite element simulations // *European Journal of Vascular and Endovascular Surgery.* 2010. 40, 2. 176–185.

- Gasser T Christian, Ogden Ray W, Holzapfel Gerhard A.* Hyperelastic modelling of arterial layers with distributed collagen fibre orientations // *Journal of the royal society interface.* 2005. 3, 6. 15–35.
- Glor FP, Ariff B, Hughes AD, Crowe LA, Verdonck PR, Barratt DC, Thom SA McG, Firmin DN, Xu XY.* Image-based carotid flow reconstruction: a comparison between MRI and ultrasound // *Physiological measurement.* 2004. 25, 6. 1495.
- Grinnell Frederick.* Fibroblast biology in three-dimensional collagen matrices // *Trends in cell biology.* 2003. 13, 5. 264–269.
- Gruttmann F, Taylor RL.* Theory and finite element formulation of rubberlike membrane shells using principal stretches // *International Journal for Numerical Methods in Engineering.* 1992. 35, 5. 1111–1126.
- Grytsan Andrii, Eriksson Thomas SE, Watton Paul N, Gasser T Christian.* Growth description for vessel wall adaptation: a thick-walled mixture model of abdominal aortic aneurysm evolution // *Materials.* 2017a. 10, 9. 994.
- Grytsan Andrii, Watton Paul N, Gasser T Christian.* Isotropic versus anisotropic growth description for abdominal aortic aneurysm evolution // *Proceedings of the 5th International Conference on Computational & Mathematical Biomedical Engineering.* 2017b. 127–130.
- Grytsan Andrii, Watton Paul N, Holzapfel Gerhard A.* A thick-walled fluid–solid-growth model of abdominal aortic aneurysm evolution: Application to a patient-specific geometry // *Journal of biomechanical engineering.* 2015. 137, 3. 031008.
- Gupta Vishal, Grande-Allen K Jane.* Effects of static and cyclic loading in regulating extracellular matrix synthesis by cardiovascular cells // *Cardiovascular research.* 2006. 72, 3. 375–383.
- Hansen F, Mangell Peter, Sonesson Björn, Länne Toste.* Diameter and compliance in the human common carotid artery—variations with age and sex // *Ultrasound in medicine & biology.* 1995. 21, 1. 1–9.
- Hariton I, Gasser TC, Holzapfel GA, others .* Stress-driven collagen fiber remodeling in arterial walls // *Biomechanics and modeling in mechanobiology.* 2007. 6, 3. 163–175.
- Harris Albert K, Stopak David, Wild Patricia.* Fibroblast traction as a mechanism for collagen morphogenesis // *Nature.* 1981. 290, 5803. 249.
- Hasan David, Chalouhi Nohra, Jabbour Pascal, Hashimoto Tomoki.* Macrophage imbalance (M1 vs. M2) and upregulation of mast cells in wall of ruptured human cerebral aneurysms: preliminary results // *Journal of neuroinflammation.* 2012. 9, 1. 222.

- Hasan David M, Hesitad Donald.* Early Change in Ferumoxytol-Enhanced Magnetic Resonance Imaging Signal Suggests Unstable Human Cerebral Aneurysm. A Pilot Study. 2013.
- Hasan David M, Mahaney Kelly B, Brown Jr Robert D, Meissner Irene, Piepgras David G, Huston John, Capuano Ana W, Torner James C, Unruptured Intracranial Aneurysms Investigators International Study of.* Aspirin as a promising agent for decreasing incidence of cerebral aneurysm rupture // *Stroke*. 2011. 42, 11. 3156–3162.
- Hashimoto Tomoki, Meng Hui, Young William L.* Intracranial aneurysms: links among inflammation, hemodynamics and vascular remodeling // *Neurological research*. 2006. 28, 4. 372–380.
- Hassler Ove.* Morphological studies on the large cerebral arteries, with reference to the aetiology of subarachnoid haemorrhage. // *Acta psychiatrica Scandinavica. Supplementum*. 1961. 154. 1.
- Hatami J, Tafazzoli-Shadpour M, Haghhighipour N, Shokrgozar MA, Janmaleki M.* Influence of cyclic stretch on mechanical properties of endothelial cells // *Experimental Mechanics*. 2013. 53, 8. 1291–1298.
- He Chang M, Roach Margot R.* The composition and mechanical properties of abdominal aortic aneurysms // *Journal of vascular surgery*. 1994. 20, 1. 6–13.
- Herrmann Harald, Bär Harald, Kreplak Laurent, Strelkov Sergei V, Aebi Ueli.* Intermediate filaments: from cell architecture to nanomechanics // *Nature Reviews Molecular Cell Biology*. 2007. 8, 7. 562.
- Hodis Simona, Uthamaraj Susheil, Smith Andrea L, Dennis Kendall D, Kallmes David F, Dragomir-Daescu Dan.* Grid convergence errors in hemodynamic solution of patient-specific cerebral aneurysms // *Journal of biomechanics*. 2012. 45, 16. 2907–2913.
- Hoh Brian L, Sistrom Christopher L, Firment Christopher S, Fautheree Gregory L, Velat Gregory J, Whiting Jobyna H, Reavey-Cantwell John F, Lewis Stephen B.* Bottleneck factor and height-width ratio: association with ruptured aneurysms in patients with multiple cerebral aneurysms // *Neurosurgery*. 2007. 61, 4. 716–723.
- Holzapfel Gerhard A, Gasser Thomas C, Ogden Ray W.* A new constitutive framework for arterial wall mechanics and a comparative study of material models // *Journal of elasticity and the physical science of solids*. 2000. 61, 1-3. 1–48.
- Hong Yuan, Wang Yong-Jie, Deng Zheng, Wu Qun, Zhang Jian-Min.* Stent-assisted coiling versus coiling in treatment of intracranial aneurysm: a systematic review and meta-analysis // *PloS one*. 2014. 9, 1. e82311.
- Hsu Hui-Ju, Lee Chin-Fu, Kaunas Roland.* A dynamic stochastic model of frequency-

- dependent stress fiber alignment induced by cyclic stretch // *PloS one*. 2009. 4, 3. e4853.
- Huang David, Chang Thomas R, Aggarwal Achal, Lee Raphael C, Ehrlich H Paul*. Mechanisms and dynamics of mechanical strengthening in ligament-equivalent fibroblast-populated collagen matrices // *Annals of biomedical engineering*. 1993. 21, 3. 289–305.
- Humphrey JD*. Remodeling of a collagenous tissue at fixed lengths // *Journal of biomechanical engineering*. 1999. 121, 6. 591–597.
- Humphrey JD*. Vascular adaptation and mechanical homeostasis at tissue, cellular, and sub-cellular levels // *Cell biochemistry and biophysics*. 2008. 50, 2. 53–78.
- Humphrey Jay D, Holzapfel Gerhard A*. Mechanics, mechanobiology, and modeling of human abdominal aorta and aneurysms // *Journal of biomechanics*. 2012. 45, 5. 805–814.
- Hurley Nicole E, Schildmeyer Lisa A, Bosworth Kami A, Sakurai Yumiko, Eskin Suzanne G, Hurley Laurence H, McIntire Larry V*. Modulating the functional contributions of c-Myc to the human endothelial cell cyclic strain response // *Journal of vascular research*. 2010. 47, 1. 80–90.
- Iba Toshiaki, Sumpio Bauer E*. Morphological response of human endothelial cells subjected to cyclic strain in vitro // *Microvascular research*. 1991. 42, 3. 245–254.
- Investigators Unruptured Intracranial Aneurysms, others*. Unruptured intracranial aneurysms: Risk of rupture and risks of surgical intervention-International Study of Unruptured Intracranial Aneurysms Investigators // *N Engl J Med*. 1998. 339. 1725–1733.
- Isaksen Jørgen Gjernes, Bazilevs Yuri, Kvamsdal Trond, Zhang Yongjie, Kaspersen Jon H, Waterloo Knut, Romner Bertil, Ingebrigtsen Tor*. Determination of wall tension in cerebral artery aneurysms by numerical simulation // *Stroke*. 2008. 39, 12. 3172–3178.
- Ishibashi Ryota, Aoki Tomohiro, Nishimura Masaki, Hashimoto Nobuo, Miyamoto Susumu*. Contribution of mast cells to cerebral aneurysm formation // *Current Neurovascular Research*. 2010. 7, 2. 113–124.
- Ivanov Dmitry, Dol Aleksandr, Polienko Asel*. Patient-specific hemodynamics and stress-strain state of cerebral aneurysms // *Acta of bioengineering and biomechanics*. 2016. 18, 2.
- Jamous Mohammad A, Nagahiro Shinji, Kitazato Keiko T, Satoh Koichi, Satomi Junichiro*. Vascular corrosion casts mirroring early morphological changes that lead to the formation of saccular cerebral aneurysm: an experimental study in rats // *Journal of neurosurgery*. 2005. 102, 3. 532–535.

- Janiga Gábor, Berg Philipp, Beuing Oliver, Neugebauer Mathias, Gasteiger Rocco, Preim Bernhard, Rose Georg, Skalej Martin, Thévenin Dominique.* Recommendations for accurate numerical blood flow simulations of stented intracranial aneurysms // *Biomedizinische Technik/Biomedical Engineering*. 2013. 58, 3. 303–314.
- Joldes Grand Roman, Miller Karol, Wittek Adam, Doyle Barry.* A simple, effective and clinically applicable method to compute abdominal aortic aneurysm wall stress // *Journal of the mechanical behavior of biomedical materials*. 2016. 58. 139–148.
- Jou L-D, Lee DH, Morsi H, Mawad ME.* Wall shear stress on ruptured and unruptured intracranial aneurysms at the internal carotid artery // *American Journal of Neuroradiology*. 2008. 29, 9. 1761–1767.
- Jou Liang-Der, Wong Gregory, Dispensa Brad, Lawton Michael T, Higashida Randall T, Young William L, Saloner David.* Correlation between luminal geometry changes and hemodynamics in fusiform intracranial aneurysms // *American journal of neuroradiology*. 2005. 26, 9. 2357–2363.
- Jufri Nurul E, Abidali Mohamedali, Alberto Avolio, Baker Mark S.* Mechanical stretch: physiological and pathological implications for human vascular endothelial cells // *Vascular*. 2015. 7. 8.
- Juvela Seppo, Porras Matti, Poussa Kristiina.* Natural history of unruptured intracranial aneurysms: probability of and risk factors for aneurysm rupture // *Journal of neurosurgery*. 2008. 108, 5. 1052–1060.
- Kaneko Naoki, Mashiko Toshihiro, Namba Katsunari, Tateshima Satoshi, Watanabe Eiju, Kawai Kensuke.* A patient-specific intracranial aneurysm model with endothelial lining: a novel in vitro approach to bridge the gap between biology and flow dynamics // *Journal of neurointerventional surgery*. 2017. 10, 3. 306–309.
- Karšaj Igor, Horvat Nino, Virag Lana.* Implementation of growth and remodeling model in 3D finite element code: application to abdominal aortic aneurysm // *EC-COMAS Congress 2016*. 2016.
- Kashiwazaki Daina, Kuroda Satoshi.* Size ratio can highly predict rupture risk in intracranial small (< 5 mm) aneurysms // *Stroke*. 2013. 44, 8. 2169–2173.
- Kassam Amin, Horowitz Michael, Chang Yue-Fang, Peters David.* Altered arterial homeostasis and cerebral aneurysms: A review of the literature and justification for a search of molecular biomarkers // *Neurosurgery*. 2004. 54, 5. 1199–1212.
- Kataoka Kazuo, Taneda Mamoru, Asai Toshiharu, Kinoshita Akira, Ito Mamoru, Kuroda Ryotaro.* Structural fragility and inflammatory response of ruptured cerebral aneurysms: a comparative study between ruptured and unruptured cerebral aneurysms // *Stroke*. 1999. 30, 7. 1396–1401.

- Khe AK, Cherevko AA, Chupakhin AP, Bobkova MS, Krivoshapkin AL, Orlov K Yu.* Haemodynamics of giant cerebral aneurysm: A comparison between the rigid-wall, one-way and two-way FSI models // *Journal of Physics: Conference Series.* 722, 1. 2016. 012042.
- Kılıc Türker, Sohrabifar Mehran, Kurtkaya Özlem, Yildirim Özlem, Elmaci Ilhan, Günel Murat, Pamir M Necmettin.* Expression of structural proteins and angiogenic factors in normal arterial and unruptured and ruptured aneurysm walls // *Neurosurgery.* 2005. 57, 5. 997–1007.
- Kim Samuel C, Singh Meharvan, Huang Judy, Prestigiacomo Charles J, Winfree Christopher J, Solomon Robert A, Connolly E Sander C.* Matrix metalloproteinase-9 in cerebral aneurysms // *Neurosurgery.* 1997. 41, 3. 642–647.
- Kohn Julie C, Lampi Marsha C, Reinhart-King Cynthia A.* Age-related vascular stiffening: causes and consequences // *Frontiers in genetics.* 2015. 6. 112.
- Kondo Soichiro, Hashimoto Nobuo, Kikuchi Haruhiko, Hazama Fumitada, Nagata Izumi, Kataoka Hideo.* Cerebral aneurysms arising at nonbranching sites: an experimental study // *Stroke.* 1997. 28, 2. 398–404.
- Kosierkiewicz Tomasz A, Factor Stephen M, Dickson Dennis W.* Immunocytochemical studies of atherosclerotic lesions of cerebral berry aneurysms // *Journal of Neuropathology & Experimental Neurology.* 1994. 53, 4. 399–406.
- Krings Timo, Mandell Daniel M, Kiehl Tim-Rasmus, Geibprasert Sasikhan, Tymianski Michael, Alvarez Hortensia, Hans Franz-Josef, others.* Intracranial aneurysms: from vessel wall pathology to therapeutic approach // *Nature Reviews Neurology.* 2011. 7, 10. 547.
- Krishna C. Vamsi, Suja Vineeth Chandran, Watton Paul, Arakeri Jaywant H, Gundiah Namrata.* Shear Stress Rosettes Capture the Complex Flow Physics in Diseased Arteries. submitted. n.d.
- Kroon Martin, Holzapfel Gerhard A.* A model for saccular cerebral aneurysm growth by collagen fibre remodelling // *Journal of theoretical biology.* 2007. 247, 4. 775–787.
- Kroon Martin, Holzapfel Gerhard A.* Modeling of saccular aneurysm growth in a human middle cerebral artery // *Journal of biomechanical engineering.* 2008. 130, 5. 051012.
- Kroon Martin, Holzapfel Gerhard A.* A theoretical model for fibroblast-controlled growth of saccular cerebral aneurysms // *Journal of Theoretical Biology.* 2009. 257, 1. 73–83.
- Ku DN, Giddens DP, Phillips DJ, Strandness DE.* Hemodynamics of the normal human carotid bifurcation: in vitro and in vivo studies // *Ultrasound in medicine & biology.* 1985. 11, 1. 13–26.

- LaMack Jeffrey A, Friedman Morton H.* Individual and combined effects of shear stress magnitude and spatial gradient on endothelial cell gene expression // *American Journal of Physiology-Heart and Circulatory Physiology*. 2007. 293, 5. H2853–H2859.
- LaMack Jeffrey A, Himburg Heather A, Li Xue-Mei, Friedman Morton H.* Interaction of wall shear stress magnitude and gradient in the prediction of arterial macromolecular permeability // *Annals of biomedical engineering*. 2005. 33, 4. 457–464.
- Langille B Lowell.* Remodeling of developing and mature arteries: endothelium, smooth muscle, and matrix. // *Journal of cardiovascular pharmacology*. 1993. 21. S11–7.
- Lantz Jonas, Gårdhagen Roland, Karlsson Matts.* Quantifying turbulent wall shear stress in a subject specific human aorta using large eddy simulation // *Medical Engineering and Physics*. 2012. 34, 8. 1139–1148.
- Lasheras Juan C.* The biomechanics of arterial aneurysms // *Annu. Rev. Fluid Mech.* 2007. 39. 293–319.
- Lee Robert MKW.* Morphology of cerebral arteries // *Pharmacology & therapeutics*. 1995. 66, 1. 149–173.
- Lei M, Giddens DP, Jones SA, Loth F, Bassiouny H.* Pulsatile flow in an end-to-side vascular graft model: comparison of computations with experimental data // *Journal of Biomechanical Engineering*. 2001. 123, 1. 80–87.
- Lei M, Kleinstreuer C, Archie Jr JP.* Geometric design improvements for femoral graft-artery junctions mitigating restenosis // *Journal of biomechanics*. 1996. 29, 12. 1605–1614.
- Lin WJ, Iafrati MD, Peattie RA, Dorfmann L.* Growth and remodeling with application to abdominal aortic aneurysms // *Journal of Engineering Mathematics*. 2018. 109, 1. 113–137.
- Lin WJ, Iafrati MD, Peattie RA, Dorfmann L.* Non-axisymmetric dilatation of a thick-walled aortic aneurysmal tissue // *International Journal of Non-Linear Mechanics*. 2019. 109. 172–181.
- Liu Minliang, Liang Liang, Liu Haofei, Zhang Ming, Martin Caitlin, Sun Wei.* On the computation of in vivo transmural mean stress of patient-specific aortic wall // *Biomechanics and modeling in mechanobiology*. 2018. 1–12.
- Lu Jia, Zhou Xianlian, Raghavan Madhavan L.* Inverse method of stress analysis for cerebral aneurysms // *Biomechanics and modeling in mechanobiology*. 2008. 7, 6. 477–486.
- Ma Baoshun, Harbaugh Robert E, Raghavan Madhavan L.* Three-dimensional geometrical characterization of cerebral aneurysms // *Annals of biomedical engineering*. 2004. 32, 2. 264–273.

- Ma Baoshun, Lu Jia, Harbaugh Robert E, Raghavan Madhavan L.* Nonlinear anisotropic stress analysis of anatomically realistic cerebral aneurysms // *Journal of biomechanical engineering*. 2007. 129, 1. 88–96.
- Maltzahn Wolf W von, Warriyar Rema G, Keitzer W Ford.* Experimental measurements of elastic properties of media and adventitia of bovine carotid arteries // *Journal of biomechanics*. 1984. 17, 11. 839–847.
- Malvern Lawrence E.* Introduction to the Mechanics of a Continuous Medium. Monograph. 1969. book.
- Mandaltsi Aikaterini.* Modelling the mechanobiological evolution of aneurysms: An integrative in vivo, in vitro and in silico approach. 2016. PhD thesis.
- Mantha A, Karmonik Christof, Benndorf G, Strother C, Metcalfe Ralph.* Hemodynamics in a cerebral artery before and after the formation of an aneurysm // *American Journal of Neuroradiology*. 2006. 27, 5. 1113–1118.
- Matrisian Lynn M.* Metalloproteinases and their inhibitors in matrix remodeling // *Trends in Genetics*. 1990. 6. 121–125.
- Max Nelson.* Weights for computing vertex normals from facet normals // *Journal of Graphics Tools*. 1999. 4, 2. 1–6.
- McMillan DONALD E.* Blood flow and the localization of atherosclerotic plaques. // *Stroke*. 1985. 16, 4. 582–587.
- Menashi Suzanne, Campa Juan S, Greenhalgh Roger M, Powell Janet T.* Collagen in abdominal aortic aneurysm: typing, content, and degradation // *Journal of vascular surgery*. 1987. 6, 6. 578–582.
- Meng Hui, Swartz Daniel D, Wang Zhijie, Hoi Yiemeng, Kolega John, Metaxa Eleni M, Szymanski Michael P, Yamamoto Junichi, Sauvageau Eric, Levy Elad I.* A MODEL SYSTEM FORMAPPING VASCULARRESPONSES TO COMPLEX HEMODYNAMICS AT ARTERIAL BIFURCATIONS IN VIVO // *Neurosurgery*. 2006. 59, 5. 1094–1101.
- Meng Hui, Wang Zhijie, Hoi Yiemeng, Gao Ling, Metaxa Eleni, Swartz Daniel D, Kolega John.* Complex hemodynamics at the apex of an arterial bifurcation induces vascular remodeling resembling cerebral aneurysm initiation // *Stroke*. 2007. 38, 6. 1924–1931.
- Merrilees Mervyn J, Tiang Kim M, Scott Lesley.* Changes in collagen fibril diameters across artery walls including a correlation with glycosaminoglycan content // *Connective tissue research*. 1987. 16, 3. 237–257.
- Metaxa Eleni, Tremmel Markus, Nataraajan Sabareesh K, Xiang Jianping, Paluch Rocco A, Mandelbaum Max, Siddiqui Adnan H, Kolega John, Mocco J, Meng Hui.*

- Characterization of critical hemodynamics contributing to aneurysmal remodeling at the basilar terminus in a rabbit model // *Stroke*. 2010. 41, 8. 1774–1782.
- Mettinger KARL LENNART*. Fibromuscular dysplasia and the brain. II. Current concept of the disease. // *Stroke*. 1982. 13, 1. 53–58.
- Meyer Mark, Barr Alan, Lee Haeyoung, Desbrun Mathieu*. Generalized barycentric coordinates on irregular polygons // *Journal of graphics tools*. 2002. 7, 1. 13–22.
- Mitchell P, Jakubowski J*. Estimate of the maximum time interval between formation of cerebral aneurysm and rupture // *Journal of Neurology, Neurosurgery & Psychiatry*. 2000. 69, 6. 760–767.
- Montes Gregorio S*. Structural biology of the fibres of the collagenous and elastic systems // *Cell biology international*. 1996. 20, 1. 15–27.
- Moretti Matteo*. Endothelial Cell Alignment on Deforming Silicone Surfaces. 2002. PhD thesis.
- Nakagawa Toshio, Hashi Kazuo*. The incidence and treatment of asymptomatic, unruptured cerebral aneurysms // *Journal of neurosurgery*. 1994. 80, 2. 217–223.
- Nelson Peter Kim, Lylyk P, Szikora I, Wetzel SG, Wanke I, Fiorella D*. The pipeline embolization device for the intracranial treatment of aneurysms trial // *American Journal of Neuroradiology*. 2011. 32, 1. 34–40.
- Nelson W James*. Regulation of cell–cell adhesion by the cadherin–catenin complex. 2008.
- Nissen Reinhart, Cardinale George J, Udenfriend Sidney*. Increased turnover of arterial collagen in hypertensive rats // *Proceedings of the National Academy of Sciences*. 1978. 75, 1. 451–453.
- Nyström SHM*. Development of intracranial aneurysms as revealed by electron microscopy // *Journal of neurosurgery*. 1963. 20, 4. 329–337.
- O'Rourke Michael*. Mechanical principles in arterial disease // *Hypertension*. 1995. 26, 1. 2–9.
- Oka Syoten, Nakai Masatsugu*. Optimality principle in vascular bifurcation // *Biorheology*. 1987. 24, 6. 737–751.
- Okamoto Ei-ichi, Couse Tracey, De Leon Hector, Vinten-Johansen Jakob, Goodman Richard B, Scott Neal A, Wilcox Josiah N*. Perivascular inflammation after balloon angioplasty of porcine coronary arteries // *Circulation*. 2001. 104, 18. 2228–2235.
- Osborn Eric A, Rabodzey Aleksandr, Dewey Jr C Forbes, Hartwig John H*. Endothelial actin cytoskeleton remodeling during mechanostimulation with fluid shear stress // *American Journal of Physiology-Cell Physiology*. 2006. 290, 2. C444–C452.
- Owatverot Tomas B, Oswald Sara J, Chen Yong, Wille Jeremiah J, Yin Frank CP*. Effect of combined cyclic stretch and fluid

- shear stress on endothelial cell morphological responses // *Journal of biomechanical engineering*. 2005. 127, 3. 374–382.
- Pakravan HA, Saidi MS, Firoozabadi B.* A mechanical model for morphological response of endothelial cells under combined wall shear stress and cyclic stretch loadings // *Biomechanics and modeling in mechanobiology*. 2016. 15, 5. 1229–1243.
- Peiffer Veronique, Sherwin Spencer J, Weinberg Peter D.* Does low and oscillatory wall shear stress correlate spatially with early atherosclerosis? A systematic review // *Cardiovascular research*. 2013. 99, 2. 242–250.
- Penn David L, Witte Samantha R, Komotar Ricardo J, Connolly Jr E Sander.* The role of vascular remodeling and inflammation in the pathogenesis of intracranial aneurysms // *Journal of clinical neuroscience*. 2014. 21, 1. 28–32.
- Pierce David M, Fastl Thomas E, Rodriguez-Vila Borja, Verbrugghe Peter, Fourneau Inge, Maleux Geert, Herijgers Paul, Gomez Enrique J, Holzapfel Gerhard A.* A method for incorporating three-dimensional residual stretches/stresses into patient-specific finite element simulations of arteries // *Journal of the mechanical behavior of biomedical materials*. 2015. 47. 147–164.
- Pober Jordan S, Sessa William C.* Evolving functions of endothelial cells in inflammation // *Nature Reviews Immunology*. 2007. 7, 10. 803.
- Raghavan Madhavan L, Ma Baoshun, Harbaugh Robert E.* Quantified aneurysm shape and rupture risk // *Journal of neurosurgery*. 2005. 102, 2. 355–362.
- Reymond Philippe, Merenda Fabrice, Perren Fabienne, Rüfenacht Daniel, Stergiopoulos Nikos.* Validation of a one-dimensional model of the systemic arterial tree // *American Journal of Physiology-Heart and Circulatory Physiology*. 2009. 297, 1. H208–H222.
- Ridley Anne J, Hall Alan.* The small GTP-binding protein rho regulates the assembly of focal adhesions and actin stress fibers in response to growth factors // *Cell*. 1992. 70, 3. 389–399.
- Rinkel Gabriel JE, Djibuti Mamuka, Algra Ale, Van Gijn J.* Prevalence and risk of rupture of intracranial aneurysms // *Stroke*. 1998. 29, 1. 251–256.
- Rizzo Robert J, McCarthy Walter J, Dixit Saryu N, Lilly Michael P, Shively Vera P, Flinn William R, Yao James ST.* Collagen types and matrix protein content in human abdominal aortic aneurysms // *Journal of vascular surgery*. 1989. 10, 4. 365–373.
- Roach Margot R, Burton Alan C.* The reason for the shape of the distensibility curves of arteries // *Canadian journal of biochemistry and physiology*. 1957. 35, 8. 681–690.
- Robertson Anne M, Duan Xinjie, Aziz Khaled M, Hill Michael R, Watkins Si-*

- mon C, Cebral Juan R.* Diversity in the strength and structure of unruptured cerebral aneurysms // *Annals of biomedical engineering*. 2015. 43, 7. 1502–1515.
- Rusinkiewicz Szymon.* Estimating curvatures and their derivatives on triangle meshes // *3D Data Processing, Visualization and Transmission, 2004. 3DPVT 2004. Proceedings. 2nd International Symposium on*. 2004. 486–493.
- Sakaki T, Kohmura E, Kishiguchi T, Yuguchi T, Yamashita T, Hayakawa T.* Loss and apoptosis of smooth muscle cells in intracranial aneurysms studies with in situ DNA end labeling and antibody against single-stranded DNA // *Acta neurochirurgica*. 1997. 139, 5. 469–475.
- Sanchez Mathieu, Ambard Dominique, Costalat Vincent, Mendez Simon, Jourdan Franck, Nicoud Franck.* Biomechanical assessment of the individual risk of rupture of cerebral aneurysms: a proof of concept // *Annals of biomedical engineering*. 2013. 41, 1. 28–40.
- Schmid H, Pauli L, Paulus A, Kuhl Ellen, Itskov M.* Consistent formulation of the growth process at the kinematic and constitutive level for soft tissues composed of multiple constituents // *Computer methods in biomechanics and biomedical engineering*. 2012. 15, 5. 547–561.
- Schrauwen JTC, Vilanova A, Rezakhaniha R, Stergiopoulos N, Van De Vosse FN, Boven-deerd PHM.* A method for the quantification of the pressure dependent 3D collagen configuration in the arterial adventitia // *Journal of structural biology*. 2012. 180, 2. 335–342.
- Schumacher H, Allenberg JR.* Increased apoptosis and decreased density of medial smooth muscle cells in human abdominal aortic aneurysms // *Chinese medical journal*. 2003. 116, 10. 1549–1552.
- Scott Susan, Ferguson Gary G, Roach Margot R.* Comparison of the elastic properties of human intracranial arteries and aneurysms // *Canadian journal of physiology and pharmacology*. 1972. 50, 4. 328–332.
- Sekhar Laligam N, Heros Roberto C.* Origin, growth, and rupture of saccular aneurysms: a review // *Neurosurgery*. 1981. 8, 2. 248–260.
- Selimovic Alisa.* Patient-specific models of cerebral aneurysm evolution. 2013. PhD thesis.
- Selimovic Alisa, Ventikos Yiannis, Watton Paul N.* Modelling the evolution of cerebral aneurysms: Biomechanics, mechanobiology and multiscale modelling // *Procedia IUTAM*. 2014. 10. 396–409.
- Sforza Daniel M, Kono Kenichi, Tateshima Satoshi, Viñuela Fernando, Putman Christopher, Cebral Juan R.* Hemodynamics in growing and stable cerebral

- aneurysms // *Journal of neurointerventional surgery*. 2016. 8, 4. 407–412.
- Shimizu Koichi, Mitchell Richard N, Libby Peter*. Inflammation and cellular immune responses in abdominal aortic aneurysms // *Arteriosclerosis, thrombosis, and vascular biology*. 2006. 26, 5. 987–994.
- Shimogonya Yuji, Ishikawa Takuji, Imai Yohsuke, Matsuki Noriaki, Yamaguchi Takami*. Can temporal fluctuation in spatial wall shear stress gradient initiate a cerebral aneurysm? A proposed novel hemodynamic index, the gradient oscillatory number (GON) // *Journal of biomechanics*. 2009. 42, 4. 550–554.
- Shirinsky Vladimir P, Antonov Alexander S, Birukov Konstantin G, Sobolevsky Alexander V, Romanov Yuri A, Kabaeva Naile V, Antonova Galina N, Smirnov Vladimir N*. Mechano-chemical control of human endothelium orientation and size. // *The Journal of Cell Biology*. 1989. 109, 1. 331–339.
- Shojima Masaaki, Oshima Marie, Takagi Kiyoshi, Torii Ryo, Hayakawa Motoharu, Katada Kazuhiro, Morita Akio, Kirino Takaaki*. Magnitude and role of wall shear stress on cerebral aneurysm: computational fluid dynamic study of 20 middle cerebral artery aneurysms // *Stroke*. 2004. 35, 11. 2500–2505.
- Sinha Ravi, Le Gac Séverine, Verdonschot Nico, Van Den Berg Albert, Koopman Bart, Rouwkema Jeroen*. Endothelial cell alignment as a result of anisotropic strain and flow induced shear stress combinations // *Scientific reports*. 2016. 6. 29510.
- Sommer Gerhard, Holzapfel Gerhard A*. 3D constitutive modeling of the biaxial mechanical response of intact and layer-dissected human carotid arteries // *Journal of the mechanical behavior of biomedical materials*. 2012. 5, 1. 116–128.
- Sommer Gerhard, Regitnig Peter, Koltringer Lukas, Holzapfel Gerhard A*. Biaxial mechanical properties of intact and layer-dissected human carotid arteries at physiological and supraphysiological loadings // *American Journal of Physiology-Heart and Circulatory Physiology*. 2009. 298, 3. H898–H912.
- Spiegel Martin, Redel Thomas, Zhang Y Jonathan, Struffert Tobias, Hornegger Joachim, Grossman Robert G, Doerfler Arnd, Karmonik Christof*. Tetrahedral and polyhedral mesh evaluation for cerebral hemodynamic simulation—a comparison // *Engineering in Medicine and Biology Society, 2009. EMBC 2009. Annual International Conference of the IEEE*. 2009. 2787–2790.
- Stehbens We E*. Histopathology of cerebral aneurysms // *Archives of neurology*. 1963. 8, 3. 272–285.
- Stehbens William E*. Pathology of the cerebral blood vessels. 1972.
- Sinha Ravi, Le Gac Séverine, Verdonschot Nico, Van Den Berg Albert, Koopman Bart,*

- Stossel Thomas P, Condeelis John, Cooley Lynn, Hartwig John H, Noegel Angelika, Schleicher Michael, Shapiro Sandor S.* Filamins as integrators of cell mechanics and signalling // *Nature reviews Molecular cell biology.* 2001. 2, 2. 138.
- Sukriti Sukriti, Tauseef Mohammad, Yazbeck Pascal, Mehta Dolly.* Mechanisms regulating endothelial permeability // *Pulmonary circulation.* 2014. 4, 4. 535–551.
- Sumner DS.* Stress-strain characteristics and collagen-elastin content of abdominal aortic aneurysms // *Surg. Gynecol. Obstet.* 1970. 130. 459–466.
- Taber Larry A, Humphrey Jay D.* Stress-modulated growth, residual stress, and vascular heterogeneity // *Journal of biomechanical engineering.* 2001. 123, 6. 528–535.
- Takamizawa Keiichi, Hayashi Kozaburo.* Strain energy density function and uniform strain hypothesis for arterial mechanics // *Journal of biomechanics.* 1987. 20, 1. 7–17.
- Takemura Yusuke, Hirata Yoko, Sakata Noriyuki, Nabeshima Kazuki, Takeshita Morishige, Inoue Tooru.* Histopathologic characteristics of a saccular aneurysm arising in the non-branching segment of the distal middle cerebral artery // *Pathology-Research and Practice.* 2010. 206, 6. 391–396.
- Tanoue T, Tateshima S, Villablanca JP, Viñuela F, Tanishita K.* Wall shear stress distribution inside growing cerebral aneurysm // *American Journal of Neuroradiology.* 2011. 32, 9. 1732–1737.
- Thompson B Gregory, Brown Robert D, Amin-Hanjani Sepideh, Broderick Joseph P, Cockroft Kevin M, Connolly E Sander, Duckwiler Gary R, Harris Catherine C, Howard Virginia J, Johnston S Claiborne Clay, others .* Guidelines for the management of patients with unruptured intracranial aneurysms: a guideline for healthcare professionals from the American Heart Association/American Stroke Association // *Stroke.* 2015. 48, 6. 2368–2400.
- Tremmel Markus, Dhar Sujana, Levy Elad I, Mocco J, Meng Hui.* Influence of intracranial aneurysm-to-parent vessel size ratio on hemodynamics and implication for rupture: results from a virtual experimental study // *Neurosurgery.* 2009. 64, 4. 622–631.
- Tulamo Riikka, Frösen Juhana, Hernesniemi Juha, Niemelä Mika.* Inflammatory changes in the aneurysm wall: a review // *Journal of neurointerventional surgery.* 2010. 2, 2. 120–130.
- Ujiie Hiroshi, Tachi Hiroyuki, Hiramatsu Osamu, Hazel Andrew L, Matsumoto Takeshi, Ogasawara Yasuo, Nakajima Hiroshi, Hori Tomokatsu, Takakura Kintomo, Kajiya Fumihiko.* Effects of size and shape (aspect ratio) on the hemodynamics of saccular

- aneurysms: a possible index for surgical treatment of intracranial aneurysms // *Neurosurgery*. 1999. 45, 1. 119–130.
- Ujiie Hiroshi, Tamano Yoshinori, Sasaki Kuri, Hori Tomokatsu*. Is the aspect ratio a reliable index for predicting the rupture of a saccular aneurysm? // *Neurosurgery*. 2001. 48, 3. 495–503.
- Unemori Elaine N, Ferrara Napoleone, Bauer Eugene A, Amento Edward P*. Vascular endothelial growth factor induces interstitial collagenase expression in human endothelial cells // *Journal of cellular physiology*. 1992. 153, 3. 557–562.
- Vakil P, Ansari SA, Cantrell CG, Eddleman CS, Dehkordi FH, Vranic J, Hurley MC, Batjer HH, Bendok BR, Carroll TJ*. Quantifying intracranial aneurysm wall permeability for risk assessment using dynamic contrast-enhanced MRI: a pilot study // *American Journal of Neuroradiology*. 2015. 36, 5. 953–959.
- Valencia Alvaro, Contente Alvaro, Ignat Miguel, Mura Jorge, Bravo Eduardo, Rivera Rodrigo, Sordo Juan*. Mechanical test of human cerebral aneurysm specimens obtained from surgical clipping // *Journal of Mechanics in Medicine and Biology*. 2015. 15, 05. 1550075.
- Valencia Alvaro, Ledermann Darren, Rivera Rodrigo, Bravo Eduardo, Galvez Marcelo*. Blood flow dynamics and fluid–structure interaction in patient-specific bifurcating cerebral aneurysms // *International Journal for numerical methods in fluids*. 2008. 58, 10. 1081–1100.
- Valentin Arturo, Humphrey Jay D, Holzapfel Gerhard A*. A finite element-based constrained mixture implementation for arterial growth, remodeling, and adaptation: Theory and numerical verification // *International journal for numerical methods in biomedical engineering*. 2013. 29, 8. 822–849.
- Vanrossomme AE, Eker OF, Thiran J-P, Courbebaisse GP, Boudjeltia K Zouaoui*. Intracranial aneurysms: Wall motion analysis for prediction of rupture // *American Journal of Neuroradiology*. 2015. 36, 10. 1796–1802.
- Varble Nicole, Tutino Vincent M, Yu Jihneeh, Sonig Ashish, Siddiqui Adnan H, Davies Jason M, Meng Hui*. Shared and Distinct Rupture Discriminants of Small and Large Intracranial Aneurysms // *Stroke*. 2018. 49, 04. 856–864.
- Villa-Uriol MC, Berti G, Hose DR, Marzo A, Chiarini A, Penrose J, Pozo J, Schmidt JG, Singh P, Lycett R, others*. @neurIST complex information processing toolchain for the integrated management of cerebral aneurysms // *Interface Focus*. 2011. 1, 3. 308–319.
- Vito Raymond P, Dixon Stacey A*. Blood vessel constitutive models—1995–2002 // *Annual review of biomedical engineering*. 2003. 5, 1. 413–439.

- Vogel Stephen M, Malik Asrar B. Cytoskeletal dynamics and lung fluid balance // *Comprehensive Physiology*. 2011. 2, 1. 449–478.
- Wang H, Grood ES, Ip W, Boissy R. THE SIGNAL RESPONSIBLE FOR ORIENTING CELLS GROWN ON CYCLICALLY DEFORMED SURFACES // *FASEB JOURNAL*. 9, 3. 1995. A588–A588.
- Wang JH-C, Thampatty B P. An introductory review of cell mechanobiology // *Biomechanics and modeling in mechanobiology*. 2006. 5, 1. 1–16.
- Wang James H-C, Goldschmidt-Clermont Pascal, Wille Jeremiah, Yin Frank C-P. Specificity of endothelial cell reorientation in response to cyclic mechanical stretching // *Journal of biomechanics*. 2001. 34, 12. 1563–1572.
- Wang Yang, Leng Xiaochang, Zhou Xiaobin, Li Wenqiang, Siddiqui Adnan H, Xiang Jianping. Hemodynamics in a Middle Cerebral Artery Aneurysm Before Its Growth and Fatal Rupture: Case Study and Review of the Literature // *World neurosurgery*. 2018. 119. e395–e402.
- Wang Zhijie, Kolega John, Hoi Yiemeng, Gao Ling, Swartz Daniel D, Levy Elad I, Mocco J, Meng Hui. Molecular alterations associated with aneurysmal remodeling are localized in the high hemodynamic stress region of a created carotid bifurcation // *Neurosurgery*. 2009. 65, 1. 169–178.
- Watton P, Ventikos Y. Modelling evolution of saccular cerebral aneurysms // *The Journal of Strain Analysis for Engineering Design*. 2009. 44, 5. 375–389.
- Watton PN, Hill NA. Evolving mechanical properties of a model of abdominal aortic aneurysm // *Biomechanics and modeling in mechanobiology*. 2009. 8, 1. 25–42.
- Watton PN, Hill NA, Heil M. A mathematical model for the growth of the abdominal aortic aneurysm // *Biomechanics and modeling in mechanobiology*. 2004. 3, 2. 98–113.
- Watton PN, Selimovic A, Raberger NB, Huang P, Holzappel GA, Ventikos Y. Modelling evolution and the evolving mechanical environment of saccular cerebral aneurysms // *Biomechanics and modeling in mechanobiology*. 2011. 10, 1. 109–132.
- Watton Paul N, Raberger Nikolaus B, Holzappel Gerhard A, Ventikos Yiannis. Coupling the hemodynamic environment to the evolution of cerebral aneurysms: computational framework and numerical examples // *Journal of biomechanical engineering*. 2009a. 131, 10. 101003.
- Watton Paul N, Ventikos Yiannis, Holzappel Gerhard A. Modelling the growth and stabilization of cerebral aneurysms // *Mathematical medicine and biology: a journal of the IMA*. 2009b. 26, 2. 133–164.

- Weir Bryce. Unruptured intracranial aneurysms: a review // *Journal of neurosurgery*. 2002. 96, 1. 3–42.
- Weir Bryce, Amidei Christina, Kongable Gail, Findlay J Max, Kassell Neal F, Kelly John, Dai Lanting, Karrison Theodore G. The aspect ratio (dome/neck) of ruptured and unruptured aneurysms // *Journal of neurosurgery*. 2003. 99, 3. 447–451.
- Weiss Paul. Cellular dynamics // *Reviews of Modern Physics*. 1959. 31, 1. 11.
- Wheelock Margaret J, Johnson Keith R. Cadherin-mediated cellular signaling // *Current opinion in cell biology*. 2003. 15, 5. 509–514.
- Wiebers David O, *Unruptured Intracranial Aneurysms Investigators International Study of, others*. Unruptured intracranial aneurysms: natural history, clinical outcome, and risks of surgical and endovascular treatment // *The Lancet*. 2003. 362, 9378. 103–110.
- Wolters BJB, Rutten MCM, Schurink GWH, Kose Ursula, De Hart J, Van De Vosse FN. A patient-specific computational model of fluid–structure interaction in abdominal aortic aneurysms // *Medical engineering & physics*. 2005. 27, 10. 871–883.
- Wuyts FL, Vanhuyse VJ, Langewouters GJ, Decraemer WF, Raman ER, Buyle S. Elastic properties of human aortas in relation to age and atherosclerosis: a structural model // *Physics in Medicine & Biology*. 1995. 40, 10. 1577.
- Xiang Jianping, Natarajan Sabareesh K, Tremmel Markus, Ma Ding, Mocco J, Hopkins L Nelson, Siddiqui Adnan H, Levy Elad I, Meng Hui. Hemodynamic–morphologic discriminants for intracranial aneurysm rupture // *Stroke*. 2011. 42, 1. 144–152.
- Xie Jiaping, Zhou Jianbo, Fung YC. Bending of blood vessel wall: stress-strain laws of the intima-media and adventitial layers // *Journal of biomechanical engineering*. 1995. 117, 1. 136–145.
- Yahya Mohammed. Three dimensional finite-element modeling of blood flow in elastic vessels: effects of arterial geometry and elasticity on aneurysm growth and rupture // *Ryerson University*. 2010. 486. 1–86.
- Yamamoto Kimiko, Ando Joji. Vascular endothelial cell membranes differentiate between stretch and shear stress through transitions in their lipid phases // *American Journal of Physiology-Heart and Circulatory Physiology*. 2015. 309, 7. H1178–H1185.
- Zamir Eli, Katz Menachem, Posen Yehudit, Erez Noam, Yamada Kenneth M, Katz Ben-Zion, Lin Shin, Lin Diane C, Bershadsky Alexander, Kam Zvi, others. Dynamics and segregation of cell–matrix adhesions in cultured fibroblasts // *Nature cell biology*. 2000. 2, 4. 191.

- Zhang Ying, Yang Xinjian, Wang Yang, Liu Jian, Li Chuanhui, Jing Linkai, Wang Shengzhang, Li Haiyun.* Influence of morphology and hemodynamic factors on rupture of multiple intracranial aneurysms: matched-pairs of ruptured-unruptured aneurysms located unilaterally on the anterior circulation // BMC neurology. 2014. 14, 1. 253.



Procedures of Getting Principal Directions of Flow

There are two orthogonal directions \vec{e}_1 and \vec{e}_2 representing the accumulated maximal and minimal wall shear stress over one cardiac cycle. It is understandable that every instantaneous wall shear stress is resolved along these two directions.

Hence, each instantaneous WSS can be expressed as:

$$\vec{\tau}_t = \tau_1 \vec{e}_1 + \tau_2 \vec{e}_2 \quad (\text{A.0.1})$$

And the definition of direction 1 and 2 was given in (Chakraborty et al., 2012), which is

$$\int_0^T \tau_1 \tau_2 dt = 0 \quad (\text{A.0.2})$$

To solve this equation, a pair of reference directions are necessary which play as the 'provisional persona' of two principal directions. The initial selection of these two directions is arbitrary. Here we choose the instantaneous WSS at the first time step (\vec{e}_{ref1}) over one cardiac cycle, which is

$$\vec{i} = \vec{e}_{ref1} = \frac{\vec{\tau}_{t1}}{|\vec{\tau}_{t1}|} \quad (\text{A.0.3})$$

While the corresponding second reference vector (\vec{j}) should be the in-plane perpendic-

ular vector of the \vec{e}_{ref1} . Hence, we have two sets of orthogonal vectors at present, references vectors as the baseline and principal vectors as the target. The next step is to manipulate the relationship between instantaneous shear stress vectors and these two sets of vectors.

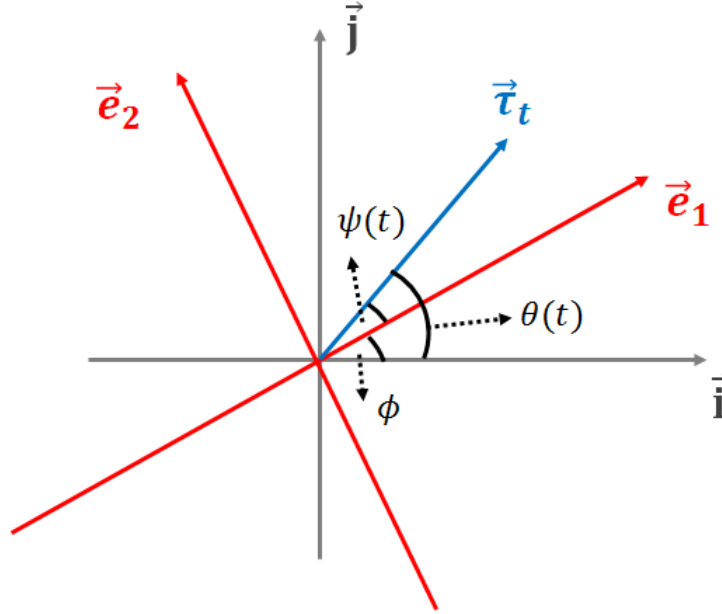


Figure A.1: Schematic diagram of the three manipulation angles in the calculation of the principal directions. ϕ : angle between the first principal direction and the reference vector \vec{i} ; $\psi(t)$: angle between the first principal direction and the instantaneous shear stress vector; $\theta(t)$: angle between the instantaneous shear stress vector and the reference vector.

The meanings of ϕ , $\theta(t)$, and $\psi(t)$ have been illustrated in the Fig A.1, it is worth to note that Φ is a time-independent variable. Then we can resolve the instantaneous shear stress to the \vec{e}_1 and \vec{e}_2 directions.

$$\vec{\tau}_1(t) = \tau_{mag} \cos \psi(t) \vec{e}_1 = \tau_{mag} \cos(\theta(t) - \phi) \vec{i} \quad (\text{A.0.4})$$

$$\vec{\tau}_2(t) = \tau_{mag} \sin \psi(t) \vec{e}_2 = \tau_{mag} \sin(\theta(t) - \phi) \vec{j} \quad (\text{A.0.5})$$

Then the Equation A.0.2 could be expressed as:

$$\begin{aligned}
\int_0^T \tau_1 \tau_2 dt &= \tau_{mag}^2 \sin \psi(t) \cos \psi(t) \\
&= \frac{1}{2} \tau_{mag}^2 \sin(2\psi(t)) \\
&= \frac{1}{2} \tau_{mag}^2 \sin(2(\theta(t) - \phi)) = 0
\end{aligned} \tag{A.0.6}$$

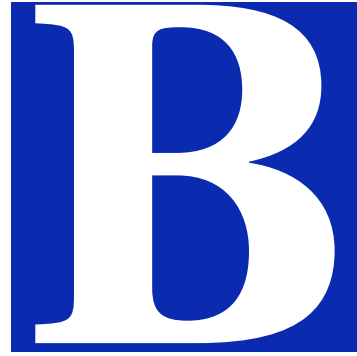
Here $\theta(t)$ is a known variable and ϕ is an time-independent variable which could be solved out by the above equation. Let us reformulate the above equation:

$$\frac{1}{2} \frac{\partial}{\partial \phi} \left(\int_0^T \tau_{mag}^2 \cos(2(\theta(t) - \phi)) dt \right) = 0 \tag{A.0.7}$$

which means the integral part reaches an extremum at the designated ϕ , named as 'I'. This 'I' could be represented by $\tau_1(t)\tau_2(t)$:

$$I = \int_0^T (\tau_1^2(t) - \tau_2^2(t)) dt \tag{A.0.8}$$

To solve this extremum problem, we can maximizing the $\int_0^T \tau_1^2(t) dt$ or minimising the $\int_0^T \tau_2^2(t) dt$, which indicates the meanings of the direction of $\vec{\tau}_1$ and $\vec{\tau}_2$, are the direction has maximum and minimum accumulating flow respectively. Therefore, after solving the Equation A.0.6, the solution of ϕ can provide the directions of $\vec{\tau}_1$ and $\vec{\tau}_2$. To be more understandable, $\vec{\tau}_1$ direction represents the preferable flow over the cardiac cycle while the $\vec{\tau}_2$ direction is due to the influence from the secondary flow.



Representative Validation Models of Principle Curvature Distribution

The benefit of testing simple geometries is the guarantee of the capability in capturing the correct principal curvature directions using the approach in Section 4.4. One idealized cylindrical model and an idealized ellipsoidal aneurysm model were created here to illustrate principal curvature directions distribution and as the validation of complex 3D models.

Refer to the definition of first and second principal curvatures and their directions described, the maximal curvature direction, i.e. first principal curvature direction, should orient to tangent direction at a point along the circumferential direction. While the minimal curvature direction, which is the second principal curvature direction ought to be in the axial direction. To be more accurately, there is no bend along the axial direction where the curvature equals zero. For the maximal curvature, it occurs at the maximal bend which is the circumferential direction where the curvature equals $1/R$ (R is the radius of the cylinder) on condition that the defined normal curvature points to the inward, otherwise the curvature equals $-1/R$ (FigB.1 left).

The cylinder model was built in Matlab (R2015b, MathWorks, Inc., United Kingdom) meshed with triangular grids. After implementing the above approach, the first and second principal

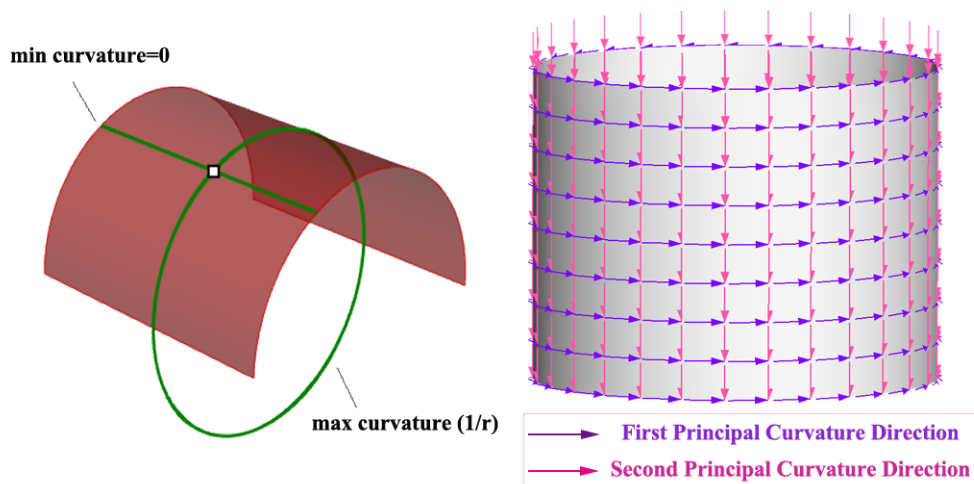


Figure B.1: Schematic diagram of the first and second principal curvatures on a cylinder surface (<http://developer.rhino3d.com/guides/general/essential-mathematics/parametric-curves-surfaces/>). The right figure shows the first and second principal curvature directions on an artificial cylinder model using the above algorithm

curvature directions were calculated out which are remarked with purple and pink arrows. Compare to the theoretical distribution of principal curvature directions which is illustrated in Fig B.1 (left), the distribution in the validation cylinder model is accordance with the analytical solutions.

Apart from this cylinder model, we also recruited an ellipsoid model which has been presented in (Ma et al., 2007). They used an idealized ellipsoidal aneurysm model to verify the accuracy and further performed the same method to model the anthropotomical aneurysm model. It would be more persuadable if we can perform the same ellipsoidal model to compare the principal curvature distribution showed in their research.

The orientation marker 1 and 2 in Fig B.2(a) denote the meridional and circumferential direction respectively. In the meantime, we built an ellipsoid model to test the principle curvature distribution which represents the coincident result compared to the previous research. Here we only plotted the principal curvature directions in the circumferential direction, the resulting minimum principal curvature direction is aligning with the meridional direction (i.e. 2 in Fig B.2(a)). Therefore, the two artificial cylinder and ellipsoid models have proved the correct distribution of first and second principal directions. However, these two models are meshed with orderly triangular grids in Matlab (Fig. B.3 A, B). To solve the irregular geometry with random triangular mesh, the resolution still needs to be detected.

The cylinder model in Fig.B.3 (C) is mapped with irregular triangles which distribute un-

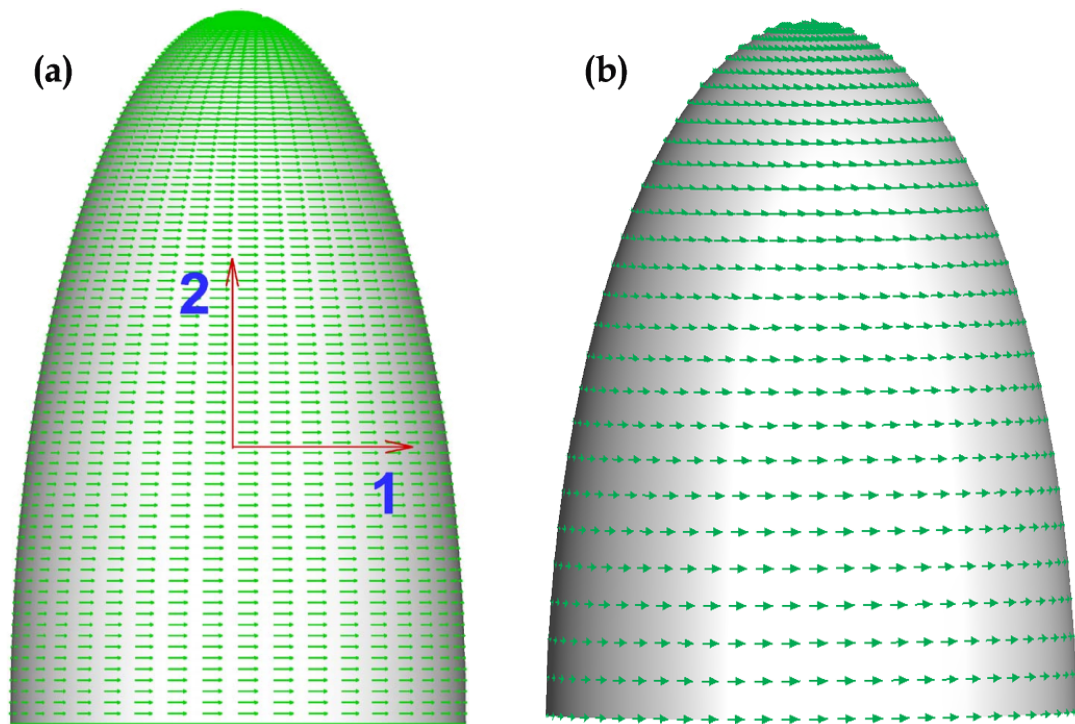


Figure B.2: Distributions of principal curvature direction on an ellipsoidal model. (a) adapted from (Ma et al., 2007). (b) validation model in this research

evenly. This type of mesh is similar to that in complex 3D aneurysm geometry and more importantly, it is able to validate the accuracy of the principal curvature direction distribution via the artificial cylinder model. The first principal curvature directions are pointing to the circumferential orientation on each vertex which is apparently showed in Fig.B.3 (E) in this cylindrical model. This result is in accordance with the analytical solution and the previous regular mapped cylindrical model. Hence, this methodology for calculating the principal curvature directions is proved to be available in the further research of complex models (i.g. aneurysm).

This part of research aims to introduce the methods of the acquisition of principal curvature directions on any triangle meshed geometry. Hence, the specific principal curvature direction distribution on aneurysm geometry could be generated and used for structural modelling.

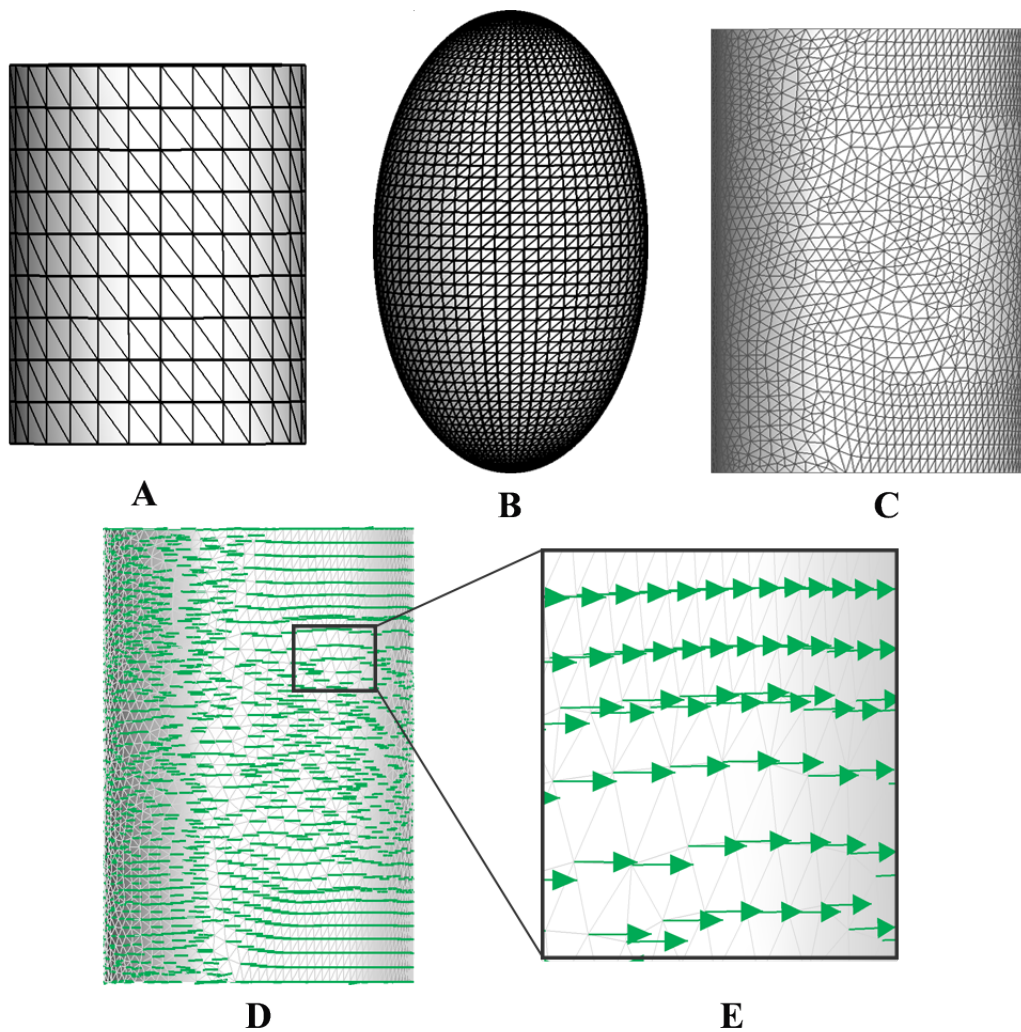


Figure B.3: Mesh of the artificially cylindrical and ellipsoidal model are showed in A and B. The uneven triangular mesh distribution on a cylinder model (C) and the calculating first principal curvature direction distribution (D). To clearly display the principal curvature direction, a magnified local distribution on a specific region (rectangular area, D) is exhibited in E.



Endothelial Cells Alignment under Combined WSS and Cyclic Stretch

Two significant mechanical factors influencing the morphology and alignment of endothelial cells are WSS and cyclic stretch of the vascular wall. Previous studies are mainly focusing on the link between individual WSS or the stretch and the ECs morphology variation, but recently some researches provide some information that ECs morphology is dependent on the interplay of WSS and CS which can represent the permeability of the arterial wall ([Sinha et al., 2016](#); [Owatverot et al., 2005](#); [Pakravan et al., 2016](#); [Yamamoto, Ando, 2015](#)). The permeability of the aneurysm wall determines the transport of intravascular cells and macromolecular substance which is highly related to the progression of aneurysm and other vascular diseases. Hence, the ECs morphology is considered as the significant parameter in the description and prediction of the aneurysm evolution and the novel sophistication is the specific definition of ECs morphology under the combined WSS and CS based on a patient-specific aneurysm. WSS is a well-known haemodynamic index with extensively used in cardiovascular researches. Endothelial cells are sensitive to the blood flow environment in both biological and mechanical pathways, which means their behaviours are dependent intensively on WSS imposing on the surface of each cell. Another key factor is the cyclic stretch derived from

the periodical pulse of the blood flow, driving the regular contraction and diastole of vessel walls. Because the endothelial cells embed themselves on the inner surface of arterial wall and their basal surfaces attach to the arterial extracellular matrix, the deformation and migration are strongly related to the mechanical stimuli from the cyclic stretch. The endothelial cells response to mechanical stimuli only considered the stimuli from the blood flow in our G&R framework, but the cyclic stretch is also an important impact factor for the morphology, alignment and function of endothelial cells. To quantify the cyclic stretch is along with great challenges in 3D anatomical geometry, hence here we start to investigate the endothelial cells alignment using the 1D model.

C.0.0.1 Response of Endothelial cells to Cyclic Stretch

Apart from the WSS produced by the friction of the blood flow, endothelial cells are also influenced by the tensile stress derived from the pulsatile nature of the blood flow. The mechanoreceptors on endothelial cells surface can detect the mechanical stretch of different intensities. They enable the information from mechanical stimuli transfer outside the cell to biochemical signals inside the cell and activate downstream signaling pathways. The consequence of this activation depends on the intensities of the mechanical stretch, whether it is within the physical stretch range or surpass the pathological stretch baseline. In the normal state, the human aorta undergoes an about 8~10% oscillation and the peripheral arteries undergo a smaller oscillation (approximate 5%) in external diameter (Boutouyrie et al., 1992; O'Rourke, 1995). In vitro experiments, The stretches of 5~10% are deemed as physiological stretch, while stretches of 20% and above are considered pathological stretch when the blood pressure is high, i.g. hypertension (Anwar et al., 2012; Hurley et al., 2010). Nurul F. Jufri summarized the different human vascular endothelial cells responses to the physiological and pathological cyclic stretch which is concluded in Fig C.1. Under the morbid stretch intensity, the expression of vascular cell adhesion molecule (VCAM-1), intercellular adhesion molecule (ICAM-1), and IL-6/8 induces the pro-atherosclerosis protein expression referring to monocyte, leukocyte, and T-cell. In this case, white blood cells will invade and accumulate in the blood vessel which can lead to atherosclerosis occurrence (Jufri Nurul et al., 2015).

Regarding the response of endothelial cells to the cyclic stretch, the early propositions are endothelial cells react as a stretch avoidance and reorient to minimize the strain to sustain the homeostatic state (Buck, 1980; Buckley et al., 1988). And Buck first reported cells oriented away from the stretch direction under cyclic stretch (Buck, 1980). Moreover, researches have proved that there was no response of cells when the stretch under small stretch amplitudes (<2%) and cells only oriented when the stretch surpassed 5-6% (Wang et al., 1995; Dartsch, Hämmerle, 1986). When imposed the uniaxial stretch on endothelial cells which were cul-

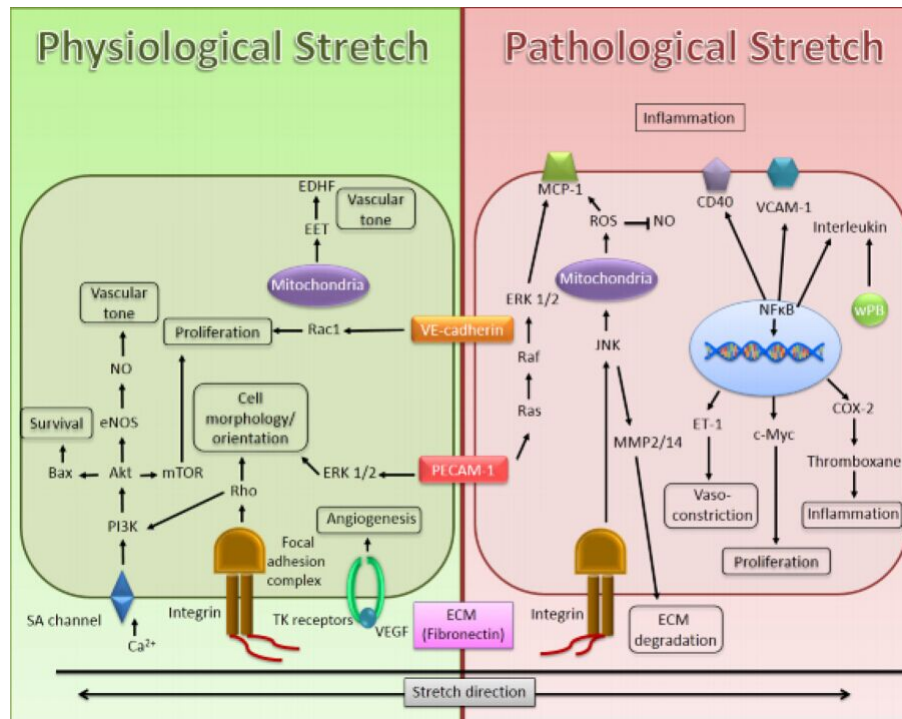


Figure C.1: Summary of the signal transduction pathway involved in human cerebral microvascular endothelial cells activated by physiological and pathological stretch tension. This mechanical stimuli will activate varies gene and protein synthesis, which would further modify the cell phenotype and function. (adapted from (Jufri Nurul et al., 2015))

tured on a deformable substrate, the stress fibres form in a perpendicular direction to uni-axial stretch for several hours (Shirinsky et al., 1989; Iba, Sumpio, 1991). Moreover, Applying different stretch durations, the endothelial cells reoriented more sensitively to the stretch magnitude than the stretch rate (Wang et al., 2001). However, stress fibres have no specific direction under the condition of a biaxial stretch. Quantification of the degree of perpendicular orientation of stress fibres shows that if the stretches less than 3%, there is no principle direction. This phenomenon is also seen in vivo condition, where the alignment of stress fibres in endothelial cells is correlated with the longitudinal axial direction of the arteries (Chien, 2007). In 2003, Konstantin G. Birukov et al. explored whether excessive cyclic stretch could directly induce vascular barrier disruption or enhances endothelial cell sensitivity to edema-genic agents (Birukov et al., 2003). This research investigate the intracellular changing under the physiological (5% elongation) and pathological (18% elongation) cyclic stretch and the results showed that cyclic stretch could activate the rapid increases in myosin light chain (MLC)

phosphorylation (10 min). Also the cyclic stretch involves in activation of p38 and extracellular signal-related kinase 1/2 MAP kinases, as well as the actomyosin remodeling. Besides, the regulation of some genes including small GTPase rho, apoptosis mediator ZIP kinase, and proteinase activated receptor-2 is dependent on the cyclic stretch magnitude analyzed by expression profiling. To model the in vivo condition of endothelial cells, Moretti M successfully cultured the human umbilical endothelial cells on plasma-treated silicone surface in 2004 and the results illustrated endothelial cells under 10% deformation for as little as 4 hours reoriented perpendicular to the stretch direction (Moretti, 2002). There is another factor can induce endothelial cells contraction accompanied with stress fiber assembly which is the small GTPase Rho activation (Ridley, Hall, 1992).

As to the computational simulations, a mathematical model containing two hypotheses was proposed by G. Civelekoglu in 1998, which depicting actin filaments disassembly and reassembly, and the experimental evidence of cyclic stretch showed that the transmembrane proteins (integrin) play as the role of messenger who transfer the external stimuli to some receptors inside the cell. His research found that even a feeble stimulus is sufficient to align actin filaments perpendicular to the direction of stretch due to the coupling of a strong internal dynamics (Civelekoglu et al., 1998). Hui-Ju Hsu established a dynamic stochastic model which is depicting stress fibres reorganization in response to diverse temporal and spatial pattern of stretch (Hsu et al., 2009). His research explained stress fibres disassembled in the direction of stretch preferentially and then these stress fibres accumulated in the direction of lowest stretch which reaching a new balance at high frequencies (1Hz). While at lower stretch frequencies (0.1 and 0.01 Hz), stress fibres adjusted themselves to eliminate the stretch effects. Meanwhile, with the rapidly developing of mechanical and in vitro cell experiment, J. Hatami developed a micropipette aspiration technique proved that the increase of the stretch magnitude and duration lead to lower deformation and further stiffening of endothelial cells (Hatami et al., 2013). It also proved that cyclic stretch causes significant alteration in mechanical properties of ECs due to remodelling of cell cytoskeleton which is coincide with previous researches.

C.0.0.2 1D Study of Endothelial Cells Alignment

For healthy arteries, the endothelial cells undergo one dimensional stretch in the circumferential direction. However, the biaxial stretch should be considered into the pathological process of aneurysm evolution. Regards to this condition, the endothelial cells have no obvious preferential orientation to minimize the stain inside the cell. Both WSS and cyclic stretch are indispensable factors in the consequence of endothelial cells alignment, hence the stimuli (non-uniform WSS and biaxial stretch) guiding EC alignment may be of synchronization

with the consequence of disorderly arrangement. Here we started with a 1D model to investigate the orientation of endothelial cells in the environment with complex flow and biaxial stretches.

The orientation of ECs is mainly determined by the combined WSS (τ) and cyclic stretch (λ_{CS}) which could be provided by CFD simulation and solid mechanical modelling respectively. Thus, the theoretical ECs direction (EC_τ) responded to individual WSS can be defined as:

$$EC_\tau = \frac{\tau}{|\tau|} \quad (C.0.1)$$

Considering the biaxial cyclic stretch are prevalent on the aneurysm region, Watton et al. proposed a novel parameter χ^{BSI} to characterize the biaxial cyclic stretch of the aneurysm tissue (Watton et al., 2011). Healthy arteries have the cylindrical configuration which determines that the cyclic stretch is one dimensional along the circumferential direction. However, the scenario is completely distinct for the aneurysm configuration which is subject to biaxial stretching. Considering this occasion, two cyclic stretches need to be defined properly:

$$\lambda_\alpha^{CS} = \frac{\lambda_\alpha^S}{\lambda_\alpha^D}, \alpha = 1, 2 \quad (C.0.2)$$

Wherein the α denotes the two stretch directions, λ^S and λ^D represent the magnitude of the stretches at systolic and diastolic configuration respectively. In terms of the stretch calculation, the definition of principle stretches could be expressed as (Gruttmann, Taylor, 1992):

$$\lambda_1 = \sqrt{\cos^2\psi(2E_{11} + 1) + \sin^2\psi(2E_{11} + 1) + 2\sin\psi\cos\psi E_{12}} \quad (C.0.3)$$

$$\lambda_2 = \sqrt{\sin^2\psi(2E_{11} + 1) + \cos^2\psi(2E_{11} + 1) + 2\sin\psi\cos\psi E_{12}} \quad (C.0.4)$$

where

$$\psi = \frac{1}{2} \arctan \frac{2E_{12}}{E_{11} - E_{22}} \quad (C.0.5)$$

The E_{11}, E_{12} and E_{22} are Green-Lagrange strain components. λ^S and λ^D are calculated according to the above three equations, but it is worth to note that the principal stretches at systole are defined relative to the diastolic configuration, i.e. $\lambda_\alpha^S = \lambda_\alpha^S(E_{11}^S, E_{22}^S, E_{12}^S, \psi^D)$, rather than ψ^S . Now the cyclic stretches in the two principal directions are quantified, i.e. λ_1^{CS} and λ_2^{CS} . However, due to the complexity of the aneurysm morphology, the principal stretch might decline after the pressurising in certain locations which means the λ_1^{CS} and λ_2^{CS} have

the possibility of smaller than one. In this case, the $\frac{1}{\lambda_{1,2}^{CS}} (> 1)$ could be used to quantify the increase of principal stretch over one cardiac cycle. Therefore, the maximum value between $\lambda_{1,2}^{CS}$ and $\frac{1}{\lambda_{1,2}^{CS}}$ is employed to decide the increase degree of principal stretches. The increase factors could be defined as

$$\xi_1 = \max\left(\lambda_1^{CS}, \frac{1}{\lambda_1^{CS}}\right) - 1 \quad (C.0.6)$$

$$\xi_2 = \max\left(\lambda_2^{CS}, \frac{1}{\lambda_2^{CS}}\right) - 1 \quad (C.0.7)$$

then the biaxial stretch index χ^{BSI} is calculated from ξ_1, ξ_2 as follows:

$$\chi^{BSI} = \frac{\min(\xi_1, \xi_2)}{\max(\xi_1, \xi_2)} \quad (C.0.8)$$

where $\chi^{BSI} = 0$ denotes 1D cyclic deformation and $\chi^{BSI} = 1$ denotes equi-biaxial stretching. Hence, the theoretical ECs direction (EC_τ) responded to individual cyclic stretch should be a function of χ^{BSI} and λ_{CS} :

$$EC_\lambda = f(\chi^{BSI}, \lambda_{CS}) \quad (C.0.9)$$

In the mathematical modelling of aneurysms, the value of χ^{BSI} would be varied from 0 to 1, not only 0 to 1. It is necessary to define a threshold to quantify the stretch impact on endothelial cells. Hence, we hypothesize if χ^{BSI} is lower than 0.2, then the influence of the smaller stretch would be neglected, i.e. one directional stretch only. In this scenario, the endothelial cells should align perpendicular to this stretch. While when χ^{BSI} is larger than 0.8, the stretch is supposed totally equi-biaxial stretch and the orientation is regulated by the WSS individually. Besides, if the χ^{BSI} is within the range of 0.2-0.8, then the resultant stretch will be calculated and the endothelial cells would align perpendicular to this resultant stretch direction. The schematic diagram is shown in Fig C.2 which explains the different scenarios of cyclic stretches distribution and the corresponding responses of endothelial cells.

Now the remain problem is how to determine the influence weight from WSS and cyclic stretch. Previous experimental study under the combined WSS and cyclic stretch condition found that ECs alignment response is dominated by cyclic stretch when WSS is less than 0.08 Pa. On contrary, ECs alignment response is dominated by shear stress when WSS is larger than 0.55 Pa (Sinha et al., 2016). Thus, we propose an weight index W which indicates the influence weight given by WSS and cyclic stretch controlling the final ECs orientation (\overline{EC}).

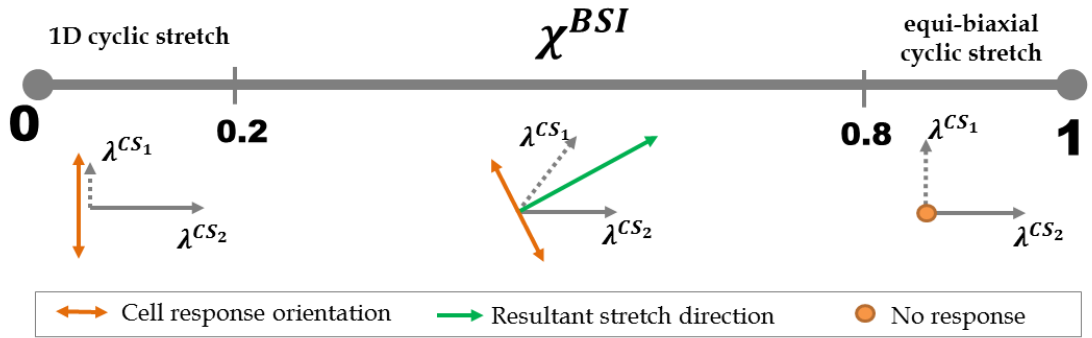


Figure C.2: Schematic diagram of different χ^{BSI} ranges and the responses of endothelial cells to the cyclic stretches in every scenario

$$\overline{EC} = W \times EC_{\tau} + (1 - W) \times EC_{\lambda} \tag{C.0.10}$$

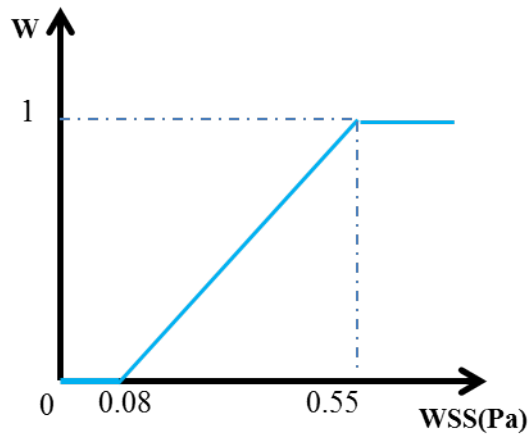


Figure C.3: Schematic diagram of the influence weight of WSS and CS (WSS-W curve) to ECs orientation varied with different WSS magnitude range.

Fig C.3 shows that under the WSS lower than 0.08 Pa, the orientation of endothelial cells is entirely determined by cyclic stretch. And when the WSS is above 0.55 Pa, the orientation is controlled by WSS. We hypothesize that there is a linear relationship within the WSS range between 0.08 to 0.55 Pa. Besides the orientation, the endothelial cells shape is also a vital indicator of the vascular permeability. However, this part of modelling has not been considered into this research at this stage. Currently, we only focus on the orientation of the cells.

C.0.0.3 Preliminary Results

To clearly show the relationship between the endothelial cells orientation and the consequence of mechanical stimuli, i.e., interplay between WSS and cyclic stretch, we started the modelling based on a 2D plane consist of squares and each square represents one endothelial cell.

The magnitude and direction of WSS and two stretches are all prescribed randomly. Given the reason that if the WSS is higher than 0.55 Pa, the stretch would have no impact on the endothelial cells, the WSS magnitude in X and Y direction here is limited to 0-1 which is sufficient to simulate the influence of WSS to endothelial cells. In the aspect of cyclic stretches, we assume that two principal stretch directions are perpendicular to each other for simplification. In 3D modelling, the real principal stretch directions should be dependent on the Green-Lagrange strain mentioned in the last section. The preliminary results are shown in Fig C.4.

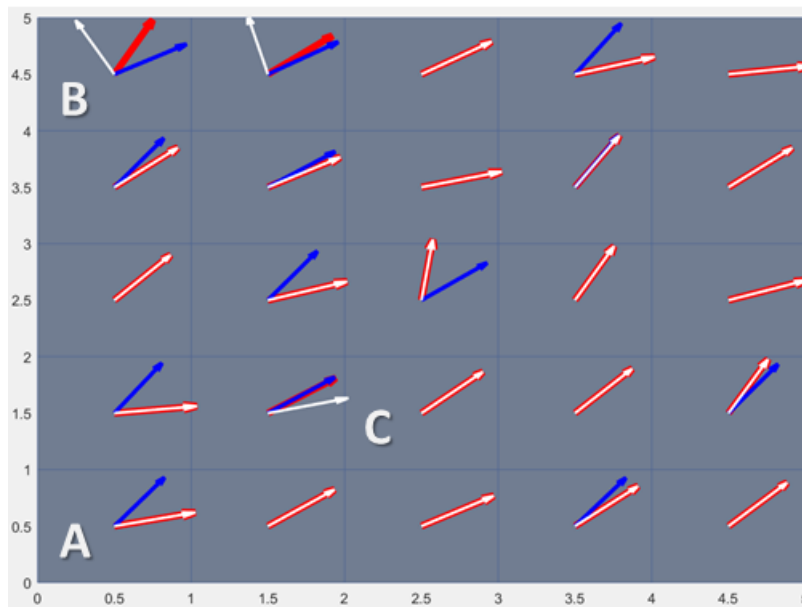


Figure C.4: Schematic diagram of the final orientation of endothelial cells influenced by WSS and cyclic stretch in a 2D space. (red arrow: WSS; blue arrow: cyclic stretch; white arrow: endothelial cells orientation)

There are 25 endothelial cells in this modelling field as representative results to illustrate the final endothelial cells alignment based on the impact from WSS and cyclic stretch. Note that all the arrows only represent the direction without the information of magnitude. All vectors have been manipulated into unit vectors to exhibit a relatively tidy appearance. The

Table C.1: Key parameters information of representative endothelial cells (ABC) showed in Fig C.4

	WSS (Pa)	χ^{BSI}	W
A	0.7779	0.7605	1
B	0.2044	0.5655	0.2647
C	1.3511	0.9712	1

WSS is manifested by red arrows here at every centre of the cell. But it shows clearly that the blue arrows are absent at some locations. This absence means cells are subjected to equibiaxial cyclic stretch, i.e. $\chi^{BSI} > 0.8$ at these locations. Therefore, the cells are regulated by WSS individually, i.e. the cell orientation in accordance with the WSS direction which showed by cell C in Fig C.4 and the Table C.1. A similar case is cell A where the χ^{BSI} is lower than 0.8, which means the cyclic stretch should have an impact on endothelial cells. However, the WSS is higher than 0.55 Pa dominating the endothelial cell orientation. Hence, the white arrow still overlaps the red arrow, i.e. the endothelial cells orient with the WSS direction. The representative case of endothelial cell influenced by both WSS and cyclic stretch is the cell B. At this location, the blue arrow means the resultant cyclic stretch direction which gives the signal to the endothelial cell to reorient perpendicular to this location. Also with the participation of WSS with the weight ($W=0.2647$), the endothelial cell orients in the direction eventually showed by the white arrow.

The above 2D space modelling could be regarded as a piece of arterial tissue. Fig C.5 provides a view of the distribution of endothelial cells population experienced with the combined WSS and cyclic stretch in cubic space. This illustration of the orientation of endothelial cells in 3D space aims to declare the possibility of modelling the endothelial cells alignment in complex geometries. All the procedures follow the method above except the orientations were set as random, not in-plane. Again, the white arrows represent the final endothelial cells orientation influenced by WSS (red arrow) and the processed cyclic stretch (blue) via the algorithm shown in Fig C.2. Furthermore, to fulfil our algorithm more understandably, a simple cylinder model was made containing 20 endothelial cells in Fig C.6 (left). The cell centres are showed by the asterisks symbols and the red arrows are the normal direction to each facet on the cylinder surface. Then the WSS and cyclic stretch were imposed with random directions in-plane for each cell. Running the same algorithm, the final orientation of each endothelial cell could be calculated (white arrow).

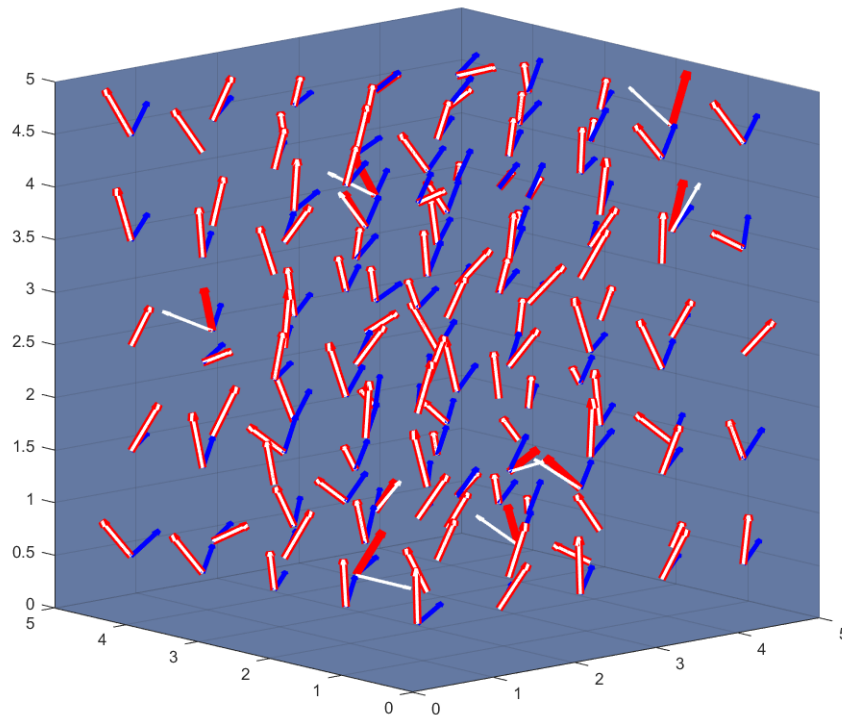


Figure C.5: Schematic diagram of the final orientation of endothelial cells influenced by WSS and cyclic stretch in a 3D space. (red arrow: WSS; blue arrow: cyclic stretch; white arrow: endothelial cells orientation)

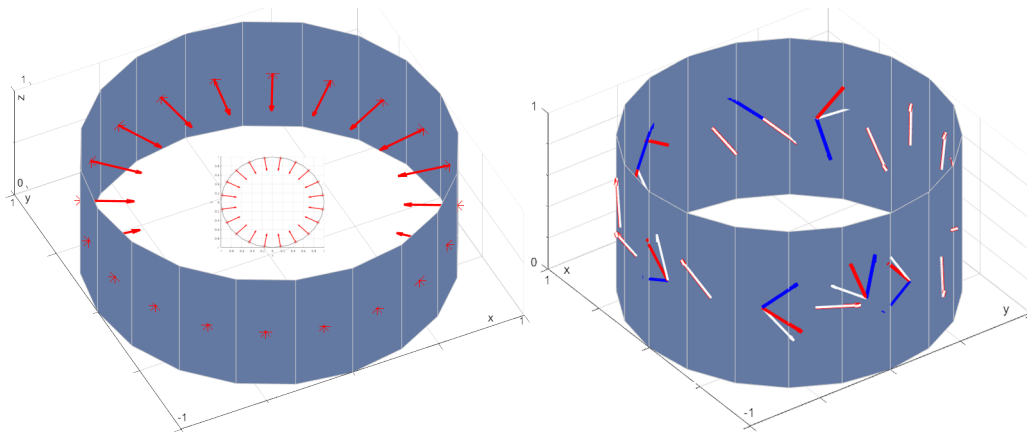
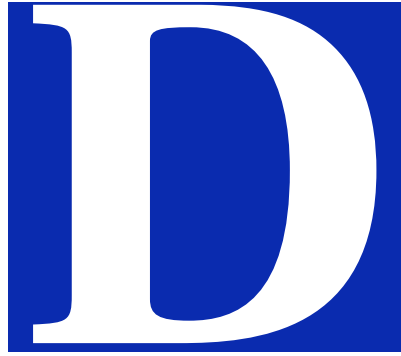


Figure C.6: Schematic diagram of the final orientation of endothelial cells influenced by WSS and cyclic stretch in a cylindrical model. (red arrow: WSS; blue arrow: cyclic stretch; white arrow: endothelial cells orientation)

Heretofore, 1D modelling of endothelial cells alignment under the impact of both WSS and cyclic stretch has been implemented in the scenarios of a 2D plane, 3D cubic space and a simple cylinder geometry. This methodology provides the possibility of further 3D modelling of endothelial cells alignment.



Matlab Script of G&R Function in the P-FSG Framework

%% main functions of this script

 % Specify time zones:

 % step 1: Material parameters for initial structural analysis ANSYS

 % step 2: Fibroblast Recruitment Stretch Field

 % step >2: Degradation, Growth & Remodelling

 % divide the region to 3 parts: aneurysm, transitional region, parent vessel

 % 1. considering the collagen mass density

 % 2. Elastin degrades with high AR (from step 3)

 % 3. collagen degrades with high AR (from step 3)

 % 4. collagen mass density regulated by fibroblasts stretch deviation (from step 3)

 % 5. collagen remodels (k2) with cauchy fibre stress deviation (from step 4)

%% Define modelling paramters here

%%Geometric parameters for specification of z-regions for G&R spatial control:

 top = 1; % top limitation of transitional region

 bottom = -1; % bottom limitation of transitional region

```
tmb = top-bottom;
% This is cap for stress-based remodelling function of k1
max-stress-diff-growth-fn = 0.5; %remodelling rate levels off is deviation exceeds 50% of original stress

%degradation rate
prescribedegradation = 1; %if 1 prescribed, else link to flow.
prescribe-el-deg-rate = 0.8;%elastin degradation rate
prescribe-col-deg-rate = 0.8;%collagen degradation rate

%Region of Degradation
localised = 1;% if prescribed and 1, localise to a specific region of sac.
%Coordinates and radius of Sphere of influence for degradation
sphere-x = -2; sphere-y = 4; sphere-z = 4;sphere-r = 8;
%Polynomial exponent for spatial degradation
polyexp = 4;

%ELASTIN
% elastin mass density
mE-p = 1; %Parent artery
mE-a = 0.05; %aneurysm sac
%Neo-Hookean shear modulus
k-p = 0.5; %Parent artery (MPa)
k-a = 0.5; %aneurysm sac (MPa)
%Effective shear modulus for ANSYS (Neo-Hookean)
c-p = k-p*mE-p; %Parent artery (MPa)
c-a = k-a*mE-a; %aneurysm sac (MPa)

%COLLAGEN
% collagen mass density
mC-p = 1; %parent artery
mC-a = 1; %aneurysm sac
%collagen mass density mC1 for degradation
mC1-I4=1;
mC1-I6=1;
%collagen mass density mC2 for growth
```

```

mC2-I4=1;
mC2-I6=1;
%collagen mass density mC
mC-I4=mC1-I4*mC2-I4;
mC-I6=mC1-I6*mC2-I6;

%k1 value
k1-a = 1; %MPa
k1-a-I4 = k1-a; k1-a-I6 = k1-a; %MPa on aneurysm
k1-p = 1;
k1-p-I4 = k1-p; k1-p-I6 = k1-p; %MPa parent-vessel
%Collagen k2
k2-a=0.01;
k2-a-I4 = k2-a; k2-a-I6 = k2-a; %k2 value of a01/a02 collagen families on aneurysm
k2-p = 0.01; %k2 value of a01/a02 collagen families on parent vessel
%k1 values for ANSYS
k1-mC-a-I4= mC1-I4*mC2-I4*k1-a-I4; %k1 in the ANSYS (I4)
k1-mC-a-I6= mC1-I6*mC2-I6*k1-a-I6; %k1 in the ANSYS (I6)
%AR metric %Thresholds for flow stimuli
AR-crit = 0.5;
AR-max = 0.75;
%Degradation parameters
%at most 10% of the existing elastinous constituents are degraded per year
max-elastin-degradation = 0.1; %maximum amount of the existing collagenous constituents
are degraded per year
max-collagen-degradation = 0.1;
%Collagen G&R parameters
%Growth (stretch-based stimulus on fibroblasts)
lambda-F-AT = 1.05; %attachment stretch of fibroblasts
alpha-F = 0.1; % a numerical parameter indicating the biological response to stretch (fibrob-
last remodelling)
beta-F = 10; % $\beta$  is a phenomenological growth parameter that relates to the rate at which the
fibroblasts increase or decrease the mass of the collagenous constituents in response to de-
viations of stretch from normotensive levels.

%Remodelling (via k1 or k2)

```

```

collagen-remodelling-rate = 0.1; % used in the collagen remodelling function

%% Files to be imported here
% load centroid coordinates of element and get the z coordinates
step-number=load('step-file.txt');
IDelement-centroid=load('.\element-centroid.dat');
x=IDelement-centroid(:,2); % x coordinate of each element centroid
y=IDelement-centroid(:,3); % y coordinate of each element centroid
z=IDelement-centroid(:,4); % z coordinate of each element centroid
[ row, ~]=size(IDelement-centroid);

%Define output files here:
fid=fopen('c-k-value.dat','wt');
% output data: c, k1-ANSYS-I4,K1-ANSYS-I6, k1(I6), k2(I6), mE, mC(I4), mC(I6), lambda-
F,lambda-F,lambda-F-Rc-I4,lambda-F-Rc-I6, % mC1-I4, mC1-I6, mC2-I4, mC-I6, k1(I4), k2(I4))

%% the Time 1, original state
if step-number==1
for i=1:row
%aneurysm sac
if (z(i)>=top)
fprintf(fid,...,c-a,mC-a*k1-a,k2-a,mC-a*k1-a,k2-a,... mE-a,mC-a,mC-a,0,0,0,0,mC1-I4,
mC1-I6,mC2-I4,mC2-I6, k1-a, k1-a);
%parent artery
elseif (z(i)<bottom)
fprintf(fid,...,c-p,mC-p*k1-p,k2-p,mC-p*k1-p,k2-p, mE-p,mC-p,mC-p,0,0,0,0,mC1-I4,
mC1-I6,mC2-I4,mC2-I6, k1-p, k1-p);
%transition region
elseif (z(i)>=bottom&&z(i)<top)
zinterp = (z(i)-bottom)/tmb;
%Elastin
mE-t(i) = mE-p+((mE-a-mE-p)*zinterp);
c-t(i) = k-p*mE-t(i);
%Collagen (mcp and mca are equal)
if mC-p =mC-a
mC-t(i) = mC-p+(mC-a-mC-p)*zinterp;
else

```

```

mC-t(i) = mC-p;
end
%interpolation of k1
k1-I4-t(i) = k1-p+(zinterp*(k1-a-I4-k1-p));
k1-I6-t(i) = k1-p+(zinterp*(k1-a-I6-k1-p));
%stiffness parameter for collagen - product of density*k1
k1-mC-I4-t(i) = mC-t(i)*k1-I4-t(i);
k1-mC-I6-t(i) = mC-t(i)*k1-I6-t(i);
%interpolation of k2
k2-I4-t(i) = k2-p+(zinterp*(k2-a-I4-k2-p));
k2-I6-t(i) = k2-p+(zinterp*(k2-a-I6-k2-p));
fprintf(fid,...,c-t(i),mC-t(i)*k1-I4-t(i),k2-I4-t(i),mC-t(i)*k1-I6-t(i),k2-I6-t(i),mE-t(i),mC-t(i),mC-
t(i),0,0,0,0, mC1-I4,mC1-I6,mC2-I4,mC2-I6, k1-I4-t(i), k1-I6-t(i));
end
end
end

%% the Time 2
if step-number==2
%THIS STEP DEFINES THE FIBROBLAST RECRUITMENT STRETCH FIELD
% load the stretch results
filename = ['stretch-cauchy-stress',int2str(step-number-1),'.dat'];
stretch = load(filename);
stretch-I4 = stretch(:,1);
stretch-I6 = stretch(:,2);
lambda-F-Rc-I4 = stretch-I4/lambda-F-AT;
lambda-F-Rc-I6 = stretch-I6/lambda-F-AT;
    for i=1:row
% aneurysm region, highest elastin and collagen degradation
        if z(i)>=top
fprintf(fid,'c-a,mC-a*k1-a-I4,k2-a-I4,mC-a*k1-a-I6,k2-a-I6,mE-a,mC-a,mC-a,
lambda-F-AT,lambda-F-AT,lambda-F-Rc-I4(i),lambda-F-Rc-I6(i),mC1-I4,mC1-I6,
mC2-I4,mC2-I6, k1-a-I4, k1-a-I6);
        elseif z(i)<bottom
fprintf(fid,c-p,mC-p*k1-p,k2-p,mC-p*k1-p,k2-p,mE-p,mC-p,mC-p,lambda-F-AT,
lambda-F-AT,lambda-F-Rc-I4(i),lambda-F-Rc-I6(i),mC1-I4,mC1-I6,mC2-I4,mC2-I6,

```

```

k1-p-I4, k1-p-I6 );
% transitional region, no elastin and collagen degradation
    elseif z(i)>=bottom && z(i)<top
zinterp = (z(i)-bottom)/tmb;
%elastin
mE-t(i) = mE-p+((mE-a-mE-p)*zinterp);
c-t(i) = k-p*mE-t(i);
%collagen mC1
mC1-I4-t(i) = mC-p+((mC-a-mC-p)*zinterp);
mC1-I6-t(i) = mC-p+((mC-a-mC-p)*zinterp);
%Collagen Growth mC2 mC2-I4-t(i) = mC2-I4;
mC2-I6-t(i) = mC2-I6;
%k1
k1-I4-t(i) = k1-p+((k1-a-I4-k1-p)*zinterp);
k1-I6-t(i) = k1-p+((k1-a-I6-k1-p)*zinterp);
%k2
k2-I4-t(i) = k2-p+(k2-a-I4-k2-p)*zinterp;
k2-I6-t(i) = k2-p+(k2-a-I6-k2-p)*zinterp;
%Collagen Mass mC
mC-I4-t(i) = mC1-I4-t(i)* mC2-I4-t(i);
mC-I6-t(i) = mC1-I6-t(i)* mC2-I6-t(i);
%ANSYS k1*mC1*mC2
k1-mC-I4-t(i)=k1-I4-t(i)*mC-I4-t(i);
k1-mC-I6-t(i)=k1-I6-t(i)*mC-I6-t(i);
%Output
fprintf(fid,...,c-t(i),k1-mC-I4-t(i),k2-I4-t(i),k1-mC-I6-t(i),k2-I6-t(i),mE-t(i),mC-I4-t(i),
mC-I6-t(i), lambda-F-AT,lambda-F-AT,lambda-F-Rc-I4(i),lambda-F-Rc-I6(i),mC1-I4-t(i),mC1-
I6-t(i),mC2-I4-t(i),mC2-I6-t(i), ... k1-I4-t(i),k1-I6-t(i));
    end
    end
end

%% the Time 3.....n
    if step-number>2
% IMPORT DATA
% read the c, k1, k2, mE, mC value from last step

```

```

filename=['c-k-value',int2str(step-number-1),'dat'];
c-k-last-step=load(filename);
c-last-step = c-k-last-step(:,1);
k1-last-step-I4 = c-k-last-step(:,17);
k2-last-step-I4 = c-k-last-step(:,3);
k1-last-step-I6 = c-k-last-step(:,18);
k2-last-step-I6 = c-k-last-step(:,5);
mE-last-step = c-k-last-step(:,6);
mC1-I4-last-step = c-k-last-step(:,13);
mC1-I6-last-step = c-k-last-step(:,14);
mC2-I4-last-step = c-k-last-step(:,15);
mC2-I6-last-step = c-k-last-step(:,16);
% recruitment stretch of fibroblasts from the last step
lambda-F-Rc-I4-last = c-k-last-step(:,11);
lambda-F-Rc-I6-last = c-k-last-step(:,12);
% load the stretch and cauchy stress result
cauchy-stress1=load('./stretch-cauchy-stress1.dat');
cauchy-stress2=load('./stretch-cauchy-stress2.dat');
% stretch in the direction of collagen fibres
stretch-I4=cauchy-stress2(:,1);
stretch-I6=cauchy-stress2(:,2);
% stretch on fibroblast
lambda-F-I4=stretch-I4./lambda-F-Rc-I4-last;
lambda-F-I6=stretch-I6./lambda-F-Rc-I6-last;
    for i=1:row % aneurysm region, highest elastin degradation, collagen remodelling
        if z(i)>=top
%ALL GROWTH AND REMODELLING IS CONTROLLED HERE and FUNCTIONS at the end.
%%%%%%%%%%
%%%%%%%%%%
            if (prescribedegradation==1)
                if (localised==1)
localdegfactor=spatialdeg(x(i),y(i),z(i),sphere-x,sphere-y,sphere-z,sphere-r,polyexp);
                    else
localdegfactor=1;
                end
            el-deg-rate = 1 + (prescribe-el-deg-rate-1)*localdegfactor;

```

```

col-deg-rate = 1 + (prescribe-col-deg-rate-1)*localdegfactor;
%elastin degradation
mE-t(i) = mE-last-step(i)* el-deg-rate;
%collagen degrades
mC1-I4-t(i) = mC1-I4-last-step(i)* col-deg-rate;
mC1-I6-t(i) = mC1-I6-last-step(i)* col-deg-rate;

    else
% load the CFD result
centroid-cfd=importdata('centroid-cfd-pulsatile.dat');
AR=centroid-cfd.data(:,6);
%Linking Growth and remodelling with flow AR in this region (see Function)
[mE - deg - i, mCdeg - i]=degradation(AR(i), AR-crit, AR-max);
%elastin degradation with AR
mE-t(i) = mE-last-step(i)*(1-mE-deg-i*max-elastin-degradation);
%collagen degrades with AR
mC1-I4-t(i) = mC1-I4-last-step(i)*(1-mCdeg-i*max-collagen-degradation);
mC1-I6-t(i) = mC1-I6-last-step(i)*(1-mCdeg-i*max-collagen-degradation);

    end
c-t(i) = k-a*mE-t(i);
%fibroblast recruitment stretch remodels
lambda-F-Rc-I4-t(i)=Fibroblast-Remodelling(lambda-F-I4(i),lambda-F-AT,alpha-F,
lambda-F-Rc-I4-last(i));
lambda-F-Rc-I6-t(i)=Fibroblast-Remodelling(lambda-F-I6(i),lambda-F-AT,alpha-F,
emolambda-F-Rc-I6-last(i));
% collagen growth mediated by fibroblasts
mC2-I4-t(i)=Fibroblast-Growth(lambda-F-I4(i),lambda-F-AT,beta-F,mC2-I4-last-step(i));
mC2-I6-t(i) =Fibroblast-Growth(lambda-F-I6(i),lambda-F-AT,beta-F,mC2-I6-last-step(i));
%collagen remodelling - k1
k1-I4-t(i) = rem-k1-CS(cauchy-stress2(i,3),cauchy-stress1(i,3),collagen-remodelling-rate,k1-
last-step-I4(i),max-stress-diff-growth-fn);
k1-I6-t(i) = rem-k1-CS(cauchy-stress2(i,4),cauchy-stress1(i,4),collagen-remodelling-rate,k1-
last-step-I6(i),max-stress-diff-growth-fn);
%collagen remodelling - k2 (no remodelling)
k2-I4-t(i) = k2-a-I4;
k2-I6-t(i) = k2-a-I6;
%%%%%%%%%%%%%%

```

```

% END OF G&R IN ANEURYSM SAC %
%%%%%%%%%%%%%%%%%%%%%%%%%%%%%%%%%%%%%%%%%%%%%%%%%%%%%%%%%%%%%%%%%%%%%%%%
% Update Total Collagen Mass Density mC
mC-I4-t(i) = mC1-I4-t(i)* mC2-I4-t(i);
mC-I6-t(i) = mC1-I6-t(i)* mC2-I6-t(i);
%Update k1 stiffness parameter for ANSYS
k1-mC-I4-t(i) = k1-I4-t(i)*mC-I4-t(i);
k1-mC-I6-t(i) = k1-I6-t(i)*mC-I6-t(i);
% parent vessel region
    elseif z(i)<bottom
%elastin
mE-t(i) = mE-p;
c-t(i) = k-p;
%collagen mC1
mC1-I4-t(i) = mC-p;
mC1-I6-t(i) = mC-p;
%Collagen Growth mC2
mC2-I4-t(i) = mC2-I4;
mC2-I6-t(i) = mC2-I6;
%Collagen Mass mC
mC-I4-t(i) = mC1-I4-t(i)* mC2-I4-t(i);
mC-I6-t(i) = mC1-I6-t(i)* mC2-I6-t(i);
%k1 k1-I4-t(i) = k1-p;
k1-I6-t(i) = k1-p;
%ANSYS k1*mC1*mC2
k1-mC-I4-t(i)=k1-I4-t(i)*mC1-I4-t(i)*mC2-I4-t(i);
k1-mC-I6-t(i)=k1-I6-t(i)*mC1-I6-t(i)*mC2-I6-t(i);
%k2 k2-I4-t(i) = k2-p;
k2-I6-t(i) = k2-p;
%Prescribe Fibroblast recruitment stretches to maintain homeostatic fibroblast stretch in
this region
lambda-F-Rc-I4-t(i) =stretch-I4(i)/lambda-F-AT;
lambda-F-Rc-I6-t(i) =stretch-I6(i)/lambda-F-AT;
% transitional region
    elseif z(i)>=bottom && z(i)<top
zinterp = (z(i)-bottom)/tmb;

```

```

%elastin
mE-t(i) = mE-p+((mE-a-mE-p)*zinterp);
c-t(i) = k-p*mE-t(i);
%collagen mC1
mC1-I4-t(i) = mC-p+((mC-a-mC-p)*zinterp);
mC1-I6-t(i) = mC-p+((mC-a-mC-p)*zinterp);
%Collagen Growth mC2
mC2-I4-t(i) = mC2-I4;
mC2-I6-t(i) = mC2-I6;
%Collagen Mass mC mC-I4-t(i) = mC1-I4-t(i)* mC2-I4-t(i);
mC-I6-t(i) = mC1-I6-t(i)* mC2-I6-t(i);
%k1 k1-I4-t(i) = k1-p+((k1-a-I4-k1-p)*zinterp);
k1-I6-t(i) = k1-p+((k1-a-I6-k1-p)*zinterp);
%ANSYS k1*mC1*mC2 k1-mC-I4-t(i)=k1-I4-t(i)*mC-I4-t(i);
k1-mC-I6-t(i)=k1-I6-t(i)*mC-I6-t(i);
%k2 k2-I4-t(i) = k2-p+(k2-a-I4-k2-p)*zinterp;
k2-I6-t(i) = k2-p+(k2-a-I6-k2-p)*zinterp;
%Prescribe Fibroblast recruitment stretches to maintain homeostatic fibroblast stretch in
this region
lambda-F-Rc-I4-t(i) =stretch-I4(i)/lambda-F-AT;
lambda-F-Rc-I6-t(i) =stretch-I6(i)/lambda-F-AT;
    end
%Output
fprintf(fid,...,c-t(i),mC-I4-t(i)*k1-I4-t(i),k2-I4-t(i),mC-I6-t(i)*k1-I6-t(i),k2-I6-t(i),mE-t(i),
mC-I4-t(i),mC-I6-t(i), lambda-F-I4(i),lambda-F-I6(i),lambda-F-Rc-I4-t(i),lambda-F-Rc-I6-t(i),mC1-
I4-t(i),mC1-I6-t(i),mC2-I4-t(i),mC2-I6-t(i), k1-I4-t(i),k1-I6-t(i));
    end
fclose(fid);
close all
    end
exit;
%%%%%%%%%%%%%%%%%%%%%%%%%%%%%%%%%%%%%%%%%%%%%%%%%%%%%%%%%%%%%%%%%%%%%%%%
% LOCAL USER-DEFINED FUNCTIONS FOR SCRIPT %
%%%%%%%%%%%%%%%%%%%%%%%%%%%%%%%%%%%%%%%%%%%%%%%%%%%%%%%%%%%%%%%%%%%%%%%%
function [deg-intensity] = spatialdeg(xloc,yloc,zloc,x0,y0,z0,r,fn-exp);
%Calculate distance of all points from centre of Sphere of Influence

```

```
distloc = ((xloc-x0)2 + (yloc-y0)2 + (zloc-z0)2)1/2;
```

```
    if (distloc<r)
```

```
deg-intensity = ((r-distloc)/r)n-exp;
```

```
    else
```

```
deg-intensity = 0;
```

```
    end
```

```
end
```

```
function [out-el,out-col]=degradation(flowstimulus, AR-crit, AR-max)
```

```
    if flowstimulus>=AR-max
```

```
out-el = 1;
```

```
out-col = 1;
```

```
    elseif flowstimulus<AR-max && flowstimulus>=AR-crit
```

```
out-el = ((flowstimulus-AR-crit)/(AR-max-AR-crit))2;
```

```
out-col = (flowstimulus-AR-crit)/(AR-max-AR-crit);
```

```
    else
```

```
out-el = 0;
```

```
out-col = 0;
```

```
    end
```

```
end
```

```
function [k1-t]=rem-k1-CS(cst,cshom,rate,k1-last-step,max-stress-diff-growth-fn)
```

```
    if cst>0
```

```
dev=(cst-cshom)/cshom;
```

```
    if dev<=max-stress-diff-growth-fn
```

```
diff = dev;
```

```
    elseif dev >max-stress-diff-growth-fn
```

```
diff = max-stress-diff-growth-fn;
```

```
    else
```

```
diff = 0;
```

```
    end
```

```
k1-t = k1-last-step-(rate*diff*k1-last-step);
```

```
    if k1-t < 0.001
```

```
k1-t = 0.001;
```

```
    end
```

```
    else
```

```
k1-t = k1-last-step;  
    end  
end
```

```
%Fibroblast Remodelling and Growth Functions
```

```
function [mCt]=Fibroblast-Growth(stretch,att-stretch,rate,var-last-step)  
mCt = var-last-step + (var-last-step*rate*(stretch-att-stretch)/att-stretch);  
    if mCt<0.01  
mCt = 0.01;  
    end  
end
```

```
%Fibroblast Recruitment Stretch Remodels
```

```
function [rec] = Fibroblast-Remodelling(stretch,att-stretch,rate,var-last-step)  
rec = var-last-step + (var-last-step*rate*(stretch-att-stretch)/att-stretch);  
    if rec<0.1  
rec = 0.1;  
    end  
end
```

